Volatile element behaviour in cometary ice analogues under irradiation

Matthieu Almayrac

To cite this version:

Matthieu Almayrac. Volatile element behaviour in cometary ice analogues under irradiation. Sciences of the Universe [physics]. Université de Lorraine, 2022. English. NNT : 2022LORR0320 . tel-04277295

HAL Id: tel-04277295

https://hal.univ-lorraine.fr/tel-04277295v1

Submitted on 9 Nov 2023

UNIVERSITE DE LORRAINE

Ecole doctorale SIReNa

Centre de Recherches Pétrographiques et Géochimiques

THESE DE DOCTORAT

Présentée et soutenue publiquement le 2 décembre 2022 pour l'obtention du titre de

Docteur de l'Université de Lorraine (spécialité Géosciences)

Par Matthieu ALMAYRAC

Volatile element behaviour in cometary ice analogues under irradiation

Comportement des éléments volatils dans les glaces cométaires irradiées

---

Membres du jury

Directeur de thèse
Prof. Bernard MARTY, Université de Lorraine, Centre de Recherches Pétrographiques et Géochimiques (France)
Co-Encadrante
Dr. Laurette PIANI, Centre de Recherches Pétrographiques et Géochimiques (France)

Rapporteurs
Prof. Katherine JOY, Department of Earth and Environmental Science, Université de Manchester (Royaume-Uni)
Dr. Martin RUBIN, Université de Berne (Suisse)

Examinateurs
Prof. Christophe SOTIN, LGP, Université de Nantes (France)

Présidente du jury
Dr. Dominique BOCKELÉE-MORVAN, LESIA, Observatoire de Paris, Université PSL (France)

Invité
Dr. David Bekaert, Université de Lorraine, Centre de Recherches Pétrographiques et Géochimiques (France)

Abstract in English

Comets represent some of the most pristine and unprocessed bodies in our solar system. As such, their analysis can provide a unique insight into the chemical makeup of the early Solar System. Furthermore, due to their volatile-rich nature, comets may have played an important role in delivering volatile elements (e.g., H, C, N, O) and organic materials to the early Earth. Understanding how comets form can therefore provide a wealth of information on how the composition of volatile elements evolved in the solar system, from the pre-solar molecular cloud up until the formation of the terrestrial planets.

Decades of cometary studies, and the recent ESA Rosetta mission to comet 67P/Churyumov-Gerasimenko (67P/C-G), have demonstrated that volatile species trapped in comets have a composition that is distinct from any other known reservoir in the Solar System. Cometary nitrogen, in particular, shows strong enrichments in the rare ^{15}N isotope. The origin of these enrichments remains unclear, potentially reflecting the isotopic fractionation of an initial ^{15}N-poor nebular gas, or inheritance from an unknown isotopic reservoir.

During this PhD, I have developed an experimental setup to form cometary ices (i.e., water-rich ices formed at very low temperatures and pressures), with the overarching objective of exploring how volatile elements (including N and noble gases) were incorporated into cometary ice during water condensation from the protosolar nebula. Different temperatures of formation (from 28K to 80K) and irradiation conditions have been tested in order to investigate the conditions that best reproduce the actual volatile composition of comet 67P/C-G.

It was found that condensing cometary ice analogues at temperatures ~70K is best able to reproduce the nitrogen and noble gas abundances measured in 67P/C-G. Moreover, we discovered that the incorporation of nitrogen and noble gases into, and subsequent release from, cometary ices does not produce significant isotope variations, indicating that isotope signatures in comets were most likely inherited from their environment of formation rather than the result of fractionation during ice formation.

Finally, I also investigated the effect that UV irradiation can have on the composition of volatiles trapped within cometary ice. Irradiation during and after ice deposition was found to not have a significant effect on the isotopic composition of the trapped volatile species. However, it was discovered that irradiating the surface of the ice had a major effect on the release pattern of trapped volatiles, with the ice being retentive of trapped volatiles even after the amorphous-to-crystalline ice transition (120-140K), temperatures at which point all trapped volatiles are released from non-irradiated ice. The enhanced retention of volatiles in irradiated cometary ice may have major implications on the potential for comets to deliver volatile elements to the inner solar system.

Résumé en français

Les comètes sont parmi les corps les plus primitifs et inaltérés de notre système solaire. Leur étude peut fournir un aperçu unique de la composition chimique du système solaire primitif. De plus, en raison de leur nature riche en élément volatils, les comètes ont probablement joué un rôle crucial dans l’apport d’éléments pré-biotiques (H, C, N et O) et de matières organiques à la Terre primitive. Comprendre comment se forment les comètes peut donc fournir une mine d'informations sur l'évolution de la composition des éléments volatils dans le système solaire, depuis le nuage moléculaire pré-solaire jusqu'à la formation des planètes telluriques.

Des décennies d'études cométaires, et la récente mission Rosetta de l'ESA sur la comète 67P/Churyumov-Gerasimenko (67P/C-G), ont démontré que les espèces volatiles piégées dans les comètes ont une composition distincte de tout autre réservoir connu du système solaire. L'azote cométaire, en particulier, présente de forts enrichissements en isotope ^{15}N. L'origine de ces enrichissements reste incertaine, reflétant potentiellement la présence de processus permettant de produire de forts fractionnements isotopiques d'un gaz nébulaire initial pauvre en ^{15}N, ou l'héritage d'un réservoir isotopique riche en ^{15}N inconnu.

Au cours de cette thèse, j'ai développé une expérience pour former des glaces cométaires (c'est-à-dire des glaces riches en eau formées à des températures et des pressions très basses), avec l'objectif principal d'explorer comment les éléments volatils (l’azote et les gaz nobles) sont incorporés dans les glaces cométaires à partir de la nébuleuse proto-solaire. Différentes températures de formation (de 28K à 80K) et conditions d'irradiation ont été testées afin d'étudier les paramètres reproduisant le plus fidèlement la composition de la comète 67P/C-G.

Les analogues de glace cométaires formés expérimentalement autour de 70K ont des abondances relatives d'azote et de gaz nobles plus proches de celles mesurées dans 67P/C-G que les analogues formés à plus basses températures (≤ 60K). De plus, j'ai mis en évidence que les processus d'incorporation de l'azote et des gaz nobles dans la glace et leur libération ultérieure ne produisent pas de variations isotopiques significatives. Cela indique que les signatures isotopiques des comètes ont très probablement été héritées de leur environnement de formation, et ne résultent pas de processus de fractionnements isotopiques pendant la formation/sublimation de la glace.

Enfin, j'ai également étudié l'effet que l'irradiation UV peut avoir sur la composition des gaz piégés dans la glace cométaire. L'irradiation pendant et après le dépôt de glace n'a que peu d'effet sur la composition isotopique des espèces volatiles piégées. Cependant, l'irradiation de la surface de la glace a un effet majeur sur le schéma de libération des gaz piégés. Une glace irradiée conserve ses éléments volatils piégés à des températures supérieures à la température de transition de la glace amorphe à cristalline (120-140K), à l’inverse d’une glace non-irradiée. La rétention prolongée des gaz piégés dans les glaces cométaires irradiées peut avoir des implications majeures sur la capacité des comètes à contribuer à l’apport d’éléments volatils aux planètes du système solaire interne.

Table of Content

Chapter 1

Introduction

I. Solar System Formation

1) Formation of Stellar Systems from a Molecular Cloud

Stellar systems form in regions of molecular clouds where the gas density becomes locally high enough to collapse and form a central star. Molecular clouds are areas in the interstellar medium with relatively high concentrations of gas and dust that enable simple molecules (e.g., H_2 and CO) to form, in contrast to the ionised gas that makes up the interstellar medium. They can correspond either to "diffuse" molecular clouds, where the gas density is in the order of ~ 10^2 atoms per cm^3, or "dense" molecular clouds (DMC) with ~ 10^4 atoms per cm^3 (Herbst 2005). As a comparison, the atom density generally reached in ultra-vacuum systems in the laboratory in is the order of ~10^6 atoms per cm^3 (pressure ~ 10^{-10} mbar), so a hundred times denser than the denser areas found in the interstellar medium where stars are born. The temperatures in the central parts of DMCs are in the order of 10-20K, which is colder than the outer parts or in diffuse molecular clouds (~ 50-100K), due to the attenuation of radiating light from neighbouring stars by the higher gas density (Le Petit et al. 2004). Dense molecular clouds can be observed from Earth and identified due to their ability to absorb visible light from background stars, as illustrated in Figure 1.1 for the "black cloud" Barnard 68. They are primarily studied by ground-based or satellite astronomical spectroscopy, probing the infrared absorption spectra emitted from the gas phase (e.g., McCall et al. 1999).

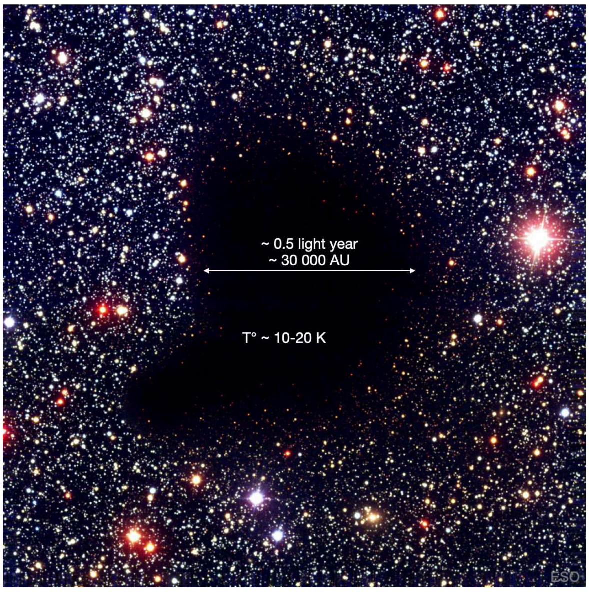

Figure 1.1: The dense molecular cloud called Barnard 68, distant from 500 light years and 0.5 light years across. The cloud absorbs visible light emitted from background stars. Taken from web site https://apod.nasa.gov/apod/ap201122.html.

Molecular clouds are mainly composed of molecular hydrogen gas H_2, with many elements in decreasing abundance such as He, C, N, O, Mg, Si, S and Fe (Snow & Witt 1996). Along with gas, some dust is also present in molecular clouds, in much smaller abundance, with an average gas/dust mass ratio of ~ 100 (Herbst 2005). This dust is mainly composed of nanometric and micrometric silicate grains (Si, Fe, Mg, O) and organic dust (O, C, N) (Greenberg 2002). The precise nature and composition of the gas and dust in a molecular cloud result from the neighbouring stars injecting material into the cloud, when they explode, for example as supernovae (Greenberg 2002; Gaidos et al. 2009). The surfaces of silicate grains are where interstellar ice formation takes place by the adsorption and condensation of atoms and molecules, resulting in ices mainly composed of H_2O, CO, CO_2, CH_3OH or NH_3 (Öberg & Bergin 2021). Irradiation from ultraviolet (UV) photons from nearby stars and cosmic ray particles can affect the gas, grains and ices, but this effect decreases toward the denser centre of the DMC. The lifetime of a molecular cloud in the order of 10 to 30 Myr, before it collapses into one or several stars and their associated forming stellar systems (Blitz & Shu 1980; Murray 2011).

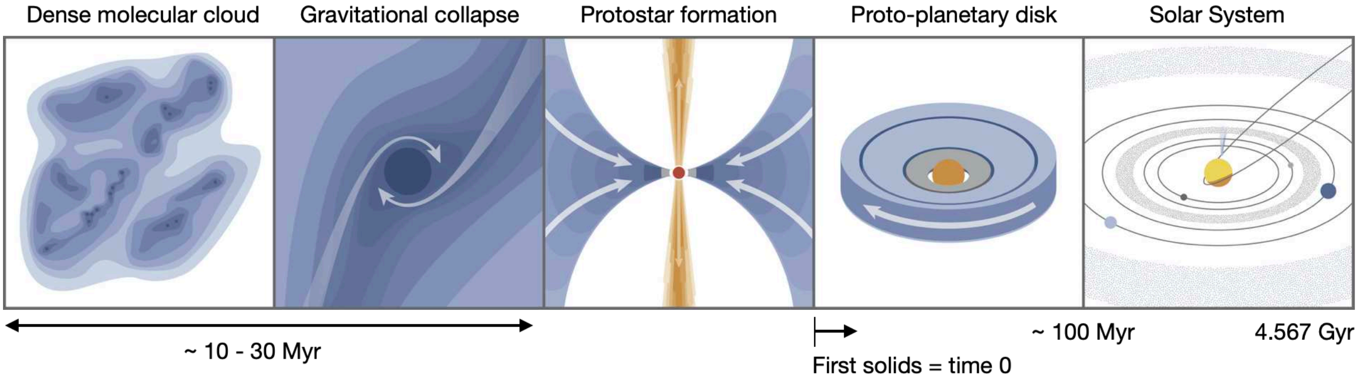

Figure 1.2: Schematics of the Solar System formation, adapted from Öberg & Bergin 2021. The lifetime of a dense molecular cloud before its collapse is in the order of few million years. Complete planetary formation is achieved within the first ~10-100 Myr.

Once the cold and dense molecular cloud gravitationally collapses, matter falls toward the centre and heats up to form a protostar. The cloud material forms a disk around the star (as a consequence of the conservation of angular momentum), called the proto-planetary disk. From the cooling cloud of gas and dust (called the protosolar nebula) the first solids form, and later agglomerate into larger planetesimals and planets. A schematic of the formation of our Solar System is displayed on Figure 1.2.

2) Our Solar System: From Building Blocks to Planets

During the infall of matter from the parent molecular cloud towards the forming protoplanetary disk, because of the intense heat generated by the collapse, most of the grains and ices are melted and sublimated if close enough to the central proto-Sun. Most of the cloud material ends up in the Sun (~99% of the mass of the Solar System at present), with the rest forming the protoplanetary disk made of gas and, further out in the disk, dust settling to the mid-plane. Figure 1.3 shows a schematic depiction of a protoplanetary disk.

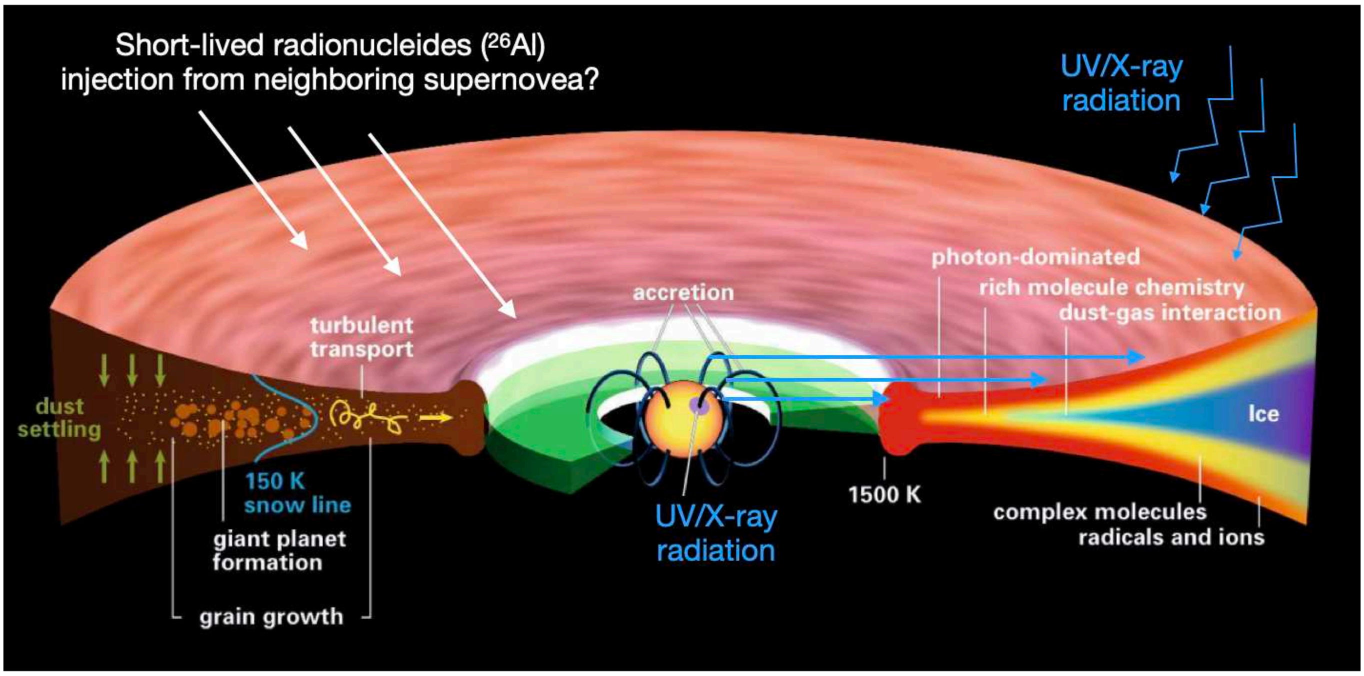

Figure 1.3: schematic representation of the structure of the ~ 1-5 Myr old protoplanetary disk around the central Sun, adapted from Hennings & Semenov (2013).

In the innermost part of the disk where temperature decreases below ~1500°C (Figure 1.3), the first highly refractory solids of the Solar System form: the Calcium-Aluminum-Rich inclusions (CAIs, Krot et al. 2005). The CAIs are used to define the time zero of our Solar System formation since they are the oldest objects formed in our Solar System, with an absolute Pb-Pb age of 4567.3 ± 0.16 Myr (Connelly et al. 2012). Chondrules (silicate nodules rich in olivine and pyroxene) formed between 1 to 3 Myr later (Villeneuve et al. 2009) and agglomerated together with CAIs and organic material to form chondrites, primitive agglomerates of material present in the early Solar System. In the outer part of the disk, beyond the condensation line of water at T ~150 K (the so-called "snow line", Figure 1.3), pristine bodies such as comets may form from the accretion of silicate dusts, organic matter, and ices that sustained limited thermal processing. Ices can either settle into the disk directly from the molecular cloud and/or condense onto grains/dusts beyond their respective condensation front (< 150K, ~ 3 AU for water, or < 50K, ~ 30 AU for CO, where 1 AU is the astronomical unit, Earth-Sun distance) (Mumma & Charnley 2011). The position of the water snow line is crucial for the distribution of water in our Solar System. Inward of the snow line water exists as vapour, and cannot be efficiently incorporated into solids, whilst beyond the snow line the stable ice can be efficiently accreted to form icy bodies such as comets.

The nebular gas in the protoplanetary disk dissipated around ~5 Myr after CAIs (Wang et al. 2017), mostly by accretion to the central star. During the lifetime of the protosolar nebula, the solid materials experienced radial transport inward and outward the disk, leading to agglomeration and accretion into larger bodies, planetesimals and eventually planets (Wetherill, 1980). Turbulent transport of the solid material did not, however, result in the homogenisation of the disk, as the rapid formation of Jupiter (< 2 Myr) likely formed a barrier, limiting mixing between the inner and outer Solar System (Kruijer et al. 2017). The inner Solar System, composed of the rocky planets and the asteroid belt (un-agglomerated planetesimals), is relatively poor in volatile elements because of the high temperatures that existed in early in the Solar System (Figure 1.4). The outer Solar System on the other hand is composed of volatile-rich gaseous and icy planets, and in its most outer parts the Kuiper belt and Oort cloud that are populated with km-sized comets (Figure 1.4).

Earth and the other rocky planets formed inward of the snow line are thus expected to be dry. The origin of rather high contents of water and other volatile elements (C, N, O, etc.) necessary to build life, as we know it on Earth, is longstanding issue in planetary science.

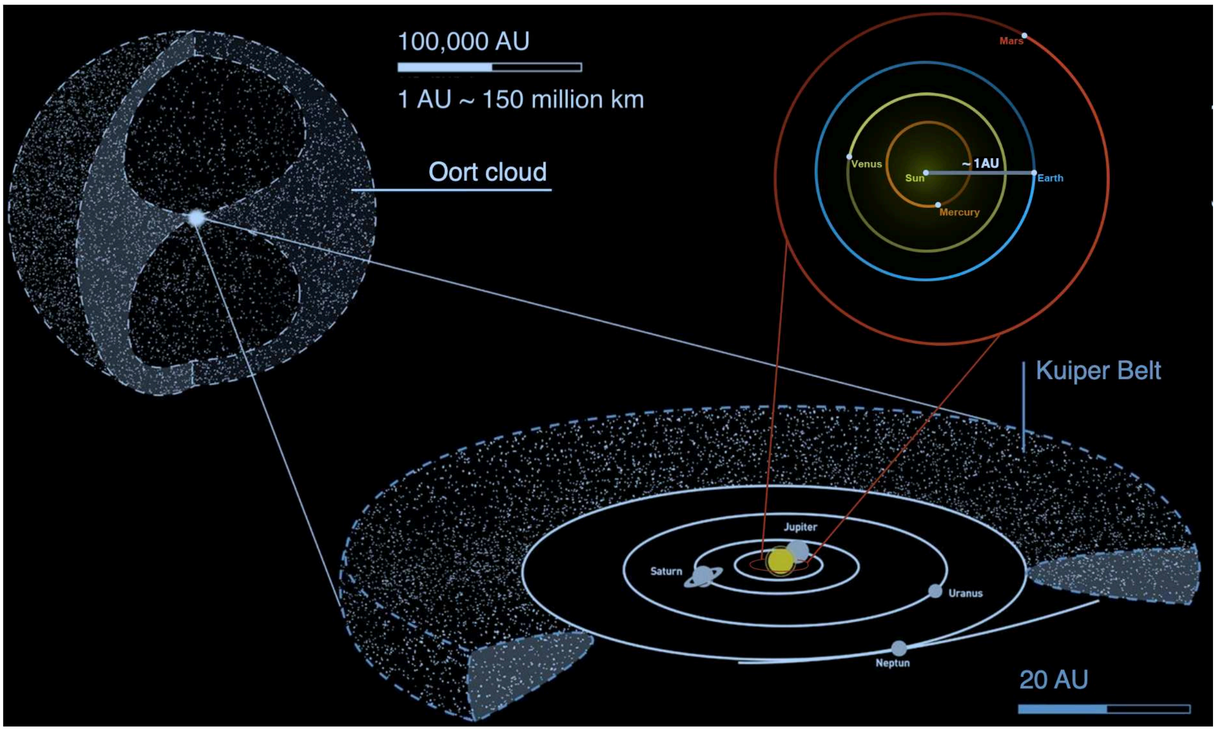

Figure 1.4: Present organization of the planets in the inner and outer Solar System, and the comet reservoirs (Kuiper Belt and Oort Cloud). Modified from Donald K. Yeoman's illustration (NASA, JPL).

II. Volatile Elements on Earth

1) The Origin of Earth's Volatiles

Primitive asteroids and comets found today in the Solar System are made of an assortment of the early building blocks (CAIs, chondrules, ices, organics and silicates) and have remained relatively unprocessed since their formation in the protosolar nebula (PSN). Their study informs us about the building blocks that formed the Earth and the other terrestrial planets, as well as the origin of life-forming volatile elements.

Primitive asteroids can be sampled and analysed directly on Earth thanks to the fall of meteorites. The elemental and isotopic composition of Earth appears to match the composition of a certain type of chondrite: the volatile-poor enstatite chondrites, formed in the inner Solar System (Dauphas 2017). This resemblance to enstatite chondrites indicates that Earth presumably accreted as a dry planetesimal, with its volatile element budget being inherited from a different source (Albarède 2009). Volatile elements including hydrogen (H), carbon (C), nitrogen (N) or oxygen (O) present in the Earth's atmosphere and the bulk silicate Earth have elemental and isotopic composition distinct from those of the PSN (Burnett et al.

2011). Therefore, Earth's volatiles could not have solely been inherited from the gaseous protosolar nebula, but require the contribution from materials originating from the outer parts of the PSN such as carbonaceous chondrites (volatile-rich type of chondrites, CC) and comets (Marty et al. 2012; Alexander et al. 2012).

2) The Role of Noble Gases

Noble gases (He, Ne, Ar, Kr and Xe) are key tools to trace the origin of the life-forming elements on Earth and more generally in the Solar System. Firstly, noble gases are chemically inert, making their abundance and isotopic variability in different objects mainly a result of physical processes such as mixing, evaporation/condensation, diffusion or degassing. Secondly, they are generally found in very low abundances in Solar System material, making them highly sensible to processes changing their composition. Finally, they have elemental and isotopic composition markedly different between the cosmochemical end-members (chondrites, comets, Earth's atmosphere, protosolar nebula) rendering them ideal to trace mixing between reservoirs.

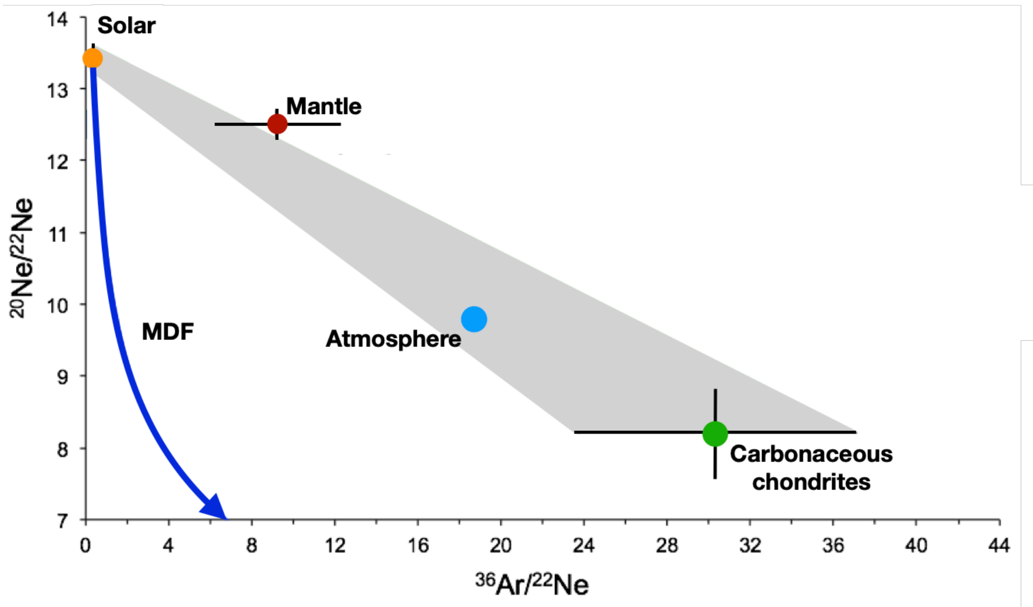

Figure 1.5: Mixing diagram between Solar and carbonaceous chondrite to account for the ^{20}Ne/^{22}Ne vs. ^{36}Ar/^{22}Ne composition of the Earth's atmosphere. Adapted from Marty et al. 2012. MDF = mass-dependent fractionation.

Evidence for the late delivery of volatile elements after Earth's formation from dry material (enstatite-like building blocks, Dauphas 2017) partially relies on the Ar and Ne isotope composition of the Earth's atmosphere. The observation that atmospheric Ar and Ne are isotopically different from the mantle or the solar composition (Figure 1.5), even after accounting for mass-dependent fractionation process, suggests that the atmosphere must have acquired part of its noble gases from a different source than what is found in the mantle. The addition of material similar to carbonaceous chondrites can account for the atmospheric Ar/Ne composition (Figure 1.5, Marty et al. 2012). This is further substantiated by the fact that the composition of highly siderophile elements (e.g., Ru), in the mantle requires the addition of carbonaceous chondrite material after the moon forming impact (Fischer-Gödde et al. 2020). Carbonaceous chondrites are rich in organic matter and volatile elements, therefore their late addition to Earth from the outer Solar System may have played a major role in delivering life-forming elements to Earth.

The recent noble gas measurements in comet 67P/Churyumov-Gerasimenko (67P/C-G) by the European Spatial Agency's Rosetta spacecraft provided clues that comets may also have contributed to the volatile inventory of the Earth. The measurement of the Xe isotope composition of 67P/C-G revealed similar features (deficit in ^{134}Xe and ^{136}Xe) as the initial Xe composition of the Earth (Marty et al. 2017, Figure 1.6). This is taken as evidence that comets delivered ~20% of the total amount of Xe in the Earth's atmosphere (Marty et al. 2017), together with other relevant volatile and organic materials (Rubin et al. 2019; Bekaert et al. 2020).

Although the role of comets in participating to the volatile budget of the Earth was suspected/proposed for many years (Pepin 1991; Owen et al. 1992; Morbidelli et al. 2000), the in-situ measurements performed by Rosetta allowing the first noble gas data for a cometary coma provided the first direct evidence that comets contributed volatiles to Earth. The Rosetta measurements of comet 67P/C-G further motivated the need for understanding the origin of comets and their volatile signatures. Questions on the probable isotope diversity between comets and the representativity of 67P/C-G remains to be investigated. More generally, how and in what environment comets form is still not fully understood, and the origin of their exotic isotope signatures remains to be deciphered.

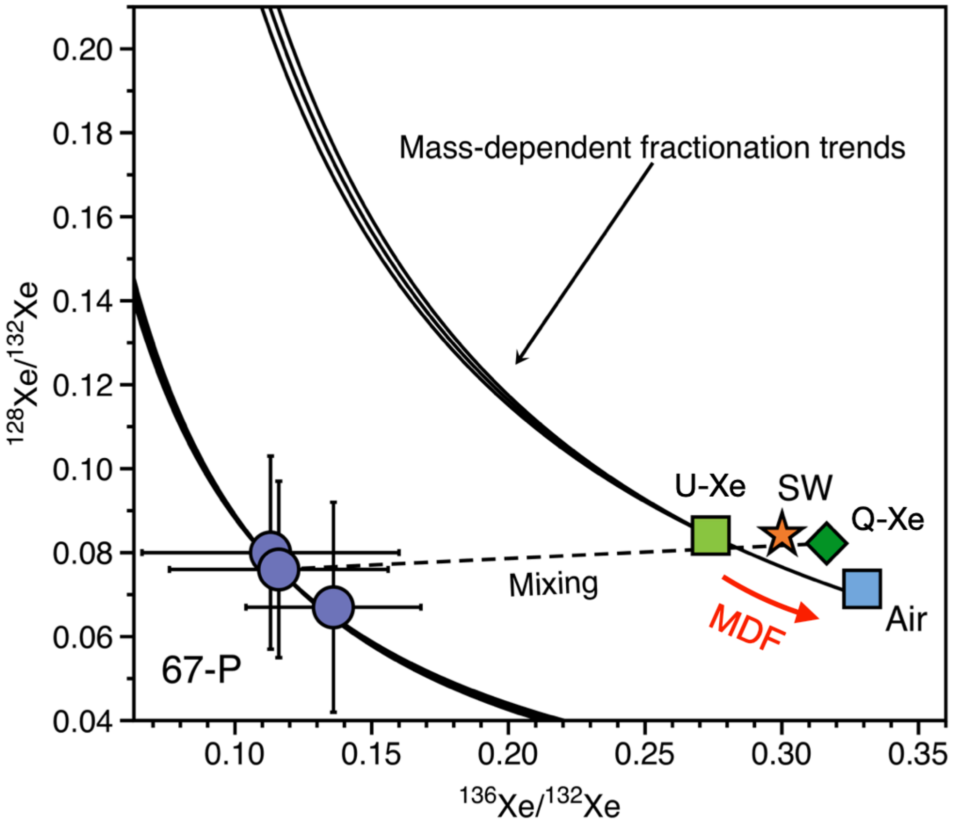

Figure 1.6: Three isotopes plot of Xe (modified from Marty et al., 2017), where the initial Xe composition of the Earth's atmosphere (U-Xe, Pepin 1991) appears to be a mixture of cometary Xe (67P/C-G) and chondritic Xe (Q-Xe, Busemann et al. 2000). MDF = mass-dependent fractionation; SW = solar wind (Meshik et al. 2014).

III. Volatile Elements in Comets: Composition and Origin

Comets, presumably formed in the outermost parts of the PSN, are made of ice (~ 30 – 50 wt.%, Marty et al. 2016) and organic matter and silicates (in variable proportions, Rubin et al. 2019). Comets are thought to be among the most pristine objects in the Solar System. Their origin, whether from the molecular cloud and interstellar medium (Klinger 1980; Bar-Nun et al. 2007) or the PSN (Mousis et al. 2016), remains a major question in the scientific community. Because of their volatile-rich nature, cometary samples are not directly found on Earth due to intense heating and disintegration when they penetrate the atmosphere, contrary to the rocky chondrites. The study of comets is thus relying mostly on remote measurements from ground-based observation and more rarely by space missions.

1) Nitrogen

The nitrogen isotopic composition of comets when compared to other cosmochemical bodies can provide clues on their environment of formation. Nitrogen has two stable isotopes, ^{14}N the most abundant, and ^{15}N. In the Earth's atmosphere the ^{15}N/^{14}N ratio has a value of 0.003676 (Nier, 1950). Amongst the different bodies of the Solar System, nitrogen shows some of the largest isotopic variations (after the hydrogen D/H ratio) (Füri & Marty 2015). These variations are expressed in permil relative to the terrestrial composition by using the delta notation where $\delta^{15}N = (^{15}N/^{14}N\ /\ ^{15}N/^{14}N_{atm} - 1) * 1000$, with $\delta^{15}N_{atm} = 0$ ‰ by definition. Figure 1.7 presents an overview of the δ^{15}N variability in the Solar System, from the ^{15}N-poor composition (e.g., Solar with $\delta^{15}N = -383 \pm 8$ ‰, Marty et al. 2011) to the most ^{15}N-enriched bodies (e.g., comets with δ^{15}N averaging +890 ± 40 ‰, Bockelée-Morvan et al. 2015). High $\delta^{15}N \sim 4500$‰ can also be found at the micrometre-scale in chondritic organic matter (see "hotspots" Figure 1.7; Busemann et al. 2006; Briani et al. 2009).

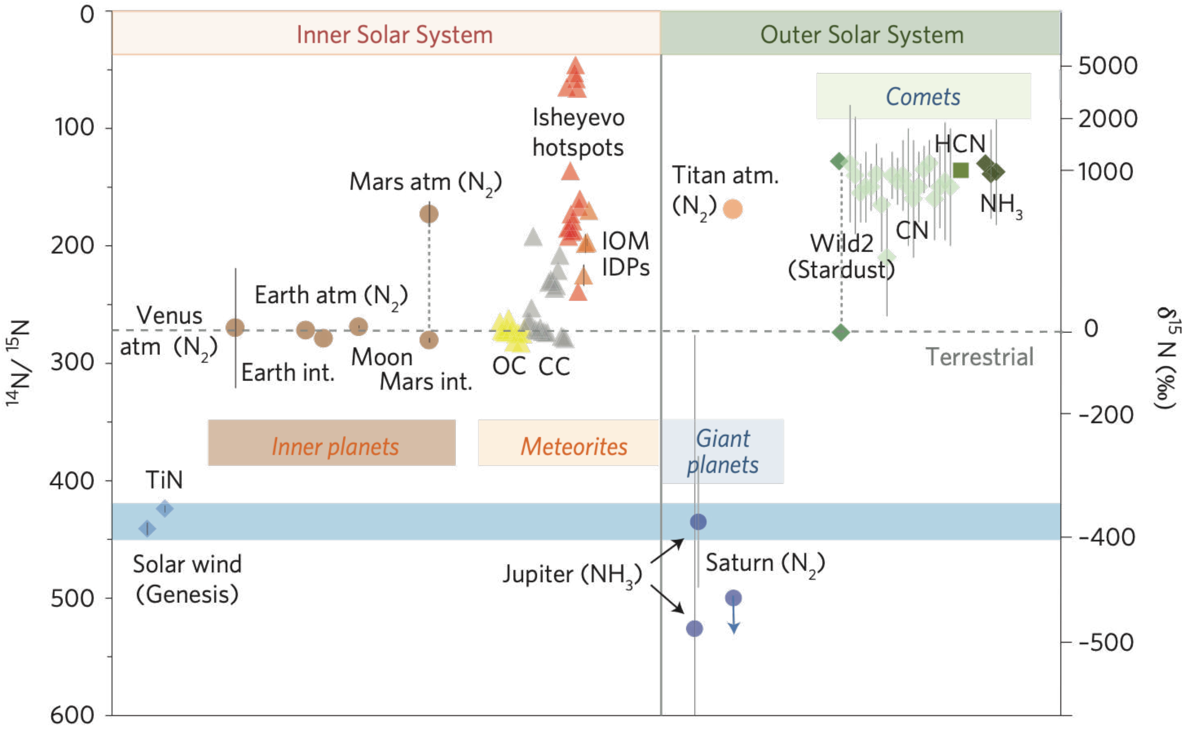

Figure 1.7: Nitrogen isotope variations in Solar System object and reservoirs, adapted from Füri & Marty (2015). Values are more commonly given ^{14}N/^{15}N by astrophysicists, and in δ^{15}N by cosmochemists.

The relatively ^{15}N-poor compositions of inner Solar System bodies are considered to be the result of early thermal processing (~0.3 Myr after CAIs, Füri et al. 2015; Grewal et al. 2022). Because N isotope signatures are broadly homogeneous between comets (Bockelée-Morvan et al. 2015), they may indeed have preserved the isotope composition of a common reservoir. The main nitrogen bearing molecules in cometary comas are N_2, NH_3 and HCN (Altwegg et al. 2019). Ground-based measurements by infrared spectroscopy of N isotopes in comets mainly focus on NH_3, CN and HCN molecules, and show similar δ^{15}N across the different comets for the different N-bearing molecules (~ +900‰, Figure 1.7). The measurement of N_2 is however more challenging and was only remotely observed as an ion N_2^+ in few comets, but its abundance only was computed and not its isotope composition (Cochran & McKay 2018). In-situ measurements in the coma of comet 67P/C-G by Rosetta provided the first isotope composition of cometary N_2 being released from the ice of the comet. The δ^{15}N was determined for three molecules: N_2 (1090 ± 480 ‰), NO (1270 ± 470 ‰) and NH_3 (1300 ± 490 ‰) (Altwegg et al. 2019), all compatible within previous measurements of comets (Figure 1.8).

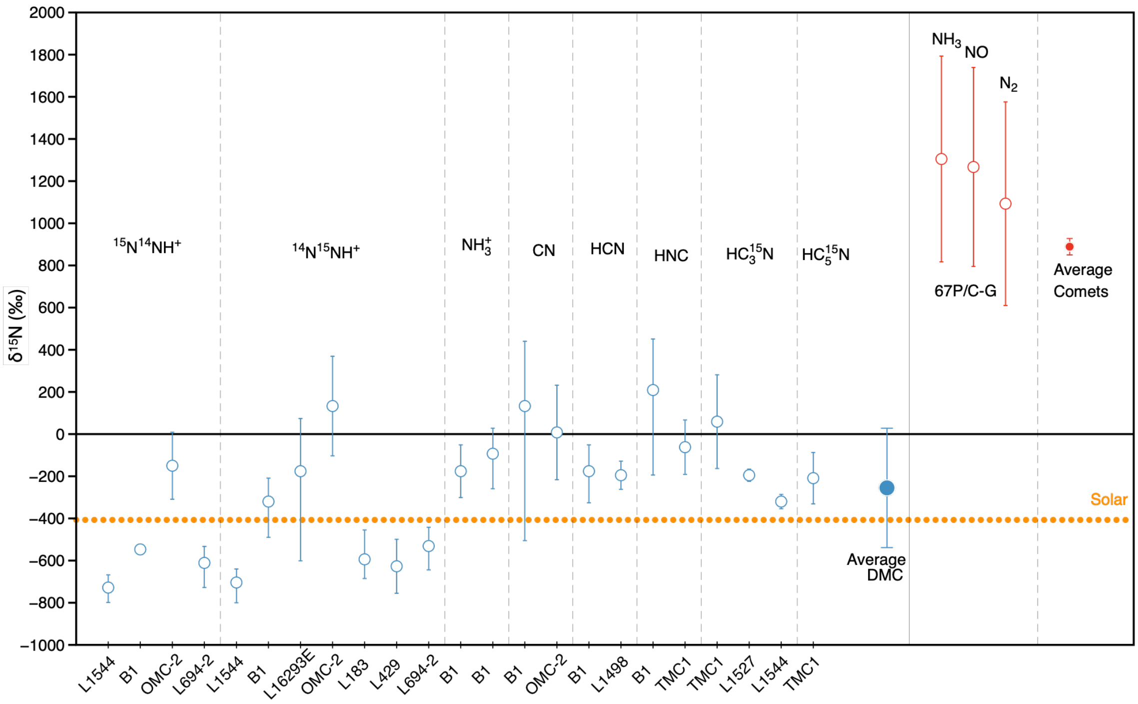

Figure 1.8: Nitrogen data compilation of 67P/C-G (open red circles, Altwegg et al. 2019) and other comets (filled red circle, average value taken from Hily-Blant et al. 2017). Open blue circles are the composition of different molecular clouds, for various N-bearing molecules (from Loison et al. 2019) and the filled blue circle is the average with its standard deviation. Solar from Marty et al. 2011.

Interestingly, the ^{15}N-poor signature of the Sun (~ -400‰), and thus the PSN, is similar to that measured in molecular clouds (Figure 1.8), with values ranging from ~ -500 ‰ to 0 ‰ (Loison et al. 2019, and references therein). Although these measurements are associated with large uncertainties, that may be strongly underestimated (Loison et al. 2019), this shows a consistent enrichment of ^{15}N in comets compared to both the PSN and molecular cloud compositions.

Self-shielding effects during the photo-dissociation of nebular N_2 have been modelled (Heays et al. 2014; Muskatel et al. 2011) and are viable processes to produce early enrichment in ^{15}N in products from a gas phase. Experimental investigations demonstrated the possibility to produce strong ^{15}N enrichment (> 10 000 ‰) by irradiating N_2-H_2 gas with photons with wavelengths around 90 nm (Chakraborty et al. 2014). It is however important to note that in any scenario of N_2 photo-dissociation, the ^{15}N enrichments are preserved in the products, such as HCN (Heays et al. 2014) or NH_3 (Chakraborty et al. 2014), and not in the N_2 gas being dissociated. The observation in comet 67P/C-G that both N_2 and NH_3 are isotopically heavy is thus difficult to reconcile with the scenario of N fractionation.

To understand the origin of the high 15N-enrichments found in cometary N_2 compared to PSN or molecular cloud gases, it is necessary to apprehend the way nitrogen isotopes are fractionated during their incorporation into cometary ices. For example, possible isotopic fractionation of Ar and Kr were reported during their trapping into ices (Notesco et al. 1999). Interestingly, molecular N_2, being a highly stable and unreactive species, behaves similarly to noble gases, and thus could also fractionate during its incorporation from the gas phase to cometary ices. While Bar-Nun et al. (2007) reported the effect of temperature on the trapping efficiency of N_2 relative to CO, isotopic effects resulting from trapping N into cometary ice analogues have not yet been investigated experimentally.

2) Noble Gases

Before the Rosetta mission to comet 67P/C-G, the noble gas composition of cometary ices was unknown, and only predicted by experimental investigations (Bar-Nun et al. 1987; Owen et al. 1992; Bar-Nun & Owen 1998; Notesco et al. 2003). Amongst the five noble gases, only Ar, Kr and Xe were detected in the coma of 67P/C-G by the ROSINA (Rosetta Orbiter

Spectrometer for Ion and Neutral Analysis, Balsiger et al. 2007) mass spectrometer onboard the Rosetta spacecraft. Helium and neon were not sufficiently abundant to be detected, probably due to their very low condensation temperatures (<15 K). The measurements of Ar, Kr and Xe indicate that comets are highly enriched in noble gases relatively to other Solar System solids (Marty et al. 2016; Rubin et al. 2018). Noble gases are more concentrated in cometary ices than in the insoluble organic matter phases of carbonaceous chondrites for instance, which are the main carriers of heavy noble gases in chondrites (Busemann et al. 2000). In terms of delivery of noble gases to Earth, this suggests that even a small amount of cometary material could greatly affect the noble gas budget of the Earth (Marty et al. 2016). The elemental ratios of Ar, Kr and Xe (the relative abundances) of comet 67P/C-G are non-solar, with a strong depletion in ^{36}Ar (or enrichment in ^{132}Xe and ^{84}Kr) of ~3 orders of magnitude as displayed on Figure 1.9 (Rubin et al. 2018). Interestingly, the elemental ratios of noble gases in the initial Earth atmosphere appears to fall between 67P/C-G and the chondritic range, suggesting it is made up of a mixture between comets and chondrites (Figure 1.9). The initial Earth atmosphere composition refers to the noble gas atmospheric budget before the loss of Xe (by a factor of ~10, Bekaert et al. 2020) from the atmosphere by hydrodynamic escape (Avice et al. 2018; Zahnle et al. 2019; Almayrac et al. 2021).

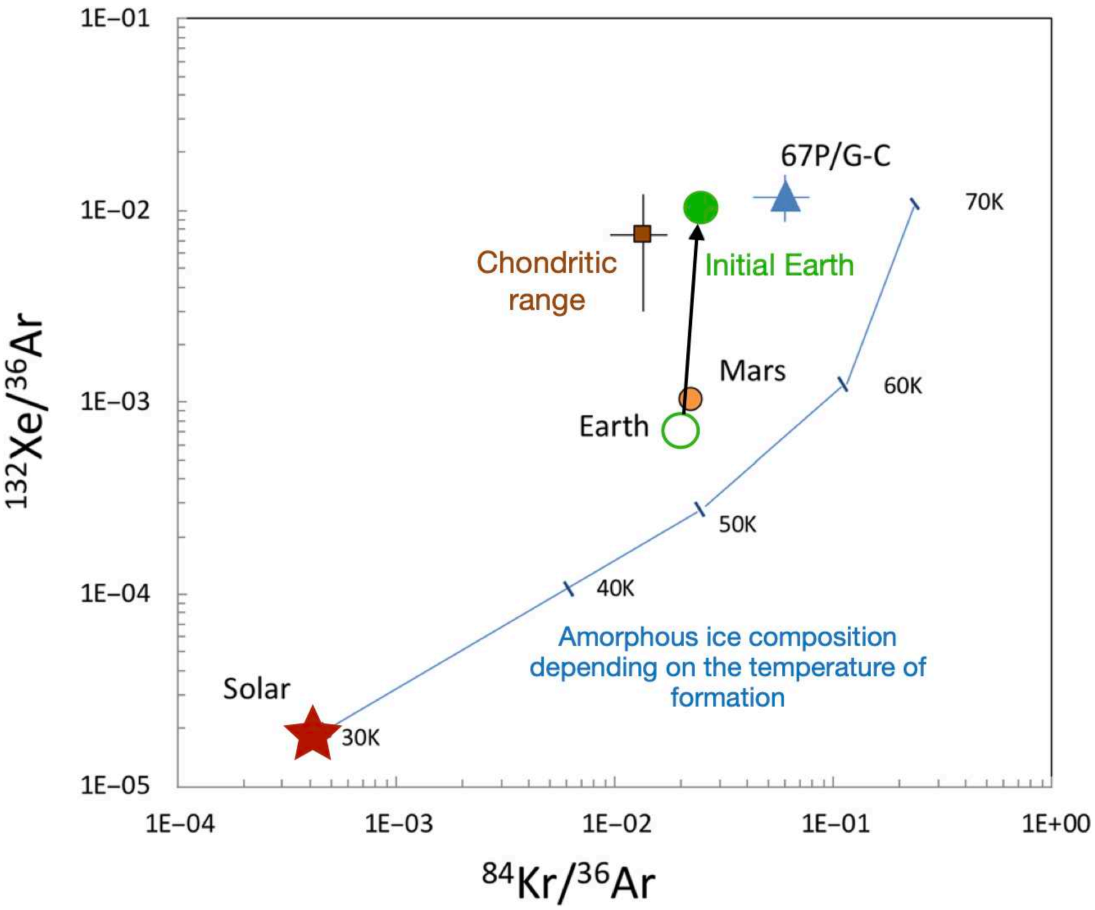

Figure 1.9: Noble gas elemental composition of comet 67P/C-G and several other cosmochemical end-members, adapted from Rubin et al. (2018). The blue line is the evolution of the composition of noble gases in cometary ice analogues for different temperatures of formation, starting from a solar composition.

Both Ar (Balsiger et al. 2015) and Kr (Rubin et al. 2018) isotope compositions showed little (Kr), to no (Ar), variations relative to the solar composition (Meshik et al. 2014). However, Xe, as already presented above, showed an isotope signature distinct from the solar composition (Meshik et al. 2014) with deficits in ^{134}Xe and ^{136}Xe, and an excess in ^{129}Xe relative to solar (Marty et al. 2017). The origin of this non-solar Xe signature is thought to be nucleosynthetic in nature and of a likely pre-solar origin, suggesting that cometary building blocks may have acquired their noble gas composition prior to the Solar System formation (Avice et al. 2020).

These observations raise several important questions. Firstly, are the noble gas (and nitrogen) contents of 67P/C-G measured by Rosetta in the coma representative of the interior of the comet? Secondly, did volatiles isotopically fractionate during their incorporation into the ice? In other words, are the isotopic compositions of 67P/C-G directly depicting the composition of the gas from which it formed? As we can observe on Figure 1.9, experimental predictions on the noble gas composition of comets (Bar-Nun & Owen 1998; Notesco et al. 2003) fail to reproduce the composition measured in 67P/C-G, when assuming a PSN starting composition. Because the measurement of noble gases in comets are rare (one mission so far, and no major comet exploration mission planned at the moment), further experimental investigations are therefore crucial to better understand the origin of comets, especially after the Rosetta mission. Since the extensive studies of the group of Akiva Bar-Nun from Tel-Aviv University in the 80s, 90s and early 2000s, the study of noble gases in cometary ice analogues has slowed down, and deserves to be revitalised.

IV. How the Highly Volatile Noble Gas Elements are Captured and Preserved in Comets

1) Ices on Comets

Water (H_2O) is the most abundant molecule in comets, followed by CO_2 and CO (~10% and 5% relative to water, respectively, Feldman et al. 1997). Other molecules such as H_2S, O_2 or C_2H_6 represent around 1%, and the most abundant N-bearing molecule NH_3 around 0.4% (in comet 67P/C-G, Läuter et al. 2020). The Ar/H_2O ratio is in the order of ~ 6×10^{-6} (Rubin et al. 2018), with Kr and Xe abundances being one order of magnitude lower (Figure 1.9). Because water dominates the ice budget of comets, its structural form in comets, whether as amorphous ice, crystalline (as we have on Earth) or in clathrates hydrates (crystalline solids that form in a cage-like structure), will have strong implications on the behaviour of other volatile elements. Indeed, amorphous water ice and clathrates have the potential to trap other volatile elements within their structure (Ghormley et al. 1967; Englezos 1993). The actual structure of water ice in comets however remains unknown, even after the Rosetta mission on 67P/C-G. This in mainly because ices are buried below the surface and inaccessible to direct observation, and only manifesting themselves indirectly by sublimating in the coma (Prialnik & Jewitt 2022).

To account for the gas outbursts observed in comets, it was proposed that cometary ices were in the form of amorphous water ice (Patashnick 1974), liberating the trapped volatiles within its structure as outbursts during its phase transition into crystalline ice (Smoluchowski 1981; Prialnik et al. 1993). This was also supported with experimental investigation by infrared spectroscopy of water condensation at low pressures (<10^{-3} mbar) and temperatures (< 100 K), leading to the formation of amorphous water ice, rather than crystalline or clathrate hydrates (Sandford & Allamandola 1988). The presence of water clathrates would also lead to gas entrapment (Mousis et al. 2010), although in more limited amounts than amorphous water ice, but would necessitate much higher pressures upon formation than prevailing in the molecular cloud or PSN (Sandford & Allamandola 1988; Prialnik & Jewitt 2022). The experimental studies of amorphous water ices, and more particularly their role as carrier of noble gases in comets, started in the 1980s (Bar-Nun et al. 1985). Here I provide a brief review on amorphous water ice and the trapping of noble gases within such ice.

2) Amorphous Water Ice

Amorphous water ice (I_a, sometimes also called "amorphous solid water" ASW) is a metastable form of ice, produced when water is condensed directly from a gas phase at very low temperatures and pressure (Ghormley 1967). The particularity of this form of ice, different from the more typical crystalline hexagonal form we can find on the surface of Earth, is its significant porosity. The structure of I_a consists of a disordered, bonded, random network of H_2O molecules where tetrahedral bonding is preferred (Mastrapa et al. 2013). This molecular arrangement results in a highly porous structure, which can be described as a network of cylindrical pores spaced 6 Å (0.6 nm) apart with diameters of 20 Å (Parent et al. 2002). As a point of comparison, the radius of a Xe atom is ~1 Å, and the radius of CO_2 is ~2 Å. Without taking into account the porosity, the density of I_a is between 0.94 g/cm^3 (low density form) and 1.1 g/cm^3 (high density form), measured by diffraction measurements techniques (Jenniskens & Blake 1994). However, because it is highly porous, bulk density of amorphous water ice can be as low as 0.6 g/cm^3, and with an adsorption surface area up to 2700 m^2/g (Stevenson et al. 1999). Note on Figure 1.10 the granular appearance of I_a compared to the much smoother surface of crystalline ice (Prialnik et al. 2022). Because of this porosity, I_a has the potential to trap and retain large amounts of volatile species within its structure (Bar-Nun et al. 1985).

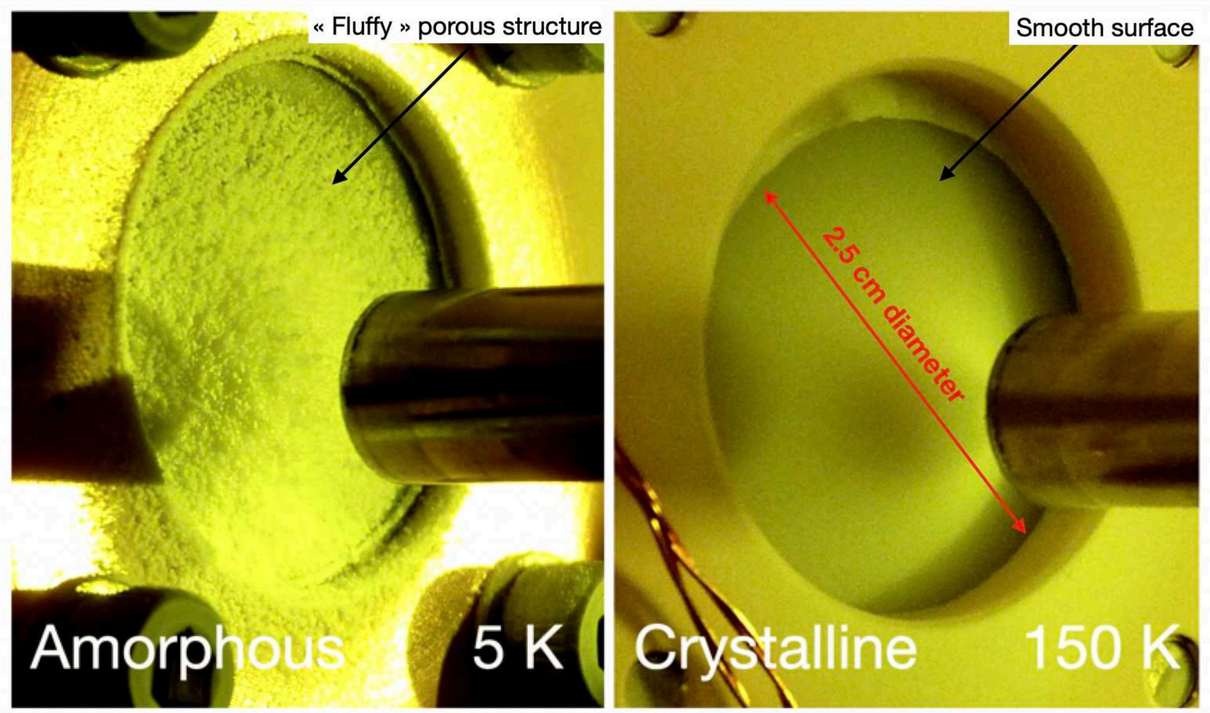

Figure 1.10: Water vapor deposited as amorphous water ice on a substrate at 5K (left), and crystalline ice at 150K (right), adapted from Prialnik & Jewitt (2022).

The heating of amorphous water ice to temperatures above 120K slowly rearranges the molecular amorphous structure and leads to the irreversible transition into crystalline ice. This transition occurs gradually over a range of temperatures, between ~120K to ~160K (Jenniskens & Blake 1994), and the forming crystalline ice has a cubic structure (I_c). Although the temperatures and timing of transition can vary depending on the heating rate (Collings et al. 2004), the transition will always occur before the sublimation of water around 180K. Any species trapped into the pores of I_a is likely to be released from the ice (at least partially, Notesco et al. 2005) during the I_a-to-I_c transition. A final transition from I_c to hexagonal crystalline ice (I_h) occurs after 160K, simultaneously as the sublimation of the water starts to take place (Jenniskens & Blake 1994; Sugisaki et al., 1969).

Interestingly, although the transition from amorphous ice to crystalline ice is described as an irreversible process (Jenniskens & Blake 1994), irradiation of crystalline ice by energetic particles such as photons, protons or electrons can amorphize the ice if below 120K (Golecki & Jaccard 1978). This suggests that even if ices condensed in the PSN at sufficiently high temperatures to form crystalline ice, the evolution of the icy grains in irradiated environments within the PSN would cause the ice to be partly lost and reformed in the amorphous state (Ciesla 2014; Prialnik & Jewitt 2022). Furthermore, the irradiation of amorphous ice results in its compaction, reducing the porosity and potentially the amount of trappable gas (Yabushita et al. 2013).

3) Volatile Trapping and Release

Volatile elements, present along with water vapor in the gas phase at the time of deposition can become trapped in the pores of the amorphous ice if a subsequent layer of ice forms before they can escape (Bar-Nun et al. 1987). These volatile elements, such as heavy noble gases (Ar, Kr and Xe) or N_2 are retained within the amorphous ice lattice by Van Der Waals interactions with the dangling-OH bond of water (Bar-Nun et al. 2007). Volatile species trapped in the ice are not released when the temperature rises above their sublimation temperature. They can only escape when the water molecules of the ice rearrange during the annealing and/or during the transformation from amorphous to crystalline structure (Bar-Nun et al. 1985). This phenomenon is displayed on Figure 1.11, and is symptomatic of the behaviour of volatile elements trapped in amorphous water ice. In summary, volatiles apart from water can be incorporated into comets by directly condensing onto the cometary ice in a frozen phase or by being trapped within the major water ice phase.

During the lifetime of cometary ices, the frozen phases (volatile elements condensed along with water, not trapped in the ice structure) would be lost earlier than the trapped phases being retained up until the ice transition (~140K) and sublimation (~160 - 180K) temperatures (Gkotsinas et al. 2022). This suggests that the trapped phases of volatile elements in comets are more likely to survive and be delivered to the inner Solar System than the frozen phases. Additionally, experiments investigating very low gas deposition rates to better reproduce the conditions of cometary ice formation (Notesco et al. 2003) showed that under PSN/DMC conditions, where noble gases are in very low abundance relative to water, noble gases would only be trapped without any frozen phase.

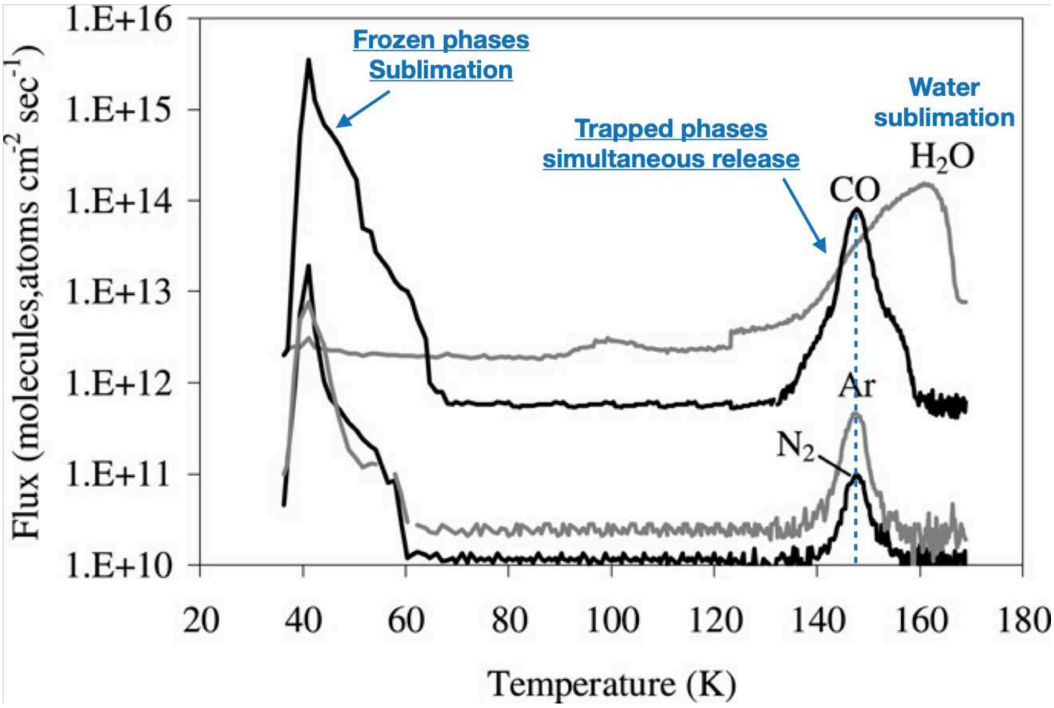

Figure 1.11: Flux of gas released from a H_2O:CO:N_2:Ar ice formed at 27K and heated to 170K (modified from Bar-Nun et al. 2007). Species frozen on the ice surface sublimate around 40K, and the species trapped in the water ice are simultaneously released around 140K during the I_a-to-I_c transition.

These observations indicates that the volatile elements present in the coma of comets are mainly trapped in water ice and only released during it transformation into a crystalline structure. Experiments of noble gas trapping into cometary ice analogues demonstrated that the temperature of deposition (Bar-Nun & Owen 1998) and deposition rate (Notesco et al. 2003) affect the trapping efficiency of noble gases. Figure 1.9 illustrates how increasing the temperature of ice deposition from 30K to 70K reduces the amount of Ar relatively to Kr and Xe in the trapped phase (Bar-Nun & Owen 1998). These experiments were used to estimate the temperature in the region of comet formation (Bar-Nun & Kleinfeld 1989; Notesco et al. 2005), and to evaluate their potential for delivering substantial amounts of volatile elements to Earth (Dauphas 2003).

The recent measurements in the coma of 67P/C-G by Rosetta revealed for the first time the noble gas composition of a comet, contradicting the predictions based on experimental studies (Rubin et al. 2018, Figure 1.9). Moreover, some of the major scientific discoveries by Rosetta relied on the isotopic composition of noble gases (Xe in particular, Marty et al. 2017), which were never explored by laboratory experiments (except some preliminary results for Ar isotopes by Notesco et al. 1999). Regarding nitrogen isotopes, no comprehensive study on its ^{15}N-enrichment relative to isotopic enrichments for noble gases in cometary ices at various temperatures of deposition yet exists. More importantly, the effect of the irradiation by energetic particles (e.g., ultraviolet photons) on noble gas and nitrogen trapping in amorphous ices, which appear to have strong impact on the ice structure (Yabushita et al. 2013) and on isotope signatures (Chakraborty et al. 2014) have also never been investigated.

For this PhD, I have developed a novel experimental setup called EXCITING (**E**xploring **X**enon in **C**ometary **I**ces by **T**rapping and **I**rradiating **N**oble **G**ases) at the CRPG noble gas laboratory, in order to reproduce past experiments and further investigate the effect of photon irradiation on the isotope composition of nitrogen and noble gas in cometary ice analogues.

A substantial part of the PhD was the technical and analytical development for the sensitive and precise measurement of Ar, Xe and N_2 at CRPG. These developments benefitted many other projects which I am involved in, particularly the isotopic analyses of ultra-low amounts of nitrogen, only achievable by noble gas mass spectrometry techniques.

Further experimental explorations on the fractionation of nitrogen isotopes were undertaken as part of the Photonis ERC project, in collaboration with the PIIM and LATMOS (Paris) laboratories. These explorations, briefly presented at the end of manuscript, have the objectives of studying the effects of photon irradiation on nitrogen isotopes in organic compounds derived from interstellar ices, and on the production of N-bearing gaseous compounds formed after the photo-dissociation / ionization of nebular gases.

Chapter 2

Instrumental Developments in the Noble Gas Lab for the EXCITING Experiment

The EXCITING experiment (Exploring Xenon in Cometary Ices by Trapping and Irradiating Noble Gases) relies on the use of different instruments to perform elemental and isotopic analyses of nitrogen and noble gases. This chapter describes the instruments used to carry out the analysis of the experimental products produced by EXCITING and the technical developments that have been achieved to make these measurements possible. I briefly present the principle behind the EXCITING experiment and the instruments used for this project. I also provide a short description of the fundamentals of noble gas mass spectrometry, before a more thorough description of the EXCITING line, the noble gas and nitrogen purification lines, and the mass spectrometers' characteristics.

During the course of this PhD, a major focus was on the technical and analytical development of several instruments: (i) the EXCITING setup, (ii) upgrades and new components of the GV instrument Helix MC mass spectrometer, and the (iii) development of the nitrogen purification line connected to the ThermoFisher Helix MC$^+$ mass spectrometer. These developments were primarily made within the framework of the EXCITING project, but benefitted from many other projects that were part of this thesis, such as nitrogen isotope measurements in synchrotron irradiated gaseous samples (mentioned in Conclusions and Perspectives) and meteorites (Byrne et al. in review). All of the developments were undertaken in close collaboration with Dr Michael Broadley, Dr David Bekaert, Dr David Byrne, and the invaluable help of the lab engineers Laurent Zimmermann and Bouchaïb Tibari.

I. The Noble Gas Lab

1) Overview of the EXCITING Experiment and Noble Gas Laboratory

The EXCITING experiment has been developed to investigate how volatile elements, specifically nitrogen and the heavy noble gases Ar, Kr and Xe, evolve elementally and isotopically when they are incorporated into, and released from, cometary water ice analogues. For a given experiment, one can either (i) measure the relative abundances of the different gases released from the ice throughout the duration of the experiment using a quadrupole mass spectrometer (QMS) located directly on the EXCITING Line (Figure 2.1), or (ii) isolate aliquots of the released gas for later purification and isotopic analysis on magnetic sector noble gas mass spectrometers (Figure 2.2 and 2.3).

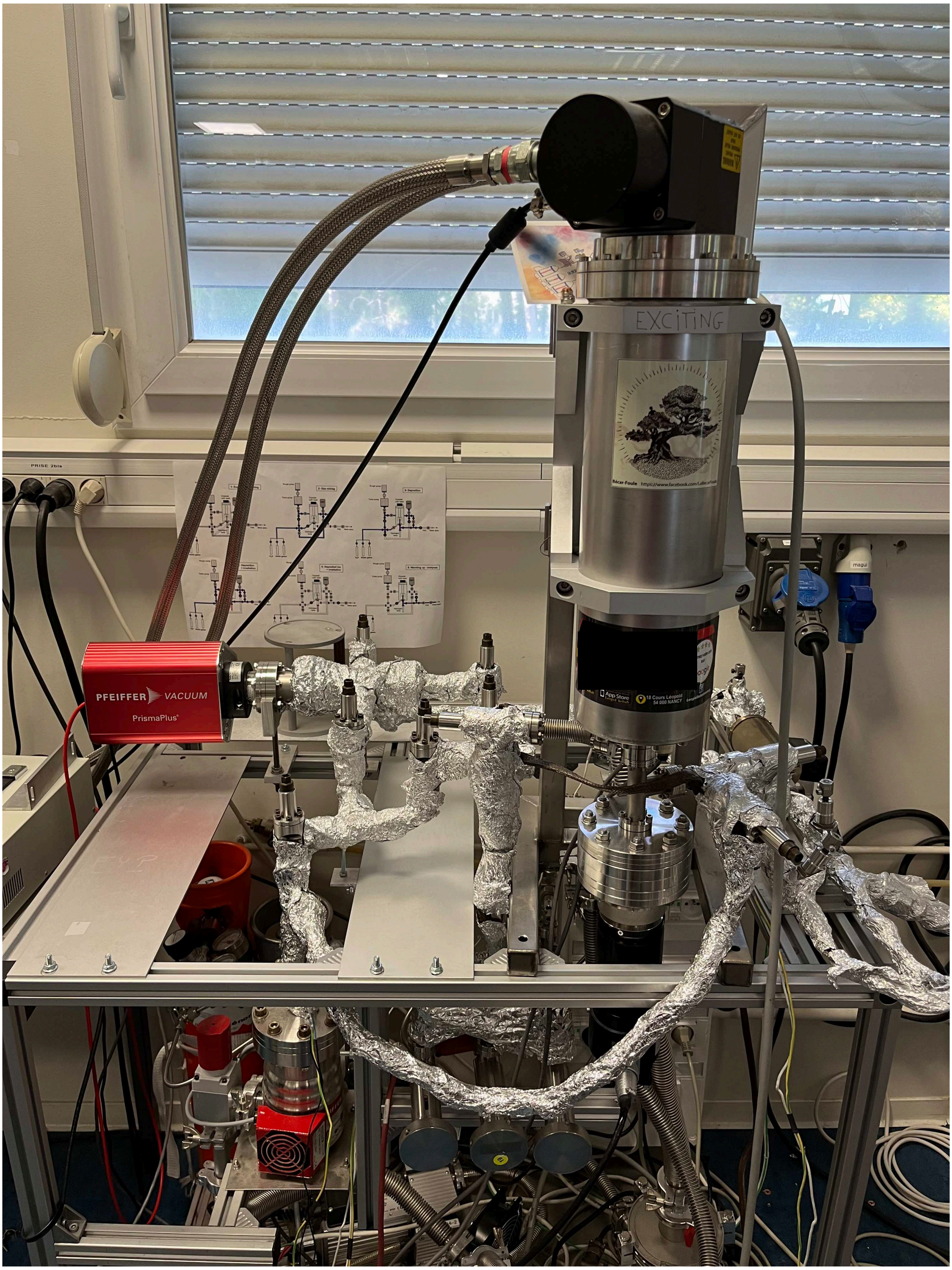

Figure 2.1: The EXCITING line. A schematic view of the setup is given in Figure 2.6.

Noble gases and nitrogen isotopes are analysed separately using two different mass spectrometers. Noble gases (Ar, Kr and Xe) isotopes are measured using a GV Instrument Helix MC noble gas mass spectrometer, and its associated purification line (called MaGui, Figure 2.2). The GV Helix MC and MaGui purification line are directly connected to the EXCITING line, allowing for the easy transfer and analysis of noble gases released from the cometary ice analogues. Nitrogen isotopes, on the other hand, are measured using the ThermoFisher Helix MC$^+$ mass spectrometer, equipped with a specific purification line for nitrogen (called ADN, Figure 2.3). Because the ADN nitrogen purification line is not directly connected to the EXCITING line, aliquots of EXCITING gas samples must be collected and stored within steel bottles before being transferred to the ADN line for nitrogen purification and analysis.

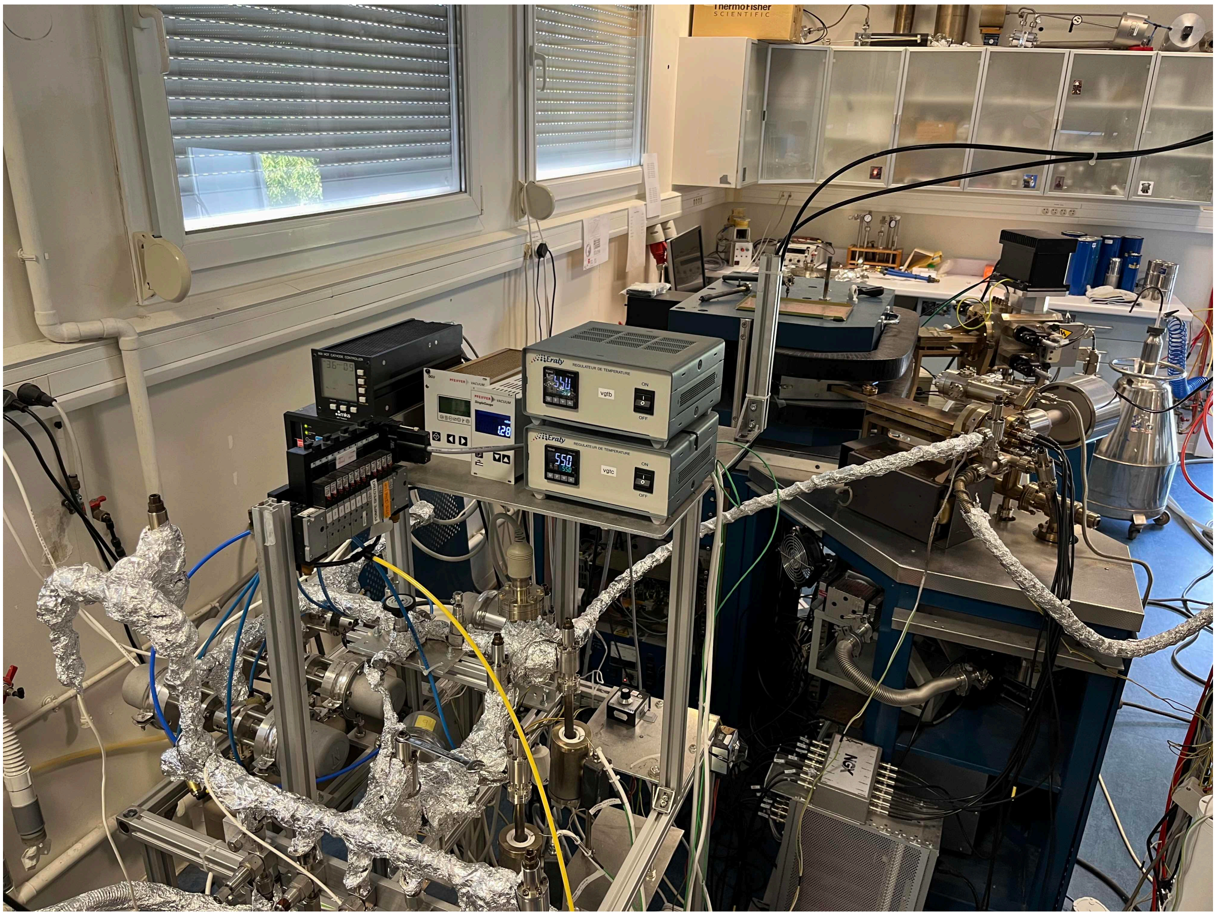

Figure 2.2: MaGui line in the foreground and GV Helix MC in the background. A schematic view of the line is given Figure 2.8.

In summary, the EXCITING project has two fundamental objectives: (i) to perform relative abundance measurements of nitrogen and noble gases using the QMS on the

EXCITING line to constraint the elemental behavior of volatile elements in ice (Chapter 3), and (ii) to perform precise measurements of noble gases and nitrogen isotopes by magnetic sector noble gas mass spectrometry (Chapter 4). The fulfilment of these objectives requires a multi mass spectrometer (QMS, GV Helix MC, Thermo Helix MC$^+$) approach, which will be outlined in detail in the following sections.

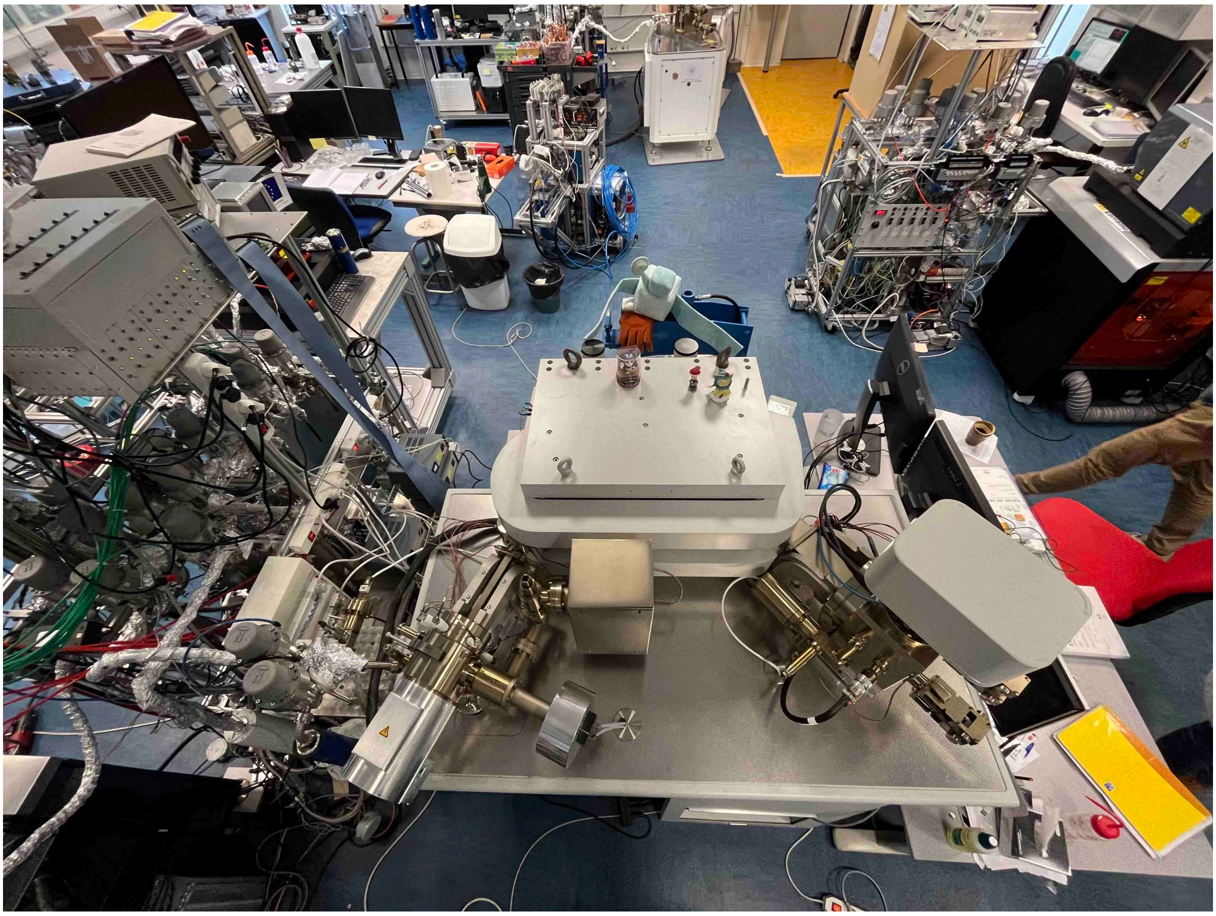

Figure 2.3: ThermoFisher Helix MC+ mass spectrometer, and the ADN purification line on the left. A schematic of the ADN line is given Figure 2.16.

2) Fundamentals of Noble Gas Mass Spectrometry applied to EXCITING

Noble gas analysis using static mass spectrometry is usually broken down in to three steps: (i) extraction, (ii) purification, (iii) and analysis. As part of the EXCITING project, no gas extraction was needed as gaseous samples were directly generated in the EXCITING experimental line.

i. Sample Generation

The EXCITING experimental line consists of stainless-steel volumes that are kept under ultra-high vacuum by a series of turbo molecular pumps. Gases (water, nitrogen and/or noble gases in bottles connected to the line) can be flowed into a cryogenic system and condensed at low temperatures (down to ~30K) to form different ice mixtures. The generation of a gas sample occurs when the ice is heated and the gas species are released from the ice structure. During sample generation, the gas is either (i) directly analysed for abundances by a QMS equipped on EXCITING (no purification, under continually dynamic pumping), or (ii) sampled using empty bottles connected to the line (under static mode, with the pumps closed), and later sent for purification on dedicated purification lines and analysed by static mass spectrometry.

ii. Quadrupole mass spectrometry (QMS)

A quadrupole mass spectrometer (Pfeiffer Vacuum©, PrismaPlus QME 220) was operated under dynamic mode (pump open) to analyse the elemental composition of the gas generated during EXCITING experiments (see the red QMS on the picture Figure 2.1). A QMS consists of a source chamber, a mass filter, and a collector, as detailed on Figure 2.4. The source chamber is composed of a positively charged inlet slit, a heated tungsten filament (> 1500 °C) generating electrons attracted towards a discharge anode, and negatively charged extraction plates. Once the neutral gas enters the chamber, the beam of electrons ionises the gas by electron impact, therefore generating cations. The cations are expelled from the source chamber by the positively charged plate, and then accelerated by the negatively charged extraction plates toward the mass filter. The mass filter consists of four parallel rods (two positively and two negatively charged). The motion of the ions across these rods depends on the electric field applied to the quadrupole, such that only ions with a particular mass to charge ratio (*m/z)* will pass through the quadrupole to the detector. The collector in our QMS is a Faraday cup connected to an amplifier with a 10^{11} Ω resistance that converts the ion flux intensity into a signal in volts.

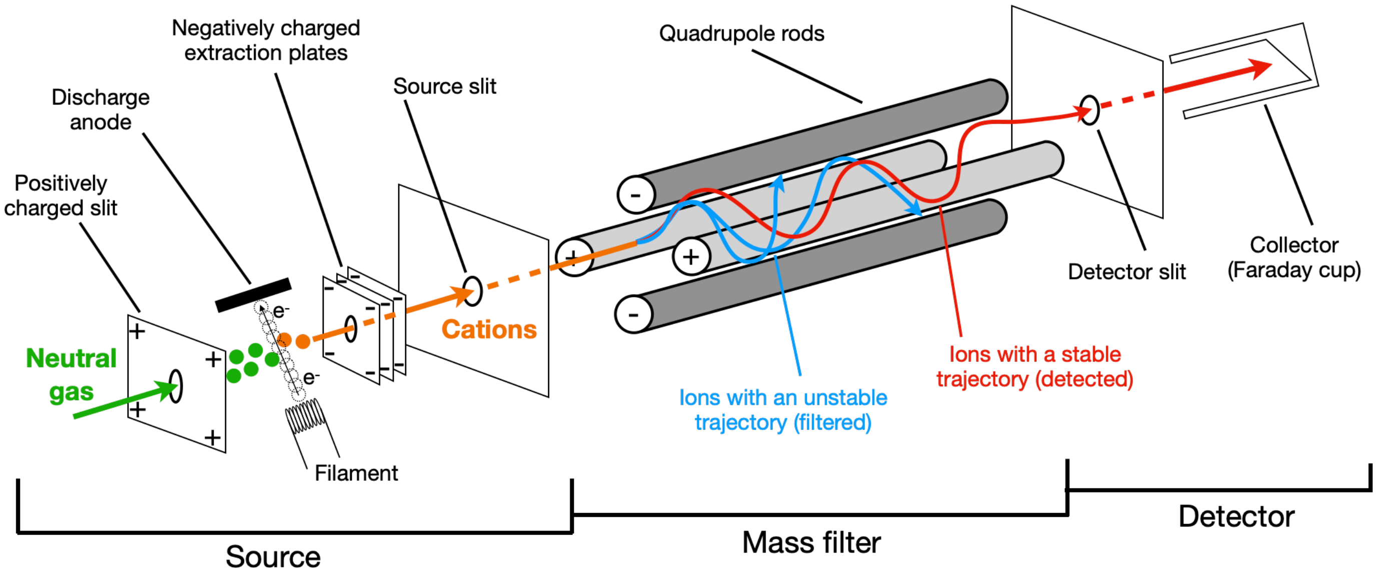

Figure 2.4: Schematic of the quadrupole mass spectrometer used to analyse gas (adapted from Warr, 2013). The source is composed of a tungsten filament generating electrons that are attracted by a discharge anode. Electrons ionise the neutral gases to form cations. A positively charged plate expels the cations from the chamber, and negatively charged extraction plates accelerate the cations through the source slit before the mass filter. The mass filter consists of four parallel rods (two positively and two negatively charged). A final slit is positioned before the collector, which is a faraday cup in the case of the QMS on EXCITING.

By adjusting the electric potential, composed of an RF voltage and a DC field offset, applied to the quadrupole rods, the QMS is capable of measuring across the 1 – 200 amu range, covering all stable noble gas isotopes. The standard energy of ionisation is ~70 eV, meaning that all the species of interest (water, N_2, Ar, Kr and Xe) are ionised efficiently. The resolution of the QMS is defined as integer resolution, meaning that only masses possessing a minimum of 1 amu difference from each other can be resolved and measured. This limited mass resolution was not an issue for the purpose of this study because there are no significant interferences at the masses of H_2O (18) and the most abundant isotopes of the different noble gas (^{40}Ar (40), ^{84}Kr (84) and ^{132}Xe (132)). However, the measurement of dinitrogen abundances at mass 28 (for its most abundant isotopologue ^{14}N-^{14}N) can suffer from an interference with CO (^{12}C^{16}O). This interference was mostly eliminated by maintaining an ultra-low background pressure (~ 1 x 10^{-8} mbar) between experiments through the combination of turbomolecular pumping and Ti sponge gettering (figure 2.6).

iii. Purification

Noble gases generally have extremely low concentrations in geological samples and are therefore analysed under static mode (pumps closed) to optimise the sensitivity and improve the detection limits. Although EXCITING samples are generated with an arbitrary amount of gas, noble gases are still incorporated into the ice at low abundance relative to water to better reproduce natural samples. As briefly mentioned in the previous section, accurate isotope analysis of noble gases can be hampered by the interference of isotopes or molecules with similar masses. Furthermore, the ionisation efficiency and mass discrimination by the mass spectrometer both depend on the amount of gas sent into the instrument. As such, it is necessary that noble gases are admitted to the mass spectrometer in the purest possible form.

The purification of noble gases relies on their inertness, by chemically removing the other reactive gases on metal surfaces called “getters”. Getters used at CRPG principally consist of a series of volumes (parts of a purification line) filled with high purity titanium sponge (Ti-sponge) held either at 500 – 600 °C to decompose any reactive species, or at room temperature to irreversibly trap them, especially H_2. Some of the most important reactive species to remove (to prevent various interferences or pressure effects) are H_2, H_2O, N_2, CO, CO_2, SO_2, and hydrocarbons, which are all typically present in the experimental line as background species. Generally, a purification line is equipped with several getters to optimise the purification: with cold getters (room temperature) purifying mostly H_2, and hot getters focusing on cracking and purifying hydrocarbons. Details on the purification protocol used during this PhD are given in section 2.III of this chapter.

The EXCITING project also studied the isotopic composition of nitrogen using noble gas mass spectrometry. Because nitrogen reacts with the Ti sponge getters, as described above, its purification (mainly from CO, the main interfering species) was performed following a different method, on a different purification line than that used for noble gases (ADN line, see section 2.IV of this chapter).

iv. Analysis by static mass spectrometry

Once noble gases (or nitrogen) are purified, they are sent for analysis in the mass spectrometer. The two mass spectrometers used during this PhD, the Helix MC (GV Instrument) and Helix MC$^+$ (Thermofisher), operate following the same principles. These mass spectrometers consist of (i) a Nier-type ion source (Nier, 1947) to ionise the gas, (ii) a magnetic sector around an arced flight tube to separate the different isotopes depending on their mass/charge (mass filter), and (iii) collectors to measure each isotope. A schematic representation of the mass spectrometer is given Figure 2.5.

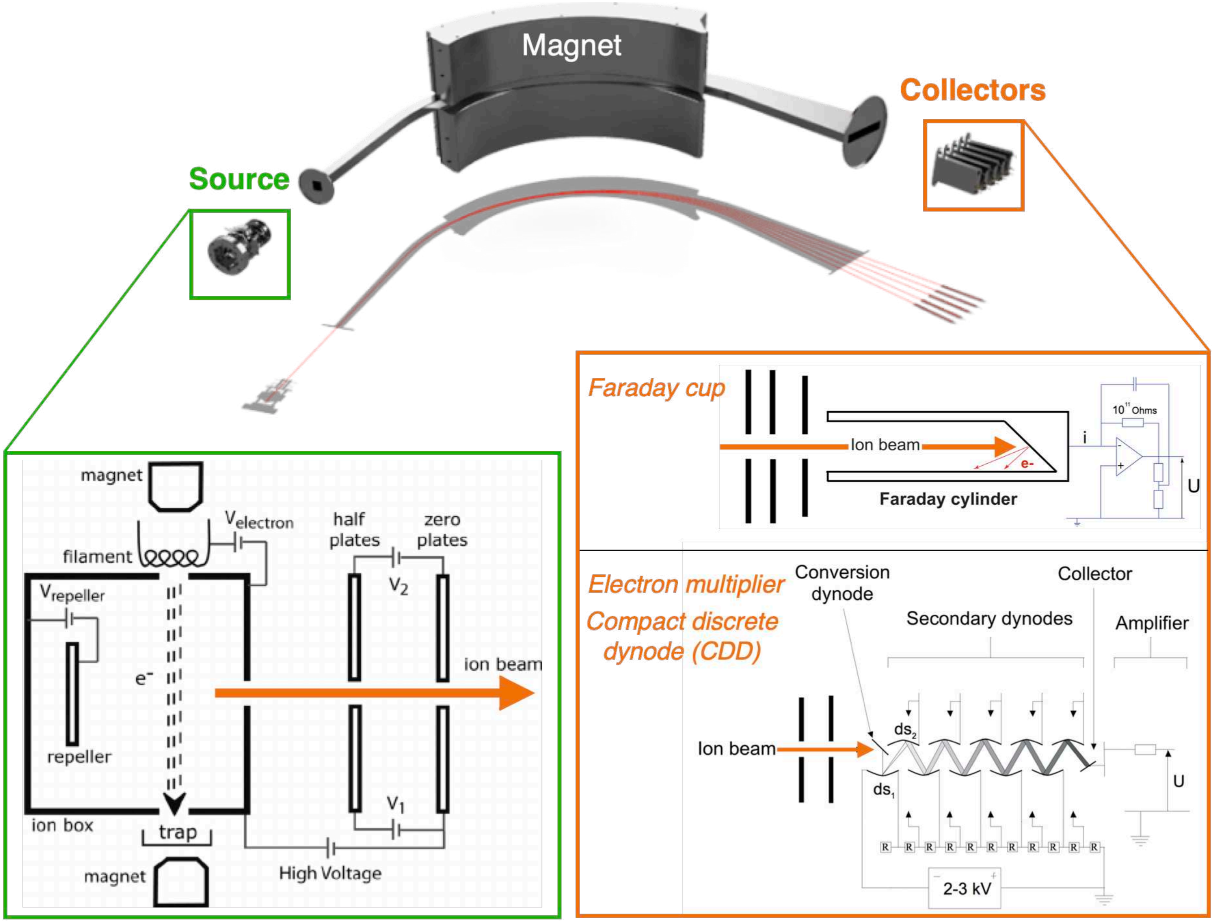

Figure 2.5: Schematic representation of the GV Helix MC and ThermoFisher Helix MC$^+$ mass spectrometers. The Nier-type ion source is adapted from Mabry et al. (2012) and the collectors schematics (Faraday cup and electron multiplier) are adapted from Bekaert (2020) and references therein.

In the source, a current is continually applied across a tungsten filament that generates electrons, which are passed through the gas in the ionisation chamber by applying a potential voltage difference between the filament and the trap electrode (Figure 2.5). The gas in the ionisation chamber is ionised by electron impacts to generate cations. The ionised gas is then expelled from the chamber by a positively charged repeller plate, and accelerated toward the flight tube by a potential difference. This potential difference, also called acceleration reference (V), is a fixed parameter that influences the trajectories of ions in the flight tube for their separation (Figure 2.5). The intensity of the current on the filament and the trap electrode, as well as the repeller and acceleration potential are different parameters that are described as “source settings”. The source settings are tuned depending on the noble gas that is analysed in order to optimise its ionisation efficiency, and hence the detection limit. The source settings of the Helix MC for noble gases and of the Helix MC$^+$ for nitrogen are given in their respective sections (section 2.III and 2.IV) describing in detail the protocol used for their analysis.

In the arced flight tube, the trajectory of an ion is controlled by applying a magnetic field (Figure 2.5). Upon entering the flight tube, all ions have the same kinetic energy, expressed as $E = zV = \frac{1}{2}mv^2$ where z is the charge of any considered ion of mass m and velocity v. The radius of the arced path the ion takes in the flight tube, noted r, then depends on the mass (m) and charge (z) of the ion, as well as the acceleration reference (V) and the magnetic field (B) applied to the magnet:

$$r = \sqrt{\frac{m}{z}} * \frac{\sqrt{2V}}{B} \quad (1)$$

This implies that at a fixed acceleration reference and magnetic field, the trajectory of an ion/isotope only depends on the square root of its mass to charge *m/z* ratio. The lightest isotopes will have the most curved trajectories (i.e., low r), and the heaviest the least curved trajectories (i.e., high r). Thus, by keeping the acceleration reference constant, the trajectories of specific isotopes can be controlled by varying the magnetic field and be directed toward specific collectors.

After having been accelerated through the flight tube, the ions arrive at the collector housing. The two main collector types used on noble gas mass spectrometers are Faraday cups and electron multipliers (often referred to as Compact Discrete Dynode or CDD for short), as shown in Figure 2.5. Faraday cups are metal cups associated with amplifiers characterized by resistances typically between 10^{10} and 10^{13} Ω. Charged particles of the ion beam impact the cup and generate a current, which is measured and used to compute the total amount of ions collected in the cup. Faraday cups are usually used to collect the more abundant noble gas isotopes, such as ^{4}He or ^{40}Ar. The amount of noble gas in samples generated by EXCITING are sufficient to be able to also measure Xe isotopes on Faraday cups. Thus, only Faraday cups collectors were used on the GV Helix MC mass spectrometer to measure noble gas isotopes ^{36}Ar, ^{38}Ar, ^{40}Ar, ^{128}Xe, ^{129}Xe, ^{130}Xe, ^{131}Xe, ^{132}Xe, ^{134}Xe, and ^{136}Xe.

The ThermoFisher Helix MC^{+}, which is mainly used at CRPG for analysing noble gas isotopes (from He to Xe) in very low concentration samples such as meteorites (e.g., Byrne et al., In Review) or ancient terrestrial rocks (e.g., Almayrac et al. (2021), Appendix B), is equipped with electron multipliers (CDD) that multiply incident charged particles through a process called secondary emission. This type of collector allows for the measurements of less abundant isotopes such as ^{3}He, ^{124}Xe and ^{126}Xe. A CDD consists of a series of 18 (for the ones used at CRPG) negatively charged dynodes as presented Figure 2.5, with a final collector. When an ion enters the CDD, it impacts a first conversion dynode that produces an electron, which further impacts a secondary dynode made of an emissive material that can produce a further 1 to 3 electrons. These generated electrons are directed towards the successive dynodes, generating more electrons. A chain reaction then occurs, with electrons hitting dynodes and generating more and more electrons as they travel towards the collector. Hence, even a tenuous ion beam of the least abundant isotopes can produce large amounts of electrons inside a CDD, which are then counted by the collector to derive the signal intensity. For the EXCITING project, nitrogen isotopes were measured on the Helix MC+ mass spectrometer. Faraday cups were used to collect ^{14}N-^{14}N and ^{14}N-^{15}N isotopologues, and a CDD was used to collect the least abundant isotopologue ^{15}N-^{15}N.

II. The EXCITING Line

The EXCITING setup was developed in collaboration with Cryoscan© at CRPG and is described in Almayrac et al. (2022), given in Chapter 3. A picture and a schematic of the setup are given Figure 2.1 and Figure 2.6, respectively. The general working principle of the EXCITING experiment is first presented, as well as a brief description of the setup and its capabilities. Here, I only provide a brief description as the whole setup is thoroughly described in Chapter 3. Finally, I discuss some of the limitations of the experiment with regards to previous laboratory investigations studying volatiles in amorphous water ice.

1) Brief Description of the Setup

The setup is built with 16 mm (internal diameter) stainless steel tubes, connected using CF and VCR connections and Swagelok© valves (Figure 2.6). The whole setup is able to maintain a low pressure of around 10^{-8} mbar using Pfeiffer Vacuum© (TMU 071P model) turbo molecular pumps. Pressure in the line is monitored using an ion gauge (MKS©, Mini Ion Gauge model). Two micro-leak valves (VAT©) connect a bottle of pure Xe (99.999%, 53 bar, Air Liquide©) and a bottle containing a mixture of N_2:Ne:Ar:Kr:Xe in the molar ratio 50:20:10:10:10 (99.999% for N_2, Ne and Ar, 99.998% for Kr and Xe, 150 bar, Messer©) to the mixing volume ahead of the cryogenic head (Figure 2.6). A third micro-leak valve connects a vapour-saturated distilled water reservoir to the mixing volume.

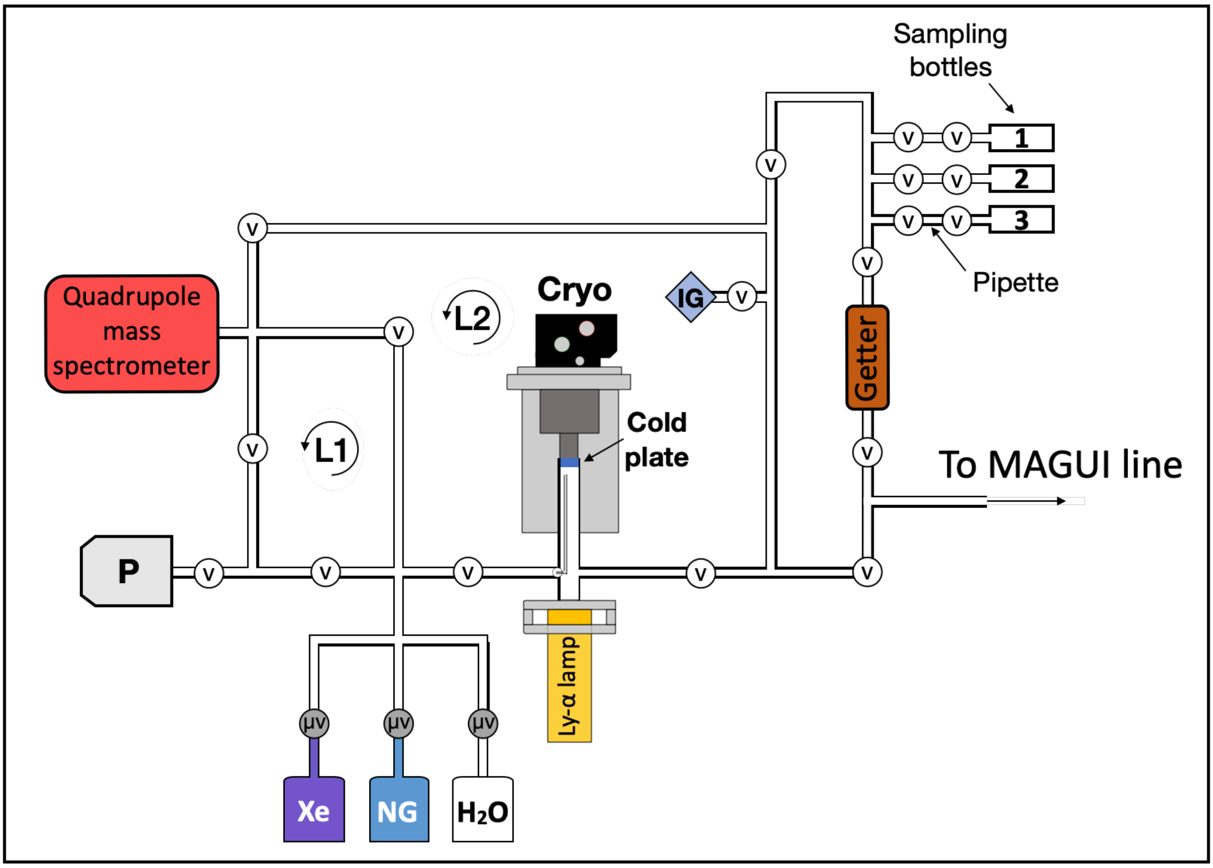

Figure 2.6: Schematic representation of the EXCITING experiment. v: high vacuum valve. µv: micrometre flow control valve. Cryo: cryogenic trap (see Figure 2.7 for details). IG: ion gauge. P: turbo molecular pump. The NG bottle contains noble gases (Ne, Ar, Kr and Xe) and nitrogen. L1 and L2 refer to the two loops of gas flow discussed in the main text.

The fundamental principle of the experiment is to introduce a controlled mixture of water vapour, N_2 and noble gases into a vacuum chamber containing a cold plate located inside a cryogenic trap, to form amorphous water ice under high vacuum (Figure 2.7). The vacuum system typically reaches pressures of $\leq 5 \times 10^{-8}$ mbar, at room temperature. The proportion of water to noble gases in the gas mixture is monitored using a quadrupole mass spectrometer (QMS, loop L1, Figure 2.6) and precisely adjusted with micrometre needle valves to reach the desired proportions. Whilst the gas mixture is being prepared in L1 with the QMS, the cryogenic trap is isolated from L1 and cooled down while being pumped through the MaGui purification line. Once the gas mixture is adjusted and the trap has reached 28 K, the Loop L1 is closed and Loop L2 is opened, allowing the gas mixture to flow through the cryotrap, ion gauge and QMS (Figure 2.6). This enables the gas to be partially condensed on the cold trap, with the remaining (uncondensed fraction) being analysed for its elemental composition using the QMS (Figure 2.6). After about 5 minutes of ice deposition, the gas flow is stopped and the rest of the line, including the cryostat, is kept under high vacuum. The ice sample can then be thermally processed and/or irradiated by an ultra-violet (UV) lamp (Figures 2.6 and 2.7). During heating of the ice, the composition of the gas flux coming from the cryotrap is continuously monitored with the QMS. The initial and released gas fractions can be analysed for their isotopic compositions with the on-line sector-type mass spectrometer working in static mode (GV instruments Helix MC). In order to prepare for an isotopic analysis, the cryotrap is heated up to the temperature required for noble gases to be released. Just before reaching this temperature, the system is put into static mode (pump closed). Sublimated gases are then equilibrated for a few minutes at the given temperature step, and an aliquot of gas is sampled in a bottle (Figure 2.6). The sampled gas can later be purified for noble gas isotope measurements (section 2.III), by first passing through the on-line getter filled with Ti-sponge held at 550°C (Figure 2.6). Alternatively, the bottles can be detached and re-attached to a different purification line for nitrogen isotope analysis (section 2.IV).

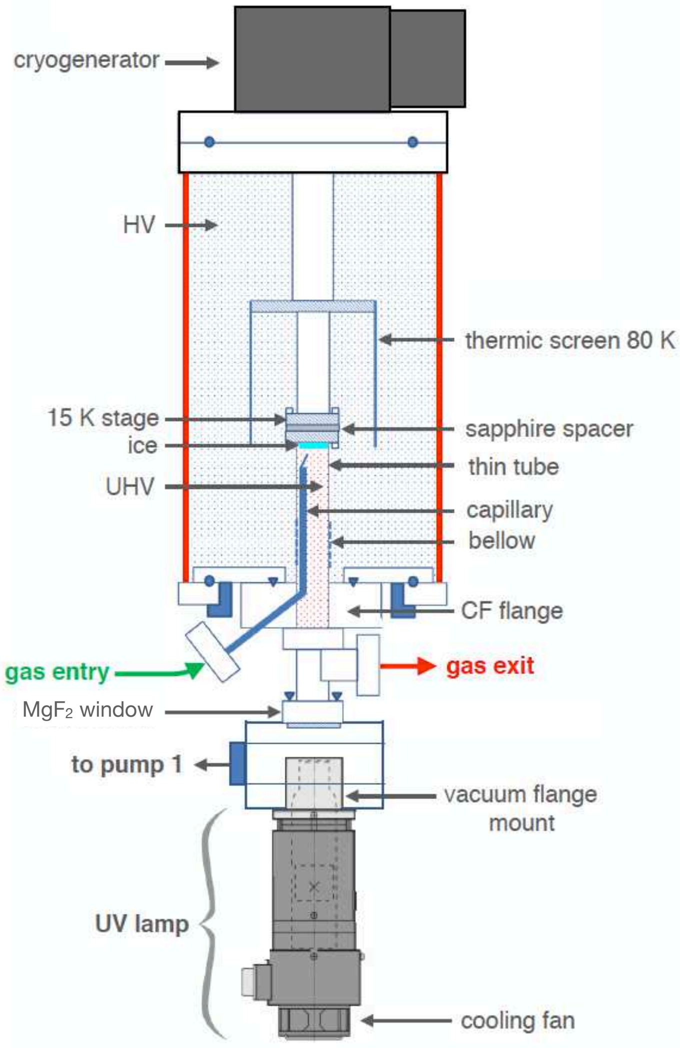

Figure 2.7: Diagram of the cryogenic head system allowing noble gases/water mixtures to be condensed down to ~30 K under high vacuum and exposed to Lyman-α light (with a H_2D_2 light source unit L11798 by Hamamatsu©). Adapted from Cryoscan© technical drawing of the modified cryogenic head (Almayrac et al. 2022). HV: high vacuum. UHV: ultra-high vacuum.

2) Sampling System for Isotope Analyses

The setup is equipped with three stainless steel bottles (see Figure 2.6) in order to sample gas released from the ice during an experiment and analyse the isotopic composition of Ar, Kr, Xe and N_2 using static noble gas mass spectrometry. The sampling system (Figure 2.6) is different from the one presented in Almayrac et al. (2022), where it initially consisted of a single on-line pipette connecting the main part of the line where the gas is released from the ice, and the on-line getter. This change was made in order to better adjust the quantity of gas sent for purification and isotopic analysis. Each bottle has a pipette system that allows the analysis of successive aliquots, in order to better control the amount of gas sent for analysis and increase the precision of isotopic measurements.

It is important to note the difference, under static or dynamic mode, between experiments with or without sampling for isotopic measurements. During a "normal" experiment on EXCITING, where the gas abundances are measured using the QMS, the whole system is permanently under dynamic pumping. For an experiment with gas sampling for isotopic analysis, the whole system is in static mode (pump closed) during the warm up of the ice, and the QMS is turned off in order to protect its filament from the higher pressures experienced in static mode. The main reason for this change in the procedure is to achieve higher gas concentrations necessary for the analysis of noble gas and nitrogen isotopes, and to avoid any potential isotopic fractionation that could occur in dynamic mode, whilst pumping across the small aperture of the valve on the sampling bottle. The gas released from the ice is thus accumulated in the experimental volume, and the sampling bottles are successively closed during warm up to sample different stages of gas release. Further details on when and why the system is operated in dynamic or static mode are given in the Methods section of Chapter 4.

3) Experimental Limitations

The EXCITING experiment was developed to answer specific scientific questions about the behaviour of noble gases (and nitrogen) in cometary H_2O ice, especially to investigate isotope fractionation during the trapping into -and release from- the ice, and the effect of irradiation on the trapping efficiency of noble gases and their isotopes. To our knowledge, EXCITING is the only ice analogue experiment that is capable of studying the isotope signatures of noble gases together with that of nitrogen at the precision achievable using static noble gas mass spectrometry. This precision in isotope composition, however, comes at the cost of some experimental limitations for the EXCITING setup.

Firstly, the cryogenic chamber is not equipped with instruments able to observe the ice, as it is the case in many ice analogues experiments (e.g., Bar-Nun et al. 1985; Jenniskens & Blake 1994; Piani et al. 2017). This design was chosen to limit the blank and internal volume of the system that can be compromised by the addition of instruments required to monitor and characterise the ice. Thus, we cannot directly observe the structure (amorphous, crystalline or clathrates) of the forming ice via spectroscopy (although the gas release pattern obtained during the heating of the ice allows to unambiguously conclude that we do form amorphous water ice, Bar-Nun et al. 1985; Almayrac et al. 2022). More importantly, we cannot measure the thickness of the ice, nor precisely quantify its deposition rate onto the cold plate. The thickness of the ice affects the behaviour of volatiles during their release from the ice (Notesco & Bar-Nun 2005), and the deposition rates can have an influence on the trapping efficiency of volatiles in amorphous water ice (Notesco et al. 2003; Ciesla et al. 2018).

Secondly, the cryogenic system equipped on EXCITING struggles to reach temperatures lower than 25K. It takes around 1 hour to reach 28K from room temperature, an additional 1 hour to reach 27K, and around 7 hours in total to reach 25K. Because the temperatures of cometary ice formation are traditionally estimated around 25K-30K (Notesco et al. 2003; Notesco & Bar-Nun 2005; Rubin et al. 2015), we consider it not necessary to explore formation temperatures lower than ~25K.

Finally, as is often the case for experimental investigations, we are limited by the simplification of our system compared to the complexity of cometary ice formation in terms of timescales and molecular ice diversity. From the formation of the ice to the total release of volatiles, an experiment typically lasts ~3-4 hours, which is obviously much quicker than deposition and heating rates experienced by cometary ices in natural environments. Fast deposition rates favour the trapping of volatiles into the pores of amorphous ice during formation (Notesco et al. 2003; Ciesla et al. 2018), and rapid heating rates limit the diffusion of volatile species out of the ice during the experiment. Regarding the molecular diversity, the EXCITING experiment explores the behaviour of nitrogen and noble gases in water ice, without the addition of other molecules such as CO, CO_2, CH_4, CH_3OH, O_2 or H_2S that are yet commonly found in the interstellar medium (Müller et al. 2005) and comets (Altwegg et al. 2019). In general, because noble gases are chemically inert, the presence of these reactive molecules does not affect the behaviour of noble gases. However, the presence of CO_2 could be of importance for noble gas behaviour because of its capacity, similarly to amorphous water, to trap other volatile elements (such as NH_4 or CO, Kouchi & Yamamoto 1995). The presence of CO_2 has been observed in several comets (~10% of the water amount, Feldman et al. 1997), and in comet 67P/C-G locally and episodically exceeding the amount of water (Läuter et al. 2020). Although no experiment exists, to our knowledge, on the trapping efficiency and repartition of noble gases between CO_2 and H_2O ices, it could ultimately provide important insight into the origin of the noble gas composition measured in comet 67P/C-G (Marty et al. 2017; Rubin et al. 2018).

III. Noble Gas Isotope Analyses

1) MaGui and the Purification of EXCITING Samples

MaGui is the noble gas purification line associated with the GV instrument Helix MC (Figure 2.2) that is mainly used here to analyse He, Ar, Kr and Xe isotopes. A schematic of the line is given Figure 2.8. The different volumes of the line are connected by manual (Swagelok©) and automated pneumatic valves. MaGui is equipped with two turbo molecular pumps (Pfeiffer Vacuum© TMU 071P model) maintaining a background pressure around 10^{-9} mbar. The pressure in the line is monitored using an ion gauge (MKS©, Mini Ion Gauge model). The three getters are filled with Ti-sponge and held at different temperatures to optimise the purification of the line from H_2, N_2, O_2, H_2O and hydrocarbons. One getter (Getter1 on Figure 2.8, model GP50 containing Zr-Al alloy, by SAES Getters©) is held at room temperature, mainly removing H_2 from the line, and two hot getters (Getter2 and Getter3 filled with Ti-sponge) are held at 550°C for cracking and purifying hydrocarbons (Zimmerman et al. 2015). Gas bottles of standard gas (noble gases with atmospheric composition) are connected to the line with automatic valves (Figure 2.8). Two additional automatic valves (connecting the pump P2 and the mass spectrometer, Figure 2.8) were installed during this PhD in order to automate standard analysis.

Because gas sampling is systematically done before the temperature of water sublimation (i.e., ~150K), gas samples from the EXCITING experiment are composed of a mixture of N_2, Ar, Kr and Xe with only limited amounts of water. First the gas is passed through an on-line getter (part of the EXCITING line, Figure 2.6) held at 550°C for 10 min, then expanded to Getter1 for 20 minutes, and finally expanded to Getter2 and Getter3 for an additional 10 minutes. Before sending the purified gas into the mass spectrometer, dilutions may be necessary to match the pressure of the standard gas and avoid any unquantified fractionation effect during analysis in the mass spectrometer.

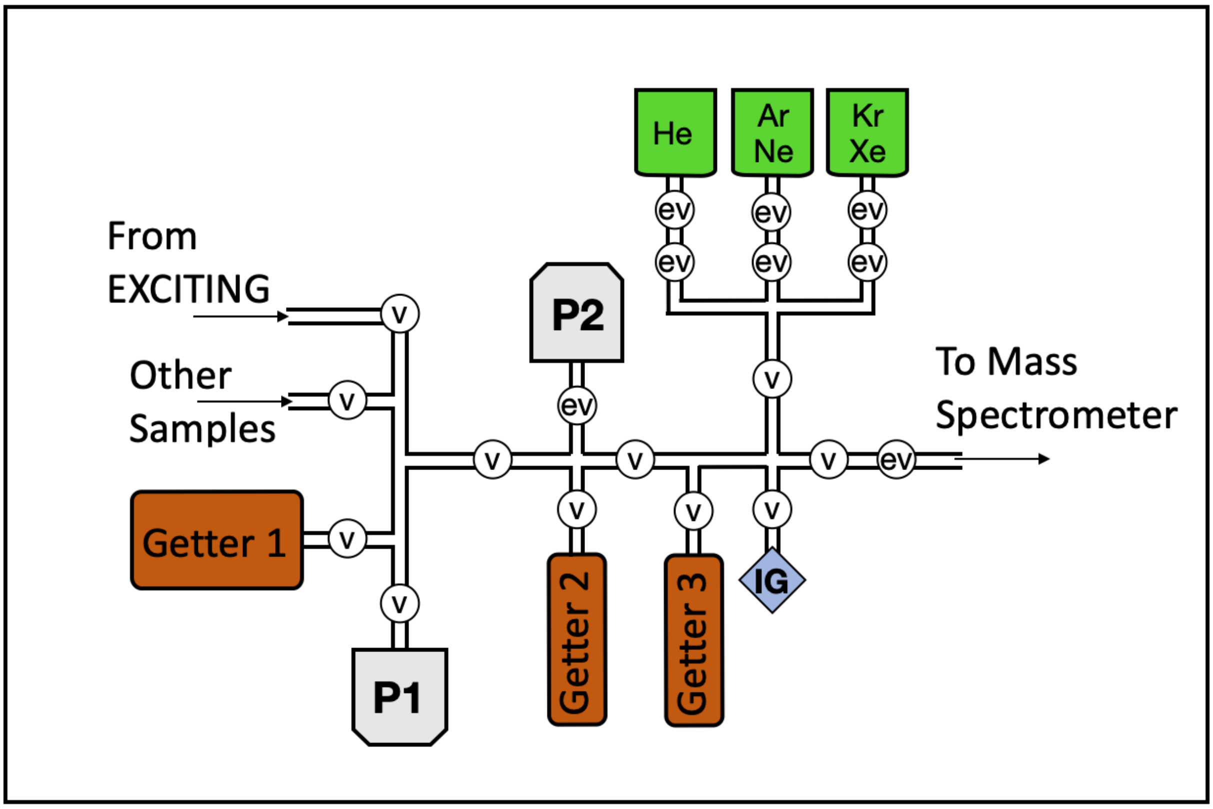

Figure 2.8: Schematic representation of the MaGui purification line for noble gases. v: high vacuum valve. ev: automated pneumatic valve. P1 and P2 are two turbo molecular pumps. IG: ion gauge.

2) GV Instrument MC Mass Spectrometer for Noble Gas Isotopes

i. Description

The GV Instrument MC is a mass spectrometer composed of three different parts (i) a Nier-type source (Nier, 1947) to ionise the gas, (ii) a magnetic sector to separate isotopes according to their mass over charge ratios m/z, and (iii) several collectors to convert arriving ions into measurable electric current. These different parts are shown Figure 2.5 and are representative of most of the static noble gas mass spectrometers (in particular the second mass spectrometer used during this PhD, the ThermoFischer Helix MC$^+$ presented in next section).

The GV is equipped with three Faraday Cups (10^{11} Ω and 10^{12} Ω resistances) that were upgraded during the first year of the PhD, in 2019, by IsotopX©. As part of the EXCITING project, and other projects involving the analysis of hydrothermal fluids (Broadley et al. in prep), and volcanic gases (CO_2-rich gas from Yellowstone, Byrne et al. in prep, and Massif Central, Contamine et al. in prep), I developed the measurement of He, Ar and Xe isotopes.

The EXCITING project focused on analysing ^{36}Ar, ^{38}Ar and ^{40}Ar, and the most abundant Xe isotopes ^{128}Xe, ^{129}Xe, ^{130}Xe, ^{131}Xe, ^{132}Xe, ^{134}Xe and ^{136}Xe. For the project, isotopes ^{124}Xe and ^{126}Xe were not analysed because of their under-abundance, which would require them to be measured on an electron multiplier, not currently installed on the GV Helix MC. Krypton isotope measurements were briefly investigated but not developed further due to their limited relevance compared to Ar (lighter) or Xe (more isotopes) to investigate mass-dependent isotopic fractionation effects. The mass spectrometer has a mass resolution around 700, allowing for the interference at mass 38, between ^{38}Ar and hydrocarbon C_3H_2 (see the ^{38}Ar peak Figure 2.9), to be resolved. All the other possible interferences with Ar and Xe isotopes are either well resolved or not present because of the efficient hydrocarbon purification.

ii. Analytical method

For both standard and sample analysis, Ar and Xe were analysed separately from different aliquots of gas. Two different source settings were used to analyse Ar and Xe isotopes, given in Appendix Table A1. The choice of these source settings mainly results from optimising the signal size (i.e., the sensitivity) and the peak shape of each isotope (Figure 2.9), as well as maintaining the source settings as similar as possible for Ar and Xe analysis to avoid abrupt changes in the source causing it to be unstable over time.

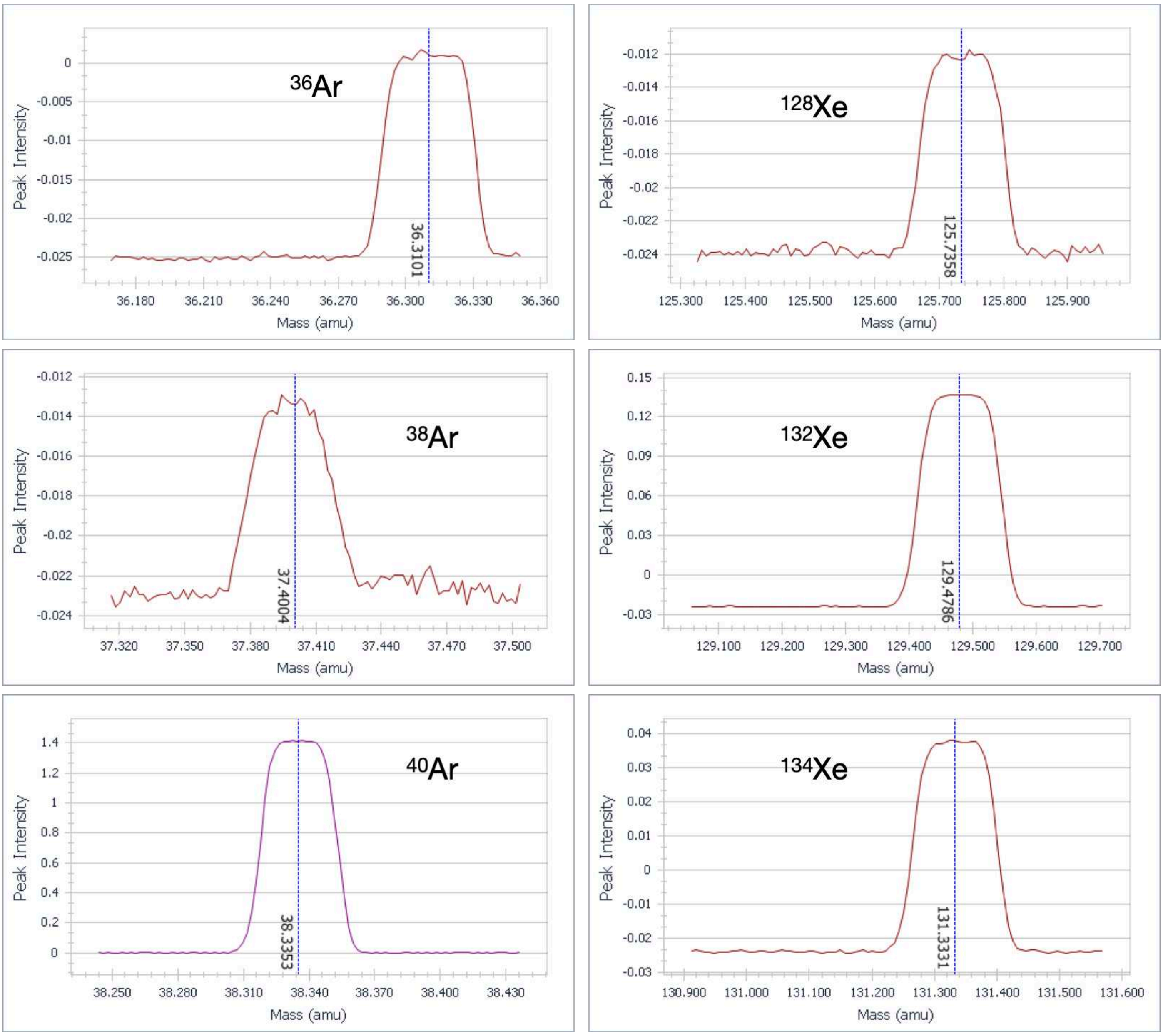

Figure 2.9: Peak centering window of the IsoLinx software from IsotopX© of ^{36}Ar, ^{38}Ar (measured in the 10^{12} Ω) and ^{40}Ar (measured on the 10^{11} Ω) in the left-hand side, and ^{128}Xe, ^{132}Xe and ^{134}Xe (10^{12} Ω) is the right-hand side. The intensity signals are in volts.

Both Ar and Xe were analysed in mono-collection peak jumping mode, using faraday cups. Isotopes ^{36}Ar and ^{38}Ar were measured using a 10^{12} Ω resistance, and ^{40}Ar using a 10^{11} Ω resistance. Ar isotopes were analysed over 20 repeated cycles. During one cycle, the ^{36}Ar intensity was measured 15 times, 20 times for ^{38}Ar and 5 times for ^{40}Ar, with an integration time of 1 second for each measurement. All Xe isotopes were measured using a single collector with 10^{12} Ω resistance. Xenon isotopes were analysed over 15 cycles. ^{128}Xe and ^{130}Xe were measured 20 times and $^{129-131-132-134-136}$Xe 15 times, also with 1-second integration time for each measurement. Atmospheric Ar and Xe isotopic ratios, as well as the measurement protocols described above, are given Table 2.1. One analysis of Ar and Xe typically lasts around 30 minutes.

Isotope	Air ratio	Resistance	Measurements per cycle	Number of cycles
^{36}Ar	≡1	10^{12} Ω	15	20
^{38}Ar	0.1885 (3)	10^{12} Ω	20	
^{40}Ar	298.56 (31)	10^{11} Ω	5	
^{128}Xe	0.07136 (9)	10^{12} Ω	20	15
^{129}Xe	0.9832 (12)	10^{12} Ω	15	
^{130}Xe	0.15136 (12)	10^{12} Ω	20	
^{131}Xe	0.7890 (11)	10^{12} Ω	15	
^{132}Xe	≡1	10^{12} Ω	15	
^{134}Xe	0.3879 (6)	10^{12} Ω	15	
^{136}Xe	0.3294 (4)	10^{12} Ω	15	

Table 2.1: Atmospheric isotope composition of Ar (Lee et al. 2006) and Xe (Basford et al. 1973) normalised to ^{36}Ar and ^{132}Xe, respectively. Numbers in parenthesis are the uncertainties on the last digits. The resistance of the receptor used, as well as analytical protocol are given for each isotope.

During the analysis of both Ar and Xe, the gas abundance is continually decreasing as the gas is consumed by the source (see figure 2.10, for ^{36}Ar and ^{40}Ar, and Figure 2.11 for ^{128}Xe and ^{132}Xe, respectively). An exponential regression to time zero is done using the LabView software to compute the abundances of Ar and Xe isotopes at the time they were admitted into the mass spectrometer. An exponential regression is preferred because it best fits the signal evolution and gives smaller uncertainties on the intercept than a linear regression. In addition, we note that the noble gas consumption in a Nier type source should in theory follow an exponential decrease (Nier, 1947).

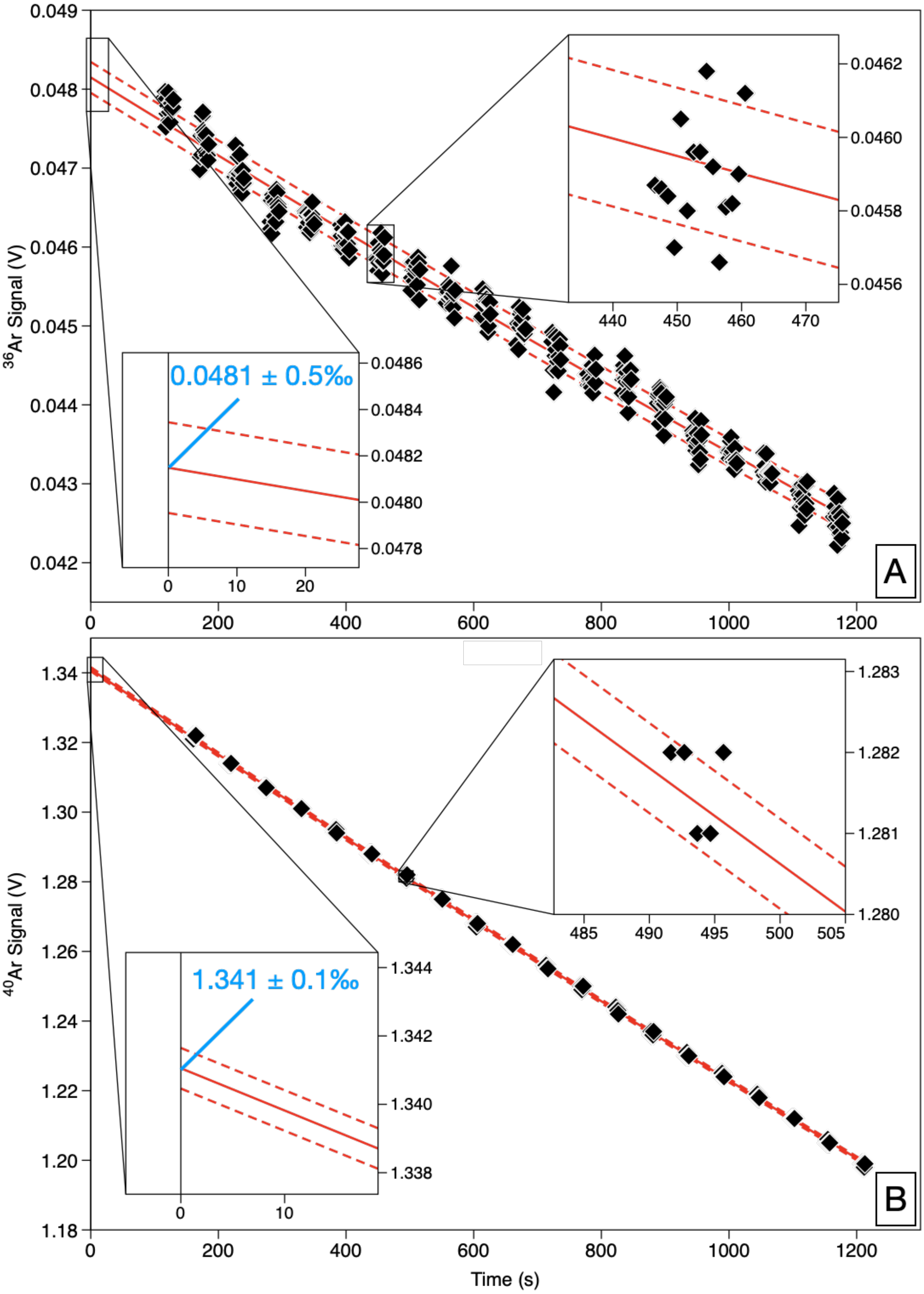

Figure 2.10: Evolution of the ^{36}Ar (**A**) and ^{40}Ar (**B**) signals with time after they have been sent into the mass spectrometer. The red line and the red dashed lines are the exponential regression of the data, and the 1σ (67% confidence) uncertainty envelope, respectively. The intercept at t=0 is given for both isotopes, together with the associated uncertainties, which represents the internal error of the abundance measurement, in permil.

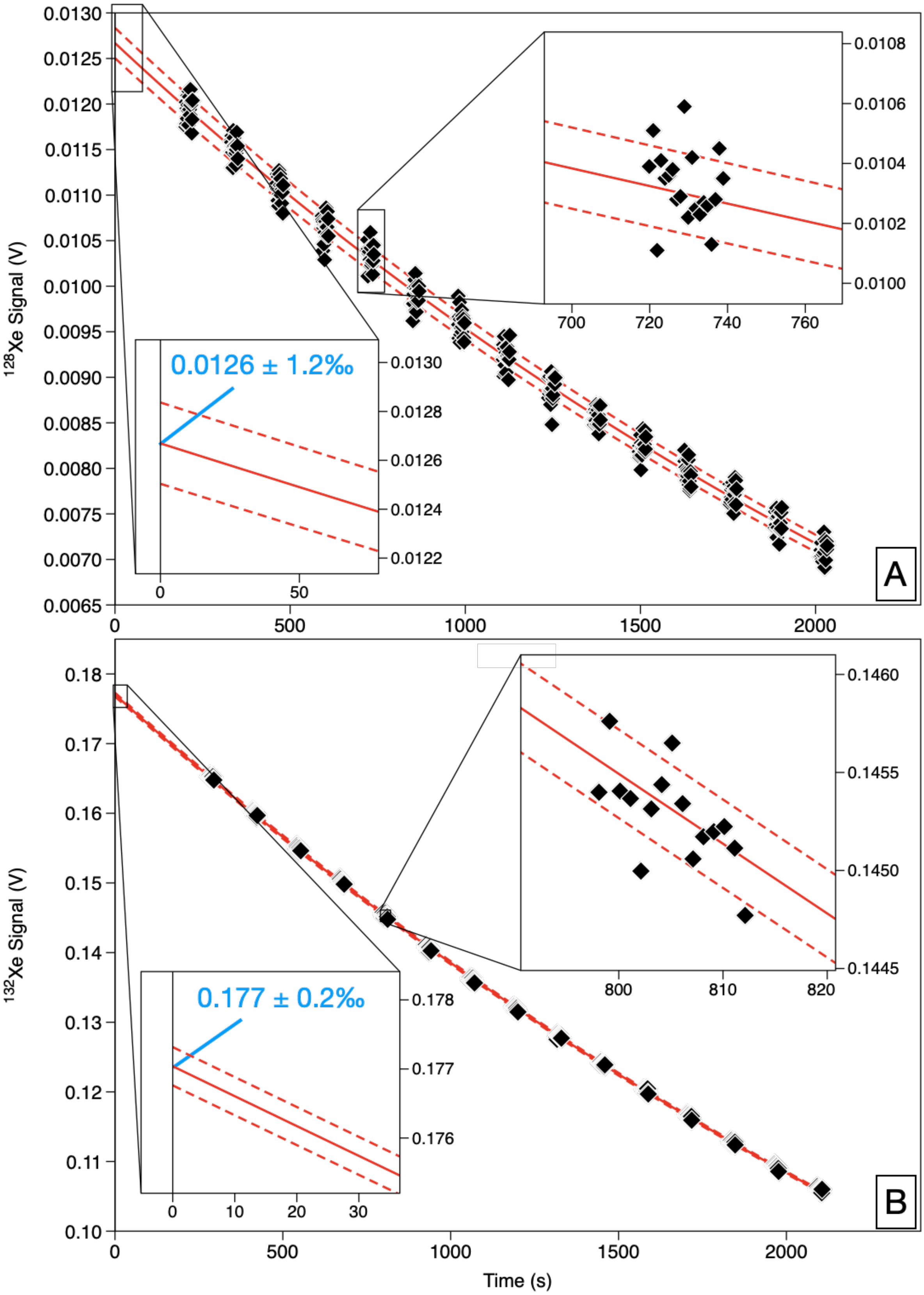

Figure 2.11: Same as Figure 2.10 but with ^{128}Xe (**A**) and ^{132}Xe (**B**).

iii. Performance: reproducibility and precision

Standard gas of Ar and Xe with atmospheric isotope compositions (from gas bottle in the MaGui line, Figure 2.8) were analysed before and after samples to monitor and quantify the reproducibility and the instrumental mass discrimination (or fractionation) of the mass spectrometer. Each standard of Ar and Xe has an atmospheric isotopic composition (see Table 2.1) and an amount of 3 x 10^{-8} mol of ^{40}Ar, and 6 x 10^{-11} mol of ^{132}Xe. The reproducibility for a given isotope ratio is given by the standard deviation, at 1σ, relative to a series of standards. Figure 2.12 shows the reproducibility for Ar isotope ratios (normalised to the non-radiogenic isotope ^{36}Ar by convention), corresponding to 0.75% and 0.37% at 1σ for the ratios of ^{38}Ar/^{36}Ar and ^{40}Ar/^{36}Ar, respectively. The instrumental mass fractionation on Ar isotopes can be visualized in a ^{40}Ar/^{36}Ar vs. ^{38}Ar/^{36}Ar plot, Figure 2.13. Details on how the internal error is calculated and how errors are propagated are given in the next section (III.2.iv).

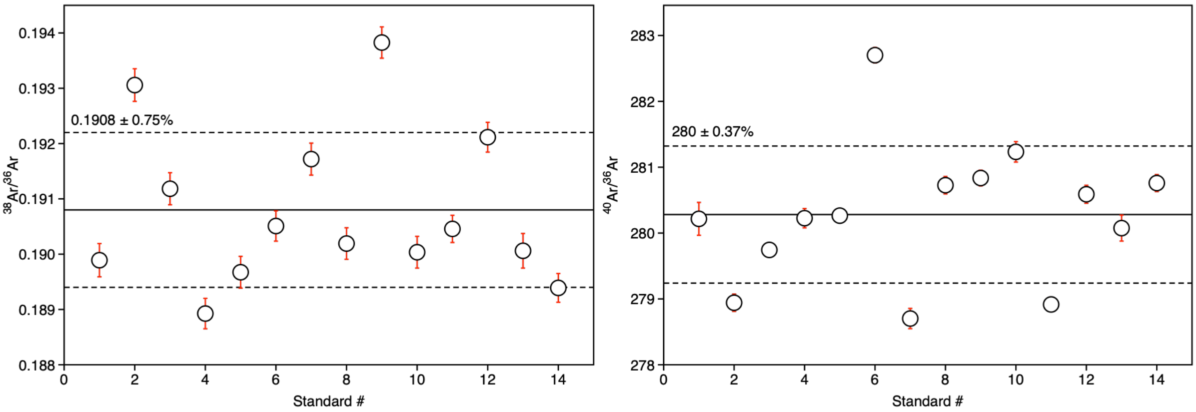

Figure 2.12: ^{38}Ar/^{36}Ar and ^{40}Ar/^{36}Ar ratios of 14 standards done over one month. Red error bars represent the internal error for each ratio. The black lines are the averages of the standards, and the dashed lines are the 1σ envelope of the standard deviation of the standards. The reason why the internal error is much smaller than the external reproducibility for Ar measurements is discussed in the main text, next section III.2.iv about error calculation method.

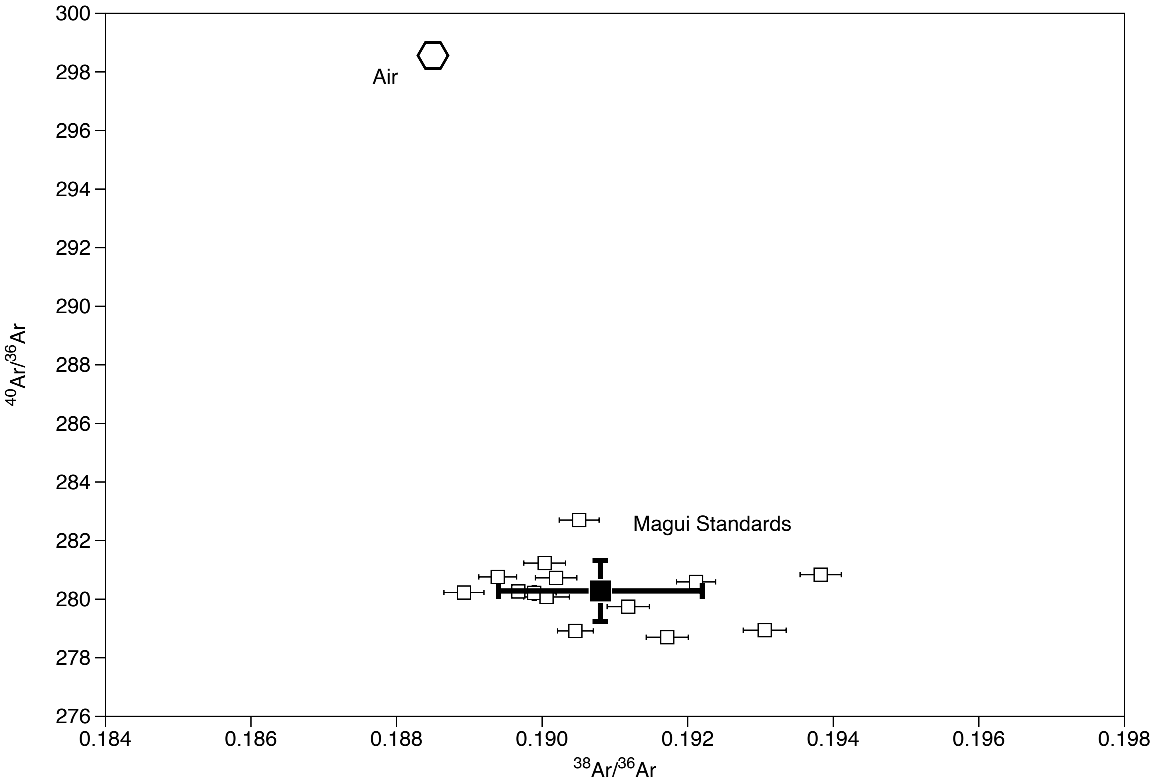

Figure 2.13: Ar isotope composition of the standards (open squares). Error bars are the internal error for each standard ratio. The isotope composition is different from air (hexagon) because of the instrumental mass discrimination. The closed black square is the average and its associated error bars are the standard deviation of the standards. All uncertainties are at 1σ.

The reproducibility of the 6 ratios of Xe isotopes (normalised to the most abundant isotope ^{132}Xe) $^{128\text{-}129\text{-}130\text{-}131\text{-}134\text{-}136}Xe/^{132}Xe$, are all below 1% (Figure 2.14). The most abundant Xe isotopes (after ^{132}Xe) ^{129}Xe, ^{131}Xe, ^{134}Xe and ^{136}Xe, show better reproducibility than the lesser abundant ^{128}Xe and ^{130}Xe isotopes. This is related to the "quality" of their peak shape (see Figure 2.9), where ^{128}Xe and ^{130}Xe have a lower signal to noise ratio, making their peak intensities less reproducible than the more abundant isotopes (Gedcke 2001). The instrumental mass fractionation on Xe isotopes can be visualized on Figure 2.15, where we use the delta notation to quantify the difference between a measured value and a reference. For noble gas studies, the reference isotope value is often the modern atmospheric isotope composition (Basford et al. 1973). For a given isotope ratio, the delta notation is defined as $\delta^{i}Xe = [\ ^{i}Xe/^{132}Xe_{sample}\ /\ ^{i}Xe/^{132}Xe_{atm} - 1] * 1000$, where *atm* refers to the atmospheric composition. In this manuscript, Xe isotope data are primarily expressed as delta variation relative to a reference, whilst raw Ar isotope ratios (corrected for mass discrimination) are used with no normalisation.

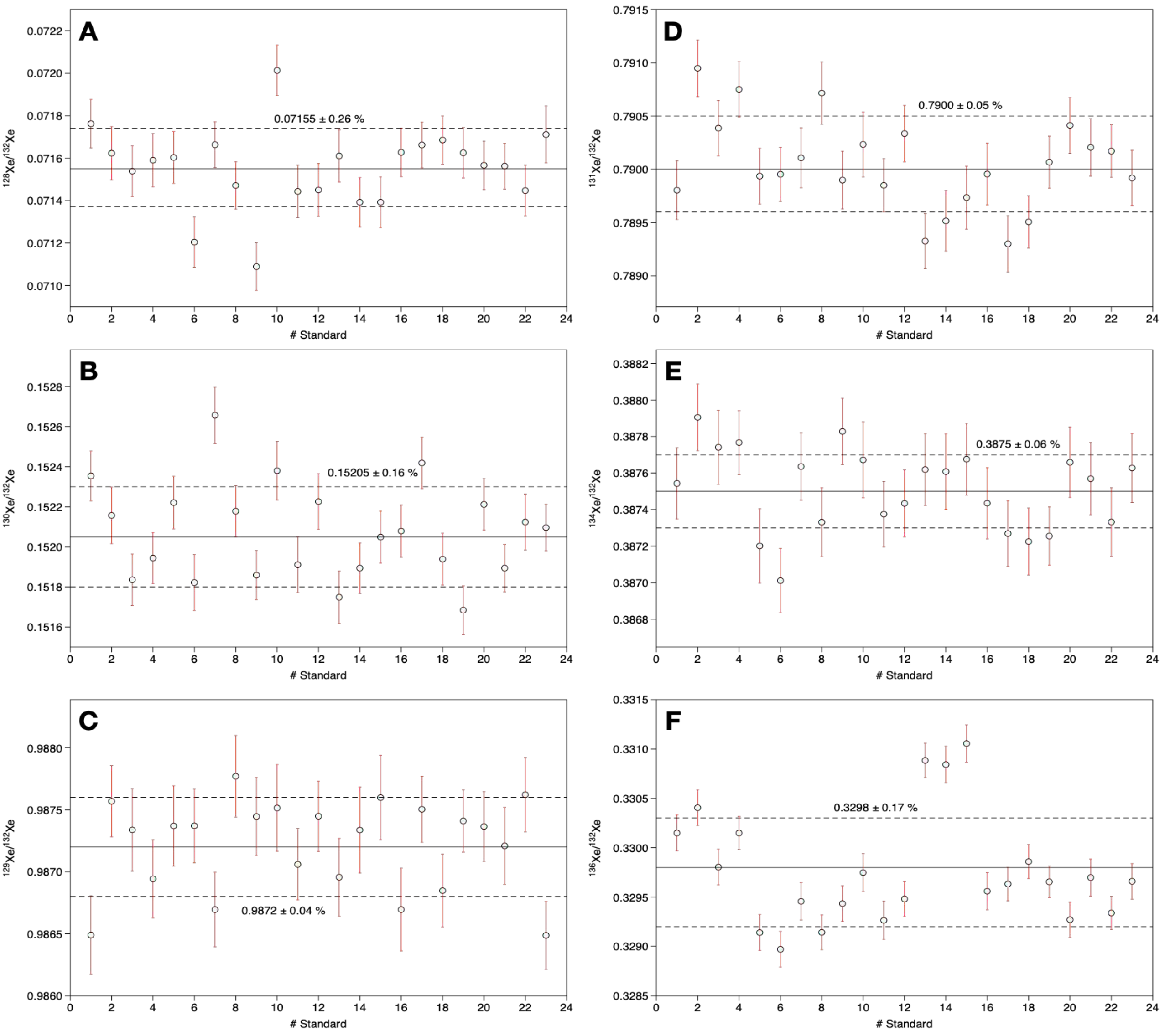

Figure 2.14: Xe isotope ratios $^{128\text{-}129\text{-}130\text{-}131\text{-}134\text{-}136}$Xe/^{132}Xe of 23 standards done over one month. The black line is the average and the dashed lines are the uncertainty envelopes (i.e., one standard deviation) of the mean value of the standards. Error bars are the internal error for each standard ratio (1σ).

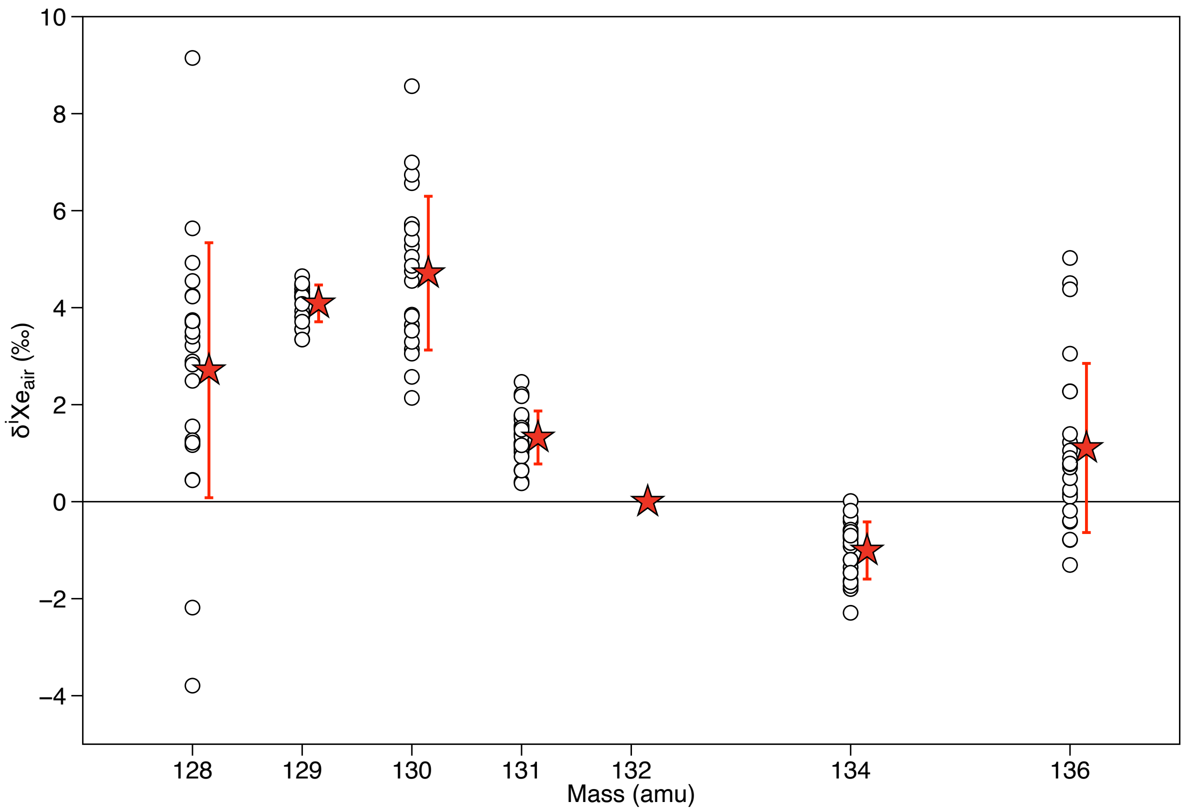

Figure 2.15: Xenon isotopic spectra of the standards (circles) normalised to ^{132}Xe relative to the atmospheric composition ($\delta^iXe = [\,^iXe/^{132}Xe_{\,sample} / \,^iXe/^{132}Xe_{\,atm} - 1] * 1000$, air composition from Basford et al. 1973). Since the standard bottle has an atmospheric composition, deviations from 0‰ result from the instrumental mass discrimination. Red stars are the average of the repeated standards (offset for better visibility), and the associated error bars are the standard deviation (reproducibility at 1σ).

iv. Calculation of uncertainties and error propagation

During the past 5 years at CRPG, we have strived to homogenise our calculation method to avoid any under- or over-estimation of the uncertainties. The LabView software is now used in almost all noble gas mass spectrometers at CRPG to perform linear/exponential regression on the repeated cycles to time zero for each isotope. The uncertainty of the regression on the intercept value for t=0 represents the internal error on the isotope abundance measurement. The uncertainty calculation for isotope ratios is done using the following error propagation formula:

$$\text{when } z = f(x_1, x_2, \ldots), \sigma_z{}^2 = \sum_i \left(\frac{\partial z}{\partial x_i} \times \sigma_{x_i}\right)^2 \quad (2)$$

In the example of the ^{40}Ar/^{36}Ar ratio, the associated uncertainty is:

$$\sigma_{(^{40}\mathrm{Ar}/^{36}\mathrm{Ar})} = \sqrt{\left(\frac{\sigma_{^{40}Ar}}{^{36}Ar}\right)^2 + \left(^{40}Ar \times \frac{\sigma_{^{36}Ar}}{^{36}Ar^2}\right)^2}\,, \quad (3)$$

$$\text{or } \sigma_{(^{40}\mathrm{Ar}/^{36}\mathrm{Ar})} = \frac{^{40}\mathrm{Ar}}{^{36}\mathrm{Ar}} \times \sqrt{\left(\frac{\sigma_{^{40}Ar}}{^{40}Ar}\right)^2 + \left(\frac{\sigma_{^{36}Ar}}{^{36}Ar}\right)^2} \quad (4)$$

where $\sigma_{^{36}Ar}$ and $\sigma_{^{40}Ar}$ are the internal error on the measured ^{36}Ar and ^{40}Ar signals, respectively.

The same formula is then used to propagate errors when normalising different ratios, to the air composition or any reference composition. To this internal error we finally add the external reproducibility of the mass spectrometer (i.e., the standard deviation of the standards) as follow:

$$\sigma_{(^{40}\mathrm{Ar}/^{36}\mathrm{Ar})t} = \sqrt{\sigma_{(^{40}\mathrm{Ar}/^{36}\mathrm{Ar})int}{}^2 + repro_{(^{40}\mathrm{Ar}/^{36}\mathrm{Ar})}{}^2} \quad (5)$$

Where $\sigma_{(^{40}\mathrm{Ar}/^{36}\mathrm{Ar})t}$ is the total uncertainty on the ^{40}Ar/^{36}Ar ratio, *int* refers to the internal error propagated as described above, and *repro* refers to the standard deviation of the ^{40}Ar/^{36}Ar ratios of the standards (the external error). For all isotope data presented in this manuscript, we can observe (especially on Figure 2.12 showing standard reproducibility of Ar isotopes, in the previous section) that the internal error is always smaller than the external reproducibility (external error). Very small internal error (~0.1 ‰, Figure 2.10) can be reached for ^{40}Ar because of the large amount of gas analysed (3 x 10^{-8} mol of ^{40}Ar in a standard pipette). The internal error can be predicted based on the amount of signal (1 V of ^{40}Ar using the 10^{11} Ω Faraday cup on the GV Helix MC) and the counting time (1 second), as shown Appendix Figure A1. On the other hand, the external error depends (for a given purification protocol) on the stability of the source and the quality of the electronics inside the mass spectrometer, which are not at the state-of-the-art for the relatively old GV Helix MC, leading to a high contribution of the external error in the total uncertainty of a given ratio (also described in Wright et al. 1988).

All the isotopic ratio or normalised ratio uncertainties given in this manuscript are calculated following this error propagation method. Nitrogen isotope data (see following section) reduction follows the same method as for noble gases.

IV. Nitrogen Isotope Development

Nitrogen in the form of N_2 is a highly stable/unreactive molecule comparable to noble gases and their inherent chemical inertness. The development of N_2 measurements by static noble gas mass spectrometry started in the 1980's (Becker and Pepin 1984, Boyd et al. 1988) and emerged from the need to measure increasingly small amounts of nitrogen in terrestrial and extra-terrestrial samples (< 1ppm). Conventional instruments to measure nitrogen isotopes in minerals do not typically achieve the sensitivity required to reach a sub-ppm detection limit (for instance by ion probe, Deligny et al. 2021, or Isotope-Ratio-Mass-Spectrometer IRMS, Vacher et al. 2020). Because noble gas mass spectrometers are operated in static mode, they can reach very high sensitivities. The measurement of small amounts of N_2 by noble gas mass spectrometry is however complicated by (i) air contamination and nitrogen generation during sample extraction, (ii) nitrogen purification and reduction/oxidation from NO or NH_3 into N_2, and (iii) mass interferences at mass 28 and 29 (^{14}N-^{14}N and ^{15}N-^{14}N, respectively) with ^{28}CO and hydrocarbon C_2H_4, and ^{29}CO, N_2H and C_2H_5.

The recent development of the nitrogen purification line connected to the ThermoFisher Helix MC$^+$ relies on the knowledge accumulated over decades of N_2 isotope measurement at CRPG (Marty 1995; Hashizume and Marty 2004; Marty et al. 2010; Füri et al. 2012; Füri et al. 2015; Boulliung et al. 2020) using a (now decommissioned) Micromass© VG5400 mass spectrometer and a newly acquired Nu Instrument Noblesse mass spectrometer (Boulliung, 2020; Zimmermann et al. in prep). So far, the line has successfully been used to analyse nitrogen in EXCITING samples (Chapter 4), Synchrotron irradiated samples and Ryugu samples returned from the Hayabusa2 space mission by JAXA (Okazaki et al., 2022).

In this section, I provide (i) a description of the nitrogen purification line, and the purification protocol used for the EXCITING samples, (ii) the specifications of the Helix MC+ spectrometer and the data processing method used to deconvolute N_2 from the CO interferences, and (iii) the performances in precision and sensitivity achieved by the new setup.

1) The Nitrogen Purification Line

i. The line

The nitrogen purification line is a part of the "ADN" purification line for noble gases, connected to the Helix MC+ mass spectrometer (Figure 2.3). The N_2 line is composed of a single volume made of glass, and connected to the rest of the stainless steel noble gas line by glass-steel CF (ConFlat) type connections. A schematic of the line is given Figure 2.16. The line is made of glass to reduce adsorption of atmospheric nitrogen (and high blank contributions from degassing surfaces during analysis) and avoid the potential for nitrogen to react with the metallic surfaces (Yokochi & Marty 2006). The blank contribution for nitrogen measurements is a matter of prime interest in order to be able to analyse an amount of gas as small as possible.

The line is equipped with two glass fingers (F1 and F2 on Figure 2.16) that can be cooled down to 93K (-180°C) and ~118K (-155°C), respectively, using liquid nitrogen. Finger F1 is equipped with a thermoregulator system that allows the temperature to be precisely set at -180°C, instead of reaching the actual temperature of liquid nitrogen at -196°C. A volume filled with CuO rods (solid copper oxide) wrapped in platinum foil is located in between F1 and F2, and can be heated up to 905°C using a small furnace. A glass balloon containing a calibrated amount of diluted air is also connected to the line and serves as a nitrogen standard. Finally, the line is equipped with a turbo molecular pump (P3, Figure 2.16), and a baratron (MKS instruments©).

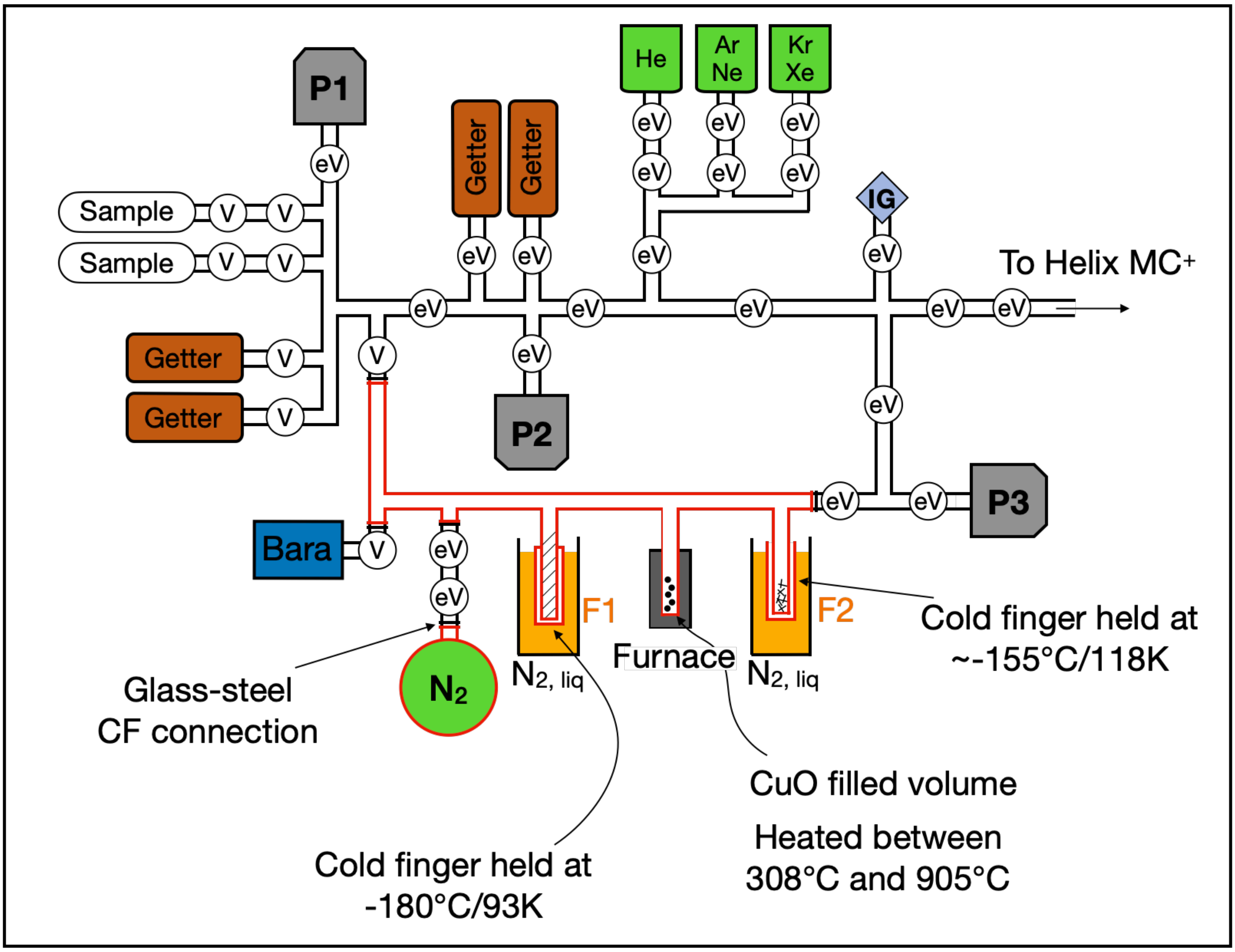

Figure 2.16: Schematic representation of the ADN purification line. The red part, made of glass, corresponds to the nitrogen purification line. The black part is made of stainless-steel. V: high vacuum valve. eV: automated pneumatic valve. P1, P2 and P3 are three turbo molecular pumps. IG: ion gauge. Bara: Baratron. F1 and F2 are two glass fingers (volumes) that can be immerged in a dewar filled with liquid nitrogen ($N_{2,\ liq}$). F2 is filled with platinum foils. A third glass finger is filled with CuO rods and platinum foil with a small furnace around it that can reach temperatures of 905°C. N_2: glass sphere filled with diluted (and calibrated) atmosphere, used as a nitrogen standard.

ii. The purification

The purification of nitrogen mainly refers to the removal of CO, CO_2, H_2O, and SO_2 from the gas sample by cold traps, as well as the transformation of N-bearing molecules (NH_4, NO_x, organics) into N_2. The method is adapted from the protocol first established by Boyd et al. (1988). The purification procedure relies on the oxidation, followed by the reduction of the gas using a copper-oxide furnace (CuO, Figure 2.16). Initially the CuO furnace is at 450°C when the gas sample is first introduced in the line. The furnace is then set at 905°C for 25 minutes, hence triggering the liberation of oxygen from the CuO and the oxidation of the gas in the line. The Pt foil catalyses the reaction of oxidation of CO into CO_2, while also causing the cracking of hydrocarbons. Hydrocarbon are then oxidised into CO_2 and H_2O, and any sulfur compounds are oxidized into SO_2. Nitrogen-bearing species are oxidized into NO_x molecules. Simultaneously to this first step, liquid nitrogen is placed on the first trap F1 (Figure 2.16), and CO_2, H_2O, SO_2 products are trapped at ~ -180°C. The second step of the purification is the slow decrease in temperature of the CuO from 905°C to 308°C (over 1 hour) in order to recover the O_2 into the CuO and reduce the NO_x species into N_2, whilst the oxidised products remain trapped inside the cold finger. In detail, the temperature decrease is performed by steps: 15 minutes at 746°C, 15 minutes at 634°C, 15 minutes at 523°C and 15 minutes at 308°C. Once reaching the 634°C temperature step, the second finger F2, which is double walled to limit the temperature decrease (between -160 and -150°C), is submerged in liquid nitrogen in order to increase the trapping efficiency of CO_2 and H_2O. After the purification, the purified N_2 is sent into the rest of the line for pressure control (and necessary dilutions are made, if necessary, to match the standard gas pressure) and subsequent inlet into the Helix MC^+ mass spectrometer for analysis.

2) Helix MC^+ and Data Reduction

Nitrogen isotope measurements were performed using a ThermoFisher Helix MC^+ mass spectrometer (Figure 2.3). The source settings, given in Appendix Table A2, are similar to the settings used for noble gases (Ar and Xe on the GV Helix MC Appendix Table A1), except for the trap current used. The trap current basically describes the intensity of the electron production to ionise the gas, with lower trap current leading to less ionisation. The trap current used for nitrogen measurement is lower (50 µA) than for noble gases (~300 µA for Ar and Xe measurements on the GV Helix MC). A lower trap current is preferred because it limits the production of CO and N_2H in the source (Hashizume & Marty 2004), which are the main species interfering during the analysis of N_2. Analysing nitrogen at higher trap currents to increase the sensitivity is usually not worth because of the loss of precision due to the increasing CO interference. The three N_2 isotopologues ^{14}N-^{14}N ($^{28}N_2$), ^{14}N-^{15}N ($^{29}N_2$) and ^{15}N-

^{15}N ($^{30}N_2$) were measured by peak jumping in mono-collection. Similarly to Ar and Xe measurements on the GV instrument MC, we use mono-collection rather than multi-collection because we can reach equal precision with simpler (and more stable) receptor settings. $^{28}N_2$ and $^{29}N_2$ are collected using faraday cups with 10^{11} Ω and 10^{12} Ω resistances, respectively. Isotopologue $^{30}N_2$ being much less abundant, it is collected using a CDD electron multiplier. Table 2.2 provides the relative abundances of N_2 isotopologues in air (Nier et al. 1950) and the receptors used for their analysis. N_2 was analysed over 20 repeated cycles. For each cycle, the three isotopes were measured once with an integration time of 1 second for $^{28}N_2$ and 8 seconds for $^{29}N_2$ and $^{30}N_2$.

N_2 isotope	**Air**	**Helix MC$^+$ Collector**			**Interferences**		
		Pos	**Type**	**Resist**	**Ion**	**Reso**	
$^{28}N_2$	≡1	H1	FC	10^{11} Ω	$^{12}C^{16}O$	2493	Yes
$^{29}N_2$	7.35 x 10^{-3}	H2	FC	10^{12} Ω	$^{13}C^{16}O$ ($^{12}C^{17}O$)	5918	No
					$^{14}N^{14}N^{1}H$	2675	Yes
					$^{12}C_2{}^{1}H_5$	807	Yes
$^{30}N_2$	1.35 x 10^{-5}	H2	CDD	-	$^{12}C^{18}O$ ($^{13}C^{17}O$)	~30000	No
					$^{15}N^{14}N^{1}H$	2768	Yes
					$^{12}C_2{}^{1}H_6$	639	Yes

Table 2.2: Atmospheric abundance of N_2 isotopes (Nier et al. 1950), normalised to that of $^{28}N_2$. Details on the collector type (FC: faraday cup, CDD: compact discrete dynode), position (Pos), and resistance are given. All ion interferences are cations (such as $^{12}C^{16}O^+$), and CO ions in parenthesis are usually negligible (Hashizume & Marty 2004) compared to the other primary CO isotope. For each interference the mass resolution (Reso) required to fully resolve them is given (Zimmermann & Bekaert 2020). The mass resolution of the Helix MC+ (~1800) permits to fully resolve C_2H_5 and C_2H_6 interferences, and partially resolve (see Figure 2.17) ^{28}CO, $^{28}N_2H$ and $^{29}N_2H$ interferences. ^{29}CO and ^{30}CO interferences cannot be resolved and must be corrected by making assumption on their composition (method described in this section).

A major concern when measuring N_2 isotopes is the multiple interferences with CO, N_2H and hydrocarbon C_2H_x. The important interferences and the mass resolution necessary to resolve them are given in Table 2.2. The Helix MC$^+$ has a mass resolution of ~1800, which allows to completely or at least partially, in the case of $^{12}C^{16}O$ at mass 28, resolve most of those interferences, leaving only the interference between ^{29}CO and $^{29}N_2$, and between ^{30}CO and $^{30}N_2$. Figure 2.17 shows the different N_2 peaks and at which masses the peak centering are performed to avoid the interferences from N_2H and hydrocarbons. The unresolved interference from the small CO contribution at mass 29 and 30 were corrected following the protocol set out in Hashizume and Marty (2004) and Barry et al. (2012).

To summarize, the correction method is based on the assumption that (i) N_2 molecules are in isotopic equilibrium and the abundance ratios are $^{14}N^{14}N : {}^{15}N^{14}N : {}^{15}N^{15}N = 1 : 2r : r^2$, where $r = {}^{15}N/{}^{14}N$ and (ii) the CO contribution has an atmospheric isotope composition so we have:

$$^{13}C^{16}O = {}^{13}C/{}^{12}C_{\ atm} * {}^{18}O/{}^{16}O_{\ atm} * {}^{12}C^{18}O. \quad (6)$$

where $^{13}C/{}^{12}C_{\ atm} * {}^{18}O/{}^{16}O_{\ atm}$ is a constant k.

Mass balance equations are:

$$\text{Mass } 28 = {}^{28}N_2 \quad (7)$$

$$\text{Mass } 29 = {}^{29}N_2 + {}^{13}C^{16}O \quad (8)$$

$$\text{Mass } 30 = {}^{30}N_2 + {}^{12}C^{18}O \quad (9)$$

And can be expressed as:

$$\text{Mass } 29 = 2r*{}^{28}N_2 + k*{}^{12}C^{18}O \quad (10)$$

$$\text{Mass } 30 = {}^{28}N_2*r^2 + {}^{12}C^{18}O \quad (11)$$

The two unknowns r ($^{15}N/{}^{14}N$ of the sample) and $^{12}C^{18}O$ (^{30}CO, and thus ^{29}CO, contributions) can then be solved simultaneously using a simple second-degree equation solving algorithm.

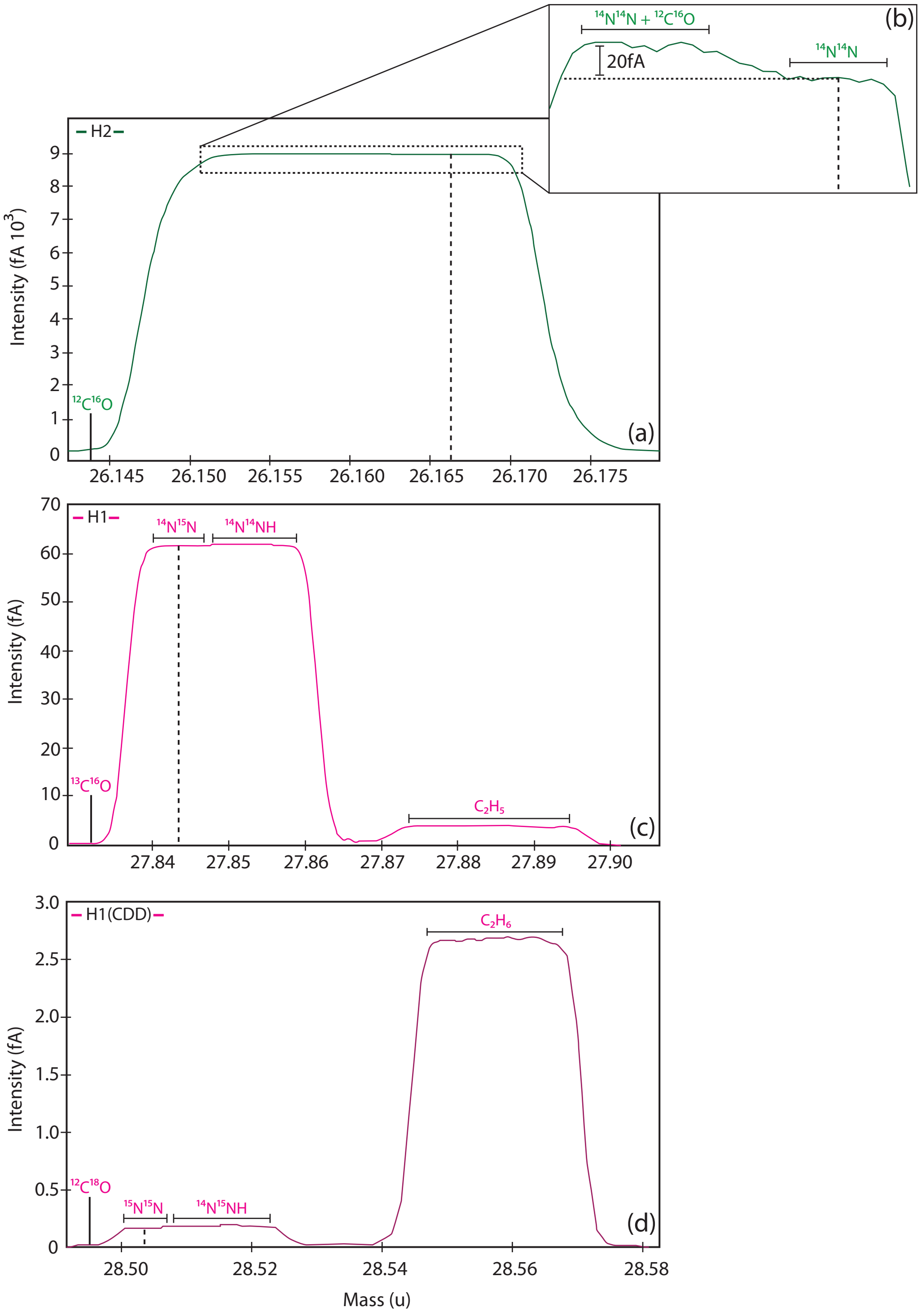

Figure 2.17: Discrimination of species at *m/z* ratios of 28 (**a**,**b**), 29 (**c**) and 30 (**d**) of atmospheric nitrogen standards measured on the Helix MC$^+$. The high resolution of the Helix MC+ permits to fully resolve the C_2H_5 and C_2H_6 interferences at mass 29 and 30, respectively. The $^{12}C^{16}O$ (mass 28), $^{28}N_2H$ (mass 29), and $^{29}N_2H$ (mass 30) interferences are partially resolved, and the dashes vertical lines indicates the masses at which the analyses were performed in order to avoid the interferences. The small contributions from $^{13}C^{16}O$ (mass 29) and $^{12}C^{18}O$ (mass 30) to the nitrogen peaks cannot be resolved and are corrected using the protocol described in the text (adapted from Hashizume & Marty 2004).

3) Performance

A calibrated glass bottle of diluted air (2158.8 cm^3 at P = 1.25 x 10^{-2} mbar, Figure 2.16) is used as a nitrogen standard to monitor the instrumental mass fractionation and the reproducibility of the mass spectrometer. Figure 2.18 shows the $^{28}N_2$ signal (fA) and $\delta^{15}N$ (‰ variation relative to air) of 56 standards analysed over 1 month. Each standard is a pipette of gas (0.191 cm^3) containing 1.02 x 10^{-10} mol of N_2, purified following the purification protocol described above. We observe that for the first dozen of standards (1 week after the start of nitrogen analysis) the signal of $^{28}N_2$ and the isotope composition are still unstable and generally increasing. This is also observed on the Nu Instrument© Noblesse mass spectrometer at CRPG when nitrogen measurements are performed after a long period of noble gas analysis (Zimmermann et al., in prep). This instability may result from nitrogen adsorption onto the inside walls of the mass spectrometer, which becomes negligible once the spectrometer is sufficiently "coated" in nitrogen after a few days or weeks of being in contact nitrogen from the standard (L. Zimmermann, personal communication). Once stability is reached, we obtain a reproducibility of 1.1 ‰ (standard deviation of the standards) for an isotopic composition $\delta^{15}N$ = 0.2 ‰, indicating negligible instrumental mass fractionation from the mass spectrometer (Figure 2.18).

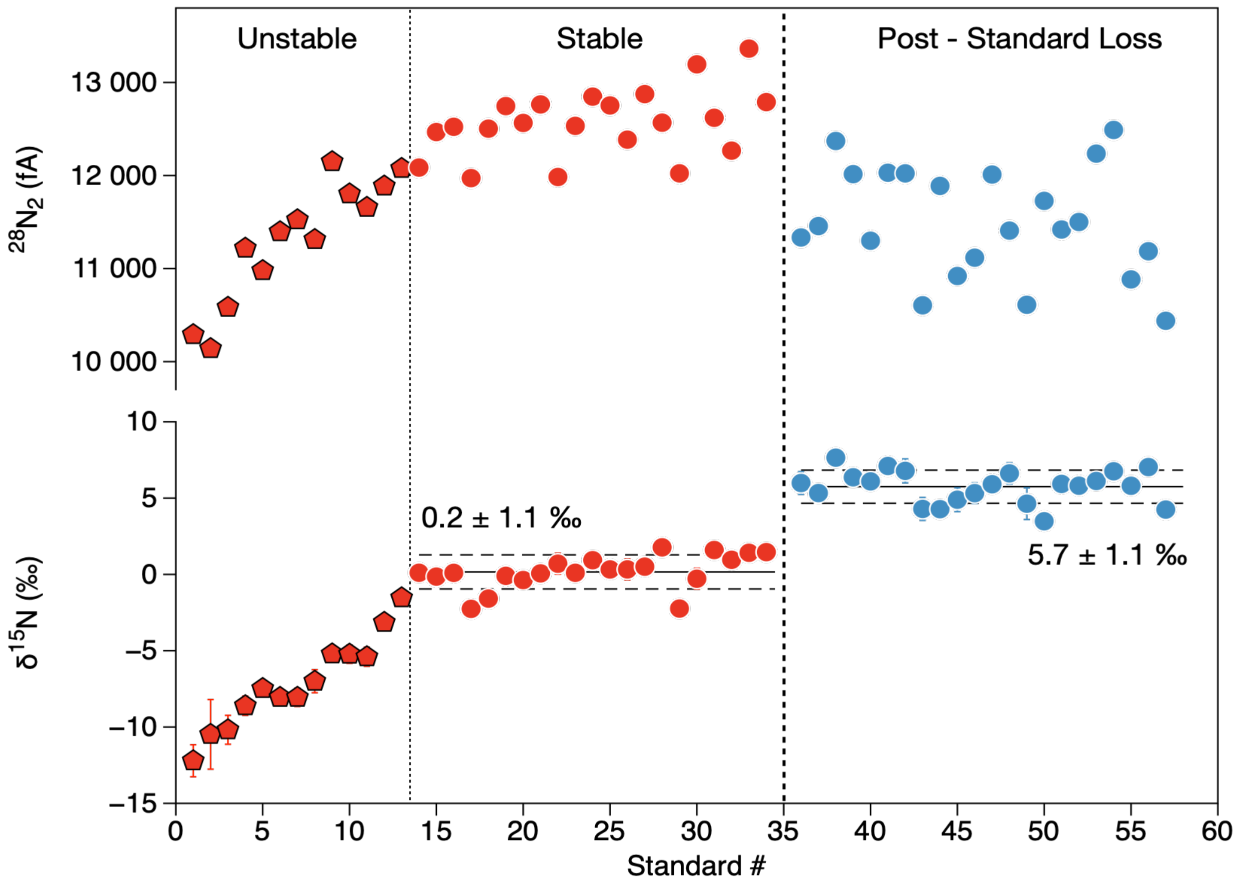

Figure 2.18: $^{28}N_2$ signal (fA, top panel) and isotope composition (δ^{15}N in permil variation from air composition, Nier et al. 1950, bottom panel) of 56 standard measurements performed over a period of 1 month. Red pentagons show standard composition before stability (circles), for both $^{28}N_2$ signal and isotope composition. Blue circles correspond to standard analyses performed after the partial loss of gas from the standard bottle, mentioned in the main text. Error bars are the internal error of each standard, often smaller than the symbol size. Black horizontal lines correspond to the average of the δ^{15}N values of the standard (before the partial loss of the standard), with the dashed line envelopes being the standard deviation of the standards (reproducibility).

The standard bottle was unfortunately partially pumped due to a gas-handling mistake. The bottle lost ~10% of its amount of N_2 and N_2 isotopes in the bottle were fractionated by ~+5‰ (Figure 2.18). After this event, the reproducibility remained the same as before, around 1.1 ‰.

The good correlation between the corrected and measured δ^{15}N (before ^{29}CO correction) (Figure 2.19-A) indicates that the correction method is adequate for the range of gas pressures considered (all the standards are measured between 10 to 13 x 10^3 fA, Figures

2.18 and 2.19-B). Diluted standards and doubled standards have been measured in order to check the linearity of the mass spectrometer for lower and higher gas amount samples. Down to ~4000 fA, the CO correction appears to be appropriate (Figure 2.19-A) and the isotope signature is in the range of the non-diluted standards (Figure 2.19-B). At lower signal intensities (~1000 fA, 1/10th of a standard), the CO correction becomes worse and the isotope signature (both the value and precision, Figure 2.19-B) appears to be affected. This non-linearity effect at very low signal intensity is important because it defines the analytical limit at which isotope measurements can be performed accurately for samples with very low amounts of N_2. The blank of the line (purification protocol without any sample) is on the order of ~1.7 x 10^{-12} mol (200 fA), which corresponds to the lower limit of nitrogen that can be measured (N_2 abundance measurements). The lower limit for reliable isotope measurement is about 5 times higher than the blank, i.e. around 8.5 x 10^{-12} mol (1000 fA).

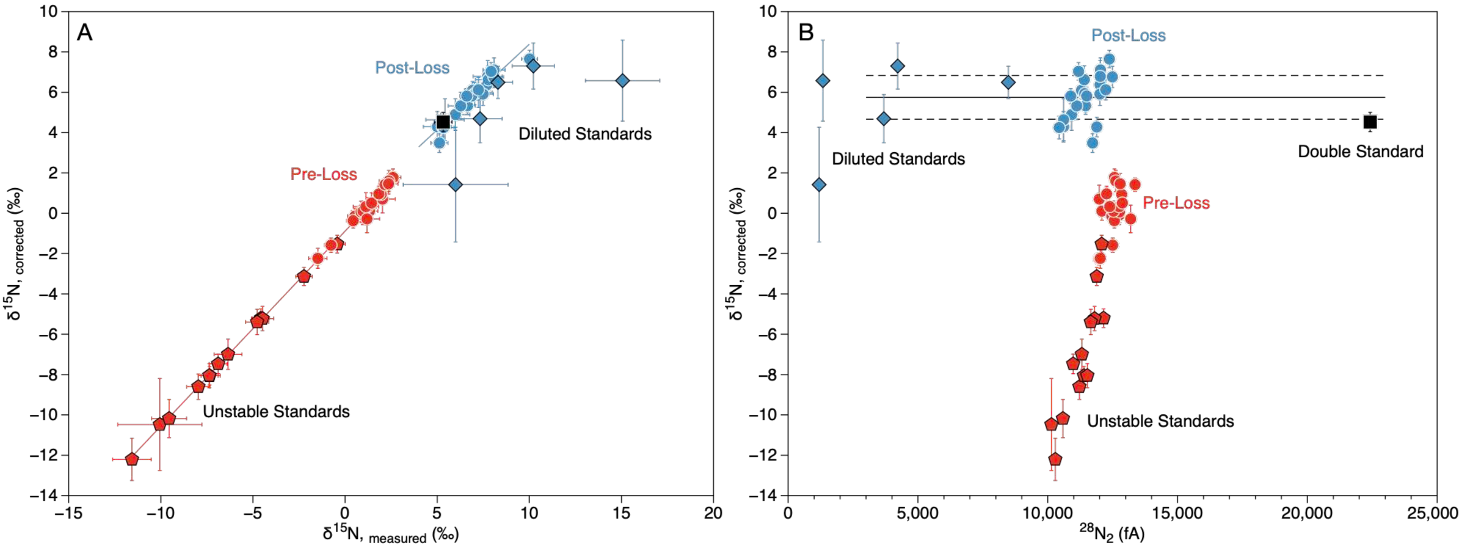

Figure 2.19: **A.** $\delta^{15}N$ of the standards (relative to air composition) before and after the correction for the ^{29}CO contribution. Red symbols are unstable (pentagons) and stable (circles) standards before the loss of standard gas (mentioned in the main text). Blue symbols are diluted (diamonds) and regular standards after the standard loss. The measured and corrected $\delta^{15}N$ of the non-diluted standards around 10 to 13 x 10^3 fA correlate well, as opposed to diluted standards plotting away from the correlation. **B.** Corrected $\delta^{15}N$ of the standards as a function of the ^{28}N signal intensity. Diluted standards (with signal size above ~1000 fA), regular standards, and double-standards have a similar isotope signature, indicating the absence of significant linearity effect for a wide range of sample abundances.

Chapter 3

Noble Gas and Nitrogen Elemental Behaviour in Cometary Ice: Insights from EXCITING

I. Introduction

The mission Rosetta, launched in 2004 by the European Space Agency toward comet 67P/Churyumov-Gerasimenko (hereafter 67P/C-G), undertook in 2014 an unprecedented campaign of *in situ* measurements of the volatile composition of a cometary coma. The isotope analyses of a variety of volatile elements, such as nitrogen and the heavy noble gases Ar, Kr and Xe, were performed by the ROSINA (Rosetta Orbiter Spectrometer for Ion and Neutral Analysis, Balsiger et al. 2007) mass spectrometer onboard the Rosetta spacecraft. These analyses revealed unique elemental and isotopic compositions, providing unprecedented insight into the noble gas budget of cometary matter (Balsiger et al. 2015; Marty et al. 2017; Rubin et al. 2018). The unique noble gas isotope signature measured in the coma of 67P/C-G, and specifically xenon isotopes (Marty et al. 2017), constituted the first direct evidence that comets contributed to the early volatile inventory of the Earth. The supply of cometary noble gases on Earth has strong implications on the delivery of other volatiles of biological interest, such as H, N, C, O, S and pre-biotic molecules (Rubin et al. 2019).

Before the Rosetta era, the study of noble gases in comets was limited to experimental investigations of cometary ice analogues. Based on the observation that amorphous water ice can trap large amounts of volatiles in its structure during formation (Ghormley 1967), Bar-Nun et al. (1985) predicted the high abundance of noble gases relative to water in cometary material, as measured by the Rosetta mission (Marty et al. 2016). Decades of investigations on the behavior of noble gases in cometary ice analogues by Bar-Nun's team at Tel-Aviv University (e.g., Bar-Nun et al. 1987; Notesco et al. 1991; Owen et al. 1992; Bar-Nun & Owen 1998; Notesco et al. 2003; Notesco & Bar-Nun 2005; Bar-Nun et al. 2007) have been dedicated to the study of the nature and formation conditions of cometary ices, with the overarching goal of determining the temperature at which they form. Noble gases, specifically Ar, Kr and Xe, have different condensation temperatures (Ar ~ 40K, Kr ~ 60K, Xe ~ 80K, variable depending on substrates and pressure conditions, Fray & Schmitt 2009), and their relative abundances in the ice can thus be used to infer on the temperature conditions at the time of trapping into condensing amorphous water ice.

Surprisingly, noble gas abundances measured in 67P/C-G did not match any experimental predictions at the range of investigated formation temperatures (Bar-Nun & Owen 1998; Notesco et al. 2003). This called for further experimental development and exploration of the conditions required to reproduce the noble gas signatures of comet 67P/C-G. This chapter explores the elemental behaviour of noble gases (and N_2, which can be as inert and intriguing as noble gases) by using our newly developed experiment called EXCITING. Section 3.II is my recently published paper that details the EXCITING apparatus and our observations on the effect of temperature on the relative abundances of noble gases trapped in the ice (Almayrac et al. 2022). Our main observation, discussed in the context of the limitations of the experimental approach, is that temperatures of formation around 70-80 K may better reproduce the N_2-Kr-Xe/Ar ratios of comet 67P/C-G than temperatures ~30K. Section 3.III presents how the addition of photon irradiation affects the trapping efficiency of noble gases and nitrogen into the amorphous water ice, as well as their behaviour during the release from the ice. The isotopic measurements of noble gases and nitrogen trapped in the amorphous water ice are presented in Chapter 4.

II. Article in Planetary Science Journal

The EXCITING experiment exploring the behaviour of nitrogen and noble gases in interstellar ice analogues

Matthieu G. Almayrac, David V. Bekaert, Michael W. Broadley, David J. Byrne, Laurette Piani,
Bernard Marty

Abstract

Comets represent some of the most pristine bodies in our solar system and can provide a unique insight into the chemical makeup of the early solar system. Due to their icy volatile-rich nature they may have played an important role in delivering volatile elements and organic material to the early Earth. Understanding how comets form can therefore provide a wealth of information on how the composition of volatile elements evolved in the solar system from the pre-solar molecular cloud up until the formation of the terrestrial planets. Because noble gases are chemically inert and have distinct condensation temperatures, they can be used to infer the temperatures of formation and thermal history of cometary ices. In this work we present a new experimental setup called EXCITING to investigate the origin and formation conditions of cometary ices. By trapping nitrogen and noble gases in amorphous water ice, our experiment is designed to study the elemental and isotopic behaviour of volatile elements in cometary ice analogues. We report new results of noble gas and nitrogen enrichment in cometary ice analogues, and discuss the limitations of the experimental conditions in light of those supposed for comets. We show that forming ice analogues at ~70K best reproduce the noble gas and N_2 abundances of comet 67P/Churyumov-Gerasimenko, considering a solar-like starting composition. This formation temperature is higher than previous estimates for cometary ices and suggests that the formation of cometary building blocks may have occurred in the protosolar nebula rather than in the colder molecular cloud.

1. Introduction

The Earth is unique amongst the terrestrial planets in that it has liquid water on its surface, which is a vital feature for rendering it habitable for life. The similarity in isotope signatures (such as O, Ti, Ru or Mo) between the Earth and enstatite chondrites suggests that our planet formed mainly from non-carbonaceous (NC) volatile-poor material originating from the inner solar system (Dauphas 2017; Burkhardt et al. 2021). During the early stage of Earth's accretion, the solar nebula at around 1 AU would likely have been too hot for water ice to condense and be incorporated into Earth's NC-like building blocks. To account for the Earth's current volatile budget and its overall oxygen fugacity, the addition of volatile-rich material analogous to carbonaceous chondrites or comets has been previously advocated (Marty 2012; Alexander et al. 2012; Rubie et al. 2015).

Comets, which formed in the cold outer solar system, are rich in ices and constitute potential candidates for the delivery of large amounts of volatile elements to early Earth (Pepin 1991; Owen et al. 1992). However, the paucity of measurements of volatile elements in cometary matter has hampered quantification of any cometary contribution to the terrestrial volatile budget (Owen & Bar-Nun 2001). Fundamental insights into the nature and origin of cometary volatiles have relied mainly on by ground-based observations (Arpigny et al. 2003; Hutsemékers et al. 2008; Bockelée-Morvan et al. 2015) and laboratory analogue experiments (Bar-Nun et al. 1985; Notesco et al. 2003). The NASA-led Stardust mission to comet 81P/Wild was able to return for the first time refractory comet material to Earth for analysis (Brownlee et al. 2006). This mission did not directly return any cometary ice due to the highly energetic capture process, such that our knowledge of the volatile composition of cometary ice is limited. However, the recent European Space Agency's Rosetta mission to comet 67P/Churyumov-Gerasimenko (hereafter 67P/C-G) in 2014 provided the first in-situ analyses of cometary volatiles including noble gases and delivered crucial insights into the chemical and isotopic composition of the coma of comet 67P/C-G, using the Rosetta Orbiter Spectrometer for Ion and Neutral Analysis (ROSINA) instrument (Balsiger et al. 2007; Le Roy et al. 2015).

Constraints brought by the analysis of hydrogen isotopes in 67P/C-G (Müller et al. 2022) and other comets (from ground-based observation, Bockelée-Morvan et al. (2015) and references therein), suggest that comets are unlikely to have provided significant amounts (> 1%) of Earth's water based on the extreme difference in D/H between comets and Earth's surface water (Altwegg et al. 2015; Alexander et al. 2018). Nonetheless, in light of recent isotopic measurements of noble gases within the coma of comet 67P/C-G, comets may have contributed up to 25% of the Earth's krypton and xenon (Marty et al. 2017; Rubin et al. 2018, 2020; Bekaert et al. 2020). The difference between the potential cometary contribution of noble gases and H is due to the high noble gas to water ratio in comets compared to Earth (Marty et al. 2016; Bekaert et al. 2020).

Contrary to primitive meteorites, in which volatiles are mainly present in hydrated minerals and organic material, a significant fraction of the volatile (H, C, N, O, S, noble gases) budget of comets is contained within ices (Rubin et al. 2019). The presence of large amounts of guest volatile species in cometary ice is considered to be the result of them being trapped in the amorphous structure of water ice (I_a type, Ghormley 1967; Bar-Nun et al. 1985) when water molecules condense at low temperature and pressure (such as those found within the interstellar medium or the outer part of the protosolar nebula). The highly porous structure of I_a is able to trap large amounts of guest volatile species (Bar-Nun et al. 1987; Parent et al. 2002) and retain them within the lattice by Van Der Waals forces (Bar-Nun et al. 2007), even when the temperature rises above the sublimation temperatures of the guest volatile species. When the cometary ice is heated above ~120-140K, its structure changes from amorphous to a crystalline cubic ice structure (I_c, Jenniskens & Blake 1994) and guest species are released from the pores of the I_a structure (Bar-Nun et al. 1987). Such a transition is likely to occur during the inward migration of cometary bodies in the solar system, resulting in the partial loss of volatiles from the cometary ice (Rubin et al. 2019; Gkotsinas et al. 2022). Moreover, the trapping efficiency of different volatile species depends on the temperature of formation of the amorphous cometary ices (Bar-Nun & Owen 1998; Notesco et al. 2003), and the rate of ice deposition (Ciesla et al. 2018). The efficiency decreases when the deposition rate decreases because guest species are prone to diffusing out of the amorphous ice porosity, before another H_2O layer "closes" the pores (Ciesla et al. 2018). Consequently, the volatile budget of comets is highly dependent on the condensation conditions and on thermal evolution of cometary ices (Rubin et al. 2018). The elemental abundances of cometary volatiles can thus be used to infer the conditions of comets' formation and evolution.

Laboratory-based experimental observations have shown that the N_2/CO ratio may be sensitive to the temperature of ice formation due to the distinct sublimation temperatures of N_2 and CO (~25K for N_2, ~30K for CO, Luna et al. 2014) and polarizabilities (Bar-Nun et al. 2007). As such, the low N_2/CO measured in the coma of 67P/C-G relative to a protosolar composition suggested that the ice fraction of 67P/C-G formed from a gas of solar composition at temperatures below 30K (Rubin et al. 2015). However, the Xe isotopic composition measured for 67P/C-G is clearly distinct from a solar composition (Marty et al. 2017), suggesting that the elemental composition may have a non-solar origin, at least for heavy noble gases. The Xe isotopic signature is thought to be influenced by the signature of a nucleosynthetic anomaly of pre-solar origin, suggesting that cometary building blocks may have acquired their noble gas composition prior to solar system formation (Avice et al. 2020). Moreover, the physical and chemical processes controlling the elemental and isotopic compositions of cometary ices are poorly constrained (Bar-Nun et al. 2013). Therefore, the nature of the primordial (solar or pre-solar) environment from which cometary ice formed needs to be investigated.

Heavy noble gases (Ar, Kr and Xe) and nitrogen are highly volatile species, with condensation temperatures ranging from 40K to 90K. Noble gases (and N_2 to some extent) are inert and their elemental and isotopic signatures are altered primarily by physical processes. These elements can thus be used as tracers regarding the cometary ice formation and evolution history. Studies on the capacity of amorphous cometary ice analogues to trap and retain gases above their sublimation temperature have been used previously to predict the elemental noble gas composition of comets reaching the terrestrial planet regions (Bar-Nun et al. 1987; Jenniskens & Blake 1994; Stevenson et al. 1999; Notesco et al. 2003; Yokochi et al. 2012). Because of their different condensation temperatures, noble gases can be used as cosmochemical thermometers to infer the temperature of formation of cometary ices, and thus provide key constraints on the formation environment of comets (Yokochi et al. 2012).

We have developed a novel experimental setup to form cometary ice analogues from mixtures of water, nitrogen and noble gases under vacuum, at temperatures between 28K and 80K. Using this apparatus, we investigate potential elemental fractionation of volatiles during their trapping in - and release from - water ice, under a variety of conditions relevant to the interstellar medium or protoplanetary disk (i.e., formation temperature, level of irradiation by Lyman-α photons). By definition, any elemental fractionation will change the N_2/Ar, Kr/Ar or Xe/Ar ratios in the ice compared to the initial composition of the gas mixture due to differences in condensation temperatures and rates of diffusion within the ice between different gas species. Ultimately, the use of this experimental setup aims to improve our knowledge of the chemistry of early cometary ices, providing new constraints on their formation environment(s). One of the primary goals of this experiment is to investigate whether it is possible to reproduce fractionation behaviour that could yield elemental and isotopic compositions similar to those measured on 67P/C-G.

2. Methodology

The experimental setup known as **EXCITING** (**E**xploring **X**enon in **C**ometary **I**ces by **T**rapping and **I**rradiating **N**oble **G**ases) was developed at CRPG (Nancy, France) to create cometary ice analogues from mixtures of water, nitrogen and noble gases. The experimental setup is shown Figure 1. The general working principle of the EXCITING experiment is first presented, followed by a more detailed description of the setup.

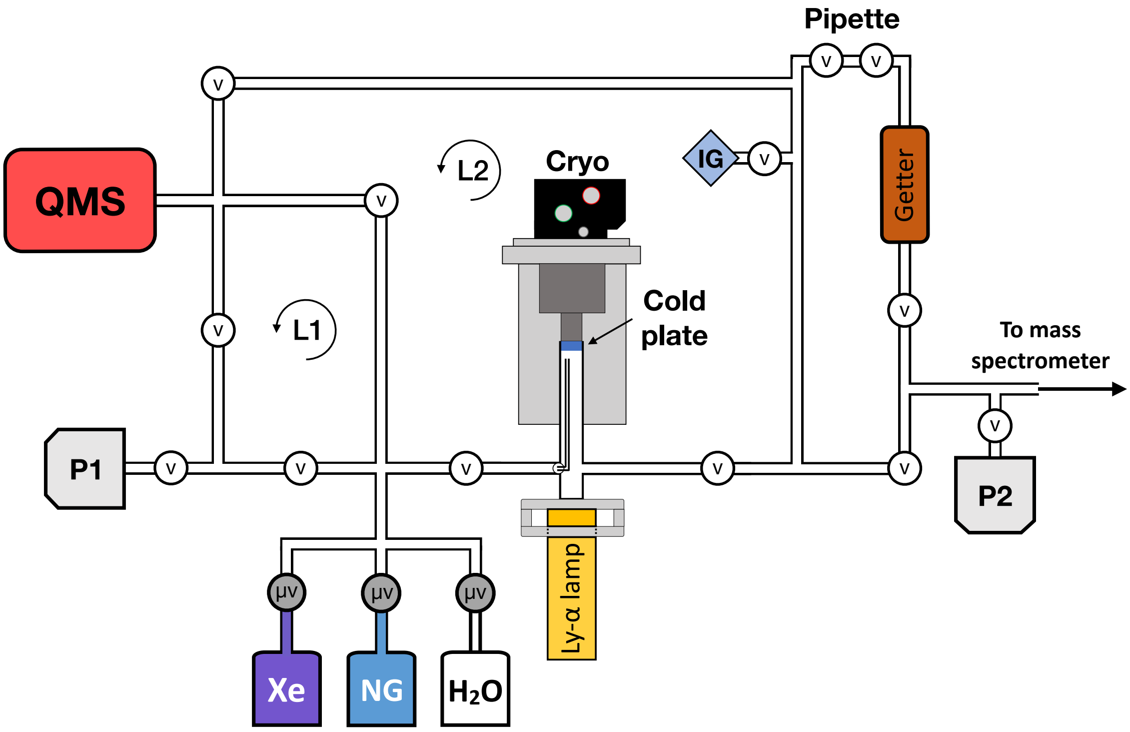

Figure 1. Schematic representation of the EXCITING experiment. v: high vacuum valve. µv: micrometre flow control valve. Cryo: cryogenic trap (see Figure 2). IG: ion gauge. QMS: quadrupole mass spectrometer. The NG bottle contains noble gases (Ar, Kr and Xe) and nitrogen. L1 and L2 refer to the two loops of gas flow discussed in the main text. P1 and P2 are two turbo molecular pumps.

2.1 General Working Principle

The fundamental principle of the experiment is to introduce a controlled mixture of water vapor, N_2 and noble gases to a vacuum chamber containing a cooled plate located inside a cryogenic trap to form amorphous water ice under vacuum (Figure 1). The vacuum system reaches typical maximum pressure of ≤ 5×10^{-8} mbar at room temperature. The proportion of water and noble gases in the gas mixture is monitored using a quadrupole mass spectrometer (QMS, loop L1, Figure 1) and precisely adjusted with micrometre needle valves to the desired proportions. The cryogenic trap is isolated from Loop L1, pumped through the mass spectrometer's purification line and cooled down. Once the gas mixture is adjusted and the trap is held at 28 K, Loop L1 is closed and Loop L2 is opened, allowing the gas mixture to flow through the cryotrap, ion gauge and QMS. This enables the gas to be partially condensed on the trap and be analysed for its elemental composition using the QMS (Figure 1). After around 5 min deposition, the gas supply is closed and the rest of the line, including the cryostat, is kept under high vacuum using Pump 1. The ice sample can then be thermally processed and/or irradiated by an ultra-violet (UV) lamp. During heating of the ice, the composition of the gas flux coming from the cryotrap is continuously monitored with the QMS. The initial and released gas fractions can be analysed for their isotopic compositions with an on-line sector-type mass spectrometer working in static mode (GV instruments Helix MC). In order to prepare an isotopic analysis, the cryotrap is heated up to the temperature required for noble gases to be released. Just before reaching this temperature, the system is set to static mode (pumps closed). Sublimated gases are then equilibrated for a few minutes at the given temperature step, and an aliquot of gas is sampled with a pipette, which is directly sent to an on-line getter connected to the purification line of the static noble gas mass spectrometer (Figure 1). The different sections of this apparatus are described in greater detail here below.

2.2 Setup Description

The setup is built with 16 mm (internal diameter) stainless steel tubes, connected using CF and VCR connections and Swagelok© valves (Figure 1). The whole setup is able to maintain a low pressure of around 10^{-8} mbar using Pfeiffer Vacuum© (TMU 071P model) turbo molecular pumps. Pressure in the line is monitored using an ion gauge (MKS©, Mini Ion Gauge model). Two micro-leak valves (VAT©) connect a bottle of pure Xe (99.999%, 53 bar, Air Liquide©) and a bottle containing a mixture of N_2:Ne:Ar:Kr:Xe in the molar ratio 50:20:10:10:10 (99.999% for N_2, Ne and Ar, 99.998% for Kr and Xe, 150 bar, Messer©) to the mixing volume ahead of the cryogenic head (Figure 1). A third micro-leak valve connects a vapour saturated distilled water reservoir to the steel tube mixing volume (~30 cm^3, Figure 1).

2.2.1 Cryo Head, Temperature Control, Capillary and UV Lamp

The cryostat consists of an adapted cryogenic system built by Cryoscan© (Nancy, France), containing a copper plate (18 mm in diameter) that can be cooled down to 25 K by helium circulation in a closed system. The temperature of the plate can be adjusted from 25 K to room temperature using a resistance heater connected to a Scientific Instrument@ (model 9700) temperature controller. A high vacuum between the inside of the cryogenic head and the exterior is maintained using a turbo molecular pump (Pfeiffer Vacuum©, TMU 071P model) in order to maintain thermic isolation (Figure 2, Appendix Figure A1 and Figure A2). Because the device is dedicated to elemental and isotopic measurements, the chamber is not equipped with instruments able to observe and measure the thickness of deposited ice nor to identify the structure (amorphous or crystalline) of the ice.

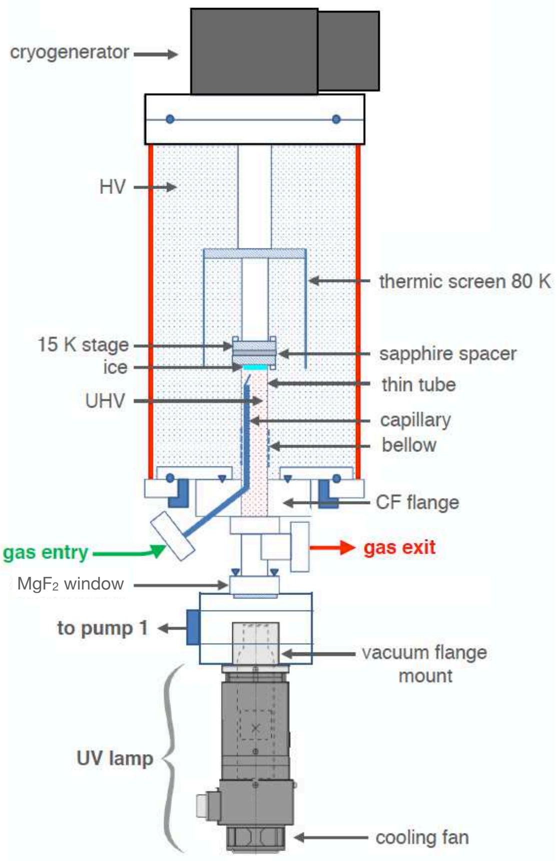

Figure 2. Diagram of the cryogenic head system allowing noble gases/water mixtures to be condensed at ~30 K under high vacuum and exposed to Lyman-α light (with a H_2D_2 light source unit L11798 by Hamamatsu company). HV: high vacuum. UHV: ultra-high vacuum.

Gas mixtures are introduced for deposition on the cold plate inside the cryogenic head through a 2 mm (internal diameter) capillary (Figure 2). The tip of the capillary is located 10 mm away from the plate. Below the horizontal plate, a deuterium lamp (H2D2 light source unit Hamamatsu© L11798) is connected to the system via a MgF_2 window, and can irradiate the gas mixtures during deposition as well as the surface of the ice (Figure 2). The wavelengths of photons range between 120 nm and 200 nm (Figure A3), with peaks at 124 nm (the Lyman-α wavelength from solar irradiation) and 160 nm (9.8 eV and 7.7 eV, respectively). Future experiments will investigate how irradiation damage of the ice (Tachibana et al. 2017) may affect trapping of volatile species. Finally, a primary pump (Pfeiffer Vacuum©, MKV 015-2 model) maintains a vacuum of around ~10^{-3} mbar in the volume between the lamp window and the cryogenic head volume (Figure 2).

2.2.2 Quadrupole and Noble Gas Mass Spectrometers

Gas species in the mass to charge *m/z* ranging from 1 to 150 (water with pure xenon, or water with nitrogen and noble gases) are monitored using a QMS (Pfeiffer Vacuum PrismaPlus© QME 220) under dynamic mode (continuous pumping with a turbo pump placed after the QMS). Micrometric valves allow the flux of gases to be precisely controlled and are used to fix the proportion of water and noble gases in the gas mixture.

During the experiments, the gas released from the Cu plate is circulated through the QMS for analysis (dynamic mode) and is pumped out. To perform isotopic analysis, larger quantities of gas are required, and gas is thus accumulated in the Loop 2 volume (Figure 1, static mode). The setup is then sampled in a pipetted volume (Figure 1) and can be used to perform precise isotopic analyses by static noble gas mass spectrometry (GV instruments Helix MC).

2.2.3 Gas Mixture

Gas mixtures are prepared by sending gas from the bottles through the cryogenic head at ambient temperature to the QMS. Relative intensities of N_2, Ar, Kr and Xe measured with the QMS (N_2:Ar:Kr:Xe of 34:8:9:10) are consistent with the bottle composition (N_2:Ar:Kr:Xe = 50:10:10:10) taking into account the difference in the first ionisation potential (FIP) that influence the ability of a species to be ionized and measured in the QMS (FIP-Xe = 12.13 eV < FIP-Kr = 14 eV < FIP-N_2 = 15.58 eV < FIP-Ar = 15.76 eV). Although 20 % of the bottle consists of neon, the amount measured by the QMS appears lower than the amount of Kr (10 %) or Xe (10 %), most likely due to the high FIP of Ne (21.56 eV). The small peak at m/z = 20 presumably results from both ^{20}Ne and doubly ionised ^{40}Ar (with second ionization potential of 27.63 eV). This however is not problematic for our experiments because the Ne condensation temperature is around 15K, which is lower than the temperature investigated with EXCITING. Notably, Ne appears to be drastically depleted in comets, as suggested by its lack of signal in the measurements done with the ROSINA instrument on the Rosetta spacecraft (Rubin et al. 2018), which suggests that Ne is not quantitatively trapped and/or retained in cometary ice. Therefore, we do not consider Ne when calculating gas mixing ratios in the following sections.

2.3 Experimental Protocol Used in the Present Study

Two gas mixtures, H_2O-Xe with mixing ratio of around 50:1, and H_2O-N_2:Ar:Kr:Xe (hereafter H_2O-NG) with mixing ratios of around 50:5:1:1:1, were condensed onto the plate. Mixing ratios were chosen to have the maximum amount of water, while balancing the level of noble gases such that there was enough gas available to perform precise and reproducible analyses using the QMS. The H_2O-Xe mixture was initially deposited onto the cold plate at 28 K. Subsequent experiments used various temperatures ranging from 28 K to 80 K to study the evolution of trapping efficiency with increasing temperatures. A temperature of 28 K is close to the limit of our experimental setup and thought to be representative of the formation temperature of cometary bodies, and 80 K is close to the limit at which amorphous water ice analogues form (Jenniskens & Blake 1996), whilst still trapping enough of the most volatile elements (N_2 and Ar) for acceptable precision on QMS analyses. During deposition, the system is in dynamic mode (continually pumping with a turbo-molecular pump under the cryogenic trap). The typical water pressure and N_2-noble gas pressure used for deposition are on the order of $5x10^{-5}$ mbar and $8x10^{-6}$ mbar, respectively. After ice deposition, the cold plate is heated to room temperature at the constant rate ramp of 1K/min. During the heating phase, the flux of gas coming from the cryogenic trap is continuously monitored with the QMS.

3. Results

Representative plots of gas release versus temperature for the H_2O-Xe and H_2O-NG mixtures deposited at 28 K are given in Figure 3 and Figure 4, respectively. The primary observation is that guest species (Xe alone or NG mixture) are released from the ice in two distinct temperature ranges. These two release steps, symptomatic of volatile behaviour in amorphous water ice, are described in detail in the following subsections.

3.1 Water and Xenon Ice

On Figure 3 we observe a first release of Xe at around 75 K, which corresponds to the sublimation of a frozen phase of Xe that was not trapped inside the amorphous ice lattice. This sublimation temperature is in agreement with that expected at pressures of around 10^{-6} mbar (Fray & Schmitt 2009). A second release of Xe occurs at 140 K which is which is below the temperature of water sublimation (Figure 3). This temperature coincides with the transition from amorphous (I_a) to crystalline (I_c) ice (Bar-Nun et al. 1985). This likely suggests that the change in the ice structure leads to the release of Xe, that was trapped within the lattice of the amorphous ice, prior to water sublimation. A similar release pattern was observed by Bar-Nun et al. (1985).

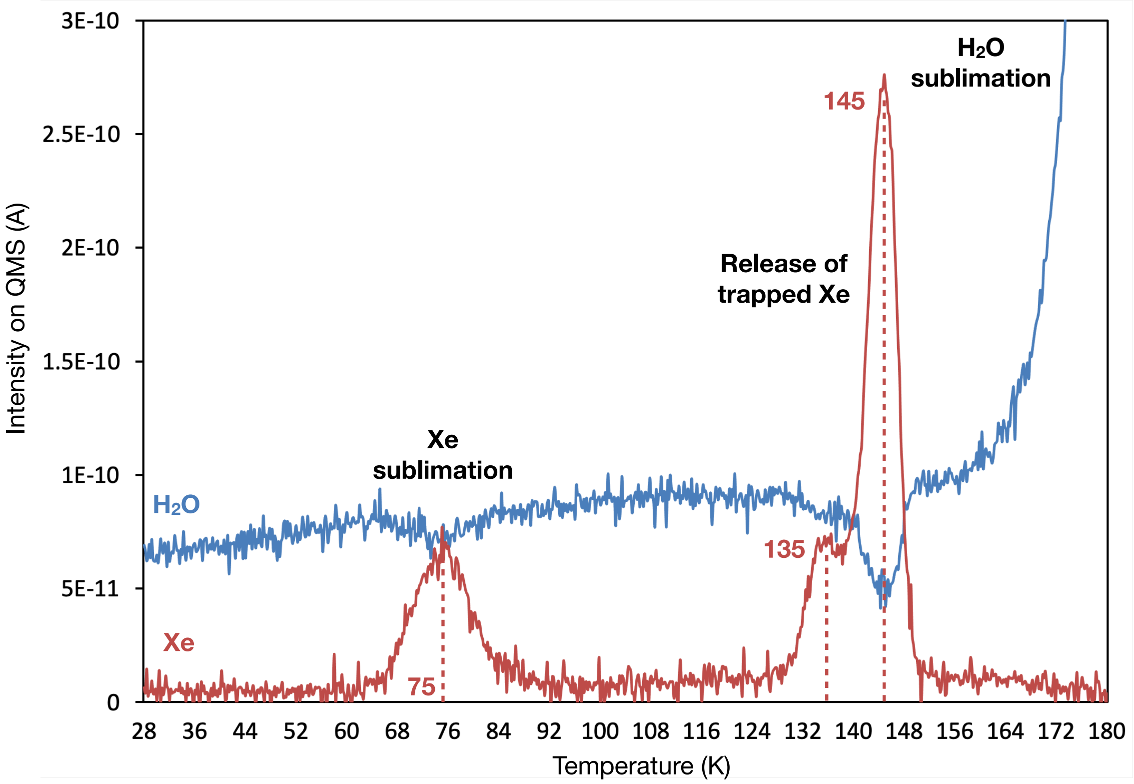

Figure 3. Xenon gas release during the heating up from 28 to 180 K at a rate of 1 K/min of a representative experiment starting with H_2O:Xe mixture. Peaks corresponding to frozen Xe sublimation and release of trapped Xe are observed at ~75 K and ~140 K, respectively. The two-step release of trapped Xe at 135 K and 144 K is discussed in the main text. Water sublimation is clearly observed from

160 K. The apparent decrease of the H_2O background signal when Xe is released results from a competition (or pressure effect) inside the QMS, since Xe has a slightly lower first ionisation potential (Xe-FIP = 12.13 eV) than water (H_2O-FIP = 12.65 eV).

In detail, we observe a "pre-peak" at 135 K, followed by a "main peak" at 145 K, especially for Xe on Figure 3 and for Xe and Kr on Figure 4. These two peaks correspond to a first partial transition of the amorphous ice into a restrained and unstable amorphous phase (I_ar) which usually affects ~30% of the ice (Jenniskens & Blake 1994, 1996), rapidly followed by the complete transition into I_c. Finally, when water itself begins to sublimate at ~160 K, there is no guest species left in the ice structure. Notesco et al. (2005) showed that if the ice exceeds 5 µm in thickness, the transition from I_a to I_c does not release all the trapped phase and a fraction of the gas remains trapped in the ice lattice. The rest of the gas is thus released by a second structural transition from I_c to hexagonal ice I_h, which occurs between 160 K and 170 K, synchronously with water sublimation (Jenniskens & Blake 1996; Notesco et al. 2003). The fact that we do not observe this third gas release at 160 K suggests that cometary ice analogues formed in our experiments are unlikely to exceed 5 µm in thickness. Given that ice formation lasted about 5 min, we can estimate that deposition rates do not exceed 1 µm/min in our experiments. These deposition rates are therefore similar to the deposition rates used in previous cometary ice analogue experiments (Bar-Nun & Owen 1998).

3.2 Water and Volatile Mixture Ice

We observe similar results for the H_2O-NG experiments (Figure 4). The first peak of gas release for each individual noble gas species and N_2 corresponds to their respective sublimation temperatures at 45 K for Ar, 46 K for N_2, 64 K for Kr and 80 K for Xe (Figure 4). These temperatures are in good agreement with their respective sublimation temperature from pure ice (Fray & Schmitt 2009). The second peak of bulk gas release occurs for all trapped volatiles (N_2, Ar, Kr and Xe) around 140 K, during the transition from amorphous to crystalline water ice. For each temperature of deposition, the experiment was repeated to assess the reproducibility of the EXCITING apparatus (see Table 1). The reproducibility of the peak gas release of the five repeat experiments at 28 K is illustrated in Figure 5. The reproducibility of N_2/Ar, Kr/Ar and Xe/Ar during this peak release is better than 10 % (standard deviation). The H_2O-NG experiment was also performed using an identical experimental procedure as described above, however this time the total gas pressure in the setup during the warm up of the ice (Appendix Figure A4) was monitored. The ion gauge (see Figure 1) measures the total pressure before the gas is analysed by the QMS. The three pressure peaks during warm up correspond to (i) the sublimation release of nitrogen and noble gases, (ii) the simultaneous gas release around 140 K and (ii) water sublimation peak around 180 K. The peak pressures are in agreement with the gas pressure sent for deposition on the cold plate, suggesting limited loss of gas during deposition onto the cold plate under dynamic pumping.

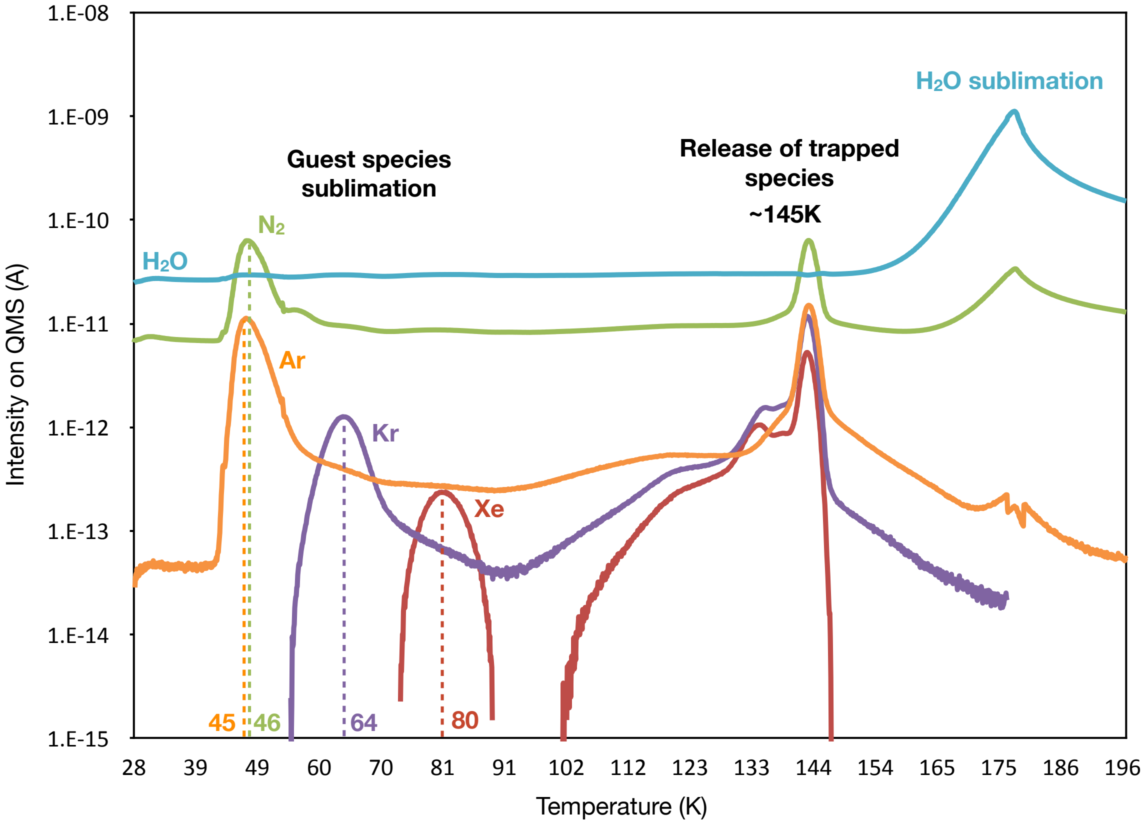

Figure 4. N_2 and noble gas release during the heating up from 28 to 200 K at a rate of 1 K/min of a representative experiment starting with a H_2O:N_2:Ar:Kr:Xe mixture. A fraction of each guest species is frozen on, or below, the ice and sublimates at their respective sublimation temperature, while the trapped fractions are released simultaneously at around 145 K, before water starts sublimating at 160 K. Note the log scale for the signal intensity.

Gas release pattern versus the temperature for experiments with starting temperature of deposition of 40 K, 50 K, 60 K, 70 K and 80 K are given in Appendix Figure A5. We observe that the amount of trapped gas decreases when the temperature of formation of the ice deposition increases. This is particularly true for Ar which has the lowest condensation temperature. To quantify how increasing the temperature of deposition decreases the trapping efficiency, we calculate the abundance of gas species trapped in the ice by integrating the signal of each element over the duration of the gas release between 100 K and 155 K (see Figure 4). We report in Table 1 the integrated N_2/Ar, Kr/Ar and Xe/Ar ratios measured in the trapped phase from H_2O-NG cometary ice analogues deposited at 28 K, 40 K, 50 K, 60 K, 70 K and 80 K, respectively. These ratios mostly reflect those observed for gas released between 135 K and 148 K (as shown in Figure 5 for the 28 K experiments). The N_2/Ar, Kr/Ar and Xe/Ar ratios increase and the reproducibility decreases with increasing ice deposition temperature (Table 1). For instance, at temperatures of deposition < 60 K, the reproducibility between experiments is ~10 %. At higher temperatures volatiles are less efficiently trapped, leading to a decrease in reproducibility (see Appendix Figure A6). This effect is particularly noticeable for Ar, due to its lower condensation temperature. As a result, the elemental ratios normalised to Ar show low reproducibility (~80 %) at higher temperatures.

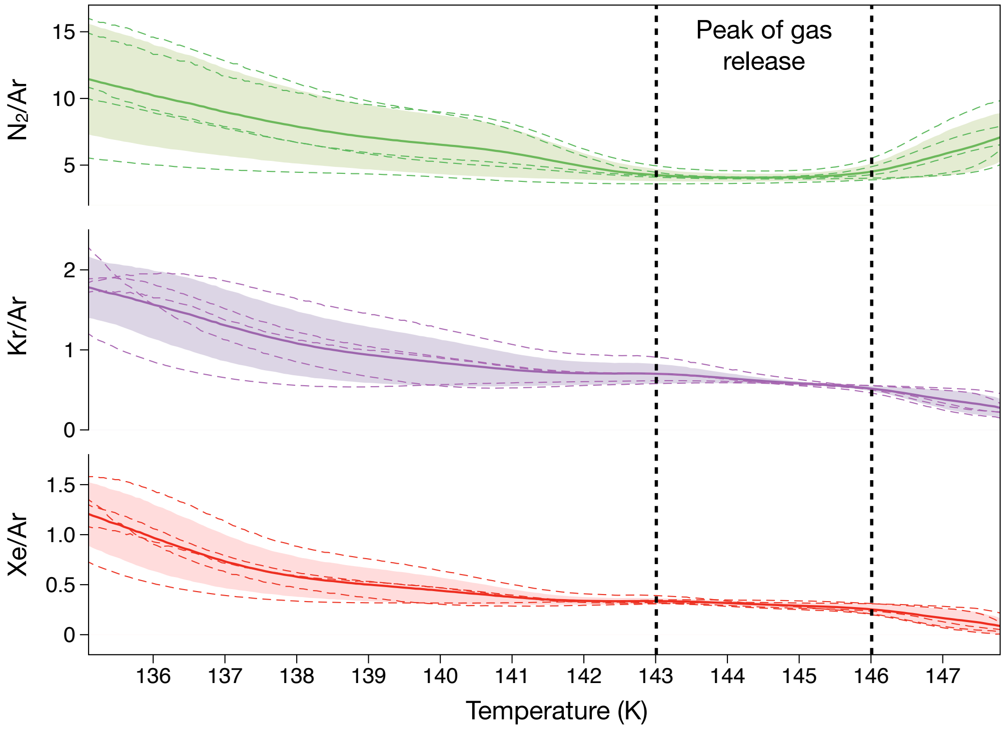

Figure 5. N_2/Ar, Kr/Ar and Xe/Ar ratios of the 5 duplicates of the experiment at 28 K (dashed lines) as a function of temperature rise between 135 K and 148 K, around the release peak of trapped gas. For each elemental ratio, the thick line is the average of the 5 repeats and the shaded envelope is the standard deviation of the 5 repeats at 1 σ. The reproducibility is maximal around the peak of gas release

between 143 K and 146 K. Elemental ratios given in Table 1 are the integrated ratios over the duration of gas release and thus reflect the value of the ratios at the release peak.

4. Discussion

For each experiment, enrichment ratios defined as the ratio X/Ar (where X = N_2, Kr or Xe) measured in the trapped phase over the X/Ar in the initial gas phase, are given in Table 1. These enrichment ratios can be used to quantify the relative trapping efficiency between the guest species. We then normalise the enrichment ratios to the solar composition, such that we can estimate the heavy noble gas composition of cometary ices formed from solar gas and thermally processed in the solar system (Figures 6 and 7).

Deposition Temperature	#	Gases trapped in the ice			Enrichment ratio in trapped gas (relative to the initial gas composition)		
		Kr/Ar	Xe/Ar	N_2/Ar	Kr/Ar	Xe/Ar	N_2/Ar
28K	1	0.713	0.445	3.55	1.35	1.77	0.868
	2	0.667	0.403	3.88	1.26	1.60	0.948
	3	0.781	0.365	3.41	1.48	1.45	0.834
	4	0.720	0.345	3.54	1.36	1.37	0.864
	5	0.709	0.329	3.89	1.34	1.30	0.950
Average 28K		0.718	0.377	3.65	1.36	1.50	0.893
	±	0.020	0.023	0.108	0.039	0.093	0.026
40K	1	1.23	0.903	3.12	2.31	3.59	0.762
	2	1.11	0.813	3.04	2.10	3.23	0.743
Average 40K		1.17	0.858	3.08	2.21	3.40	0.752
	±	0.081	0.064	0.054	0.153	0.254	0.013
50K	1	2.10	1.28	2.49	3.97	5.07	0.608
	2	1.96	1.18	2.49	3.71	4.68	0.607
	3	4.55	1.40	2.40	8.60	5.54	0.587
Average 50K		2.87	1.28	2.46	5.42	5.10	0.601
	±	1.03	0.08	0.04	1.95	0.30	0.01
60K	1	29.5	29.0	5.38	55.7	115	1.31
	2	31.2	25.0	4.50	59.0	99.2	1.10
Average 60K		30.3	27.0	4.94	57.3	107	1.21
	±	1.23	2.84	0.622	2.32	11.3	0.152
70K	1	59.2	215	19.7	112	855	4.82
	2	8.25	60.3	42.7	15.6	239	10.4
	3	7.48	168	98.1	14.1	666	24.0
Average 70K		25.0	148	53.5	47.2	587	13.1

	±	21.0	56.2	28.5	39.6	223	6.96
80K	1	8.46	276	21.6	16.0	1100	5.27
	2	42.4	1150	93.7	80.2	4560	22.9
Average 80K		25.4	713	57.6	48.1	2830	14.1
	±	24.0	617	51.0	45.4	2450	12.5

Table 1. Elemental ratios of Kr-Xe-N_2/Ar measured in the trapped phase depending on the temperature of deposition of the amorphous ice, from 28 K to 80 K. These ratios are computed by integrating the signal of each element between 100 K and 155 K during the heating phase. The enrichment ratio values were obtained by dividing the trapped X/Ar by the X/Ar ratio in the gas mixture (where X = Kr, Xe or N_2). All experiments were reproduced at least once. The decrease in reproducibility toward higher deposition temperature of formation is due to the decreasing amount of gas trap, especially Ar. The averages of the repeated experiments are given with the associated standard error (standard deviation divided by $\sqrt{n-1}$, where n is the number of repeats).

4.1 Experimental Constraints on the Temperature Conditions of Cometary Ices

The overall variations of the Ar-Kr-Xe elemental composition of the ice as a function of the ice deposition temperature are comparable to those obtained during previous experimental works (Figure 6, Bar-Nun & Owen 1998). At 28 K below the condensation temperature of Ar, Kr and Xe, the ice has a composition similar to that of the original gas mixture because the guest species are all efficiently trapped. When the temperature of the ice formation increases above Ar condensation temperature (above ~40 K) for the 40-50-60 K experiments, Kr and Xe are more efficiently trapped than Ar and the composition of the ice thus evolves roughly along a 1:1 line in ^{84}Kr/^{36}Ar versus ^{132}Xe/^{36}Ar space (Figure 6). At higher deposition temperatures (70-80 K, close to temperature limit to form amorphous ice), above the point at which Kr condenses (~64 K), we observe a more efficient trapping of Xe relative to Kr, in agreement with Bar-Nun & Owen (1998). This results in a stronger increase of the ^{132}Xe/^{36}Ar ratio compared to the ^{84}Kr/^{36}Ar ratio, resulting in a deviation from the 1:1 correlation (Figure 6). Experiments by Notesco et al. (2003) show high depletion in Ar relative to Kr and Xe even at low temperatures because of the very slow deposition rate they used, down to 10^{-5} µm/min. At these low deposition rates, guest species are more prone to diffusing out of the amorphous ice porosity, before being trapped by the formation of a subsequent H_2O layer (Ciesla et al. 2018). Although the deposition rate cannot be precisely estimated in our experiments (EXCITING does not have an in-situ infrared spectrometer), the similarity of the noble gas behaviour with that of Bar-Nun & Owen (1998)'s experiments strongly suggests that the EXCITING deposition rates are likely on the order of 0.1-1 µm/min.

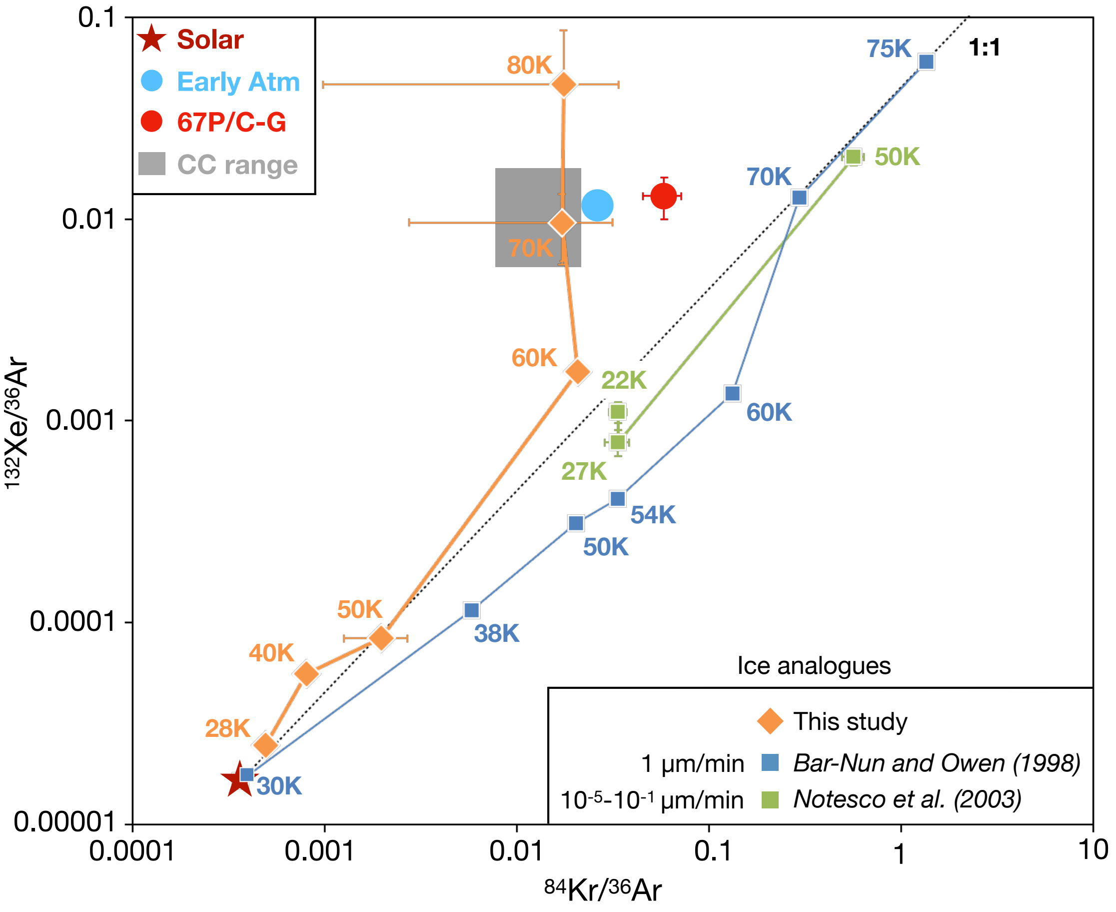

Figure 6. Plot of ^{84}Kr/^{36}Ar vs ^{132}Xe/^{36}Ar with several notable cosmochemical endmembers: Solar (Lodders 2003; Meshik et al. 2014), CC grey box (range of the carbonaceous chondrite compositions, compilation from Bekaert et al. 2020), 67P/C-G (comet 67P/Churyumov-Gerasimenko, Rubin et al. 2018) and Early Atm (initial Earth atmospheric composition before Xe loss, Zahnle et al. 2018). Squares (blue and green, from Bar-Nun & Owen (1998) and from Notesco et al. (2003), respectively) and orange diamonds (this study) show the composition of experimental cometary ices if formed from a solar composition at various temperatures of formation. Error bars for both this study and Notesco et al. (2003) represent the standard error of the repeated experiments for one temperature of formation at 1 σ. Lines between symbols are for visual aid only. Starting from a solar composition, a depletion in Ar alone will lead to variation along the 1:1 (black dashed line) direction. All three experiments show variations along this line when increasing the temperature to 50-60 K. Both Bar-Nun & Owen study

and ours show a shift toward higher $^{132}Xe/^{36}Ar$ when forming ice above 60 K. Although this shift appears critical to reach the observed composition of 67P/C-G, none of those experiments achieve it.

Based on (i) the N_2/CO of comet 67P/C-G (Rubin et al. 2015), which matched laboratory predictions of ice analogues formed below 30K with low deposition rates (Bar-Nun et al. 2007), and (ii) the nuclear spin temperature derived from the ortho/para ratio of H_2O and NH_3 in various comets (Mumma et al. 1988; Crovisier 1999; Kawakita et al. 2004), it has been proposed that the ice of the comet 67P/C-G was formed below 30 K (Rubin et al. 2015). The second observation was however challenged by Hama et al. (2016), who argued that the ortho/para ratio was not related to the prevailing temperatures during the formation of the cometary ice. Our experimental results obtained with a low (25-30 K) deposition temperature do not match the Rosetta observations of 67P/C-G heavy noble gas composition (Figure 6), similarly to previous experiments (Bar-Nun & Owen 1998; Notesco et al. 2003). As shown in Figure 6, we find that, for an initially solar composition, formation temperatures as high as 70 K – 80 K best reproduce the elemental noble gas composition of comet 67P/C-G and other "planetary" end-members (e.g., early Earth atmosphere or chondritic, Figure 6). These "high" potential temperatures of formation allow amorphous ice presumably composing cometary ices to be formed, and high abundances of Kr and Xe found in comet 67P/C-G relative to the solar abundances to be reproduced.

In addition to the noble gas experiments outlined above, we make the first comprehensive investigation of nitrogen behaviour relative to the heavy noble gases over a wide range of temperatures (from 28 K to 80 K). This builds on previous studies which have investigated N_2 and Ar fractionation below 30 K (Bar-Nun et al. 2007), as well as N_2, Ar and Kr at 77 K (Yokochi et al. 2012). The study of nitrogen in comets is of prime interest regarding the potential for small bodies to have brought prebiotic molecules to the early Earth (Chyba & Sagan 1992). In our experiment, nitrogen was incorporated in the amorphous ice in the form of molecular N_2. In this state, the triple bond between nitrogen atoms makes N_2 highly stable/unreactive and nitrogen behaviour becomes similar to that of chemically inert noble gases. N_2 and Ar have similar sublimation temperature around 45 K (Figure 4) and are both released together with the other noble gases when amorphous ice crystallises (Figure 4). This is in agreement with observations of comet 67P/C-G where N_2 and ^{36}Ar abundances showed a strong positive correlation within the coma of the comet, with a relatively constant $N_2/^{36}Ar$ of 182 ± 50 (Rubin et al. 2018). This ratio is one order of magnitude higher than the solar composition of $N_2/^{36}Ar = 11$ (computed from the N_2/Ar and solar Ar isotopic composition reported by Lodders 2003 and Meshik et al. 2014, respectively), suggesting that comets are enriched in nitrogen relative to argon compared to a putative initial solar composition.

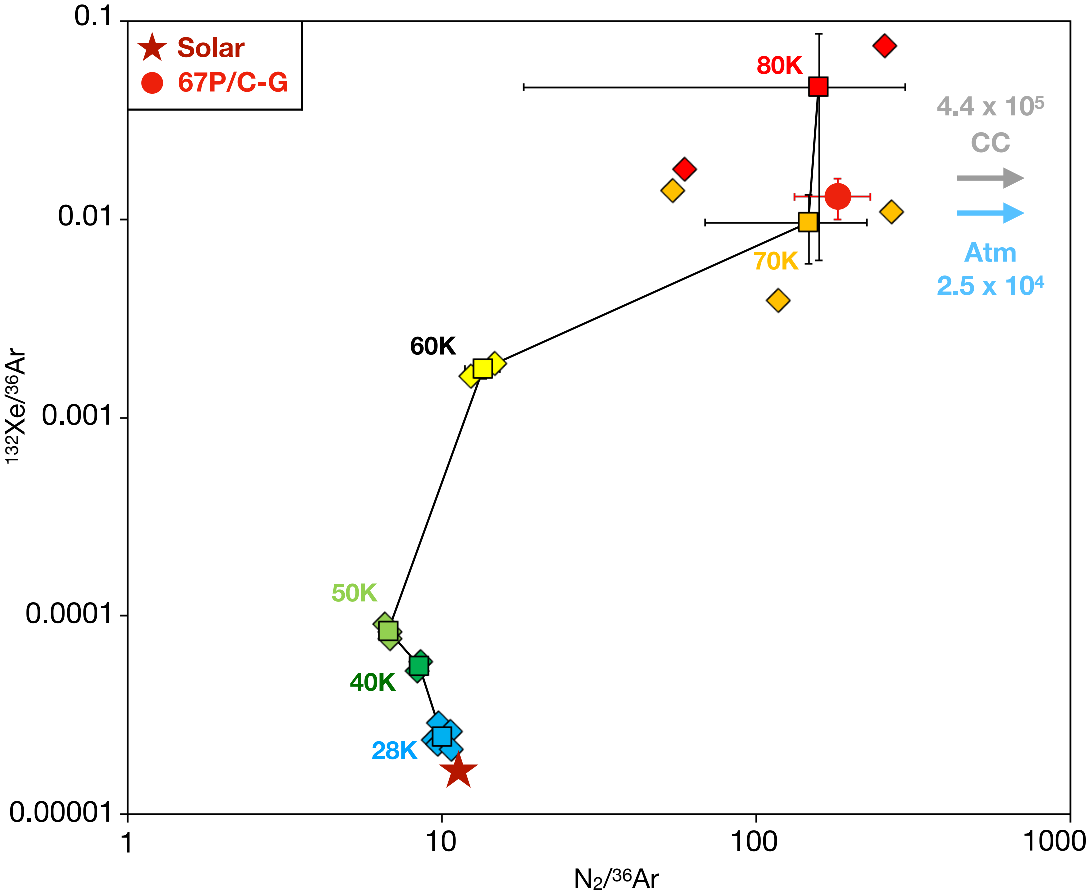

Figure 7. Three isotope plot of $N_2/^{36}Ar$ vs $^{132}Xe/^{36}Ar$ of the experimental cometary ices considering a solar-like starting composition and various temperatures of formation. Cosmochemical endmembers are the same as in Figure 6. Squares represent the average of the repeated experiments (shown as diamonds) for a given temperature of deposition. Error bars represent the standard error of the repeated experiments at 1 σ. Line between symbols is for visual aid only. Similar detailed plot for $^{84}Kr/^{36}Ar$ vs $^{132}Xe/^{36}Ar$ is given in Appendix Figure A6.

Our experimental results show no enrichment in the $N_2/^{36}Ar$ ratio relative to the initial gas composition when ice is formed at 28, 40 or 50 K (Figure 7). $N_2/^{36}Ar$ ratios are computed from enrichment ratios (Table 1) using the same method as previously described for noble gases, considering an initial solar composition. We observe a depletion in N relative to Ar for low temperatures of formation, which was also observed in experiments at 24 K, 27 K and 30 K from Notesco et al. (2003). However, when the temperature of the ice formation exceeds the sublimation temperature of N_2 and Ar (~ 40-50 K, Figure 4), we observe an enrichment in the $N_2/^{36}Ar$ ratio reaching ~ 150 (Figure 7) for temperatures of formation of 70 K and 80 K. The cometary $N_2/^{36}Ar$ measured in 67P/C-G (182 ± 50, Rubin et al. 2018) thus is better reproduced by "high" temperatures of deposition (70-80 K) than low temperatures (28-50 K). This nitrogen enrichment relative to argon for 70-80 K experiments possibly results from the small difference between N_2 and Ar condensation temperatures (~ 46 K and 45 K respectively, Figure 4). Differences in their ionic radius and polarizabilities could also induce subtle differences in their trapping efficiency at high temperatures of deposition. At such temperatures, Ar is slightly less efficiently trapped in the amorphous ice than nitrogen, and the $N_2/^{36}Ar$ of the trapped component therefore tends to be higher than the initial composition of the gas phase (solar in Figure 7). This was also observed to a lesser extent for our experiment at 60K, because the temperature of deposition is closer to the condensation temperatures of N_2 and Ar, with a small enrichment in N_2 ($N_2/^{36}Ar$ ~ 13) relative to the solar composition (11).

Finally, it is important to note that for all the experiments (with various temperature of deposition) we consider only the composition of the trapped phase in the water ice when computing enrichment ratios from the initial gas phase. We assume that any volatile element frozen on the water ice would be either in negligible amount or lost during the lifetime of a comet, especially in the case of N_2 and Ar, which have the lowest sublimation temperatures (~40-50 K, Figure 4). In our experiments, the amount of frozen volatile is calculated by integrating the gas release between the starting temperatures (28 K to 80 K) and 100 K, and can be compared to the amount of trapped gas (100 K to 155 K) in Table A1. We observe that the amount of frozen N_2, Ar, Kr and Xe is always negligible relative to the amount trapped, except for N_2 and Ar when the ice forms at 28 K (Table A1). Rosetta observations of comet 67P/C-G indicate that at high heliocentric distances (~3 au) CO_2 still sublimates independently of water (Läuter et al. 2020). Since CO_2 has a sublimation temperature around 100 K (Fray & Schmitt 2009), close to the sublimation temperature of Xe (and Kr), this could indicate that the frozen phase of Xe (and possibly Kr) was not completely lost. Considering this possibility, we have evaluated whether the addition of this frozen phase could contribute to changing the enrichment ratios of the comet relative to the initial gas composition. The maximum contribution from the frozen Kr and Xe phase would be around 10 %, when the ice is formed at 28 K (Figure 4 and Table A1), and rapidly decreases for higher temperatures of deposition (Figure A5 and Table A1). An addition of 10 % of Kr and Xe would not be sufficient to change Kr/Ar and Xe/Ar of an ice formed at 28 K toward cometary-like values (Figure 6). Importantly, Notesco et al. (2003) showed that decreasing the deposition rate of the ice decreases the amount of frozen gas relative to the (constant) amount of trapped gas. Although we do not quantitatively know the deposition rate of EXCITING, it is manifestly faster by several orders of magnitude compared to the actual formation rate of cometary ices. Thus, we consider that any frozen volatiles on cometary ice, preserved during the lifetime of the comet, would be negligible with regard to the amount trapped in the ice. The elemental signature of comet 67P/C-G for noble gases is therefore unlikely to be the result of the loss of frozen volatile phases during the lifetime of the comet, but rather the result of elemental fractionation during the trapping of volatiles into amorphous water ice.

Taken together, N and noble gas elemental compositions in our experiments provide new constraints on the temperature of formation of cometary ices. We were able to reproduce comet 67P/C-G composition of highly volatile elements (N, Ar, Kr and Xe) from a solar-like initial composition with a formation temperature around 70K.

4.2 Origin of Cometary Nitrogen and Noble Gases

Our experimental observations on nitrogen and noble gases are in agreement with the formation of cometary ices at ~70 K in the outer part of the protoplanetary disk, or within the dense molecular cloud, from a reservoir with a solar composition. Forming cometary ices from a solar composition at lower temperatures (<30 K, Rubin et al. 2015) cannot be excluded, but would require secondary nitrogen addition and/or elemental fractionating process(es) to account for the nitrogen and noble gas abundances of comet 67P/C-G. To differentiate between the protoplanetary disk or the dense molecular cloud as the putative formation environment of cometary ices, it is important to also consider the isotopic composition of comets. The study of comet 67P/C-G, and other comets from ground-based observation or sample return, revealed specific (non-solar) isotopic composition for some volatile elements such as N and Xe (Altwegg et al. 2019, and references therein; Marty et al. 2017).

Nitrogen in particular (with its two isotopes ^{14}N and ^{15}N) presents strong isotopic variability between the different solar system reservoirs (solar, planetary, cometary or chondritic), the reasons for which are still poorly understood (Füri & Marty 2015). The isotopic composition of N can be expressed as permil variations from the terrestrial atmospheric N_2, with $\delta^{15}N = (^{15}N/^{14}N_{sample} / ^{15}N/^{14}N_{air} - 1) * 1000$, where air refers to the modern composition of atmospheric N_2 (Nier et al. 1950). The nitrogen isotopic composition of comets is strongly enriched in the heavy isotope ^{15}N ($\delta^{15}N$ = ~ +900 ‰, Bockelée-Morvan et al. 2015) compared to the solar composition ($\delta^{15}N$ = ~ -400 ‰, Marty et al. 2011). This cometary $\delta^{15}N$ composition of ~ 900‰ is an average from a compilation of mostly ground-based observations of cometary comas. It is important to note that this value is not derived from N_2 gas but from molecular nitrogen in the form of HCN, CN or NH_2 ions (Bockelée-Morvan et al. 2015). Because these molecules found in comets all exhibit the same nitrogen isotope composition, it is likely that they formed from a common N reservoir (Bockelée-Morvan et al. 2015). Comet 67P/C-G (the only comet with in-situ measurements of the coma) also shows a strong enrichment in the heavy isotope ^{15}N of ~ +1000 ‰, for NH_3, NO and most importantly N_2 molecules (Altwegg et al. 2019). This consistent isotopic composition between different nitrogen-bearing molecules further supports a common N source for comets.

The solar-derived elemental composition of cometary ices formed at 70 K (as suggested by this study to fit the N/Ar and Xe/Ar of comets) appears to indicate the outer part of the protoplanetary disk, during the lifetime of the solar nebula, as a favourable environment to form the cometary building blocks (Pignatale et al. 2018). The non-solar N isotopic composition consistently observed in comets however requires additional process(es) capable of fractionating N isotopes from the solar composition, before or during N incorporation into the cometary ices. Studies of nitrogen isotopes in organic matter synthetised from cometary ice analogues have shown only limited fractionation of nitrogen isotopes between the gas phase and the organic residue (+ 3 ‰, Sugahara et al. 2019). To our knowledge, no studies of nitrogen isotope behaviour trapped in, and released from, amorphous ice exist. If nitrogen isotopes are not fractionated during their incorporation into cometary ices or organic matter, fractionating processes in the molecular cloud or in the protoplanetary disk are required to account for the non-solar cometary composition.

Self-shielding of UV irradiation from the Sun and nearby stars has been proposed as a process to extensively fractionate isotopes in the outer part of the solar nebula (Clayton 2002). Laboratory experiments demonstrated the possibility for differential N_2 photodissociation and/or self-shielding effect occurring in the solar nebular to account for the variability in nitrogen signatures (Chakraborty et al. 2014). This would result in an enrichment of ^{15}N available for nitrogen bearing molecules, before their incorporation in cometary ices, in the outer part of the disk (analogous to ^{17}O- and ^{18}O-enrichment by self-shielding processes; Lee et al. 2008). The isotopic anomaly of Xe, identified in comet 67P/C-G (Marty et al. 2017), cannot however be produced by photochemical processes. High temperature (~1000 K) experiments were able to produce Xe isotopic fractionation when ionized in plasma conditions, and incorporated into organic matter (Kuga et al. 2015), however these conditions do not apply to the cold environment of the outer solar system required to form volatile-rich cometary ices.

Conversely, if cometary ices formed at temperatures of ~30 K, as suggested by Rubin et al. (2015), it would require a non-solar initial elemental composition for noble gases and nitrogen. A non-solar composition would be consistent with the isotopic composition of N in 67P/C-G which is highly enriched in ^{15}N relative to solar (Altwegg et al. 2019) and that of Xe which is markedly depleted in heavy isotopes relative to solar (Marty et al. 2017). Forming cometary ice analogues at 28 K, as done this study, shows very limited elemental fractionation of noble gases (as well as in Bar-Nun & Owen 1998 at 30 K). In such a case, the noble gas-N elemental composition would directly reflect that of the gas which was trapped in comet 67P/C-G. It follows that the initial gas would be enriched in N_2 and Kr over Ar relative to a solar composition by factors of ~15 and ~150, respectively (Rubin et al. 2018) and Xe would be even more enriched relative to Kr by a factor of 5 (Rubin et al. 2018). Whether or not such a hypothetical gas existed in the comet-forming region is uncertain, and will require further measurements of volatiles trapped in outer solar system objects.

Experimental studies of the isotopic fractionation behaviour of N and noble gases in cometary ice analogues are currently lacking. Here we have shown the capability of the EXCITING experiment to reproduce and investigate cometary ice analogues in the laboratory. Further studies will be focussed on extending these investigations to include the identification and quantification of any resulting isotope fractionation effects. The potential for mass-dependent fractionation effects during trapping/release should be considered, as well as the effect of UV irradiation on ices. Such experiments should provide further constraints on the origin of their peculiar isotopic signatures in comets.

4.3 Experimental Limitations and Future Developments

It is important to consider that all experiments on the behaviour of highly volatile elements in cometary ices reported so far and including the one reported in the present study are extremely simplified in comparison to the actual complexity of cometary ice compositions and their thermal history. For our experiments, we have chosen a heating rate of 1K/min to strike a balance between keeping the rate as low as possible while maximising the signal size of the sublimating gas species and keeping a convenient duration for experiments (about 5 hours to go from 30 to 300 K). Similar heating rates have also been commonly used in previous similar experiments (Bar-Nun and co-workers' extensive studies at 1 K/min, Martin-Doménech et al. 2014 at 1 K/min, Vinogradoff et al. 2011 at 4 K/min or Collings et al. 2004 at 5 K/min), and therefore our heating rate allows for more direct comparisons between this study and previous works. Comets presumably experienced variable, and much lower, heating rates, during their Centaur stage (beyond 10 au, Gkotsinas et al. 2022) and their transit in the inner solar system, than we are able to replicate in the laboratory. The temperatures at which water or the guest species sublimate depends on the heating rate of the ice (Collings et al. 2004; Martin-Doménech et al. 2014). Indeed, Collings et al. (2004) modelled several desorption profiles of water ice and showed that for low heating rates (down to 0.01 K/yr, 8 orders of magnitude slower than 1 K/min), the sublimation of water initiates around 100 K (against ~170 K in our experiment at 1 K/min). This effect becomes important when considering the thermal history of comets and the temperature inside the comet, computed using the sublimation temperature of water and its presence in the coma of comets (Hu et al. 2017). Slow heating rates also increase the possibility for trapped species to diffuse out during the slow annealing of the amorphous water ice (Bar-Nun et al. 1987). Diffusion experiments of noble gases in cometary ice analogues do not exist yet, but would help further understand the origin of the noble gas composition of comet 67P/C-G. Indeed, differences in the capacity to diffuse out from the ice structure between Ar, Kr and Xe could induce elemental fractionation, and possibly be the cause of the mismatch in ^{84}Kr/^{40}Ar between 67P/C-G composition (Rubin et al. 2018) and our experiments (as well as Bar-Nun & Owen 1998) when forming ice at 70 K.

The temperature of volatile sublimation thus depends on the heating rate but also on the composition of the ice. For a given element/molecule, the timing of sublimation as a pure phase (as in Fray & Schmitt 2009) will be different between experiments that contain other additional species in the ice phase (this study, or Martin-Domenech et al. 2014). We observe this difference, with Appendix Figure A7 showing the sublimation pattern of N_2, Ar, Kr and Xe with and without water. The actual composition of cometary ices is much more complex than a pure nitrogen-noble gas-water mixture (see comet 67P/C-G composition in Altwegg et al. 2019). Further experiments taking into account this ice complexity will ultimately bring more reliable constraints on the behavior of the frozen phases of nitrogen and noble gases.

Some of the most common molecules found in the interstellar medium (Müller et al. 2005) and comets, such as H_2O, CO_2, CO, CH_4, O_2 and H_2S, play a crucial role in the organic budget of cometary ices and as pre-biotic molecules (Danger et al. 2013; Vinogradoff et al. 2011; Muñoz Caro et al. 2004). Regarding the behaviour of noble gases, the presence of CO_2 (equivalent to around 10 % of the total water amount in average in comets, Feldman et al. 1997, Läuter et al. 2020) can be of prime importance because of its capacity, similar to that of amorphous water ice, to trap and retain other volatile elements above their sublimation temperature. The capacity of CO_2 to trap CO and CH_4 was experimentally studied by Kouchi & Yamamoto (1995) and raises the importance of the compositional complexity of ice with regards to the behaviour of cometary volatiles. Whilst a portion of CO_2 would be trapped in the amorphous water ice, at least 50% of CO_2 could present as a frozen phase (Kouchi & Yamamoto 1995), making it potential carrier of cometary volatiles. The relationship between CO_2 and noble gases in the coma of comet 67P/C-G was investigated (Rubin et al., 2018), and it appeared that the outgassing of Ar better correlates with CO_2 than H_2O. Additionally, in the case of 67P/C-G, the amount of CO_2 is subject to seasonal effects and can locally exceed the amount of water in the outgassing coma (Hässig et al. 2015; Läuter et al. 2020). These observations indicate that CO_2 ice could also be a carrier of trapped nitrogen and noble gases in addition to the amorphous water ice. To our knowledge, experiments of noble gases in CO_2-water ice mixtures do not yet exist, but could be one of the future targets of the EXCITING experiment.

Finally, the present experiment does not explore the effect of varying the deposition rate on the volatile composition of the ice. Models show that the trapping efficiency of noble gases follows different regimes depending on the deposition rate (Ciesla et al. 2018). We estimate the deposition rate used in this study to be in the order of 10^{-1}-10^{0} µm/min, based on comparable volatile behaviour with previous studies (Bar-Nun & Owen 1998). Models predict that the Ar trapping regime changes at around 10^{-4} µm/min, resulting in lower amount of trapped Ar with decreasing deposition rates (Ciesla et al. 2018). At deposition rates between 10^{-5} and 10^{-1} µm/min, Notesco et al. (2003) showed constant Ar/Xe and Kr/Xe enrichment ratios for a given temperature, differing from our experiment (and from Bar-Nun & Owen 1998) at 10^{-1}-10^{0} µm/min**.** The change of volatile behaviour observed between those experiment is around 10^{-1} µm/min, which does not fit the model predictions by Ciesla et al (2018). So far, experiments and models on the effect of deposition rate of noble gas trapping efficiency are limited, and do not permit extrapolation of our result to more realistic conditions. At slower, more realistic, deposition rates, the trapping efficiency of the volatile guest species will decrease and can likely result in different trapped phase composition (elemental fractionation) for a given temperature of deposition because of the different volatility of the guest species.

Considering all these aspects, the EXCITING experiment and the first results described in this study offers a simplified version of cometary ices, that are more complex in terms of composition and thermal history (with local heterogeneities, as opposed to a homogeneous layer of ice). Other species, in particular CO_2, will be added to the setup to complement the N_2-noble gas-H_2O ices, and provide more realistic conditions to study the behaviour of the highly volatile elements in comets. Variable temperature regimes shall also be investigated to study possible volatile loss (and thus potential fractionation) during the lifetime of the ice. The purpose of this study was to firstly evaluate the capabilities of EXCITING in the context of previous experiments and will be adapted to more complex systems.

5. Conclusion and Perspectives

We have reported an overview of the specification, capabilities, experimental limitations, and preliminary results from the new EXCITING experimental apparatus designed to investigate the behaviour of highly volatile (N_2, Ar, Kr and Xe) elements in extra-terrestrial water ice analogues. Amorphous water ice trapping nitrogen and noble gases can be obtained with a large range of experimental conditions (starting gases, deposition temperature, heating rate, etc.) allowing us to investigate the elemental and isotopic composition of the volatile elements released from the ice upon warming, analogous to coma of comets. Here we have performed a series of reproducible experiments on the formation of H_2O ice mixed with N_2, Ar, Kr and Xe as guest species deposited at different temperature 28 K, 40 K, 50 K, 60 K, 70 K and 80 K. We showed that the elemental composition of the volatiles trapped in the amorphous ice, and subsequently released when the water ice becomes crystalline, varies depending on the temperature of formation of the ice. The obtained noble gases ratios (Kr/Ar and Xe/Ar) show discrepancies with previous similar studies (Bar-Nun et al. 1998; Notesco et al. 2003). Toward high temperature of formation of the ice, between 70 K and 80 K, we were able to reproduce a similar noble gas composition to that of comet 67P/C-G, as measured by the Rosetta spacecraft, with however still a depletion in the Kr/Ar ratio, in opposition to the excess of Kr/Ar for similar temperature range by Bar-Nun et al. (1998). We also have provided the first coupled nitrogen and heavy noble gases measurements in experimental ices, with the N_2/Ar of comet 67P/C-G also being matched when ices were formed at 70 - 80 K. Considering the technical limitations on the timescale of the experiment and the limited ice complexity, these results suggest that cometary ice formation could occur at higher temperatures (70 - 80 K) than previously advocated (~30 K). However, experiments that incorporate other major volatile species such as CO_2 are needed to more realistically and reliably constrain the temperature formation of comets.

The unique isotope signature for noble gases, especially xenon (Marty et al. 2017), in comet 67P/C-G also motivates investigation of the isotopic behaviour of noble gases during ice formation and evolution. Ultimately, using EXCITING experiment, we will investigate how the formation of volatile-rich cometary ices affects the isotopic signature of nitrogen and noble gases. The addition of solar-like irradiation (by UV photons) during ice formation could affect the trapping efficiency of nitrogen and noble gases and modify their elemental and isotopic compositions. The effect of UV photons on ices will be also studied in the future using EXCITING.

Acknowledgments

We thank Laurent Zimmermann and Bouchaïb Tibari for their mentorship and help in building the EXCITING experiment. Grégoire Danger and Henner Busemann are thanked for the fruitful discussions that helped building this work. We thank Cryoscan© for their help constructing the design of the cryogenic system of EXCITING. We also thank the two anonymous reviewers for their comments and suggestions that improved the quality of the manuscript. This study was supported by the European Research Council (ERC) under the European Union's Horizon

2020 research and innovation program (PHOTONIS Advanced Grant # 695618). This is CRPG contribution #XXX.

References

Alexander, C. M. O'D., Bowden, R., Fogel, M. L., et al. 2012, Sci, 337, 721

Alexander, C. M. O'D., McKeegan, K. D., & Altwegg, K. 2018, SSRv, 214, 1

Altwegg, K., Balsiger, H., Bar-Nun, A., et al. 2015, Sci, 347, 1261952

Altwegg, K., Balsiger, H., & Fuselier, S. A. 2019, ARA&A, 57, 113

Arpigny, C., Jehin, E., Manfroid, J., et al. 2003, Sci, 301, 1522

Avice, G., Moreira, M., & Gilmour, J. D. 2020, ApJ, 889, 6

Balsiger, H., Altwegg, K., Bochsler, P., et al. 2007, SSRv, 128, 745

Bar-Nun, A., Herman, G., Laufer, D., & Rappaport, M. L. 1985, Icar, 63, 317

Bar-Nun, A., Dror, J., Kochavi, E., & Laufer, D. 1987, PhRvB, 35, 2427

Bar-Nun, A., & Owen, T. 1998, in Solar System Ices, ed. B. Schmitt et al. (Dordrecht, Springer), 353

Bar-Nun, A., Notesco, G., & Owen, T. 2007, Icar, 190, 655

Bar-Nun, A., Laufer, D., Rebolledo, O., et al. 2013, In The Science of Solar System Ices, ed. M. S. Gudipati, & J. Castillo-Rogez (New York, NY: Springer), 487

Bekaert, D. V., Broadley, M. W., & Marty, B. 2020, NatSR, 10, 1

Bockelée-Morvan, D., Calmonte, U., Charnley, S., et al. 2015, SSRv, 197, 47

Brownlee, D., Tsou, P., Aléon, J., et al. 2006, Sci, 314, 1711

Burkhardt, C., Spitzer, F., Morbidelli, A., et al. 2021, SciA, 7, eabj7601

Chakraborty, S., Muskatel, B. H., Jackson, T. L., et al. 2014, PNAS, 111, 14704

Chyba, C., & Sagan, C. 1992, Natur, 355, 125

Ciesla, F. J., Krijt, S., Yokochi, R., & Sandford, S. 2018, ApJ, 867, 146

Clayton, R. N. 2002, Natur, 415, 860

Collings, M. P., Anderson, M. A., Chen, R., et al. 2004, MNRAS, 354, 1133

Crovisier, J. 1997, EM&P, 79, 125

Danger, G., Orthous-Daunay, F. R., de Marcellus, P., et al. 2013, GeCoA, 118, 184

Dauphas, N. 2017, Natur, 541, 521

Feldman, P. D., Festou, M. C., Tozzi, P., & Weaver, H. A. 1997, ApJ, 475, 829

Fray, N., & Schmitt, B. 2009, P&SS, 57, 2053

Füri, E., & Marty, B. 2015, NatGe, 8, 515

Ghormley, J. A. 1967, JChPh, 46, 1321

Gkotsinas, A., Guilbert-Lepoutre, A., Raymond, S. N., & Nesvorný, D. 2022, ApJ, 928, 43

Hama, T., Kouchi, A., & Watanabe, N. 2016, Sci, 351, 65

Hässig, M., Altwegg, K., Balsiger, H., et al. 2015, Sci, 347, aaa0276

Hu, X., Shi, X., Sierks, H., et al. 2017, MNRAS, 469, S295

Hutsemékers, D., Manfroid, J., Jehin, E., Zucconi, J.-M., & Arpigny, C. 2008, A&A, 34, 2000

Jenniskens, P., & Blake, D. F. 1994, Sci, 265, 753

Jenniskens, P., & Blake, D. F. 1996, ApJ, 473, 1104

Kawakita, H., Watanabe, J., Furusho, R., et al. 2004, ApJ, 601, 1152

Kouchi, A., & Yamamoto, T. 1995, Prog. Cryst. Growth Charact. Mater., 30, 83

Kuga, M., Marty, B., Marrocchi, Y., & Tissandier, L. 2015, PNAS, 112, 7129

Läuter, M., Kramer, T., Rubin, M., & Altwegg, K. 2020, MNRAS, 498, 3995

Le Roy, L., Altwegg, K., Balsiger, H., et al. 2015, A&A, 583

Lee, J. E., Bergin, E. A., & Lyons, J. R. 2008, M&PS, 43, 1351

Lodders, K. 2003, ApJ, 591, 1220

Luna, R., Satorre, M. A., Santonja, C., & Domingo, M. 2014, A&A, 566, A27

Martin-Doménech, R., Muñoz Caro, G. M., Bueno, J., & Goesmann, F. 2014, A&A, 564

Marty, B., Chaussidon, M., Wiens, R. C., Jurewicz, A. J. G., & Burnett, D. S. 2011, Sci, 332, 1533

Marty, B. 2012, E&PSL, 313, 56

Marty, B., Avice, G., Sano, Y., et al. 2016, E&PSL, 441, 91

Marty, B., Altwegg, K., Balsiger, H., et al. 2017, Sci, 356, 1069

Meshik, A., Hohenberg, C., Pravdivtseva, O., & Burnett, D. 2014, GeCoA, 127, 326

Müller, D. R., Altwegg, K., Berthelier, J. J., et al. 2022, A&A

Müller, H. S., Schlöder, F., Stutzki, J., & Winnewisser, G. 2005, JMoSt, 742, 215

Mumma, M. J., Blass, W. E., Weaver, H. A., & Larson, H. P. 1988, BAAS, 20, 826

Muñoz Caro, G. M., Meierhenrich, U., Schutte, W. A., Thiemann, W. H.-P., & Greenberg, J. M. 2004, A&A, 413, 209

Nier, A. O. 1950, PhRv, 77, 789

Notesco, G., Bar-Nun, A., & Owen, T. 2003, Icar, 162, 183

Notesco, G., & Bar-Nun, A. 2005, Icar, 175, 546

Owen, T., Bar-Nun, A., & Kleinfeld, I. 1992, Natur, 358, 43

Owen, T. C., & Bar-Nun, A. 2001, OLEB, 31, 435

Parent, P., Laffon, C., Mangeney, C., Bournel, F., & Tronc, M. 2002, JChPh, 117, 10842

Pepin, R. O. 1991, Icar, 92, 2

Pignatale, F. C., Charnoz, S., Chaussidon, M., & Jacquet, E. 2018, ApJL, 867, L23

Rubie, D. C., Jacobson, S. A., Morbidelli, A., et al. 2015, Icar, 248, 89

Rubin, M., Altwegg, K., Balsiger, H., et al. 2015, Sci, 348, 232

Rubin, M., Altwegg, K., Balsiger, H., et al. 2018, SciA, 4, eaar6297

Rubin, M., Bekaert, D. V., Broadley, M. W., Drozdovskaya, M. N., & Wampfler, S. F. 2019, ESC, 3, 1792

Rubin, M., Engrand, C., Snodgrass, C., et al. 2020, SSRv, 216, 1

Stevenson, K. P., Kimmel, G. A., Dohnálek, Z., Smith, R. S., & Kay, B. D. 1999, Sci, 283, 1505

Sugahara, H., Takano, Y., Tachibana, S., et al. 2019, GeocJ, 53, 5

Tachibana, S., Kouchi, A., Hama, T., et al. 2017, SciA, 3, eaao2538

Vinogradoff, V., Duvernay, F., Danger, G., Theulé, P., & Chiavassa, T. 2011, A&A, 530

Yokochi, R., Marboeuf, U., Quirico, E., & Schmitt, B. 2012, Icar, 218, 760

Zahnle, K. J., Gacesa, M., & Catling, D. C. 2018, GeCoA, 244, 56

Appendix

Deposition temperature	Volatile species	% Of total gas release	
		28 K – 100 K *frozen*	100 K – 155 K *trapped*
28 K	N_2	49%	51%
	Ar	43%	57%
	Kr	13%	87%
	Xe	7%	93%
40 K	N_2	8%	92%
	Ar	9%	91%
	Kr	3%	97%
	Xe	2%	98%
50 K	N_2	2%	98%
	Ar	2%	98%
	Kr	1%	99%
	Xe	1%	99%
60 K	N_2	34%	66%
	Ar	27%	73%
	Kr	1%	99%
	Xe	1%	99%
70 K	N_2	12%	88%
	Ar	17%	83%
	Kr	1%	99%
	Xe	2%	98%
80 K	N_2	5%	95%
	Ar	28%	72%
	Kr	17%	83%
	Xe	1%	99%

Table A1. Proportions of gas release (N_2, Ar, Kr and Xe) between 28 K - 100 K and 100 K – 155 K temperature - during warm up of the ice for different temperatures of deposition (28 K, 40 K, 50 K, 60 K, 70 K and 80 K). The gas release during the 28 K - 100 K corresponds to the sublimation of the different frozen phases. The gas release during 100 K - 155 K corresponds to the release of the trapped phase, by the slow annealing of the ice during heating and the amorphous-crystalline transition around 145 K. The proportion of frozen phase is consistently smaller than the trapped phase, except for N_2 and Ar when the ice is formed at 28 K. At temperatures of deposition >60 K, the abundances of N_2, Ar and Kr are associated with large uncertainties as we can see on the N_2/Ar and Kr/Ar ratios of Figures 6 and 7.

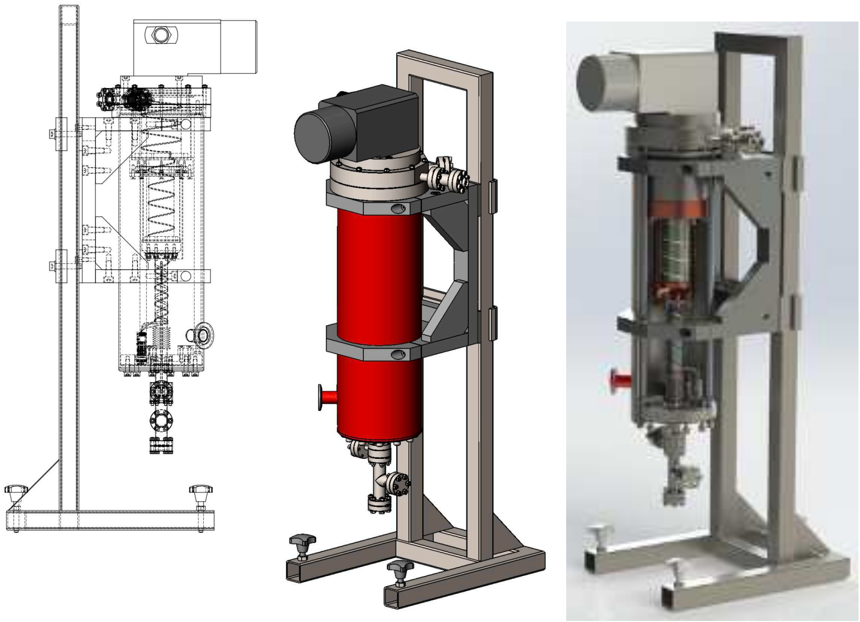

Figure A1. Drawing of the cryogenic trap designed for the EXCITING project, provided by Cryoscan©. This design is proprietary of Cryoscan©.

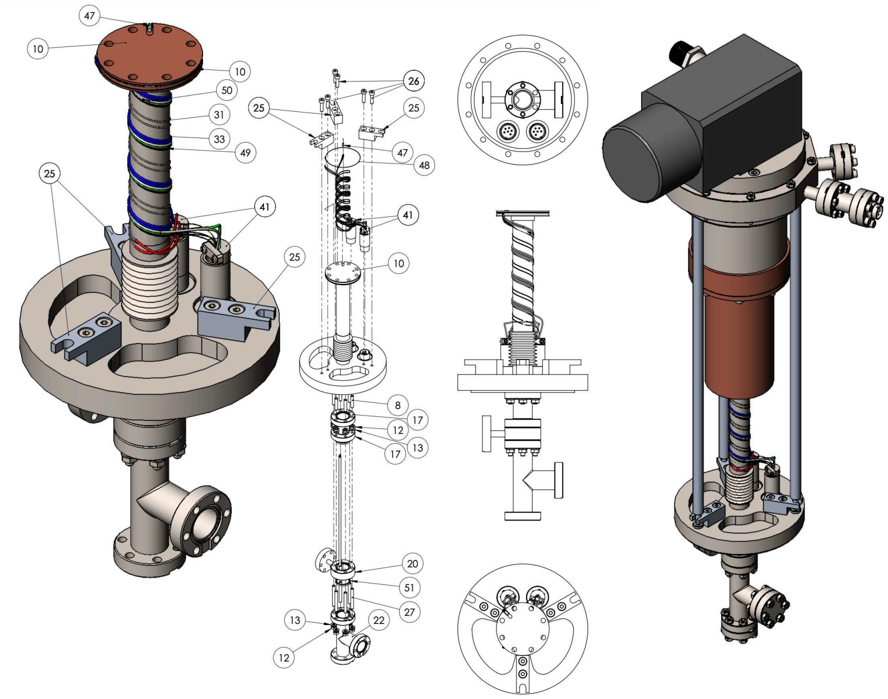

Figure A2. Detailed industrial scheme of the cold head designed for the EXCITING project, provided by Cryoscan©. This design is proprietary of Cryoscan©.

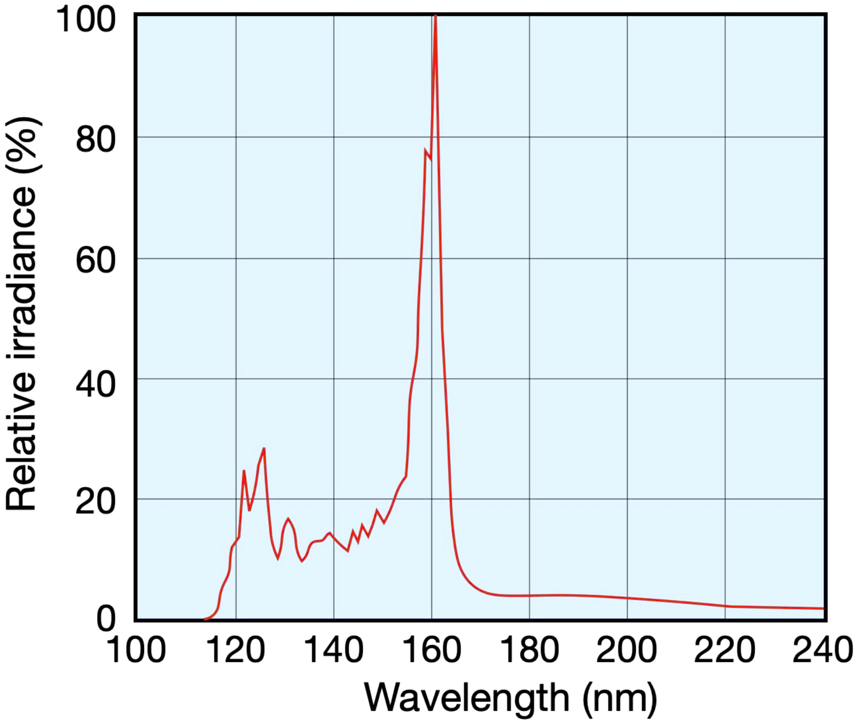

Figure A3. Wavelength distribution of the Hamamatsu H2D2 UV lamp (model L11798, MgF_2 window), with a flux of around 10^{15} photons/s (Sebree et al. 2018).

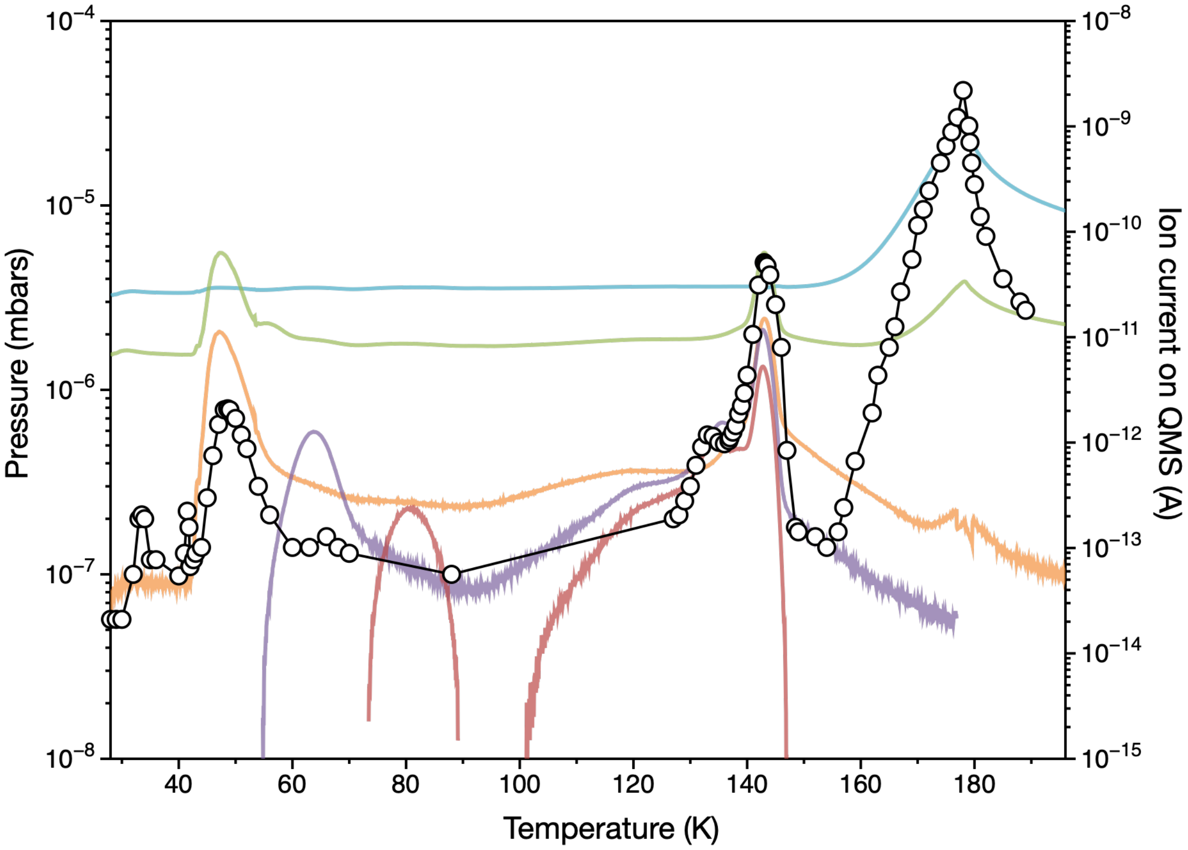

Figure A4. The circles show the evolution of the total gas pressure in the experimental volume as a function of temperature during the warm up of the ice, measured by the ion gauge positioned before the QMS (Figure 1). The ice was formed at 28 K with identical experimental procedure as the data shown in Figure 4. The slightly transparent coloured curves are the intensities of H_2O, N_2, Ar, Kr and Xe measured on the QMS (displayed as ion current), during the experiment at 28K presented in Figure 4.

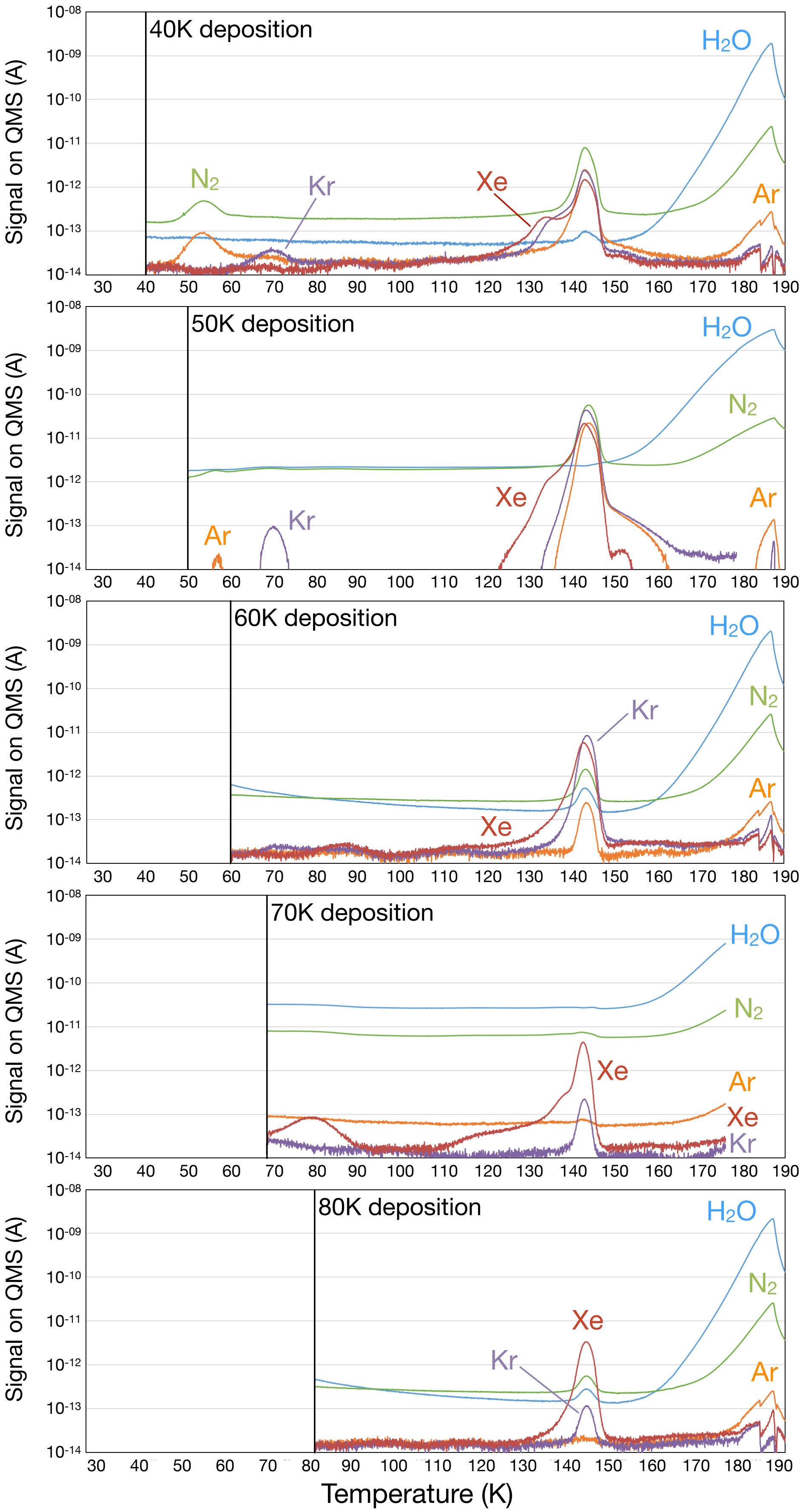
40K deposition
50K deposition
60K deposition
70K deposition
80K deposition
H2O
N2
Kr
Xe
Ar
Signal on QMS (A)
10-08
10-09
10-10
10-11
10-12
10-13
10-14
30
40
50
60
70
80
90
100
110
120
130
140
150
160
170
180
190
Temperature (K)

Figure A5. Experiments of H_2O:N_2:Ar:Kr:Xe mixtures deposited on the cold plate at 40 K, 50 K, 60 K, 70 K and 80 K, respectively, and warmed up at 190 K. When temperature of deposition increases the amount of gas trapped, and released around 140 K, decreases. The background level of H_2O and N_2 is higher for experiments at 50 K and 70 K before the filament of the QMS was replaced. This did not affect the enrichment ratio values given in Table 1.

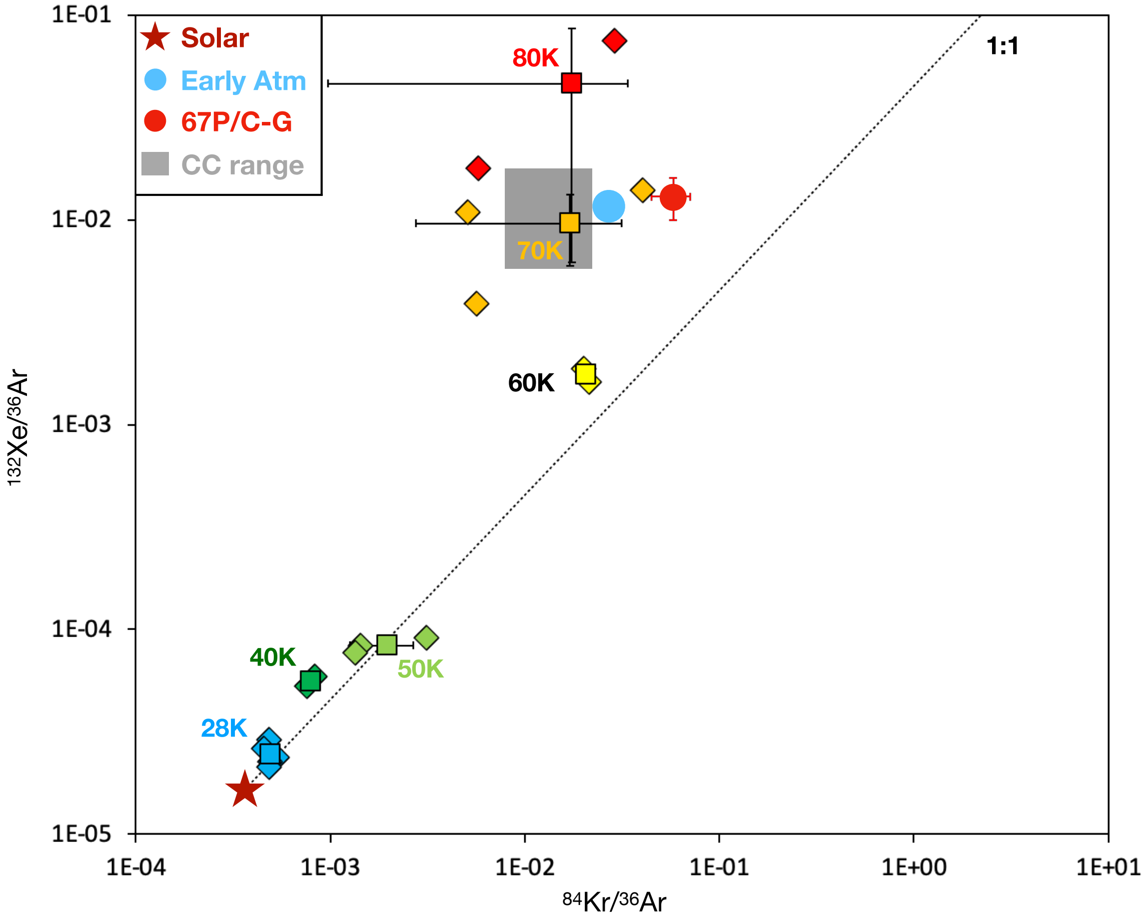

Figure A6. Plot of ^{84}Kr/^{36}Ar vs ^{132}Xe/^{36}Ar with several notable cosmochemical endmembers: Solar (Lodders 2003; Meshik et al. 2014), CC grey box (range of the carbonaceous chondrite compositions, compilation from Bekaert et al. 2020), 67P/C-G (comet 67P/Churyumov-Gerasimenko, Rubin et al. 2018) and Early Atm (initial Earth atmospheric composition before Xe loss, Zahnle et al. 2018). Diamonds show the composition of experimental cometary ices if formed from a solar composition at various temperatures of formation. Squares are the average obtained for each temperature of deposition. Error bars represent the standard error of the repeated experiments for one temperature of formation at 1 σ. Lines between symbols are for visual aid only.

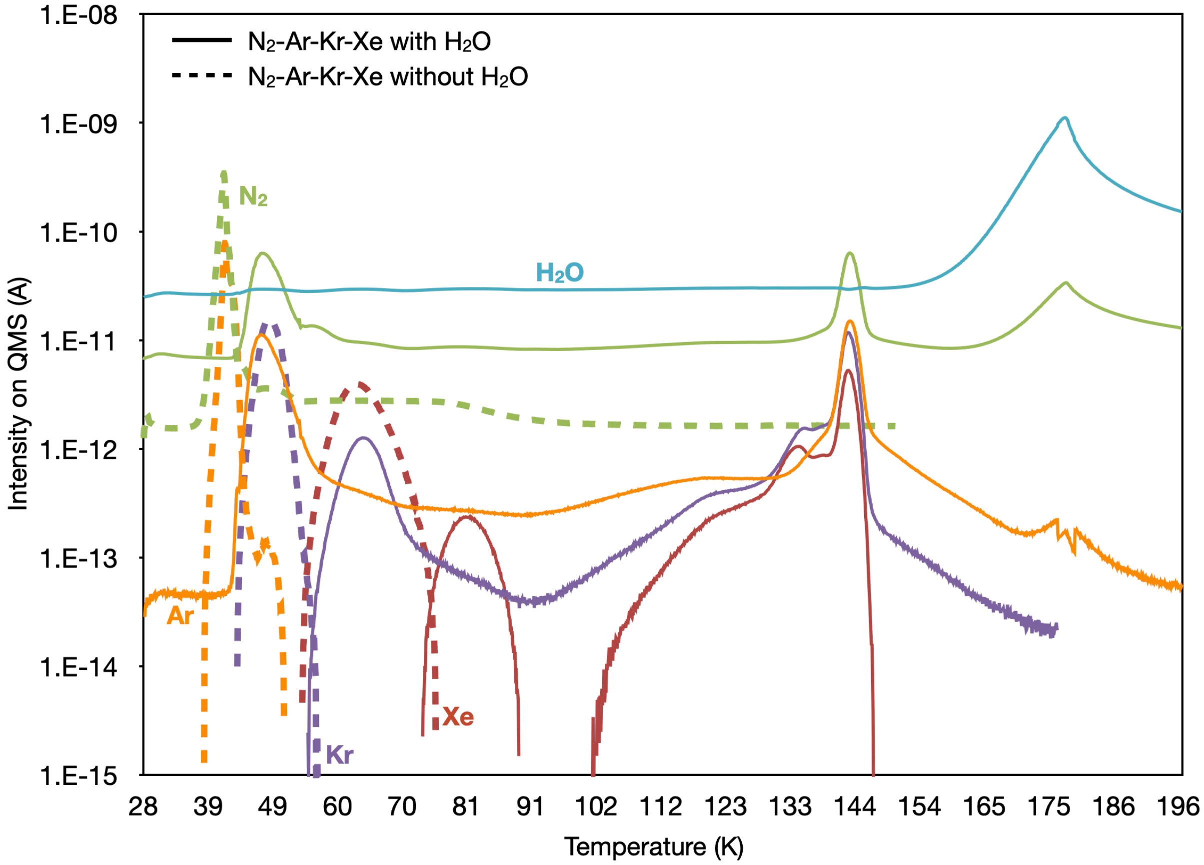

Figure A7. N_2 and noble gas release during the heating up from 28 K to 200 K at a rate of 1 K/min in two experiments (i) full line: deposited with water (similar to Figure 3) and (ii) dashed line: without water. In the experiment without water, the sublimation temperature of N_2, Ar, Kr and Xe are shifted toward lower temperatures.

References

Bekaert, D. V., Broadley, M. W., & Marty, B. 2020, NatSR, 10, 1

Lodders, K. 2003, ApJ, 591, 1220

Meshik, A., Hohenberg, C., Pravdivtseva, O., & Burnett, D. 2014, GeCoA, 127, 326

Rubin, M., Altwegg, K., Balsiger, H., et al. 2018, SciA, 4, eaar6297

Sebree, J. A., Wayson, J. M., & Lopez, J.R. 2018, J. Photochem Photobiol A, 360, 1

Zahnle, K. J., Gacesa, M., & Catling, D. C. 2018, GeCoA, 244, 56

III. The Effect of Irradiation on Trapped Volatile Behaviour

Within a dense molecular cloud, ices will at some point start to form at the surface of the grains, at which point they may be exposed to photon irradiation from neighbouring stars (Öberg & Bergin 2021). Ices in the outer parts of the protosolar nebula may also have been exposed to photon irradiation directly from the Sun, if they are sufficiently above (or below) the midplane of the protoplanetary disk (see Figure 1.3). The most abundant energic photons emitted from the Sun have a wavelength around 121.5 nm (10.2 eV), corresponding to the Lyman-alpha (Ly-α) wavelength. These photons are emitted when an excited atom of hydrogen transitions back to its fundamental state. While noble gases are not directly ionised during irradiation by Ly-α photons (Xe has the lowest first ionisation potential amongst noble gases and nitrogen at around 12.13 eV), irradiation can affect the structure of amorphous water ice and its compaction state (Yabushita et al. 2013). When subject to irradiation by energetic particles (ions at hundreds of keV, Raut et al. (2008), or electrons ~2 keV, Mifsud et al. (2022)), the porosity of amorphous ice has been shown to decrease, and therefore it has been suggested that its capacity to trap guest volatile species is also reduced (Palumbo 2006). This was demonstrated by Palumbo (2006), who showed that the potential for CO to diffuse into water ice was greatly diminished if the ice was pre-irradiated by protons, likely due to a reduction in the porosity of the ice. Irradiation with Ly-α photons has also been shown to reduce ice porosity (Palumbo et al. 2010), but its effect on volatile trapping and retention in water ice still has not been evaluated. I therefore set out to investigate the potential for irradiation to induce chemical interaction and elemental (or isotopic, as discussed in Chapter 4) fractionation of noble gases in water ice. Section III.1 presents the results on the effect of photon irradiation (~ 110 to 200 nm) during the formation of the ice on the N_2-Kr-Xe/Ar ratios of the trapped phase, for various temperatures of formation. Section III.2 shows the effect that irradiating the surface of ice has on the release pattern of noble gases.

1) Irradiation During Ice Formation

i. Method and Results

As presented in Almayrac et al. (2022), the EXCITING setup is equipped with a deuterium lamp, positioned below the horizontal cold plate that can emit photons with ultra-violet wavelengths. The wavelengths of the photons range between 120 nm and 200 nm, with peaks at 121 and 124 nm (Ly-α reproducing solar irradiation), and 160 nm (10.2 eV, 9.8 eV and 7.7 eV, respectively). The effect of irradiation on the trapping efficiency of nitrogen and noble gases was investigated for three temperatures of deposition: 28K (Figure 3.8), 50K and 70K. During the five minutes of co-deposition of N_2:Ar:Kr:Xe-H_2O mixtures, the surface of the cold plate and the flowing gas were irradiated by the photon lamp. Once the ice is formed and the lamp turned off, the ice is heated at 1K/min and the gas released from the cryogenic system is analysed on the QMS.

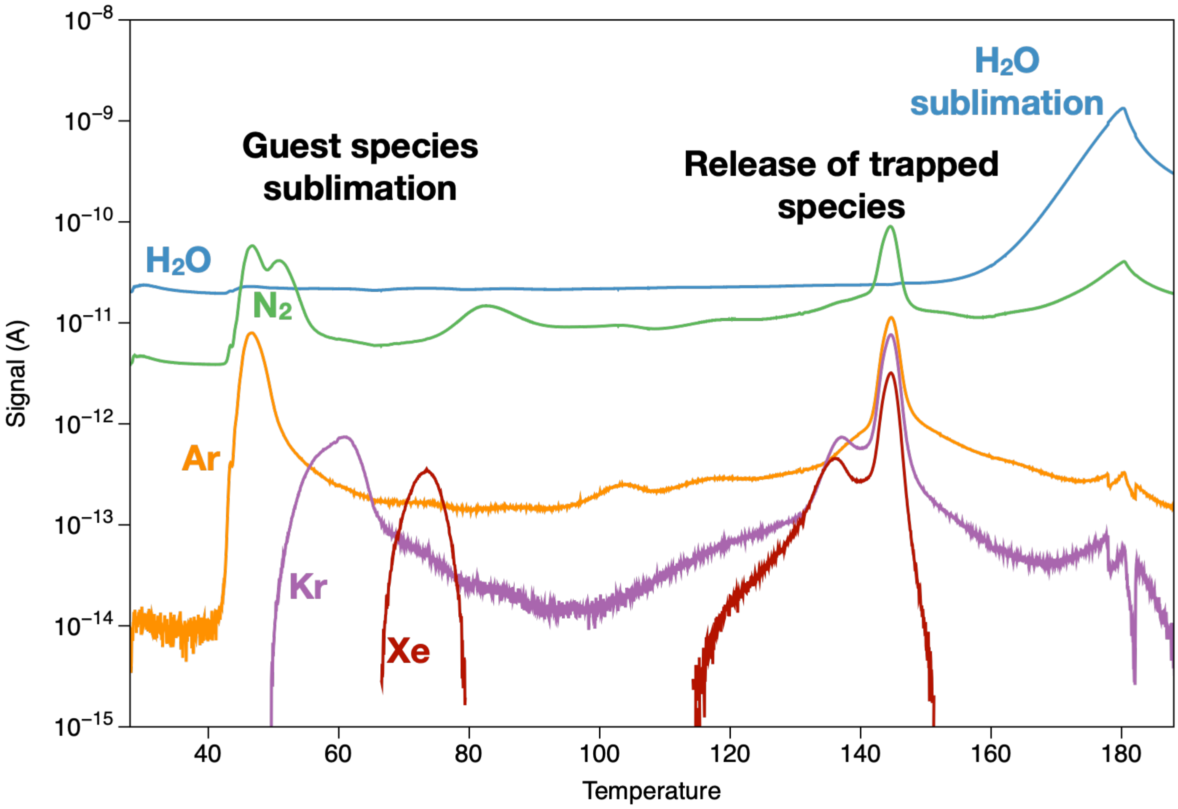

Figure 3.8: Evolution of gas release from a H_2O:N_2:Ar:Kr:Xe ice deposited at 28K with UV irradiation and heated to 190K at a rate of 1 K/min. A fraction of each guest species is frozen on, or below, the ice and sublimates at the respective sublimation temperature, while the trapped fractions are released simultaneously at around 145K, before water starts sublimating at 160K. At first glance, the release pattern appears similar to experiment without irradiation (Figure 3.4).

The relative abundances of N_2, Ar, Kr and Xe are reported in Table 3.2. The reported ratios are calculated by considering only the trapped phase, by integrating the release curves between 100K and 155K. We only consider the trapped phase so we can compare the results with previous studies (Bar-Nun and Owen 1998; Notesco et al. 2003; Almayrac et al. 2022).

Also, we assume that in realistic conditions of comet formation (slower deposition rates and smaller amounts of noble gases and N_2 relative to water) the frozen phases would be either negligible compared to the trapped phase (Notesco et al. 2003; Almayrac et al. 2022), or lost early in the lifetime of the comet (Gkotsinas et al. 2022). Interestingly, the Kr/Ar, Xe/Ar and N_2/Ar ratios of the trapped phase when the gas is irradiated during the formation of the ice (Table 3.2) are comparable to the ratios for experiments without irradiation (Almayrac et al. 2022).

Table 3.2: Elemental ratios of Kr-Xe-N_2/Ar measured in the trapped phase depending on the temperature of deposition of the amorphous ice (28K, 50K and 70K) under irradiation. These ratios are computed by integrating the signal of each element between 100K and 155K during the heating phase. The "enrichment ratios" were obtained by dividing the trapped X/Ar by the X/Ar ratio in the initial gas mixture (where X = Kr, Xe or N_2). Averages of the repeated experiments are given with the associated standard error (standard deviation divided by $\sqrt{n-1}$, where n is the number of repeats).

Deposition Temperature	**#**	**Gases trapped in the ice**			**Enrichment ratio in trapped gas** (relative to the initial gas composition)		
		Kr/Ar	**Xe/Ar**	**N_2/Ar**	**Kr/Ar**	**Xe/Ar**	**N_2/Ar**
28K	1	0.722	0.347	9.03	1.18	1.04	1.99
	2	0.669	0.428	7.51	1.21	1.54	1.90
	3	0.674	0.422	5.76	1.22	1.53	1.50
Average 28K		**0.689**	**0.399**	**7.433**	**1.21**	**1.37**	**1.79**
	±	**0.021**	**0.032**	**1.159**	**0.015**	**0.201**	**0.186**
50K	1	1.98	1.52	4.08	3.74	6.03	0.997
	2	3.36	2.33	2.50	6.35	9.26	0.610
Average 50K		**2.87**	**1.28**	**2.46**	**5.05**	**7.64**	**0.803**
	±	**1.03**	**0.08**	**0.04**	**1.85**	**2.28**	**0.274**
70K	1	20.4	134	35.8	38.5	533	8.74
	2	27.8	132	28.9	52.5	522	7.07
Average 70K		**24.1**	**133**	**32.4**	**45.5**	**528**	**7.91**
	±	**5.2**	**2**	**4.8**	**9.9**	**8**	**1.18**

ii. Discussion

The elemental ratios of noble gases trapped in ice formed in an irradiation environment across various temperatures of deposition are presented Figure 3.9 and are identical within uncertainties to non-irradiated ice analogues (Almayrac et al. 2022). These ratios (^{84}Kr/^{36}Ar and ^{132}Xe/^{36}Ar) are computed by considering a starting solar isotopic composition (Meshik et al. 2014) and the enrichment ratios given in Table 3.2. Irradiating the gas during its condensation into ice with Ly-α photons does not affect the relative trapping efficiency of Ar, Kr and Xe into water ice.

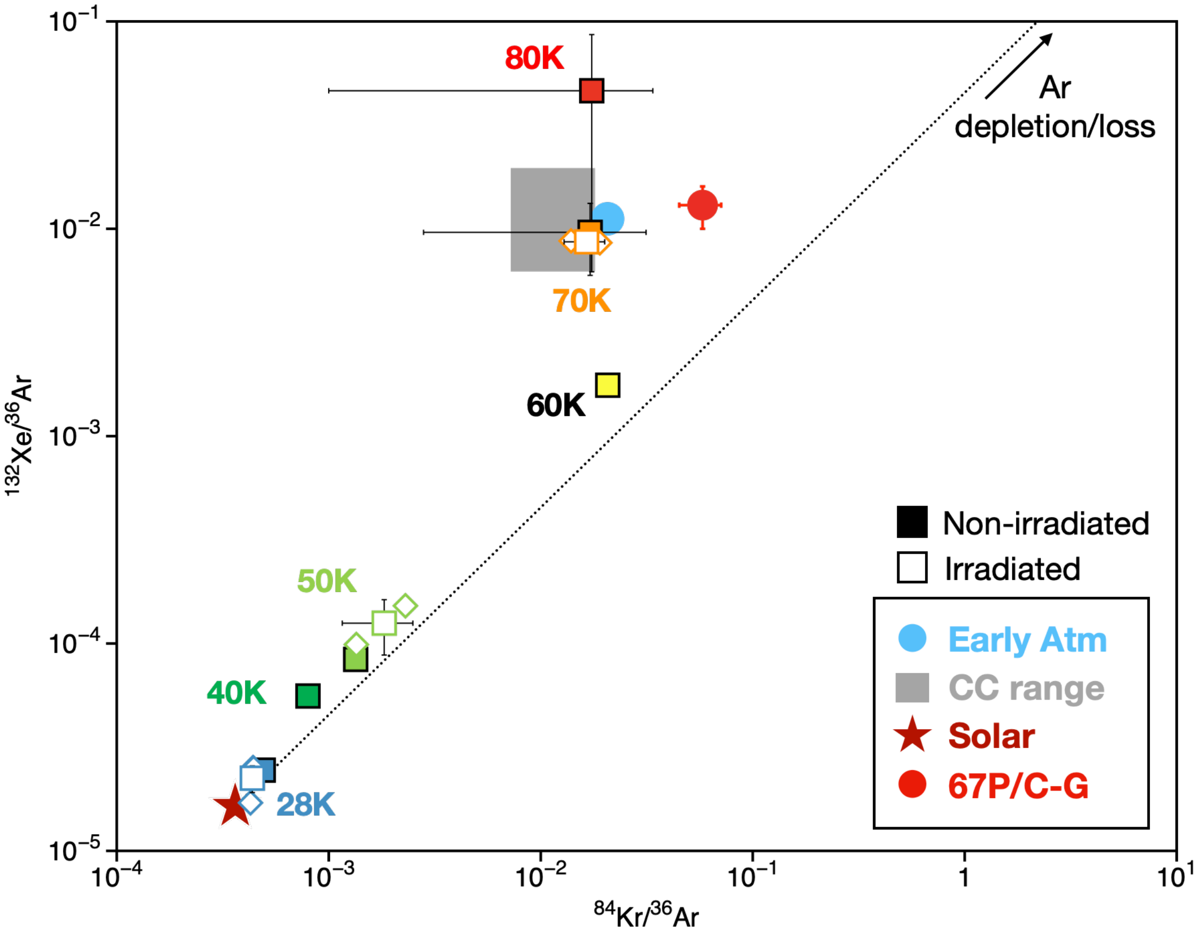

Figure 3.9: Three isotope plot of ^{84}Kr/^{36}Ar vs ^{132}Xe/^{36}Ar with several notable cosmochemical endmembers: Solar (Lodders 2003; Meshik et al. 2014), CC grey box (range of the carbonaceous chondrite compositions, compilation from Bekaert et al. 2020), 67P/C-G (comet 67P/Churyumov-Gerasimenko, Rubin et al. 2018) and Early Atm (initial Earth atmospheric composition before Xe loss, Zahnle et al. 2018). Filled squares show the composition of experimental cometary ices if formed from a solar composition at various temperatures of formation (Almayrac et al. 2022). Open symbols are the composition of such ices when they are submitted to photon irradiation during their formation at 28K, 50K and 70K. Open squares are the averages of the open diamonds, error bars represent the standard error at 1σ. The noble gas composition of irradiated ices is not significantly different from the non-irradiated ices.

Irradiating amorphous ice with energic particles reduces its porosity (Palumbo et al. 2010) and therefore likely its capacity to guest volatile species (demonstrated with CO, Palumbo 2006). However, photon irradiation during deposition, as performed in this study, appears to have only a limited effect on the relative abundances of noble gases (Figure 3.9), and nitrogen (Figure 3.10) trapped in the ice. The absolute trapping efficiency of a given species (its ratios over water) also appears to be unaffected by irradiation (similar abundances on Figure 3.8 and Figure 3.4), although less "robust" because the water to guest species ratios of an experiment are less reproducible than the elemental ratios of nitrogen and noble gases. The limited effect of photon irradiation on noble gas trapping could result from the short deposition time, preventing an efficient compaction of the ice and its porosity. Also, because nitrogen and noble gases are co-deposited with water, they are trapped before the ice compaction occurs. This experiment therefore differs from that of Palumbo (2006), which deposited CO directly onto pre-irradiated ice. This would suggest that irradiation of gas species during their condensation has less of an effect on volatile trapping efficiencies of water ice than when the surface of the ice itself is irradiated. Experiments with irradiation after ice deposition will therefore provide further information on how trapped species behave when the ice is compacted (section 3.III.2.).

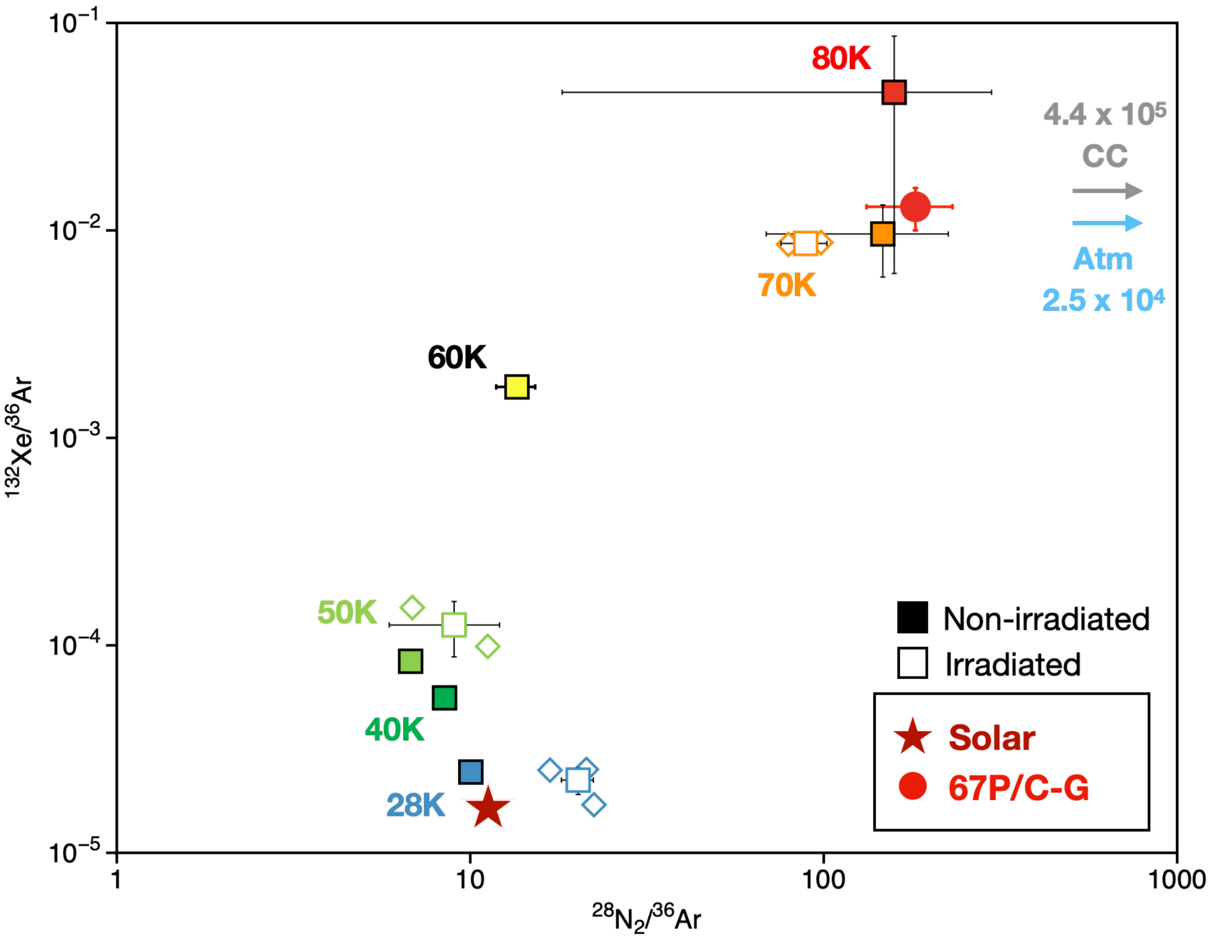

Figure 3.10: Three isotope plot of $N_2/^{36}Ar$ vs $^{132}Xe/^{36}Ar$ of the experimental ices considering a solar-like starting composition and various temperatures of formation. Cosmochemical endmembers are the same as in Figure 3.9. Filled squares are non-irradiation ices (Almayrac et al. 2022), and open symbols are ices formed under irradiation at 28K, 50K and 70K. Only when ice forms at 28K the $N_2/^{36}Ar$ ratio of the ice appears to be potentially affected by irradiation. Although the data are blank corrected, a contribution from an increase in the CO background during irradiation cannot be excluded.

2) Irradiating the Ice Surface

i. Method

In order to investigate the effect of irradiation on the surface of the ice following its deposition, two different gas mixtures, H_2O:Xe, with mixing ratio ~ 10:1 and H_2O:N_2:Ar:Kr:Xe (hereafter H_2O:NG), with mixing ratio ~ 5:5:1:1:1, were condensed onto the cold plate at 28K. The ice was then heated from 28K to 120K at a rate of 1K/min. Once at 120K, the ice sample was maintained at this temperature for 35 minutes, and the surface of the ice was irradiated using the photon lamp. The temperature of 120K was arbitrarily chosen because it precedes the transition from amorphous to crystalline ice and the release of gas. Following the irradiation, the ice was then heated to 190K at 1K/min. During the whole experiment (from 28K to 190K), the composition of the gas released from the ice was analysed on the QMS. The same experiment was also performed (for both the H_2O:Xe and H_2O:NG ices) with no irradiation during the 35 minutes at 120K, to properly identify the effect of irradiation on volatile release.

ii. Results

The gas release from the ice was monitored by the QMS between 28K and 200K. During the warm up of the ice between 28K and 120K, species (Xe for the H_2O:Xe mixture, and N_2, Ar, Kr, Xe for the H_2O:NG mixture) that have not been trapped in the amorphous water ice lattice sublimate, as observed in Almayrac et al. (2022). During the 35 minutes irradiation at 120K, no significant release above the background level is observed, suggesting that irradiation does not directly lead to gas loss from ice. Figures 3.11 and 3.12 focus on the release pattern of trapped species above 120K, after irradiation (or not) of the surface of the ice. It is observed that xenon is released from the non-irradiated H_2O:Xe ice between 125K and 150K, with a peak at 145K (Figure 3.11). This temperature range corresponds to the transition of amorphous ice I_a to its crystalline cubic form I_c, releasing all the Xe initially trapped in the pores of I_a (Bar-Nun et al. 1987). In the case where irradiation is performed at 120K (dotted and dashed lines in Figure 3.11), a significantly smaller release of Xe occurs between 125K and 150K than is observed for the non-irradiated ice. After the I_a-I_c transition, the remaining Xe continues to be released from the water ice, until it is all released at the point of water sublimation around 190K. We observe two peaks of release around 152K and 164K, with similar amplitudes as the first peak at 145K that corresponds to the I_a-I_c transition. These two additional peaks observed for the irradiated ice coincide with the transition from cubic ice I_c to hexagonal ice I_h (Jenniskens & Blake 1994; Notesco & Bar-Nun 2005). This is also supported by Sugisaki et al. (1969) who observed that the I_c-I_h transition occurs in two steps, as suggested here by the two Xe release peaks. Finally, the total amount of Xe trapped (and released) from the H_2O:Xe ice (calculated by integrating the Xe release between 120K and 190K) is the same (to within ± 1%) between the irradiated and the non-irradiated experiment.

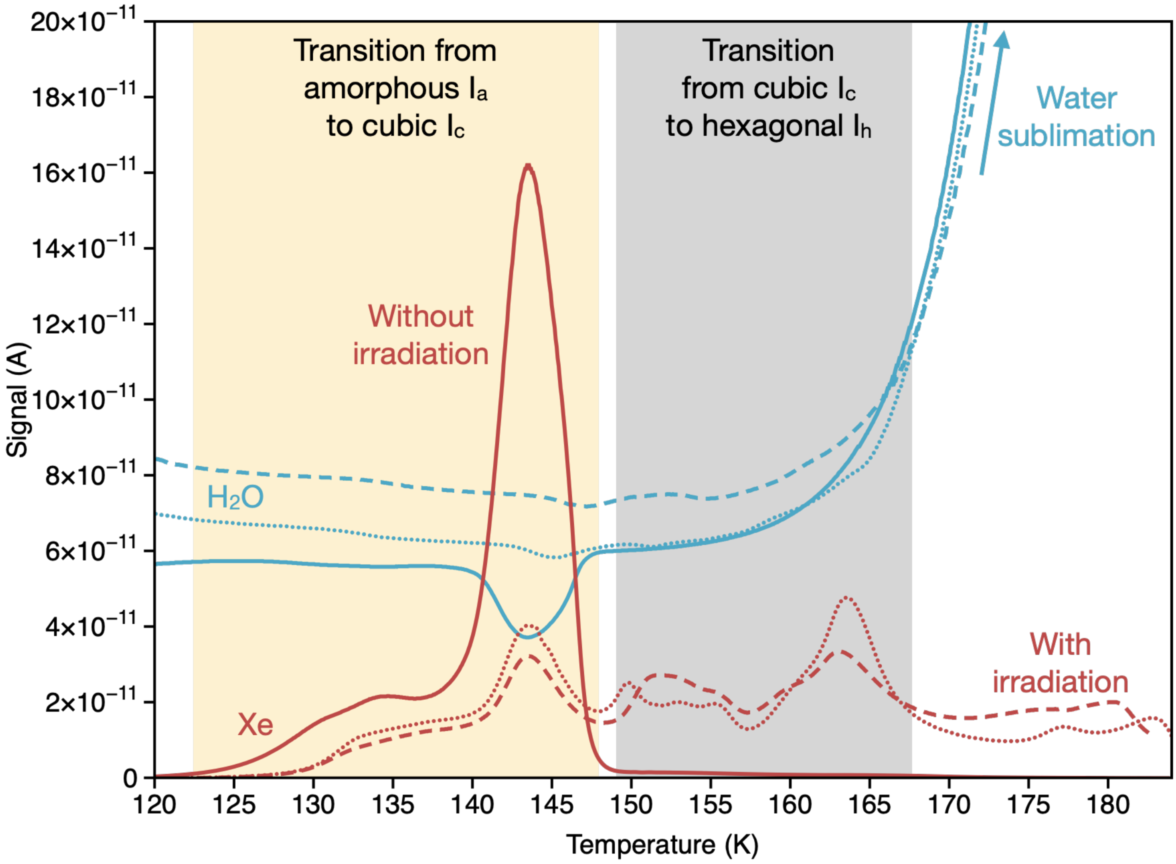

Figure 3.11: Evolution of Xe (red) and water (blue) signals measured by the QMS between 120K and 185K, for an ice (H_2O:Xe = 10:1) formed at 28K and heated at 1K/min. The ice was warmed up to 120K, and maintained at this temperature during 30 minutes, while irradiating (dashed and dotted lines) or not (solid lines) the ice surface using the photon lamp. After 30 minutes at 120K (with or without irradiation), the ice was warmed up to 185K at the same rate. As discussed in the text, we observe that the Xe release pattern is affected when the ice surface has been irradiated. The total amount of Xe trapped and released from the H_2O ice (integrated surface under the curves) is however the same for both cases to within ± 1%.

A similar retention of the trapped species in the ice structure even after the I_a-I_c transition when the ice surface has been irradiated is observed for Xe and NG ice, as shown in Figure 3.11 and 3.12. The I_c-to-I_h transition can also be identified by the simultaneous release of trapped species between ~147K and 165K. The two-step transition into hexagonal ice (Sugisaki et al. 1969) is also highlighted by the two-step release of volatiles with peaks at ~148K and ~158K. For both H_2O:Xe and H_2O:NG ices, trapped species continue to be released until the total sublimation of water ice.

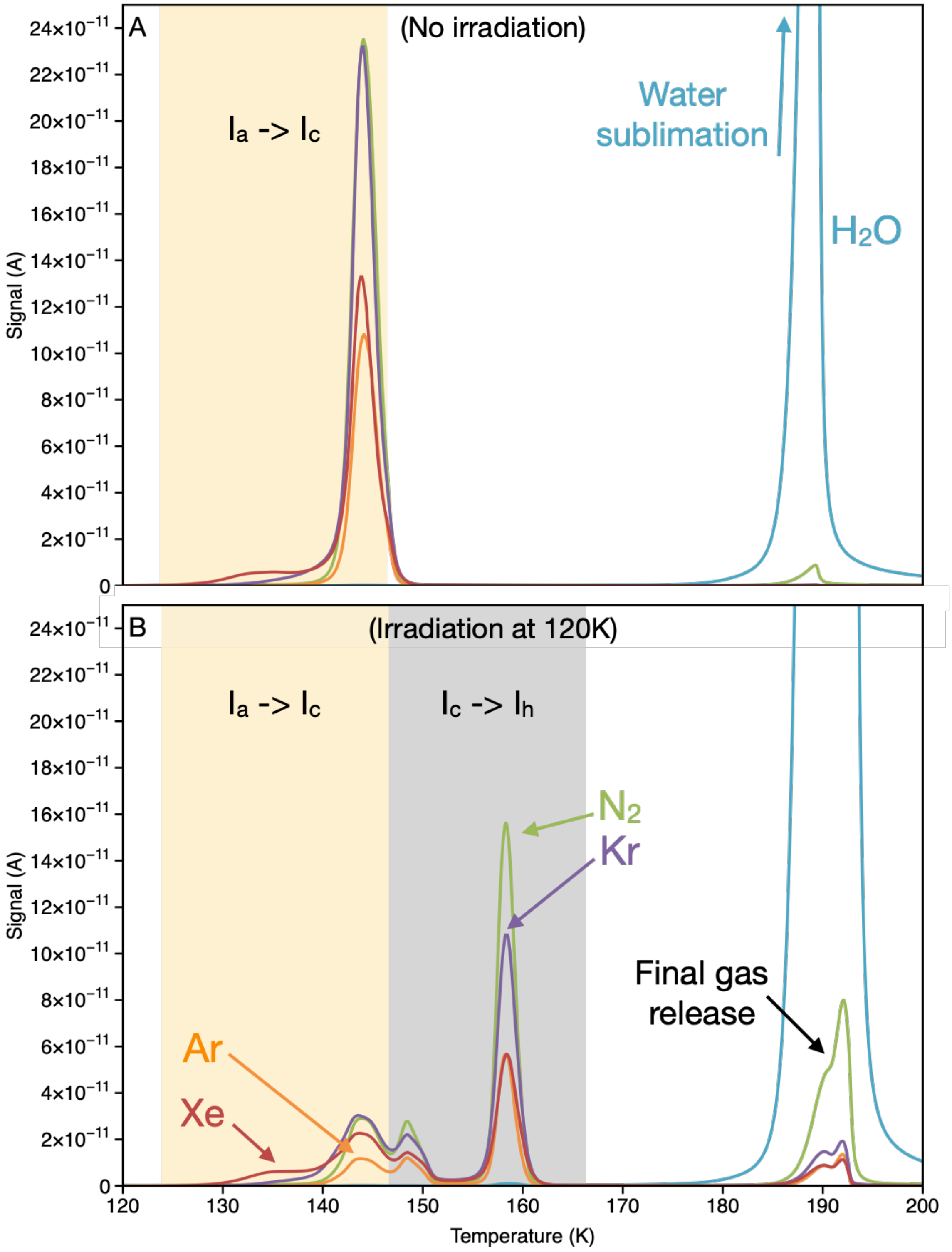

Figure 3.12: Same experimental procedure as Figure 3.11 but with an initial N_2:Ar:Kr:Xe:H_2O mixture. **A.** Non-irradiated ice. The peach-coloured area corresponds to the transition from amorphous I_a to cubic ice I_c. H_2O in blue, N_2 in green, Ar in orange, Kr in purple, Xe in red. **B.** Ice irradiated at 120K for 35 minutes. The grey area is from cubic I_c to hexagonal I_h. The irradiated ice shows a different volatile release pattern than the non-irradiated ice, retaining volatiles in the ice structure above the I_a to I_c transition.

iii. Implications

Photons typically penetrate the first ~100-300 nm of the ice (Cruz-Diaz et al. 2014) and thus presumably only affect the surface of the ice, without significantly interacting with volatiles trapped deeper within the ice. The transition from amorphous to cubic ice rearranges the water molecules and creates open channels through which trapped volatiles may escape the ice (Bar-Nun et al. 1987). Photon irradiation results in a compaction of the ice structure, reducing the overall porosity of the amorphous ice (Palumbo et al. 2010). Additionally, the irradiation of ice by photons appears to decrease the viscosity of the ice (Tachibana et al. 2017) and could potentially increase the diffusivity of gases within the ice. However, in the present experiments, where noble gases and nitrogen are already present in the pores of the ice, it appears that no gas is released from the ice during irradiation. On the contrary, irradiation resulted in a stronger retention of trapped gas by the ice, since the I_a-to-I_c transition does not liberate all the gas, as observed Figures 3.11 and 3.12. One possibility is that the formation of open channels (for the gas to diffuse through) is limited by the compaction of the ice surface, and that only further transformation (from I_c to I_h, and until the sublimation of water, Figure 3.12) of the ice permits the total release of the gas (Figure 3.13). Interestingly, ices in these experiments are presumably thicker (<5 µm, Almayrac et al. 2022) than the average photon penetration, indicating that even a surficial irradiation affects the behaviour of the whole trapped phase. The surface of ice coated grains is continually exposed to irradiated environments, and typically accumulates a photon dose of 1.6 x 10^{20} photons/cm^2 over their lifetime in the Solar System before their agglomeration into comets (Ciesla & Sandford 2012). The UV lamp used on EXCITING has a UV fluence that can be approximated around 1 x 10^{14} photons/cm^2/s, based on experiments using similar lamps (Piani et al. 2017). Given this fluence, the lamp would need to be turned on for 570 hours to reproduce the average UV dose received by natural cometary ices. With the EXCITING experiment, we show that irradiating the ice surface for only 35 minutes (UV dose of ~1 x 10^{17} photons/cm^2) significantly affects the ice and the gas behaviour. This suggests that cometary ice irradiation in natural environments may contribute to increase their volatile retention rates upon ice warming, up to water ice sublimation temperature.

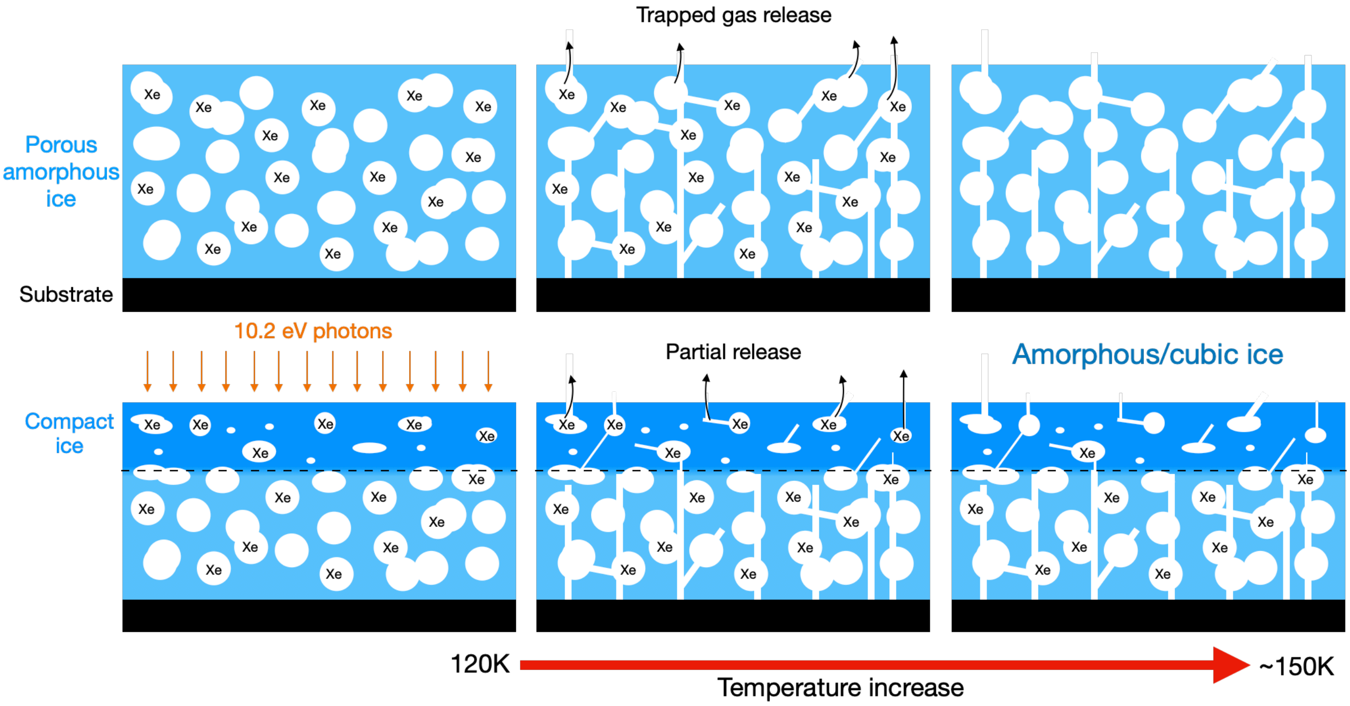

Figure 3.13: Schematic of gas release from amorphous water ice with or without photon irradiation at 120K. The irradiation compacts the ice, resulting in shorter and fewer open channels during the I_a-to-I_c transition for the trapped gas to escape.

Finally, the total amount of gas released from the ice (Xe for the H_2O:Xe ice, and N_2 and noble gases for the H_2O:NG ice) is the same between the non-irradiated and irradiated ice. However, for the H_2O:NG ice, one can observe on Figure 3.12 that the relative abundances between nitrogen and noble gases differ depending on the range of release temperatures. The release of trapped species can be divided into three ranges/steps, from ~120K to ~146K (amorphous to cubic transition), from ~147K to 165K (cubic to hexagonal), and from ~166K to 200K (water sublimation), as displayed in Figure 3.12. By computing the enrichment ratios of the gas in each temperature range, the final compositions considering starting solar-like abundances are calculated and presented on Figure 3.14. The elemental ratios N_2/Ar, Kr/Ar and Xe/Ar of the total trapped phase in the irradiated and non-irradiated ices are the same (within the inherent reproducibility of the EXCITING experiment). For the irradiated ice, the three spikes in gas release show variability (Figure 3.14), but this is limited when compared to the variability observed between experiments performed at various temperatures of deposition (Bar-Nun et al. 1998; Notesco et al. 2003; Almayrac et al. 2022).

As of yet, no experiments have been performed which combine both irradiation during, (section 3.III.1) and after (this section 3.III.2) deposition, however it is unlikely that irradiation of the ice during deposition would lead to a significantly different outcome that observed in Figure 3.14. Although irradiation of water ice surfaces can cause a significant change in the release profiles of trapped volatile species, it is important to note that elemental ratios are relatively consistent across all major release peaks (Figure 3.14). This observation implies that comparing experimental results with measurements of the coma of comet 67P/C-G, which is made up of gas released from across a variety of temperature and from different depths (Prialnik et al. 2008), is still relevant. More importantly, as shown in this experiment, the irradiation of ice and the associated reduction in porosity can delay the release of trapped volatile species from amorphous water ice. This may have important implications regarding the retention of trapped volatiles species within comets, with volatiles potentially remaining trapped within cometary ice even at temperatures above the amorphous to crystalline water ice transition (~140K).

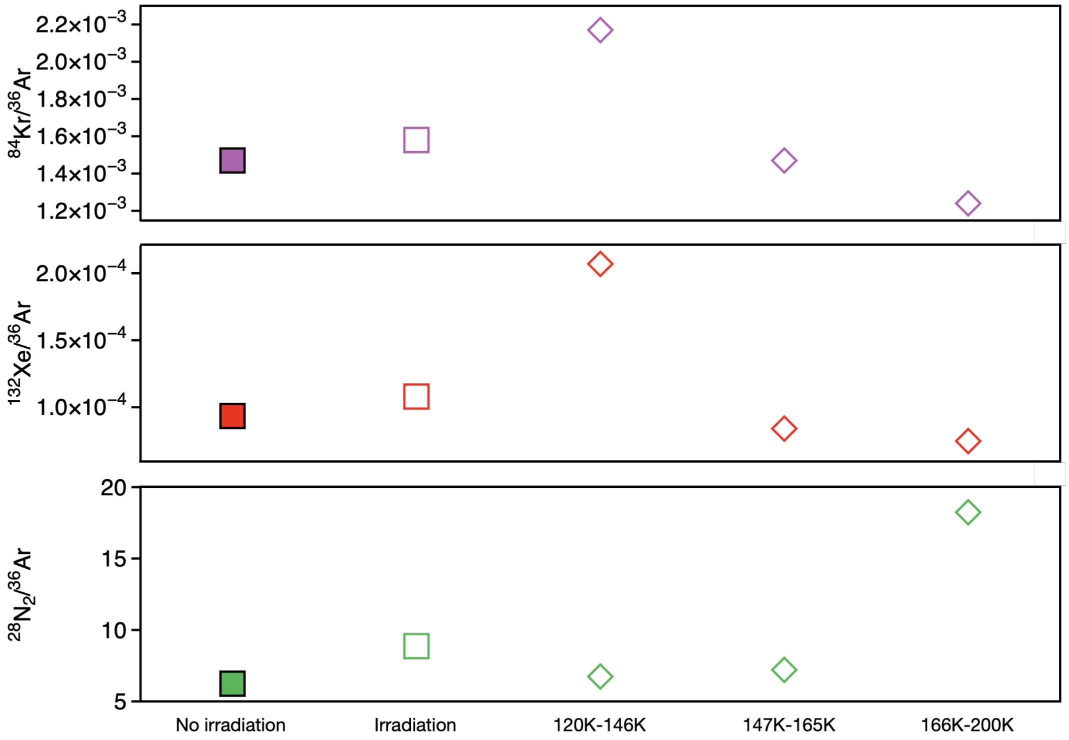

Figure 3.14: Elemental ratios of nitrogen and noble gases contained in the ice analogues considering an initial solar-like composition. Squares show the composition of the whole trapped phase with (open symbols) or without (filled symbols) irradiation of the surface at 120K. Open diamonds show the composition of the individual release of gas for the irradiated ice, as observed on Figure 3.12.

IV. Conclusion

This chapter presents the results obtained with the EXCITING experiment on the elemental behaviour of nitrogen and noble gases (Ar, Kr and Xe) cometary water ice analogues. Several temperatures of formation were tested, 28K, 40K, 50K, 60K, 70K and 80K, to quantify the elemental fractionation of the Kr/Ar, Xe/Ar and N_2/Ar ratios trapped in the ice relative to their initial composition in the gas phase. These relative abundances were calculated by measuring the composition of the gas released from the ice upon warming by using a quadrupole mass spectrometer. We find that if we consider the initial gas to be solar in composition, forming ices at ~ 70K-80K better reproduce the nitrogen and noble gas composition of comet 67P/C-G (Section II, Almayrac et al. 2022).

Similar experiments were performed by simultaneously irradiating the depositing gas with UV photons, at three different temperatures of deposition, 28K, 50K and 70K. We find that irradiating nitrogen and noble gases during their deposition and trapping into water ice does not affect their relative trapping efficiency (Section III.1). This however should be explored for longer irradiation exposure (and thus slower deposition rates to obtain comparable ices).

Finally, the effect of ice compaction by photon irradiation (after the formation of the ice and the trapping of noble gases) on the release behaviour of noble gases was investigated. We find that compaction does not release the guest species, and instead increases the ice retention capacity of the guest species. While a non-irradiated ice liberates all its trapped volatiles during the transition from amorphous to cubic crystalline form, an irradiated ice preserves its volatiles even above this transition, and needs to fully sublimate to liberate them (Section III.2). The distinct gas releases from irradiated ices, however, have similar elemental ratios.

V. Perspectives and Further Work

These experiments have highlighted the importance of noble gases in understanding cometary formation environment, yet have raised many new questions on the effect of irradiation and noble gas behaviour in ice that remain unanswered. Here I outline the remaining gaps in our knowledge and set out potential experiments that could fill in these gaps in the future.

Irradiation during deposition experiments:

- Reducing the deposition rate, and having longer deposition times, in order to have longer exposition to irradiation and increase the potential for photons to (i) interact with noble gases and nitrogen, and (ii) further compact the ice and effect on the trapping efficiencies.

Irradiation of the surface:

- Investigating different temperatures of ice formation (up to 70K) and different irradiation exposition to identify if there is a dosage threshold.
    - For instance, extended irradiation could result in no gas being released by the I_a-I_c and I_c-I_h transitions, and only during water sublimation.
- Investigating the difference in noble gas ratios between the three steps of release (Figure 3.14) for different deposition temperatures.
- Reducing the amount of guest species sent to verify if similar patterns are also observed or if this is an effect of over-abundance of guest species relative to water, compared to cometary ratios.
    - Can be complicated to observe because the amounts of trapped gas are smaller for higher temperatures of deposition (only 28K tested here when the trapping is very efficient).

Irradiation during the deposition and the warm up of the ice:

- Once the possible effects mentioned above are better constrained, irradiating the ice from deposition to its sublimation will better reproduce real cometary ices evolution and provide further clues about the nature of the noble gases measured on comet 67P/C-G.

Investigating the diffusion of volatiles into irradiated ice (Palumbo 2006):

- Reproducing Palumbo (2006)'s experiment (ice irradiation by protons followed by CO deposition and subsequent diffusion into the ice pores), but with photon irradiation and noble gas diffusion into the ice porosity after its compaction.

Chapter 4

The Isotopic Fractionation of Noble Gases and Nitrogen in Cometary Ices

I. Introduction

The isotopic composition of comets, assuming that it has not been altered during thermal processing over their lifetime, can provide clues on their environment of formation (Bockelée-Morvan et al. 2015), as well as their role in delivering volatiles into the inner Solar System planets (Pepin 1991; Owen et al. 1992).

The high D/H composition of several Oort cloud comets (Bockelée-Morvan et al. 1998; Meier et al. 2006; Biver et al. 2006; Hutsémekers et al. 2008; Villanueva et al. 2009) about 2-3 times the terrestrial value (1.5576×10^{-4}, Hallis 2017) was an argument against a significant cometary contribution to terrestrial oceans. However, the identification of a terrestrial D/H in a Jupiter-family comet 103P/Hartley provided new evidence for a possible cometary contribution to Earth (Harthog et al. 2011). Later on, the measurement of high D/H in the coma of comet 67P/Churyumov-Gerasimenko (a Jupiter-family comet, hereafter 67P/C-G) by the ESA Rosetta spacecraft and the high D/H ratios measured in molecules other than water further argued against this proposition (Altwegg et al. 2015, Alexander et al. 2018).

If comets did not bring significant amounts of water to Earth, they might still have contributed other volatile elements present in our atmosphere such as the noble gases (Marty et al. 2017; Rubin et al 2018). Because noble gases are chemically inert, they do not take part in chemical or biological reactions that can modify the composition of other volatile species. Therefore, noble gases can retain a genetic fingerprint of their origin and can be used to trace the origin of other volatile species. The Xe isotopic composition measured in the coma of comet 67P/C-G has a peculiar isotope signature, similar to the solar composition (Meshik et al. 2014) except for ^{129}Xe, which is enriched by around +400‰, and for the two heaviest isotopes ^{134}Xe and ^{136}Xe that are depleted by around -400‰ and -600‰, respectively (Marty et al. 2017; the deviation from solar expressed in permil using the delta notation where δ^{i}Xe = (^{i}Xe/^{132}Xe$_{measured}$ / ^{i}Xe/^{132}Xe$_{solar}$ – 1) * 1000). The precursor of the Earth's atmospheric Xe (U-Xe, Pepin 1991) also presents deficits, to a lesser extent, of isotopes ^{134}Xe and ^{136}Xe. This was taken as evidence that comets contributed to the initial budget of noble gases on Earth, with around 20% of the Kr and Xe in Earth's atmosphere originating from a cometary reservoir (Marty et al. 2017; Rubin et al. 2018; Bekaert et al. 2020). The origin of this non-solar Xe signature is thought to be nucleosynthetic in nature and of a likely pre-solar origin, suggesting that cometary building blocks may have acquired their noble gas composition from a region in the Solar System which resisted homogenisation, and was therefore able to retain a unique pre-solar composition (Avice et al. 2020).

Similarly, the isotopic composition of nitrogen in comets is strongly enriched in the rarer ^{15}N isotope relative to the more abundant ^{14}N (high $^{15}N/^{14}N$ ratio), compared to the composition of Earth's atmosphere (used as a reference, with $^{15}N/^{14}N_{atm}$ = 0.003676, Nier, 1950 and $\delta^{15}N_{atm}$ = 0 ‰ by definition) or the solar composition ($\delta^{15}N$ = -407 ± 5 ‰, Marty et al. 2011). Indeed, comets are ^{15}N-rich bodies (~ +890 ± 40 ‰, average of multiple comets, Bockelée-Morvan et al. 2015; Hily-Blant et al. 2017, and references therein) as established by spectroscopy measurements from ground-based observation. Comet 67P/C-G is also rich in heavy nitrogen with $\delta^{15}N$ around +1000‰ (Altwegg et al. 2019), as measured in N_2, NO and NH_3 molecules present in the coma. The origin of this nitrogen isotope variability in comets, and more generally across Solar System bodies is a matter of debate (e.g., Terzieva & Herbst 2000; Rodgers & Charnley 2008; Heays et al. 2014; Füri & Marty 2015; Hily-Blant et al. 2017; Grewal 2022) and calls for further investigation on the processes that can fractionate N isotopes.

In this study, we investigate how N_2, Xe and Ar isotopes evolve during their incorporation into cometary water ice analogues by using the EXCITING setup (Almayrac et al. 2022). These experiments aim at quantifying the degree of isotope fractionation of volatile elements caused by their trapping in amorphous water ice, and after being subject to photon irradiation. Several temperatures of formation are considered (28K, 50K and 70K). A specific focus at the formation temperature of 50K was decided in order to increase the possibility for Ar and N isotope fractionation (Notesco et al. 1999), and still trap sufficient amount of gas to perform isotope analyses (N_2 and Ar are highly depleted when ices are formed >70K, Almayrac et al. 2022). Here I present the first precise isotope measurement of N_2 and noble gases in cometary ices analogues, by using static noble gas mass spectrometry techniques. A pioneering work by Notesco et al. 1999 also investigated noble gases isotopes in ice analogues, using a quadrupole mass spectrometer, with limited precision on the order of three times lower than achieved in this study.

II. Methods

1) Forming the Ice and Generating Gas Samples

The EXCITING experimental setup as described in Almayrac et al. (2022), and shown in Figure 2.6, was used to create ices made of water, N_2, Ar, Kr and Xe. Mixtures of $H_2O:N_2:Ar:Kr:Xe = 50:5:1:1:1$ were deposited onto a cold plate inside a cryogenic system. The deposition of the gas was performed under dynamic pumping mode by a turbo-molecular pump reaching ~ 10^{-8} mbar in the system. Deposition temperatures of 28K, 50K and 70K were investigated. The gas was deposited over 5 minutes, and the ice thickness was in the order of the µm (see Almayrac et al. (2022) with identical deposition protocol as in the present study).

After ice deposition, the plate was warmed up at a rate of 1K/min. A schematic description of the sampling method is given in Figure 4.1. During the warm up of the ice between the temperature of deposition (28K, 50K or 70K) and 95K, the pumps were closed and the system was left in static mode. Any nitrogen and noble gases frozen on the ice will sublimate and accumulate in the experimental volume. When the temperature reached 95K, the accumulated gas (N_2, Ar, Kr and Xe) was sampled by closing a steel tube bottle attached to the setup (Figure 2.6). This gas sample represents the frozen phase. Once the bottle closed, the system was temporarily switched back to dynamic mode by opening the pump between 95K and 100K, in order to remove the accumulated gas from the system. At 100K, the system was set to static again to accumulate this time gas released from the ice that was trapped in the pores of the amorphous water ice. Once the temperature reached 155K, the accumulated gas was sampled in a second steel bottle; this sample represents the trapped phase. These temperature ranges were chosen based on our observations on the timing of sublimation (frozen N_2, Ar, Kr and Xe) and liberation of trapped gas during the amorphous to crystalline ice transition (Almayrac et al. 2022, Figure 3.4).

An additional set of experiments was performed at 50K while irradiating the ice with UV photons (from a H2D2 lamp, peaks at Lyman-α 121.5 nm, and 160 nm, see Chapter 2). The lamp was switched on during the 5 minutes of deposition and for a further 5 minutes after deposition, before warming up the ice. The ice surface was irradiated after its formation to reproduce the release pattern observed in Chapter 3 (Section 3.III.2 irradiating the ice surface) where the trapped phase release is divided into an "early" trapped phase (<155K) and a "late" trapped phase (>160K). The irradiation lasted only 5 minutes before the warm up of the ice in order to allow comparison with non-irradiated ices, for which warm up began directly after the deposition was stopped. Preliminary results and tests on the dosage threshold of irradiation affecting the trapped phase release pattern showed that irradiation periods as short as 5 minutes already have an effect on the ice (Appendix Figure A2).

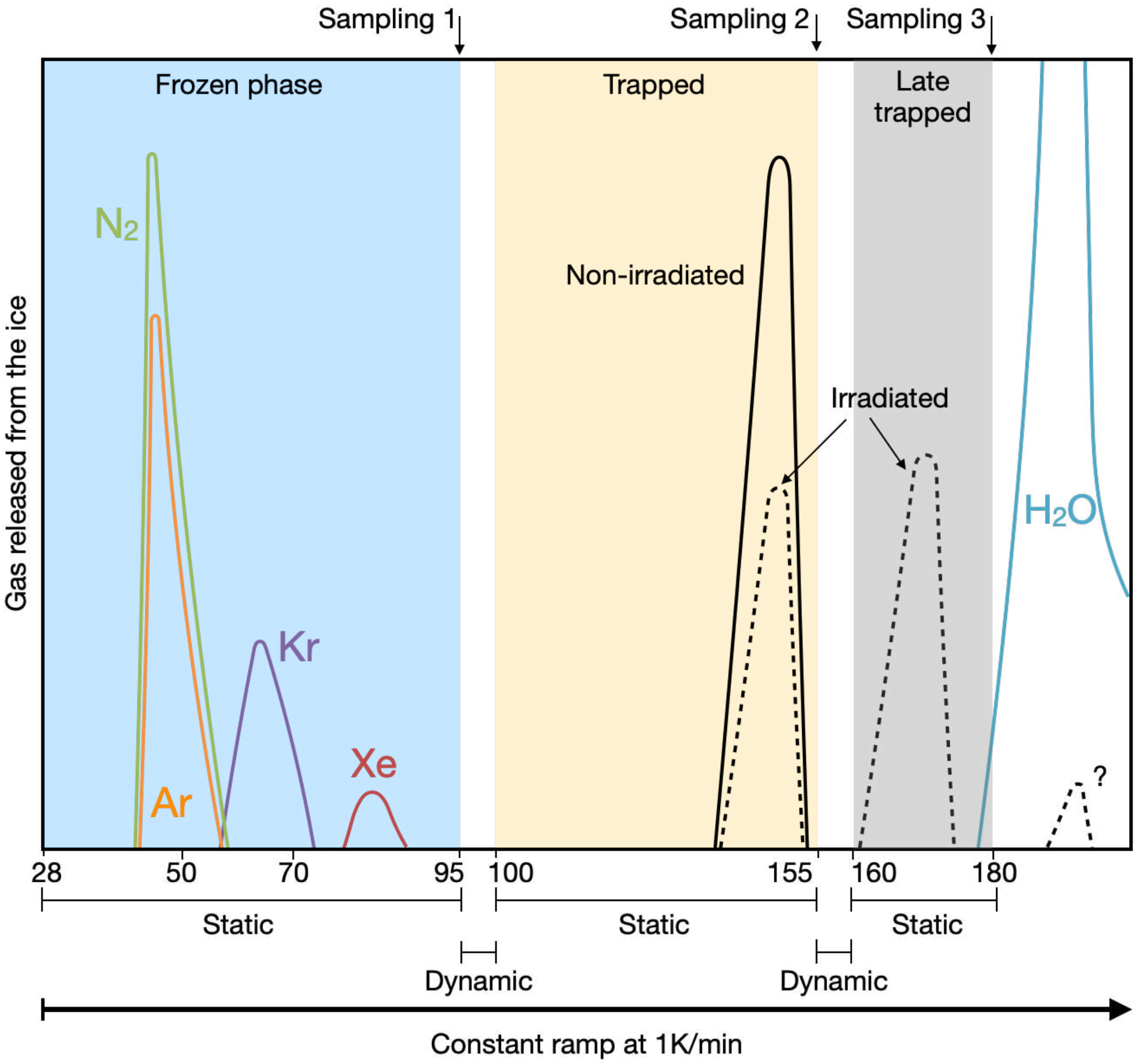

Figure 4.1: Conceptual description of the sampling protocol for the isotope analysis of the different gas releases during an experiment. Coloured curves are N_2, Ar, Kr and Xe sublimating from the ice forming the frozen phase, as sampled at 95K. Black full curve is the simultaneous release of the species, forming the trapped phase, sampled at 155K. Dashed curves are both the trapped phase and the late trapped phase for experiments with irradiation (see Chapter 3). The late trapped phase is sampled at 180K. During the accumulation of each phase in the experimental volume, the pumps were closed (static mode). Pumps were momentarily opened for 5 minutes after a sampling to remove the accumulated gas from the system.

The gas released from the irradiated ice was also sampled at 95K and 155K. After 5 minutes of pumping between 155K and 160K, the system was again set to static mode and an additional sampling, using a third steel bottle, was performed when the temperature reached 180K. This third sampling at 180K thus represents the "late" trapped phase (Figure 4.1). Above 180K water starts to sublimate, and no further sampling was performed in order to avoid excessive water contamination in the purification line.

After an experiment, gas samples were either sent for noble gas purification and isotope analysis, or for nitrogen purification and analysis, by using two different purification lines and static mass spectrometers.

2) Ar, Xe and N_2 Isotope Measurements

Noble gases and nitrogen were purified and analysed separately, using a GV Instrument Helix MC to analyse Ar and Xe isotopes, and a ThermoFisher Helix MC^+ for nitrogen isotopes. See Chapter 2 for additional details on the purification protocols, mass, analysis methods, and spectrometers' performances. The initial compositions of the noble gases and nitrogen contained in the bottle were analysed following an identical protocol as for samples without water in the gas mixture (Appendix Table A3 and A4). This initial composition was used to normalise the Xe and N_2 isotope data and to quantify the effect that trapping has on the isotope composition of the volatile species. Finally, calibrated standard gas of Ar, Xe and N_2 with atmospheric compositions were analysed before and after the samples to monitor and quantify the reproducibility and the instrumental mass discrimination of the mass spectrometers. The reproducibility of the Ar and Xe isotope ratios were better than 1‰ (1σ), and the reproducibility of the $^{15}N/^{14}N$ ratio around 2% (2σ). Each measured standard has a gas amount of 3×10^{-8} mole, 6×10^{-11} mole and 1×10^{-10} mole of ^{40}Ar, ^{123}Xe and $^{28}N_2$, respectively.

III. Results

1) Xenon

The Xe isotope compositions of the trapped phase and frozen phase of ices formed at 28K, 50K and 70K are given in Figure 4.2. The isotope compositions are normalised to the initial composition of Xe contained in the gas bottle of EXCITING. Experiments were duplicated ≥2 times. Data are given in Appendix Table A3 and Appendix Figure A3.

For the three temperatures of deposition investigated without irradiation, the isotope composition of xenon in the frozen phase (sublimated from the ice at around 80K, Almayrac et al. 2022) is indistinguishable from that of the gas bottle (Figure 4.2 **A**). Because the frozen phases contained low amount of Xe, (~1/10th of the amount analysed in standards), the precision on the least abundant isotopes ^{128}Xe and ^{130}Xe was lower than those of the other more abundant isotopes. Thus, the apparent excesses of ^{128}Xe and ^{130}Xe at the 50K experiment (Figure 4.2 **A**) are presumably not statistically significant. The trapped phases appear to be slightly enriched in their light isotopes ^{128,129,130,131}Xe, with a coincident depletion in the heavy isotopes ^{134,136}Xe for the ice formed at 50K (Figure 4.2 **B**). These isotopic deviations are very small, ~ +4‰ for ^{128}Xe and ~ -3‰ for ^{136}Xe, close to the precision limit and reproducibility reached by the GV Helix MC. In the experiment where the ice was irradiated during deposition at 50K (Figure 4.2 **C**), similar variations are also present for the frozen and early trapped phase, and higher for the late-trapped phase (stars on Figure 4.2 **C**). Maximum isotope deviations are ~ +10‰ and ~5‰ for the ^{128}Xe and ^{136}Xe isotopes, respectively.

Xe spectra showing isotopic fractionation, are enriched in the light isotopes, and depleted in the heavy isotopes. This mass-dependent fractionation (MDF) trend can be quantified with a linear regression (using the online version of IsoplotR software, Vermeesh 2018), as illustrated on Figure 4.3. The trapped phases of the different non-irradiated ices formed at 28K, 50K and 70K show similar MDF degree (~ -1 ‰/amu), and the late trapped phase in the irradiated ice formed at 50K shows slightly higher MDF degree of ~ -2‰/amu.

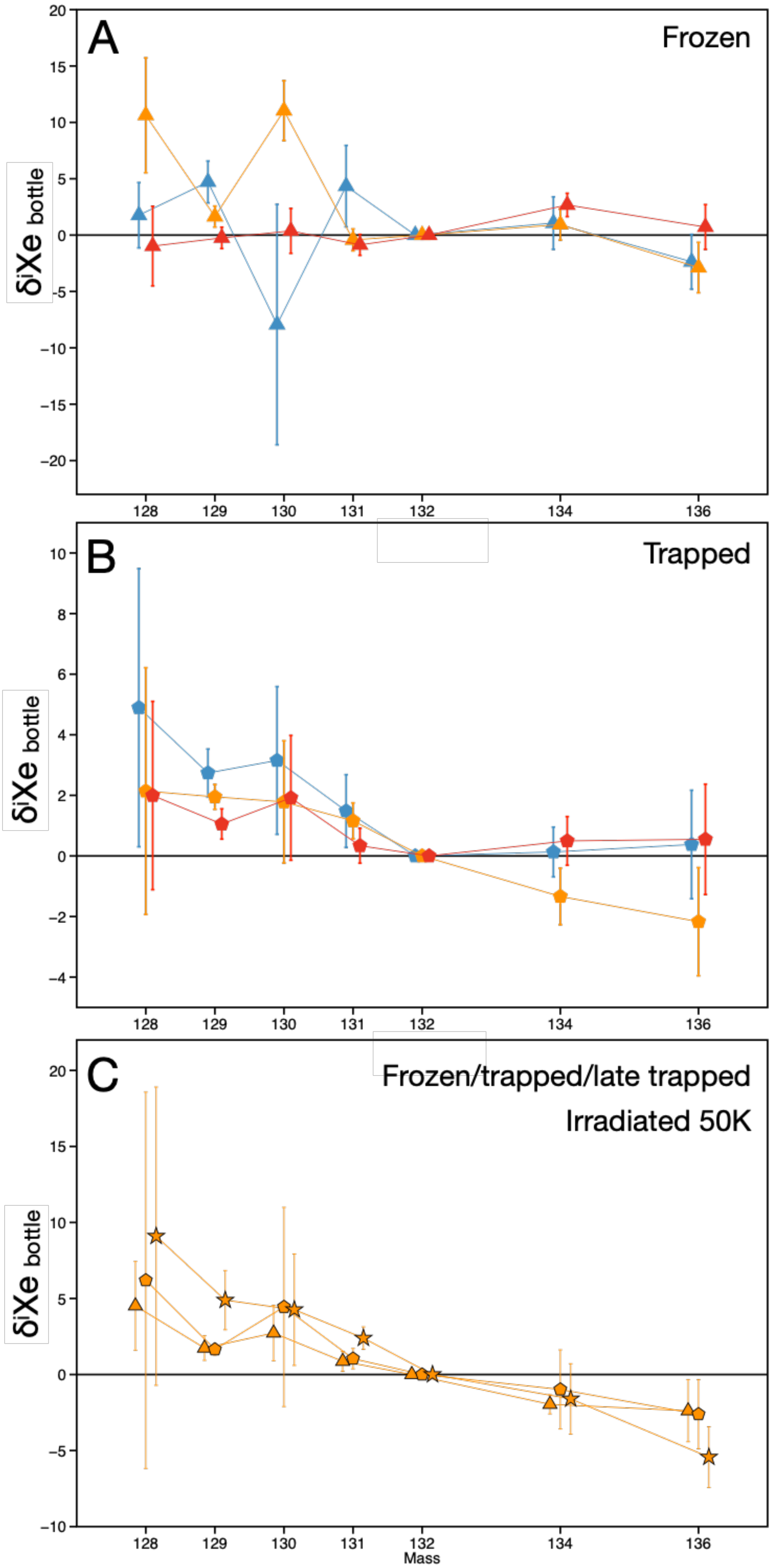

Figure 4.2: Xenon isotope composition of ices formed at different temperatures, expressed in ‰ deviation relative to the starting composition of the EXCITING gas bottle. **A** and **B** show the composition of the frozen phase (triangles) and of the trapped phase (pentagons), respectively, of ices formed at 28K (blue), 50K (orange) and 70K (red). **C** show the frozen phase, trapped phase, and "late trapped phase" (stars) of an ice formed at 50K under irradiation. All uncertainties are 1σ. Data are the average of multiple analyses, displayed in Appendix Figure A3. The frozen phases are indistinguishable from the initial Xe isotope composition. The trapped phase, for ices formed at 50K with or without irradiation, appears to be enriched in light isotopes and depleted in heavy isotopes, following a mass-dependent fractionation trend.

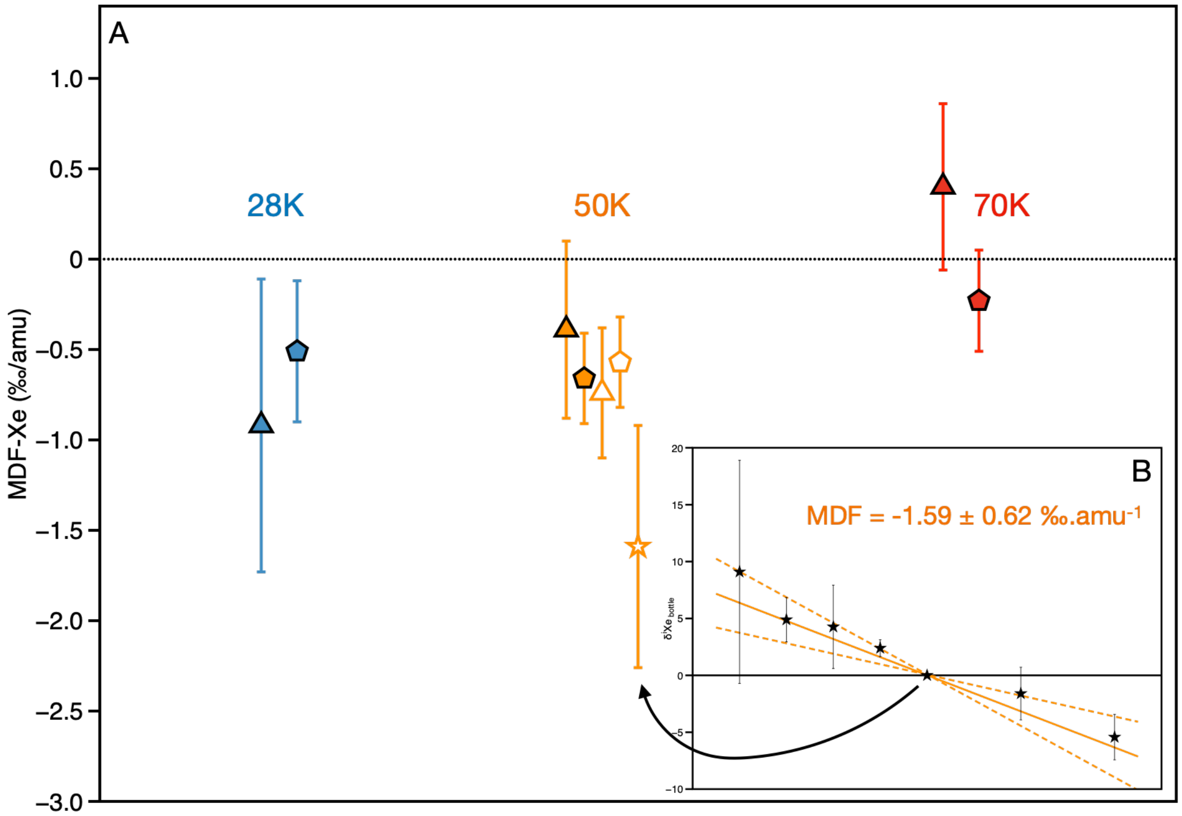

Figure 4.3: **A.** Xenon mass-dependent fractionation (MDF-Xe, in permil per mass unit) of the trapped (triangles) and frozen phases (pentagons) of ices formed at 28K (blue), 50K (orange) and 70K (red). Full symbols are non-irradiated ices, and open symbols are irradiated ice formed at 50K. The "late trapped phase" of the irradiated ice, represented by a star, shows the highest MDF degree. MDF, computed using a linear regression on all isotopes (IsoplotR, Vermeesh 2018) (**B**), represents the slope of the regression. All uncertainties at 1σ.

2) Argon

The argon isotope compositions were measured in the trapped phase of ices formed at 28K and 50K, but not at 70K because the amount of gas was too low to perform isotope measurements. Figure 4.4 (and Appendix Table A4) reports the $^{38}Ar/^{36}Ar$ vs. $^{40}Ar/^{36}Ar$ ratios of the samples and the starting gas. Forming ice at 28K does not fractionate the Ar isotope ratios of the trapped phase. Ice formed at 50K has a higher $^{40}Ar/^{36}Ar$ (314 ± 2) ratio than the initial one (289 ± 3), leading to a $^{40}Ar/^{36}Ar$ enrichment of 1.087 ± 0.013. This enrichment is only observed for $^{40}Ar/^{36}Ar$ and not for the $^{38}Ar/^{36}Ar$ ratio (Figure 4.4).

Enrichment in ^{40}Ar during trapping into amorphous ice were also found by Notesco et al. (1999), with a value of 1.076 ± 0.032, in agreement with our result. Because Notesco et al. (1999) performed their isotope measurements using a QMS, they did not have the sensitivity to measure the ^{38}Ar/^{36}Ar ratios. Three MDF processes are envisioned (kinetic, equilibrium, and gravity and centrifugal force, Young et al. 2002, Appendix A) and none of them can reproduce the Ar isotope composition of the trapped phase from the initial composition of the gas (Figure 4.4). Because only the ^{40}Ar/^{36}Ar fractionate, our result cannot be the effect of a MDF process. However, it is possible that the measurements of the ^{38}Ar/^{36}Ar ratios suffer from a consistent bias toward lower values, because of the low abundances of ^{38}Ar in the ices formed at 50K (Ar is depleted at temperatures of formation higher than 28K, Almayrac et al. 2022).

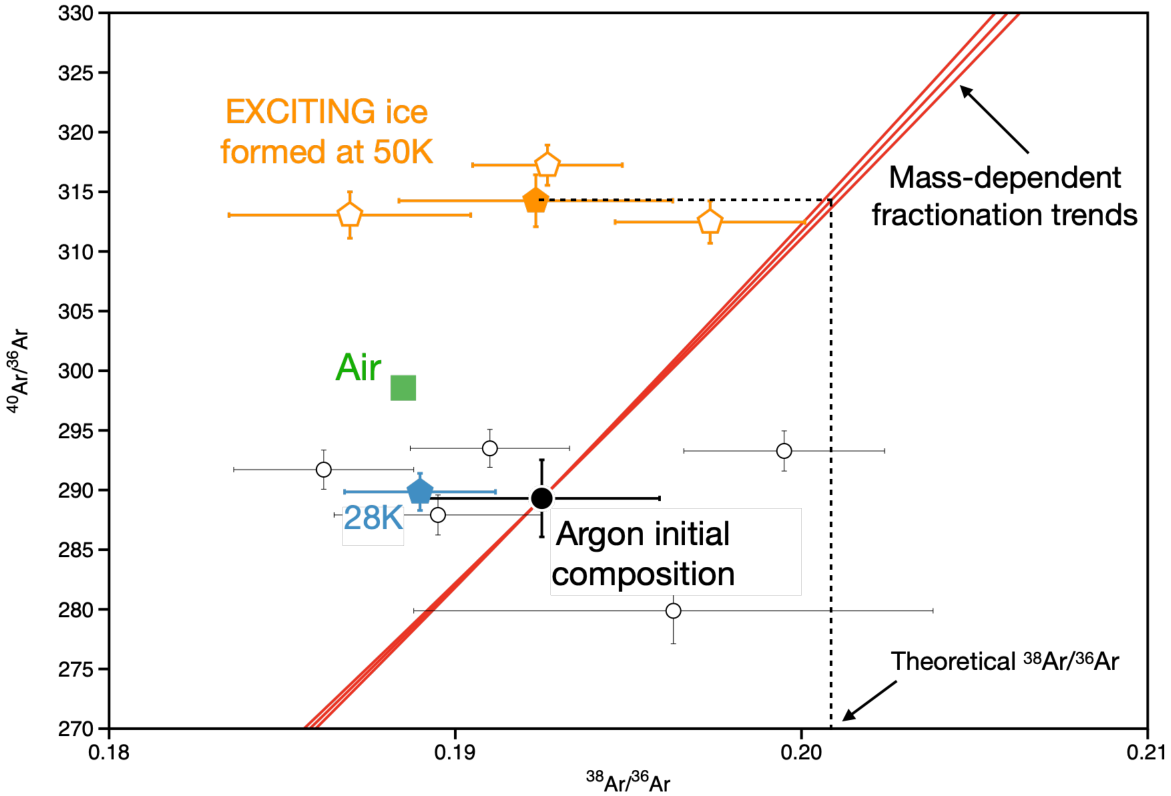

Figure 4.4: Argon isotope composition of the trapped phase of an ice formed at 50K (orange). The green hexagon represents atmospheric argon (Lee et al. 2006). The full black circle is the initial isotope composition of Ar (average of the open black circles), corrected for instrumental discrimination. The orange full pentagon is the average of the open pentagons. The red lines are three mass-dependent fractionation processes envisioned (see text), but none of these can reproduce the ice composition.

3) Nitrogen

The nitrogen isotopic fractionation was so far only explored at 50K to optimise the chance of measuring isotopic anomalies (Ar and Xe do not significantly fractionate when ice is formed at 28K), and, similarly to Ar, could not be measured for 70K ices because nitrogen concentrations trapped in the ice were too low to be successfully measured for isotopes. Nitrogen isotopes of the trapped phase are reported in Figure 4.5, normalised to the atmospheric composition, expressed in permil deviation. Gas aliquots with various amounts of N_2 were analysed to verify the linearity of the isotope measurements with the abundance (see Figure 4.5 **A** and Appendix Table A4 for standards, ice samples, and reference gas from the EXCITING bottle). The isotope composition of the trapped phase of the ice formed at 50K is enriched in the heavy isotope ^{15}N by ~32 ± 2 ‰ (2σ) relative to the starting nitrogen composition.

This enrichment in heavy N isotope is far from the order of magnitude of variation between comets ($\delta^{15}N$ = ~ +1000 ‰ in 67P/C-G, Altwegg et al. 2019, and $\delta^{15}N$ averaging +900 ‰ in other comets observed so far, Bockelée-Morvan et al. 2015) and ^{15}N-depleted reservoirs such as the Sun ($\delta^{15}N$ = ~ -400‰, Marty et al. 2011) or dense molecular clouds ($\delta^{15}N$ averaging -255 ± 283 ‰, Loison et al. 2019).

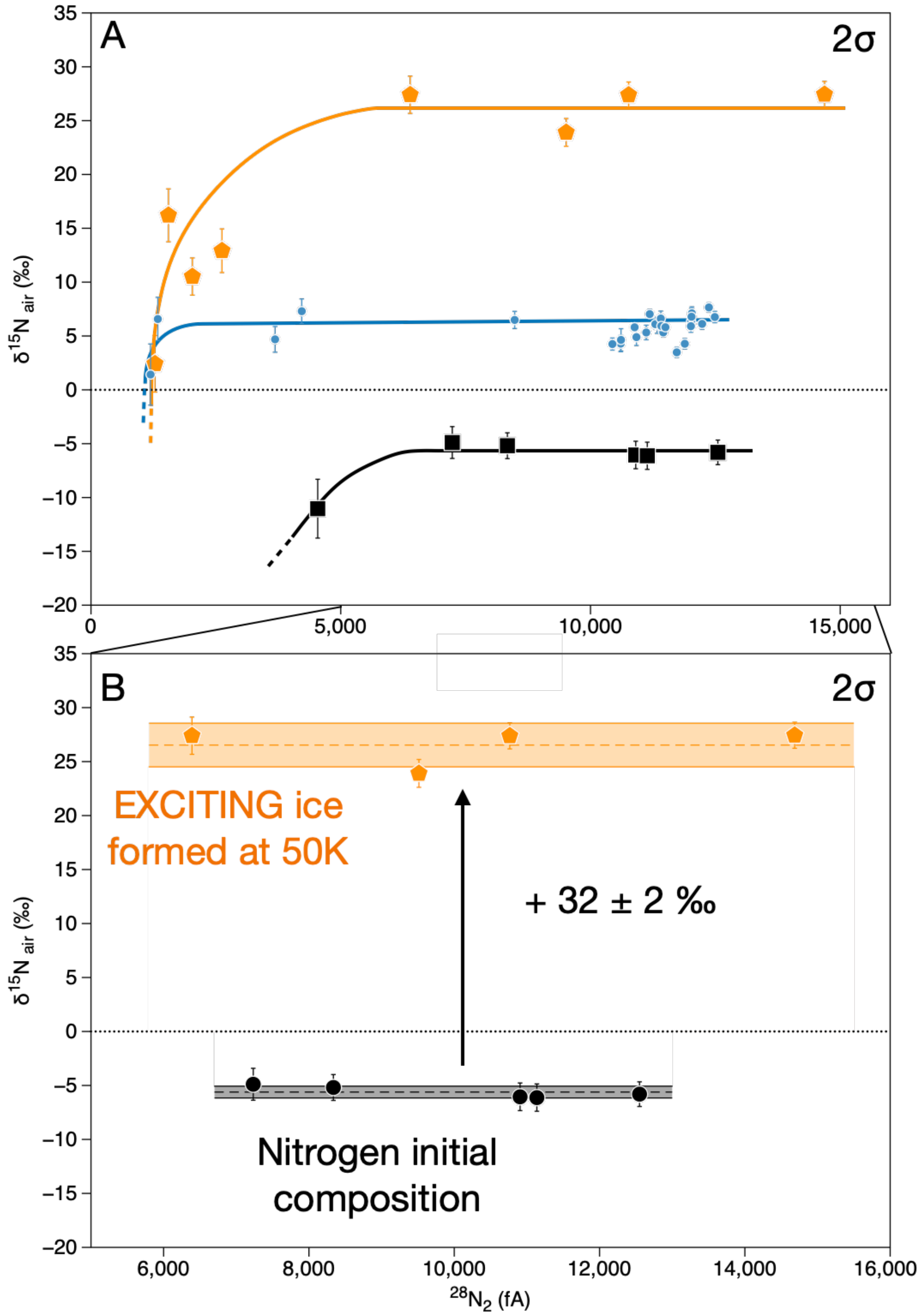

Figure 4.5: **A.** Nitrogen isotope composition, relative to the atmospheric composition (Nier, 1950) in permil deviation, of the EXCITING gas (black squares), gas standards (blue circles) and ices formed at 50K (orange pentagons), as a function of the $^{28}N_2$ abundance. Lines show how below a certain N_2 abundance the isotope composition is not linear with the signal size anymore (see Chapter 2 for the non-linearity effect at low abundances). **B.** Same plot centred where the nitrogen composition of the reference gas is linear. Envelopes are the standard error of the multiple analyses. Ice formed at 50K is enriched in the heavy ^{15}N isotope by ~32‰ relative to the starting composition. All uncertainties at 2σ.

IV. Discussion

1) Quantifying Isotope Fractionation

Argon and nitrogen (deposited in the ice as N_2) measured in the trapped phase of the ice are both enriched in heavy isotopes. The isotope enrichment factor, or isotope fractionation, from the initial gas composition and the gas trapped in the ice is 1.087 ± 0.013 for $^{40}Ar/^{36}Ar$, and 1.032 ± 0.001 for $^{15}N/^{14}N$. These fractionation degrees are not a result of kinetic or equilibrium fractionation during the degassing/release from the ice, because the measurements are made on the total amount of trapped phase (sampled after the accumulation of the gas in the experimental volume). Thus, the fractionation between the trapped phase and the initial gas must occur during the trapping of gas into the pores of the amorphous ice.

Atoms are trapped into pores when they (i) interact by Van Der Waals force with the dangling OH bonds of water (Rowland et al. 1995; Bar-Nun et al. 2013) and (ii) are recovered by a layer of water before they can escape (Ciesla et al. 2018). Because the isotopes of a given element have the same sublimation temperature, size, polarizability and strength of Van Der Waals interaction with OH, differences in trapping efficiency are likely to result from their different masses. At the deposition temperature of 50K, only a fraction of Ar and N_2 from the gas mixture is trapped into the pores (resulting in their depletion relative to Kr and Xe, Almayrac et al. 2022; Bar-Nun & Owen 1998). Additionally, the gas is continually flowed onto the cold plate during the formation of the ice, before being either trapped or removed from the cryogenic system by the pumps (dynamic mode). This indicates that the fractionation of N_2 and Ar may be approximated by an instantaneous fractionation factor between the gas phase and the ice, $\alpha_{gas\text{-}ice}$.

In a gas phase, all isotopes have equal kinetic energies ($E = \frac{1}{2} mv^2$). Consequently, for different isotopic masses, the kinetic fractionation factor $\alpha_{gas\text{-}ice}$ is equal to the ratio of their velocities, and thus the square root of their masses. For the fractionation of the $^{40}Ar/^{36}Ar$ ratios during the trapping from the gas phase into the ice, $\alpha_{gas\text{-}ice} = (40/36)^{1/2} = 1.054$. Nitrogen, being incorporated as N_2, has a kinetic $^{15}N/^{14}N$ fractionation factor of $\alpha_{gas\text{-}ice} = (29/28)^{1/2} = 1.018$, and the $^{136}Xe/^{132}Xe$ ratio should be enriched in ^{136}Xe by a factor of 1.015. For Ar and N_2, these fractionation degrees are below the actual fractionation measured in the trapped phase, both by a factor of ~2. This may be because the theoretical fractionation factor does not take into account the full complexity of the volatile trapping into amorphous ice pores. One could envision additional processes further fractionating the gas in contact with the ice, such as the thermal diffusion of the gas in the system leading to fractionation in the gas phase with the heavy isotopes being accumulated near the cold surface of the ice. Or fractionation from preferential porous media diffusion of lighter isotopes out of the ice, when they are covered by an additional layer of ice.

As opposed to Ar and N, Xe isotopes in the trapped phase do not show any isotope fractionation favouring heavy isotopes. The kinetic fractionation factor $\alpha_{\text{gas-ice}}$ is 1.015 for the ^{136}Xe/^{132}Xe ratio. On the contrary, ^{136}Xe is depleted relative to ^{132}Xe in the trapped phase compared to the initial gas composition for an ice formed at 28K or 50K (although very close to the precision limit, Figure 4.2). The non-fractionation of Xe could be explained by the higher polarizability of Xe (relative to the lighter noble gases, Kipfer et al. 2002) increasing its stickiness with dangling OH bonds. Also, Xe has a higher sublimation temperature (~80K in the conditions of the EXCITING experiments, Almayrac et al. 2022), making its trapping efficient at temperatures of 28K, 50K, and 70K, and thus without fractionating isotopes.

Interestingly, in the experiment with ice formed at 50K under irradiation, the late trapped phase (released from 155K to 180K) shows a slightly higher degree of MDF-Xe than the early trapped phase (released from ~100K to 155K), as displayed on Figure 4.2. As shown in Chapter 3, when the ice is irradiated, the early-trapped phase release corresponds to the transition from amorphous to cubic crystalline ice (Figures 3.11 and 3.12), with the gas mainly being released from the upper layers of the ice affected by the irradiation (Figure 3.13). The late trapped phase thus probably corresponds to the release of the rest of the gas trapped deeper within the ice. Because guest species keep diffusing inside the pores of the amorphous water ice after the ice formation (Palumbo 2006), one possibility is that light Xe isotopes diffuse deeper into the ice than heavier isotopes. This would result in a mass-dependent fractionation of Xe isotopes between the outer layers of the ice and the inner layers. Non-irradiated ices, releasing the totality of their trapped phase at once (Figures 3.4 and 3.12) do not show any isotope fractionation of the trapped phase relative to the starting composition (Figures 4.2 and 4.3). For irradiated ices however, the Xe trapped in the inner layers (late trapped phase) shows enrichment in light isotopes compared to the Xe trapped in the outer irradiated layers (early trapped phase), Figure 4.3.

Although this interpretation is only based on very small isotope anomalies, the set of experiments at 50K with and without irradiation was performed several times and show satisfactory reproducibility, displayed in Appendix Figure A3. Future experiments with slower deposition rates of noble gases and water, and longer exposure time to irradiation, should increase the effect of this diffusivity-related mass-dependent fractionation process. Additionally, molecular dynamic simulations would help better understand and quantify the processes at work during the trapping of noble gases into porous structures under cold conditions.

2) Origin of the Isotope Composition of N and Noble Gases

Within the experimental conditions explored so far using the EXCITING setup, trapping of Xe and N_2 into amorphous water ice does not produce large isotopic anomalies. In particular, the present experiments are not able to reproduce the N and Xe isotope compositions of comet 67P/C-G relative to a solar-like potential precursor.

Argon enrichment of its heavy isotope ^{40}Ar within ices formed at 50K reproduces the only previous attempt at measuring noble gas fractionation in cometary ice analogues by Notesco et al. (1999). Considering that the ^{40}Ar/^{36}Ar ratio of the trapped phase evolved following a mass-dependent fractionation trend, one can compute the theoretical fractionation of ^{38}Ar/^{36}Ar in the ice. The three different MDF processes, (i) kinetic, (ii) equilibrium and (iii) gravity and centrifugal force (see appendix A for the relation of the fractionation factors $\alpha(^{40}\text{Ar}/^{36}\text{Ar})$ and $\alpha(^{38}\text{Ar}/^{36}\text{Ar})$ depending on the process, Young et al. 2002) produce similar ratios of ^{38}Ar/^{36}Ar (Figure 4.4). The measured enrichment of 1.087 ± 0.013 for ^{40}Ar/^{36}Ar leads a theoretical enrichment ratio of 1.045 ± 0.012 for ^{38}Ar/^{36}Ar. Thus, a cometary ice formed from a gas with a solar-like composition (0.1818 ± 0.0001, Meshik et al. 2014) would have a ^{38}Ar/^{36}Ar of 0.190 ± 0.02. This does not contradict the ^{38}Ar/^{36}Ar measured in comet 67P/C-G of 0.1852 ± 0.0480 (Balsiger et al. 2015), indistinguishable from the solar composition within the (large) uncertainty (the ^{38}Ar abundance in the coma of 67P/C-G measured by the ROSINA instrument was barely above the background level). Our results indicate that Ar in cometary ices may be derived from a solar-like gas with only limited isotope fractionation.

Our observation of nitrogen isotope fractionation, with a ^{15}N-enrichment in the ice analogue ($\delta^{15}N$ = +32‰, Figure 4.5), is far from reproducing the composition of comets (+900‰, Bockelée-Morvan et al. 2015) if we consider a solar-like starting composition (-400‰, Marty et al. 2011). These nitrogen analyses using noble gas mass spectrometry are the first ever isotope measurements of N_2 in cometary ice analogues, and provide additional clues for the ongoing debate about the origin of N isotope variability in the Solar System (e.g., Terzieva & Herbst 2000; Rodgers & Charnley 2008; Heays et al. 2014; Füri & Marty 2015; Hily-Blant et al. 2017; Grewal 2022). Although different experimental parameters still need to be explored to better constrain the evolution of N isotopes in cometary ices, it appears that the anomalies in cometary ices are not a result of N trapping in, and subsequent released from, amorphous water ice. This would suggest that N isotopes were already non-solar in composition at the time N-bearing species were incorporated into cometary ices, as suggested by the $\delta^{15}N$ variation measured in some of the earliest forming planetesimals (Grewal et al., 2021). Ground-based spectroscopic measurements of the N composition in the gas phase of dense molecular clouds show a relatively consistent ^{15}N-poor signature ~ -255 ± 283 ‰ (average and standard deviation) between different clouds and N-bearing molecules (Loison et al. 2019 and reference therein, in N_2H, NH_3, CN, HCN, HNC, HC_3N and HC_5N, Figure 1.8). Laboratory experiments demonstrated the possibility for differential N_2 photodissociation and/or self-shielding effect to produce large variability in nitrogen signatures (Chakraborty et al. 2014). These experiments are based on the irradiation by energetic photons (90 nm, 13.7 eV) of N_2-H_2 gas mixtures, leading to selective ^{15}N-^{14}N (over ^{14}N-^{14}N) photodissociation and the formation of NH_3 products enriched in ^{15}N, up to +10,000 ‰ (Chakraborty et al. 2014). If such a process occurs in dense molecular clouds, ^{15}N-rich products (simple N-bearing molecules such as NH_3 or CN) would be separated from the gas phase (presumably mainly in the form of N_2, Öberg & Bergin 2021) and adsorbed/condensed onto silicate grains and/or trapped into ices. This would thus lead to two N reservoirs, (i) the gas phase of dense molecular cloud mainly composed of N_2 poor in ^{15}N, and (ii) grains and ices enriched in ^{15}N (Hily-Blant et al. 2017). This scenario is however challenged by the high $\delta^{15}N$ measured for N_2 in comet 67P/C-G (+ 1000‰, consistent with NO and NH_3, Altwegg et al. 2019). Additional experimental investigations on nitrogen isotope fractionation in complex cometary ice analogues under irradiated environment, will ultimately provide more clues on the origin of N isotope variability, before future spatial missions towards icy bodies.

The isotopic anomaly of Xe, identified in comet 67P/C-G (Marty et al. 2017), cannot however be produced by photochemical processes. High temperature (~700-1000 K) experiments were able to produce Xe isotopic fractionation when ionized in plasma conditions, and incorporated into organic matter (Kuga et al. 2015), however, these conditions do not apply to the cold environment of the outer Solar System required to form volatile-rich cometary ices. The small depletion in heavy Xe isotope measured in EXCITING ices formed at 28K, 50K and 70K (~ -5‰ for the $^{136}Xe/^{132}Xe$ ratio, Figure 4.2) can hardly be compared to the depletion observed in comet 67P/C-G of $^{136}Xe/^{132}Xe$ ~ -600‰ (Marty et al. 2017) relative to the solar composition (Meshik et al. 2014). Additionally, the anomalies measured in EXCITING ices follow mass-dependent fractionation trends, as opposed to the mass-independent Xe anomalies in comet 67P/C-G (only enriched in ^{129}Xe and depleted in ^{134}Xe and ^{136}Xe, Marty et al. 2017). This indicates that Xe (similarly to nitrogen) had an initial non-solar isotope composition at the time it was incorporated into 67P/C-G ices. Because we show very limited isotope fractionation during ice formation, our results do not significantly impact calculations of nucleosynthetic anomalies mixtures proposed by Marty et al. (2017) and Avice et al. (2020) to reproduce the Xe composition of 67P/C-G.

V. Conclusions and Perspectives

This chapter presents the isotopic behaviour of Ar, Xe and N_2 in water ices formed using the EXCITING setup. These volatile elements were incorporated into the amorphous water ice structure, as trapped guest species, and released upon warming to be analysed by using static noble gas mass spectrometry. The isotopic analyses required the development of Ar and Xe measurements on the GV Instrument Helix MC mass spectrometer, and N_2 measurements on the ThermoFisher Helix MC$^+$. The isotope data acquired and presented in this chapter represent the first ever precise isotope measurements of noble gases along with nitrogen in cometary water ice analogues.

We find that the trapping of Ar, Xe and N_2 in ices do not produce any large isotopic anomalies. The isotopic composition of the trapped phases of different experiment are compared to the initial gas composition and described as enrichment or depletion for different isotopes. Argon shows enrichment in its heavy isotopes ^{40}Ar ($^{40}Ar/^{36}Ar$ enriched by a factor of 1.086), but not for ^{38}Ar, which I consider to be a measurement bias due to very low amount of gas analysed. If ^{38}Ar were also enriched, it would still be in agreement with the enrichment factor between the solar composition and the Ar composition of comet 67P/Churyumov-Gerasimenko (Balsiger et al. 2015).

Nitrogen also shows an enrichment of the heavy isotope ^{15}N in the ice, of around +30‰ relative to the starting composition. This, however, does not reproduce the large, and ubiquitous, ^{15}N-enrichment observed in many comets (Altwegg et al. 2019), including 67P/C-G. This suggests that processes happening in the formation environment of cometary ices fractionated N isotopes before their incorporation into ices.

Finally, contrary to Ar and N_2, xenon does not show any heavy isotope enrichment, also suggesting that the peculiar Xe isotope signature of comet 67P/C-G was inherited from the composition of the gas at the time of ice formation (Marty et al. 2017). Xenon fractionation was also investigated for ices formed under irradiation by UV photons. Although the results still require further exploration and adapted experimental parameters, it appears that diffusion of Xe into the ice can fractionate the isotopes by few ‰ between the outer and inner layers of the ice.

Overall, the limited isotope fractionations observed in this experimental work indicate that the measurements of cometary volatile isotopes (either from ground-based observations or by in-situ measurements), would not significantly vary between the different possible phases that are analysed (frozen, trapped, or “late” trapped). Thus, astronomical isotopic measurements of comets are presumably representative of the globality of the cometary ice. This further support the hypothesis that the composition of cometary ices directly reflects the composition of the gas in their environment of formation.

Further investigations of the effect of irradiation on isotope fractionation still need to be explored, in particular on nitrogen, for which isotope measurements only began in the last year of the PhD after a long period of development.

Conclusion

The main objective of this thesis was to better understand the origin of the unique elemental and isotope composition of volatile elements present in comets. In order to achieve this primary objective, I developed an experimental setup in the laboratory capable of creating cometary ice analogues from a gas mixture of water, nitrogen and noble gases. By using noble gas mass spectrometry techniques, I have been able to study how gas entrapment into water ices affects the elemental and isotopic abundances of volatile elements found in comets.

This experimental set up, called EXCITING (Exploring Xenon in Cometary Ices by Trapping and Irradiating Nobles Gases) constituted the principal research direction of this PhD, necessitating the development of several technical and analytical approaches for the analysis of noble gases (Chapter 2). Specifically, I developed the measurements of Ar, Xe and N_2 isotopes on two different noble gas mass spectrometers, that not only benefitted the EXCITING project, but many other projects I have been involved in throughout the course of my PhD (hydrothermal fluids, volcanic gases, and meteorite studies, synchrotron irradiated gas samples, and Ryugu samples return from the Hayabusa2 space mission by JAXA).

The EXCITING experiment provided further clues on the environment of formation of comets. A major focus was to compare the behaviour of noble gases in the experiments to the composition of comet 67P/Churyumov-Gerasimenko (the only noble gas data on cometary ices, obtained by the Rosetta space mission). It showed that temperatures of formation around 70K could best reproduce the Kr/Ar, Xe/Ar and N_2/Ar ratios of the comet (Chapter 3). Such temperatures challenge the more commonly advocated temperature of ~30K for comet formation, and the cold dense molecular cloud as the formation environment for cometary ices.

The trapping of noble gases and nitrogen in EXCITING ices was found to not induce significant isotopic fractionation relative to the initial gas phase composition (Chapter 4). Moreover, it was found that irradiating the ice with UV photons affects the release of volatiles from the ice such that different isotope components could be isolated and measured separately, with only limited isotopic variations compared to the bulk value. This indicates that the measurements of volatile isotopes in cometary ice (either from ground-based observations or by in-situ measurements) would not significantly vary between the different possible phases that are analysed (volatile elements frozen along with water, or trapped within the ice structure). These experiments provide supporting evidence that isotope measurements in the coma of comet 67P/C-G are representative of the interior of the comet, as well as directly depicting the composition of the gas from which it formed. The origin of volatile element isotope signatures found in comets cannot be accounted for by the fractionation processes during trapping into ice that have been brought to light by experiments conducted in this thesis, and thus still remain to be deciphered.

Finally, despite irradiation not having a major impact on the composition of the volatiles trapped in cometary ice, it was found that irradiating the surface of the ice can significantly reduce the ability of trapped volatile species to escape the ice during the transition between amorphous and crystalline ice. The enhanced retention of volatile species in irradiated ice, even after the amorphous to crystalline transition starting at 120K, suggests that the ability of comets to retain volatiles even at the high temperatures experienced during their transit through the inner solar system may have been underestimated. This could have major implications on the ability of comets to deliver volatiles to the inner solar system and the terrestrial planets.

Side Projects and Ongoing Works

Further experimental investigations were developed in order to explore the origin of nitrogen isotope variability in comets, and more generally in the volatile-rich planetary materials enriched in ^{15}N.

Firstly, in collaboration with Dr Grégoire Danger and Vassilissa Vinogradoff from the PIIM laboratory (Physique des Interactions Ioniques et Moléculaires) at Aix-Marseille University, we estimated the N isotope composition (as well as H and C) in organic rich astrophysical ice analogues. The ices are made from a NH_3, CH_3OH and H_2O gas mixture condensed at 78K, and subsequently heated to room temperature, whilst simultaneously irradiating the ice with UV photons (120 - 160 nm, same lamp as in EXCITING). The organic products of this experiment (Danger et al. 2013) were then analysed following a multi-instrumental approach. The bulk H, C, N elemental and isotopic compositions of the organic residue were measured on using an EA-IrMS (Elemental Analyser-Isotope ratio Mass Spectrometer) at CRPG (Nancy) with Dr Thomas Rigaudier. In-situ isotope measurements were performed using a NanoSIMS at MNHN (Muséum National d'Histoire Naturelle) in Paris by Dr Laurent Rémusat. This project is the first multi-elements (H-C-N) and multi-techniques (IRMS, NanoSIMS) investigation of isotope fractionation during the synthesis of complex organic matter by irradiation, analogous to the organic phases found in meteorites. The final data acquisitions were performed during the last year of the PhD, and are in preparation for publication.

Secondly, in collaboration with Dr Nathalie Carasco and Dr Ludovic Vettier from the LATMOS laboratory (Laboratoire Atmosphères, Milieux, Observations Spatiales) in Paris and Jérémy Bourgalais from LRGP (Laboratoire de Réactions et Génie des Procédés) in Nancy, a project was devised as part of the ERC Photonis project to investigate the effect of higher energy photon irradiation on the isotope composition of gaseous organic compounds formed from the irradiation of a N-rich nebular gas. The irradiation experiments were performed at the Synchrotron SOLEIL facility in Saclay (France) in June 2022. Gases composed of H_2, CO and

N_2 were irradiated with photons at ~90 nm (13.77 eV, higher energy than the UV lamp on EXCITING of ~10.2 eV), an energy for which predissociation of $^{15}N^{14}N$ is more efficient than for $^{14}N^{14}N$. Condensable products were either analysed in situ with a quadrupole mass spectrometer (QMS) or collected for precise chemical and isotopic analyses at CRPG. The analysis of the nitrogen isotopes of the experimental products, with limited amount of N-bearing molecules (equivalent to <1 µmol of N_2), relies on the development of precise and ultra-sensitive nitrogen isotope measurement using noble gas mass spectrometry undertook during my PhD. The N isotope analyses are now on-going at CRPG and the results will be compared to isotope variations observed in meteorites and comets.

Altogether, the EXITING experiments and the different collaborative projects allowed me to investigate a wide range of conditions that govern the nature and distribution of the volatile elements in the icy and volatile-rich planetary material of our Solar System.

References

A

Albarede, F. (2009). Volatile accretion history of the terrestrial planets and dynamic implications. *Nature*, *461*(7268), 1227-1233.

Alexander, C. O. D., Bowden, R., Fogel, M. L., Howard, K. T., Herd, C. D. K., & Nittler, L. R. (2012). The provenances of asteroids, and their contributions to the volatile inventories of the terrestrial planets. *Science*, *337*(6095), 721-723.

Alexander, C. M. D., McKeegan, K. D., & Altwegg, K. (2018). Water reservoirs in small planetary bodies: meteorites, asteroids, and comets. *Space science reviews*, *214*(1), 1-47.

Almayrac, M. G., Broadley, M. W., Bekaert, D. V., Hofmann, A., & Marty, B. (2021). Possible discontinuous evolution of atmospheric xenon suggested by Archean barites. *Chemical Geology*, *581*, 120405.

Almayrac, M. G., Bekaert, D. V., Broadley, M. W., Byrne, D. J., Piani, L., Marty, B. (accepted). The EXCITING experiment exploring the behaviour of nitrogen and noble gases in interstellar ice analogues. *The Planetary Science Journal*.

Altwegg, K., Balsiger, H., Bar-Nun, A., Berthelier, J. J., Bieler, A., Bochsler, P., ... & Wurz, P. (2015). 67P/Churyumov-Gerasimenko, a Jupiter family comet with a high D/H ratio. *Science*, *347*(6220), 1261952.

Altwegg, K., Balsiger, H., & Fuselier, S. A. (2019). Cometary chemistry and the origin of icy solar system bodies: the view after Rosetta. *Annual Review of Astronomy and Astrophysics*, *57*, 113-155.

Ardoin, L., Broadley, M. W., Almayrac, M., Avice, G., Byrne, D. J., Tarantola, A., ... & Marty, B. (2022). The end of the isotopic evolution of atmospheric xenon. *Geochemical Perspectives Letters*, *20*, 43-47.

Arpigny, C., Jehin, E., Manfroid, J., Hutsemékers, D., Schulz, R., Stuwe, J. A., ... & Ilyin, I. (2003). Anomalous nitrogen isotope ratio in comets. *Science*, *301*(5639), 1522-1524.

Avice, G., Moreira, M., & Gilmour, J. D. (2020). Xenon Isotopes Identify Large-scale Nucleosynthetic Heterogeneities across the Solar System. *The Astrophysical Journal*, *889*(1), 68.

B

Balsiger, H., Altwegg, K., Bochsler, P., Eberhardt, P., Fischer, J., Graf, S., ... & Wollnik, H. (2007). Rosina–Rosetta orbiter spectrometer for ion and neutral analysis. *Space Science Reviews*, *128*(1), 745-801.

Balsiger, H., Altwegg, K., Bar-Nun, A., Berthelier, J. J., Bieler, A., Bochsler, P., ... & Wurz, P. (2015). Detection of argon in the coma of comet 67P/Churyumov-Gerasimenko. *Science advances*, *1*(8), e1500377.

Bar-Nun, A., Herman, G., Laufer, D., & Rappaport, M. L. (1985). Trapping and release of gases by water ice and implications for icy bodies. *Icarus*, *63*(3), 317-332.

Bar-Nun, A., Dror, J., Kochavi, E., & Laufer, D. (1987). Amorphous water ice and its ability to trap gases. *Physical Review B*, *35*(5), 2427.

Bar-Nun, A., & Kleinfeld, I. (1989). On the temperature and gas composition in the region of comet formation. *Icarus*, *80*(2), 243-253.

Bar-Nun, A., & Owen, T. (1998). Trapping of gases in water ice and consequences to comets and the atmospheres of the inner planets. In *Solar System Ices* (pp. 353-366). Springer, Dordrecht.

Bar-Nun, A., Notesco, G., & Owen, T. (2007). Trapping of N2, CO and Ar in amorphous ice—Application to comets. *Icarus*, *190*(2), 655-659.

Bar-Nun, A., Laufer, D., Rebolledo, O., Malyk, S., Reisler, H., & Wittig, C. (2013). Gas trapping in ice and its release upon warming. In *The Science of Solar System Ices* (pp. 487-499). Springer, New York, NY.

Barry, P. H., Hilton, D. R., Halldórsson, S. A., Hahm, D., & Marti, K. (2012). High precision nitrogen isotope measurements in oceanic basalts using a static triple collection noble gas mass spectrometer. *Geochemistry, Geophysics, Geosystems*, *13*(1).

Basford, J. R., Dragon, J. C., Pepin, R. O., Coscio Jr, M. R., & Murthy, V. R. (1973). Krypton and xenon in lunar fines. In *Lunar and Planetary Science Conference Proceedings* (Vol. 4, p. 1915).

Becker, R. H., & Pepin, R. O. (1984). The case for a Martian origin of the shergottites: Nitrogen and noble gases in EETA 79001. *Earth and Planetary Science Letters*, *69*(2), 225-242.

Bekaert, D. V. (2020). Isotopic constraints on the origin and nature of primitive material in the Solar System and on early Earth (Doctoral dissertation, Université de Lorraine).

Bekaert, D. V., Broadley, M. W., & Marty, B. (2020). The origin and fate of volatile elements on Earth revisited in light of noble gas data obtained from comet 67P/Churyumov-Gerasimenko. *Scientific reports*, *10*(1), 1-18.

Biver, N., Bockelée-Morvan, D., Crovisier, J., Lis, D. C., Moreno, R., Colom, P., ... & Womack, M. (2006). Radio wavelength molecular observations of comets C/1999 T1 (McNaught-Hartley), C/2001 A2 (LINEAR), C/2000 WM1 (LINEAR) and 153P/Ikeya-Zhang. *Astronomy & Astrophysics*, *449*(3), 1255-1270.

Blitz, L., & Shu, F. H. (1980). The origin and lifetime of giant molecular cloud complexes. *The Astrophysical Journal*, *238*, 148-157.

Bockelée-Morvan, D., Gautier, D., Lis, D. C., Young, K., Keene, J., Phillips, T., ... & Wootten, A. (1998). Deuterated water in comet C/1996 B2 (Hyakutake) and its implications for the origin of comets. *Icarus*, *133*(1), 147-162.

Bockelée-Morvan, D., Calmonte, U., Charnley, S., Duprat, J., Engrand, C., Gicquel, A., ... & Wirström, E. (2015). Cometary isotopic measurements. *Space science reviews*, *197*(1), 47-83.

Boulliung, J. (2020). Solubilité, spéciation et diffusion de l'azote dans les verres et silicates fondus (Doctoral dissertation, Université de Lorraine).

Boulliung, J., Füri, E., Dalou, C., Tissandier, L., Zimmermann, L., & Marrocchi, Y. (2020). Oxygen fugacity and melt composition controls on nitrogen solubility in silicate melts. *Geochimica et Cosmochimica Acta*, *284*, 120-133.

Boyd, S. R., Wright, I. P., Franchi, I. A., & Pillinger, C. T. (1988). Preparation of sub-nanomole quantities of nitrogen gas for stable isotopic analysis. *Journal of Physics E: Scientific Instruments*, *21*(9), 876.

Brownlee, D., Tsou, P., Aléon, J., Alexander, C. M. O. D., Araki, T., Bajt, S., ... & Taheri, M. (2006). Comet 81P/Wild 2 under a microscope. *science*, *314*(5806), 1711-1716.

Burkhardt, C., Spitzer, F., Morbidelli, A., Budde, G., Render, J. H., Kruijer, T. S., & Kleine, T. (2021). Terrestrial planet formation from lost inner solar system material. *Science advances*, *7*(52), eabj7601.

Busemann, H., Baur, H., & Wieler, R. (2000). Primordial noble gases in “phase Q” in carbonaceous and ordinary chondrites studied by closed-system stepped etching. *Meteoritics & Planetary Science*, *35*(5), 949-973.

Byrne D. J., Broadley M. W., Füri E., Tissandier L., Zimmerman L., Almayrac M. G., Bekaert D. V., Barrat J. A. and Marty B., The noble gas composition of the andesitic achondrite Erg Chech 002 (*under review in Geochimica et Cosmochimica Acta*).

C

Chakraborty, S., Muskatel, B. H., Jackson, T. L., Ahmed, M., Levine, R. D., & Thiemens, M. H. (2014). Massive isotopic effect in vacuum UV photodissociation of N2 and implications for meteorite data. *Proceedings of the National Academy of Sciences*, *111*(41), 14704-14709.

Chyba, C., & Sagan, C. (1992). Endogenous production, exogenous delivery and impact-shock synthesis of organic molecules: an inventory for the origins of life. *Nature*, *355*(6356), 125-132.

Ciesla, F. J., & Sandford, S. A. (2012). Organic synthesis via irradiation and warming of ice grains in the solar nebula. *Science*, *336*(6080), 452-454.

Ciesla, F. J. (2014). The phases of water ice in the solar nebula. *The Astrophysical Journal Letters*, *784*(1), L1.

Ciesla, F. J., Krijt, S., Yokochi, R., & Sandford, S. (2018). The Efficiency of Noble Gas Trapping in Astrophysical Environments. *The Astrophysical Journal*, *867*(2), 146.

Clayton, R. N. (2002). Self-shielding in the solar nebula. *Nature*, *415*(6874), 860-861.

Cochran, A. L., & McKay, A. J. (2018). Erratum:"Strong CO and N2 Emission in Comet C/2016 R2 (Pan-STARRS)"(2018, ApJL, 854, L10). *The Astrophysical Journal Letters*, *856*(L20), 1pp.

Collings, M. P., Anderson, M. A., Chen, R., Dever, J. W., Viti, S., Williams, D. A., & McCoustra, M. R. (2004). A laboratory survey of the thermal desorption of astrophysically relevant molecules. *Monthly Notices of the Royal Astronomical Society*, *354*(4), 1133-1140.

Connelly, J. N., Bizzarro, M., Krot, A. N., Nordlund, Å., Wielandt, D., & Ivanova, M. A. (2012). The absolute chronology and thermal processing of solids in the solar protoplanetary disk. *Science*, *338*(6107), 651-655.

Crovisier, J. (1997). Infrared observations of volatile molecules in comet Hale-Bopp. *Earth, Moon, and Planets*, *79*(1), 125-143.

Cruz-Diaz, G. A., Caro, G. M., Chen, Y. J., & Yih, T. S. (2014). Vacuum-UV spectroscopy of interstellar ice analogs-I. Absorption cross-sections of polar-ice molecules. *Astronomy & Astrophysics*, *562*, A119.

D

Danger, G., Orthous-Daunay, F. R., de Marcellus, P., Modica, P., Vuitton, V., Duvernay, F., ... & Chiavassa, T. (2013). Characterization of laboratory analogs of interstellar/cometary organic residues using very high resolution mass spectrometry. *Geochimica et Cosmochimica Acta*, *118*, 184-201.

Dauphas, N. (2003). The dual origin of the terrestrial atmosphere. *Icarus*, *165*(2), 326-339.

Dauphas, N., & Schauble, E. A. (2016). Mass fractionation laws, mass-independent effects, and isotopic anomalies. *Annual Review of Earth and Planetary Sciences*, *44*, 709-783.

Dauphas, N. (2017). The isotopic nature of the Earth's accreting material through time. *Nature*, *541*(7638), 521-524.

Deligny, C., Füri, E., & Deloule, E. (2021). Origin and timing of volatile delivery (N, H) to the angrite parent body: Constraints from in situ analyses of melt inclusions. *Geochimica et Cosmochimica Acta*, *313*, 243-256.

E

Englezos, P. (1993). Clathrate hydrates. *Industrial & engineering chemistry research*, *32*(7), 1251-1274.

F

Feldman, P. D., Festou, M. C., Tozzi, P., & Weaver, H. A. (1997). The CO2/CO abundance ratio in 1P/Halley and several other comets observed by IUE and HST. *The Astrophysical Journal*, *475*(2), 829.

Fischer-Gödde, M., Elfers, B. M., Münker, C., Szilas, K., Maier, W. D., Messling, N., ... & Smithies, H. (2020). Ruthenium isotope vestige of Earth's pre-late-veneer mantle preserved in Archaean rocks. *Nature*, *579*(7798), 240-244.

Fray, N., & Schmitt, B. (2009). Sublimation of ices of astrophysical interest: A bibliographic review. *Planetary and Space Science*, *57*(14-15), 2053-2080.

Füri, E., Marty, B., & Assonov, S. S. (2012). Constraints on the flux of meteoritic and cometary water on the Moon from volatile element (N–Ar) analyses of single lunar soil grains, Luna 24 core. *Icarus*, *218*(1), 220-229.

Füri, E., & Marty, B. (2015). Nitrogen isotope variations in the Solar System. *Nature Geoscience*, *8*(7), 515-522.

Füri, E., Barry, P. H., Taylor, L. A., & Marty, B. (2015). Indigenous nitrogen in the Moon: constraints from coupled nitrogen–noble gas analyses of mare basalts. *Earth and Planetary Science Letters*, *431*, 195-205.

G

Gaidos, E., Krot, A. N., Williams, J. P., & Raymond, S. N. (2009). 26Al and the formation of the Solar System from a molecular cloud contaminated by Wolf–Rayet winds. *The Astrophysical Journal*, *696*(2), 1854.

Gedcke, D. A. (2001). How counting statistics controls detection limits and peak precision. *ORTEC Application Notes AN59*.

Ghormley, J. A. (1967). Adsorption and Occlusion of Gases by the Low‐Temperature Forms of Ice. *The Journal of Chemical Physics*, *46*(4), 1321-1325.

Gkotsinas, A., Guilbert-Lepoutre, A., Raymond, S. N., & Nesvorny, D. (2022). Thermal Processing of Jupiter-family Comets during Their Chaotic Orbital Evolution. *The Astrophysical Journal*, *928*(1), 43.

Greenberg, J. M. (2002). Cosmic dust and our origins. *Surface Science*, *500*(1-3), 793-822.

Grewal, D. S., Dasgupta, R., & Marty, B. (2021). A very early origin of isotopically distinct nitrogen in inner Solar System protoplanets. *Nature Astronomy*, *5*(4), 356-364.

Grewal, D. S. (2022). Origin of Nitrogen Isotopic Variations in the Rocky Bodies of the Solar System. *The Astrophysical Journal*, *937*(2), 123.

H

Hallis, L. J. (2017). D/H ratios of the inner Solar System. Philosophical Transactions of the Royal Society A: Mathematical, Physical and Engineering Sciences, 375(2094), 20150390.

Hama, T., Kouchi, A., & Watanabe, N. (2016). Statistical ortho-to-para ratio of water desorbed from ice at 10 kelvin. *Science*, *351*(6268), 65-67.

Hartogh, P., Lis, D. C., Bockelée-Morvan, D., de Val-Borro, M., Biver, N., Küppers, M., ... & Blake, G. A. (2011). Ocean-like water in the Jupiter-family comet 103P/Hartley 2. *Nature*, *478*(7368), 218-220.

Hashizume, K., & Marty, B. (2004). Nitrogen isotopic analyses at the sub-picomole level using an ultralow blank laser extraction technique. In *Handbook of stable isotope analytical techniques* (pp. 361-374). Elsevier.

Hässig, M., Altwegg, K., Balsiger, H., Bar-Nun, A., Berthelier, J. J., Bieler, A., ... & Wurz, P. (2015). Time variability and heterogeneity in the coma of 67P/Churyumov-Gerasimenko. *Science*, *347*(6220), aaa0276.

Heays, A. N., Visser, R., Gredel, R., Ubachs, W., Lewis, B. R., Gibson, S. T., & Van Dishoeck, E. F. (2014). Isotope selective photodissociation of N2 by the interstellar radiation field and cosmic rays. *Astronomy & Astrophysics*, *562*, A61.

Henning, T., & Semenov, D. (2013). Chemistry in protoplanetary disks. *Chemical Reviews*, *113*(12), 9016-9042.

Herbst, E. (2005). Chemistry of star-forming regions. *The Journal of Physical Chemistry A*, *109*(18), 4017-4029.

Hu, X., Shi, X., Sierks, H., Blum, J., Oberst, J., Fulle, M., ... & Vincent, J. B. (2017). Thermal modelling of water activity on comet 67P/Churyumov-Gerasimenko with global dust mantle and plural dust-to-ice ratio. *Monthly Notices of the Royal Astronomical Society*, *469*(Suppl_2), S295-S311.

Hutsemekers, D., Manfroid, J., Jehin, E., Zucconi, J. M., & Arpigny, C. (2008). The OH/OH and OD/OH isotope ratios in comet C/2002 T7 (LINEAR). *Astronomy & Astrophysics*, *490*(3), L31-L34.

J

Jenniskens, P., & Blake, D. F. (1994). Structural transitions in amorphous water ice and astrophysical implications. *Science*, *265*(5173), 753-756.

Jenniskens, P., & Blake, D. F. (1996). Crystallization of amorphous water ice in the solar system. *The astrophysical journal*, *473*(2), 1104.

K

Kawakita, H., Watanabe, J. I., Furusho, R., Fuse, T., Capria, M. T., De Sanctis, M. C., & Cremonese, G. (2004). Spin temperatures of ammonia and water molecules in comets. *The Astrophysical Journal*, *601*(2), 1152.

Kipfer, R., Aeschbach-Hertig, W., Peeters, F., & Stute, M. (2002). Noble gases in lakes and ground waters. *Reviews in mineralogy and geochemistry*, *47*(1), 615-700.

Kouchi, A., & Yamamoto, T. (1995). Cosmoglaciology: Evolution of ice in interstellar space and the early solar system. *Progress in crystal growth and characterization of materials*, *30*(2-3), 83-107.

Krot, A. N., Yurimoto, H., Hutcheon, I. D., & MacPherson, G. J. (2005). Chronology of the early Solar System from chondrule-bearing calcium-aluminium-rich inclusions. *Nature*, *434*(7036), 998-1001.

Kruijer, T. S., Burkhardt, C., Budde, G., & Kleine, T. (2017). Age of Jupiter inferred from the distinct genetics and formation times of meteorites. *Proceedings of the National Academy of Sciences*, *114*(26), 6712-6716.

Kuga, M., Marty, B., Marrocchi, Y., & Tissandier, L. (2015). Synthesis of refractory organic matter in the ionized gas phase of the solar nebula. *Proceedings of the National Academy of Sciences*, *112*(23), 7129-7134.

L

Läuter, M., Kramer, T., Rubin, M., & Altwegg, K. (2020). The gas production of 14 species from comet 67P/Churyumov–Gerasimenko based on DFMS/COPS data from 2014 to 2016. *Monthly Notices of the Royal Astronomical Society*, *498*(3), 3995-4004.

Le Petit, F., Roueff, E., & Herbst, E. (2004). H and other species in the diffuse cloud towards Persei: A new detailed model. *Astronomy & Astrophysics*, *417*(3), 993-1002.

Le Roy, L., Altwegg, K., Balsiger, H., Berthelier, J. J., Bieler, A., Briois, C., ... & Tzou, C. Y. (2015). Inventory of the volatiles on comet 67P/Churyumov-Gerasimenko from Rosetta/ROSINA. *Astronomy & Astrophysics*, *583*, A1.

Lee, J. E., Bergin, E. A., & Lyons, J. R. (2008). Oxygen isotope anomalies of the Sun and the original environment of the solar system. *Meteoritics & Planetary Science*, *43*(8), 1351-1362.

Lee, J. Y., Marti, K., Severinghaus, J. P., Kawamura, K., Yoo, H. S., Lee, J. B., & Kim, J. S. (2006). A redetermination of the isotopic abundances of atmospheric Ar. *Geochimica et Cosmochimica Acta*, *70*(17), 4507-4512.

Lodders, K. (2003). Solar system abundances and condensation temperatures of the elements. *The Astrophysical Journal*, *591*(2), 1220.

Loison, J. C., Wakelam, V., Gratier, P., & Hickson, K. M. (2019). Chemical nitrogen fractionation in dense molecular clouds. *Monthly Notices of the Royal Astronomical Society*, *484*(2), 2747-2756.

Luna, R., Satorre, M. Á., Santonja, C., & Domingo, M. (2014). New experimental sublimation energy measurements for some relevant astrophysical ices. *Astronomy & Astrophysics*, *566*, A27.

M

Mabry, J., Burnard, P., Blard, P. H., & Zimmermann, L. (2012). Mapping changes in helium sensitivity and peak shape for varying parameters of a Nier-type noble gas ion source. *Journal of Analytical Atomic Spectrometry*, *27*(6), 1012-1017.

Martín-Doménech, R., Caro, G. M., Bueno, J., & Goesmann, F. (2014). Thermal desorption of circumstellar and cometary ice analogs. *Astronomy & Astrophysics*, *564*, A8.

Marty, B. (1995). Nitrogen content of the mantle inferred from N2–Ar correlation in oceanic basalts. *Nature*, *377*(6547), 326-329.

Marty, B., Chaussidon, M., Wiens, R. C., Jurewicz, A. J. G., & Burnett, D. S. (2011). A 15N-poor isotopic composition for the solar system as shown by Genesis solar wind samples. *Science*, *332*(6037), 1533-1536.

Marty, B. (2012). The origins and concentrations of water, carbon, nitrogen and noble gases on Earth. *Earth and Planetary Science Letters*, *313*, 56-66.

Marty, B., Avice, G., Sano, Y., Altwegg, K., Balsiger, H., Hässig, M., ... & Rubin, M. (2016). Origins of volatile elements (H, C, N, noble gases) on Earth and Mars in light of recent results from the ROSETTA cometary mission. *Earth and Planetary Science Letters*, *441*, 91-102.

Marty, B., Altwegg, K., Balsiger, H., Bar-Nun, A., Bekaert, D. V., Berthelier, J. J., ... & Wurz, P. (2017). Xenon isotopes in 67P/Churyumov-Gerasimenko show that comets contributed to Earth's atmosphere. *Science*, *356*(6342), 1069-1072.

Marty, B., Almayrac, M., Barry, P. H., Bekaert, D. V., Broadley, M. W., Byrne, D. J., ... & Caracausi, A. (2020). An evaluation of the C/N ratio of the mantle from natural CO2-rich gas analysis: geochemical and cosmochemical implications. *Earth and Planetary Science Letters*, *551*, 116574.

Mastrapa, R. M., Grundy, W. M., & Gudipati, M. S. (2013). Amorphous and Crystalline H 2 O-Ice. In *The science of solar system ices* (pp. 371-408). Springer, New York, NY.

McCall, B. J., Geballe, T. R., Hinkle, K. H., & Oka, T. (1999). Observations of H3+ in dense molecular clouds. *The Astrophysical Journal*, *522*(1), 338.

Meier, R., Owen, T. C., Matthews, H. E., Jewitt, D. C., Bockelee-Morvan, D., Biver, N., ... & Gautier, D. (1998). A determination of the HDO/H2O ratio in comet C/1995 O1 (Hale-Bopp). *Science*, *279*(5352), 842-844.

Meshik, A., Hohenberg, C., Pravdivtseva, O., & Burnett, D. (2014). Heavy noble gases in solar wind delivered by Genesis mission. *Geochimica et cosmochimica acta*, *127*, 326-347.

Mifsud, D. V., Hailey, P. A., Herczku, P., Juhász, Z., Kovács, S. T., Sulik, B., ... & Mason, N. J. (2022). Laboratory experiments on the radiation astrochemistry of water ice phases. *The European Physical Journal D*, *76*(5), 1-15.

Morbidelli, A., Chambers, J., Lunine, J. I., Petit, J. M., Robert, F., Valsecchi, G. B., & Cyr, K. E. (2000). Source regions and timescales for the delivery of water to the Earth. *Meteoritics & Planetary Science*, *35*(6), 1309-1320.

Mousis, O., Lunine, J. I., Picaud, S., & Cordier, D. (2010). Volatile inventories in clathrate hydrates formed in the primordial nebula. *Faraday discussions*, *147*, 509-525.

Mousis, O., Ronnet, T., Lunine, J. I., Luspay-Kuti, A., Mandt, K. E., Danger, G., ... & d’Hendecourt, L. L. S. (2018). Noble gas abundance ratios indicate the agglomeration of

67P/Churyumov–Gerasimenko from warmed-up ice. *The Astrophysical journal letters*, *865*(1), L11.

Müller, H. S., Schlöder, F., Stutzki, J., & Winnewisser, G. (2005). The Cologne Database for Molecular Spectroscopy, CDMS: a useful tool for astronomers and spectroscopists. *Journal of Molecular Structure*, *742*(1-3), 215-227.

Müller, D. R., Altwegg, K., Berthelier, J. J., Combi, M. R., De Keyser, J., Fuselier, S., ... & Wampfler, S. F. (2022). High D/H ratios in water and alkanes in comet 67P/Churyumov-Gerasimenko measured with the Rosetta/ROSINA DFMS. *arXiv preprint arXiv:2202.03521*.

Mumma, M. J., Blass, W. E., Weaver, H. A., & Larson, H. P. (1988, June). Measurements of the ortho-para ratio and nuclear spin temperature of water vapor in comets Halley and Wilson (1986l) and implications for their origin and evolution. In *Bulletin of the American Astronomical Society* (Vol. 20, p. 826).

Muñoz Caro, G. M., Meierhenrich, U., Schutte, W. A., & Greenberg, J. M. (2004). UV-photoprocessing of interstellar ice analogs: Detection of hexamethylenetetramine-based species. *Astronomy & Astrophysics*, *413*(1), 209-216.

Murray, N. (2011). Star formation efficiencies and lifetimes of giant molecular clouds in the Milky Way. *The Astrophysical Journal*, *729*(2), 133.

Muskatel, B. H., Remacle, F., Thiemens, M. H., & Levine, R. D. (2011). On the strong and selective isotope effect in the UV excitation of N2 with implications toward the nebula and Martian atmosphere. *Proceedings of the National Academy of Sciences*, *108*(15), 6020-6025.

N

Nier, A. O. (1947). A mass spectrometer for isotope and gas analysis. *Review of Scientific Instruments*, *18*(6), 398-411.

Nier, A. O. (1950). A redetermination of the relative abundances of the isotopes of carbon, nitrogen, oxygen, argon, and potassium. *Physical Review*, *77*(6), 789.

Notesco, G., Kleinfeld, I., Laufer, D., & Bar-Nun, A. (1991). Gas release from comets. *Icarus*, *89*(2), 411-413.

Notesco, G., Laufer, D., Bar-Nun, A., & Owen, T. (1999). An experimental study of the isotopic enrichment in Ar, Kr, and Xe when trapped in water ice. *Icarus*, *142*(1), 298-300.

Notesco, G., Bar-Nun, A., & Owen, T. (2003). Gas trapping in water ice at very low deposition rates and implications for comets. *Icarus*, *162*(1), 183-189.

Notesco, G., & Bar-Nun, A. (2005). A∼ 25 K temperature of formation for the submicron ice grains which formed comets. *Icarus*, *175*(2), 546-550.

O

Öberg, K. I., & Bergin, E. A. (2021). Astrochemistry and compositions of planetary systems. *Physics Reports*, *893*, 1-48.

Owen, T., Bar-Nun, A., & Kleinfeld, I. (1992). Possible cometary origin of heavy noble gases in the atmospheres of Venus, Earth and Mars. *Nature*, *358*(6381), 43-46.

Owen, T. C., & Bar-Nun, A. (2001). Contributions of icy planetesimals to the Earth's early atmosphere. *Origins of Life and Evolution of the Biosphere*, *31*(4), 435-458.

P

Palumbo, M. E. (2006). Formation of compact solid water after ion irradiation at 15 K. *Astronomy & Astrophysics*, *453*(3), 903-909.

Palumbo, M. E., Baratta, G. A., Leto, G., & Strazzulla, G. (2010). H bonds in astrophysical ices. *Journal of Molecular Structure*, *972*(1-3), 64-67.

Parent, P., Laffon, C., Mangeney, C., Bournel, F., & Tronc, M. (2002). Structure of the water ice surface studied by x-ray absorption spectroscopy at the O K-edge. *The Journal of chemical physics*, *117*(23), 10842-10851.

Patashnick, H., Rupprecht, G., & Schuerman, D. W. (1974). Energy source for comet outbursts. *Nature*, *250*(5464), 313-314.

Pepin, R. O. (1991). On the origin and early evolution of terrestrial planet atmospheres and meteoritic volatiles. *Icarus*, *92*(1), 2-79.

Piani, L., Tachibana, S., Hama, T., Tanaka, H., Endo, Y., Sugawara, I., ... & Kouchi, A. (2017). Evolution of morphological and physical properties of laboratory interstellar organic residues with ultraviolet irradiation. *The Astrophysical Journal*, *837*(1), 35.

Pignatale, F. C., Charnoz, S., Chaussidon, M., & Jacquet, E. (2018). Making the planetary material diversity during the early assembling of the solar system. *The Astrophysical journal letters*, *867*(2), L23.

Prialnik, D., Egozi, U., Bar-Nun, A., Podolak, M., & Greenzweig, Y. (1993). On pore size and fracture in gas-laden comet nuclei. *Icarus*, *106*(2), 499-507.

Prialnik, D., & Jewitt, D. (2022). Amorphous ice in comets: evidence and consequences. *arXiv preprint arXiv:2209.05907*.

R

Raut, U., Famá, M., Loeffler, M. J., & Baragiola, R. A. (2008). Cosmic ray compaction of porous interstellar ices. *The Astrophysical Journal*, *687*(2), 1070.

Rodgers, S. D., & Charnley, S. B. (2008). Nitrogen superfractionation in dense cloud cores. *Monthly Notices of the Royal Astronomical Society: Letters*, *385*(1), L48-L52.

Rowland, B., Kadagathur, N. S., Devlin, J. P., Buch, V., Feldman, T., & Wojcik, M. J. (1995). Infrared spectra of ice surfaces and assignment of surface-localized modes from simulated spectra of cubic ice. *The Journal of chemical physics*, *102*(21), 8328-8341.

Rubie, D. C., Jacobson, S. A., Morbidelli, A., O'Brien, D. P., Young, E. D., de Vries, J., ... & Frost, D. J. (2015). Accretion and differentiation of the terrestrial planets with implications for the compositions of early-formed Solar System bodies and accretion of water. *Icarus*, *248*, 89-108.

Rubin, M., Altwegg, K., Balsiger, H., Bar-Nun, A., Berthelier, J. J., Bieler, A., ... & Wurz, P. (2015). Molecular nitrogen in comet 67P/Churyumov-Gerasimenko indicates a low formation temperature. *Science*, *348*(6231), 232-235.

Rubin, M., Altwegg, K., Balsiger, H., Bar-Nun, A., Berthelier, J. J., Briois, C., ... & Wurz, P. (2018). Krypton isotopes and noble gas abundances in the coma of comet 67P/Churyumov-Gerasimenko. *Science advances*, *4*(7), eaar6297.

Rubin, M., Bekaert, D. V., Broadley, M. W., Drozdovskaya, M. N., & Wampfler, S. F. (2019). Volatile species in comet 67P/Churyumov-Gerasimenko: investigating the link from the ISM to the terrestrial planets. *ACS earth and space chemistry*, *3*(9), 1792-1811.

Rubin, M., Engrand, C., Snodgrass, C., Weissman, P., Altwegg, K., Busemann, H., ... & Mumma, M. (2020). On the origin and evolution of the material in 67P/Churyumov-Gerasimenko. *Space science reviews*, *216*(5), 1-43.

S

Sandford, S. A., & Allamandola, L. J. (1988). The condensation and vaporization behavior of H2O: CO ices and implications for interstellar grains and cometary activity. *Icarus*, *76*(2), 201-224.

Sebree, J. A., Wayson, J. M., & Lopez, J. R. (2018). Variation in photon flux during extended photochemical aerosol experiments: Implications for atmospheric laboratory simulations. *Journal of Photochemistry and Photobiology A: Chemistry*, *360*, 1-5.

Smoluchowski, R. (1981). Amorphous ice and the behavior of cometary nuclei. *The Astrophysical Journal*, *244*, L31-L34.

Snow, T. P., & Witt, A. N. (1996). Interstellar depletions updated: Where all the atoms went. *The Astrophysical Journal*, *468*(1), L65.

Stevenson, K. P., Kimmel, G. A., Dohnalek, Z., Smith, R. S., & Kay, B. D. (1999). Controlling the morphology of amorphous solid water. *Science*, *283*(5407), 1505-1507.

Sugahara, H., Takano, Y., Tachibana, S., Sugawara, I., Chikaraishi, Y., Ogawa, N. O., ... & Yurimoto, H. (2019). Molecular and isotopic compositions of nitrogen-containing organic molecules formed during UV-irradiation of simulated interstellar ice. *Geochemical Journal*, *53*(1), 5-20.

Sugisaki, M., Suga, H., & Seki, S. (1969). Calorimetric study of glass transition of the amorphous ice and of the phase transformation between the cubic and hexagonal ices. *Physics of Ice. Platinum Press, New York*, 329-343.

T

Tachibana, S., Kouchi, A., Hama, T., Oba, Y., Piani, L., Sugawara, I., ... & Watanabe, N. (2017). Liquid-like behavior of UV-irradiated interstellar ice analog at low temperatures. *Science advances*, *3*(9), eaao2538.

Terzieva, R., & Herbst, E. (2000). The possibility of nitrogen isotopic fractionation in interstellar clouds. *Monthly Notices of the Royal Astronomical Society*, *317*(3), 563-568.

V

Vacher, L. G., Piani, L., Rigaudier, T., Thomassin, D., Florin, G., Piralla, M., & Marrocchi, Y. (2020). Hydrogen in chondrites: Influence of parent body alteration and atmospheric contamination on primordial components. *Geochimica et Cosmochimica Acta*, *281*, 53-66.

Vermeesch, P. (2018). IsoplotR: A free and open toolbox for geochronology. *Geoscience Frontiers*, *9*(5), 1479-1493.

Villanueva, G. L., Mumma, M. J., Bonev, B. P., DiSanti, M. A., Gibb, E. L., Böhnhardt, H., & Lippi, M. (2008). A sensitive search for deuterated water in comet 8P/Tuttle. *The Astrophysical Journal*, *690*(1), L5.

Villeneuve, J., Chaussidon, M., & Libourel, G. (2009). Homogeneous distribution of 26Al in the solar system from the Mg isotopic composition of chondrules. *Science*, *325*(5943), 985-988.

Vinogradoff, V., Duvernay, F., Danger, G., Theulé, P., & Chiavassa, T. (2011). New insight into the formation of hexamethylenetetramine (HMT) in interstellar and cometary ice analogs. *Astronomy & Astrophysics*, *530*, A128.

W

Wang, H., Weiss, B. P., Bai, X. N., Downey, B. G., Wang, J., Wang, J., ... & Zucolotto, M. E. (2017). Lifetime of the solar nebula constrained by meteorite paleomagnetism. *Science*, *355*(6325), 623-627.

Warr, O. W. P. (2013). *Understanding phase behaviour in the geological storage of carbon dioxide* (Doctoral dissertation, University of Manchester).

Wetherill, G. W. (1980). Formation of the terrestrial planets. *Annual review of astronomy and astrophysics*, *18*, 77-113.

Wright, I. P., Boyd, S. R., Franchi, I. A., & Pillinger, C. T. (1988). High-precision determination of nitrogen stable isotope ratios at the sub-nanomole level. *Journal of Physics E: Scientific Instruments*, *21*(9), 865.

Y

Yabushita, A., Hama, T., & Kawasaki, M. (2013). Photochemical reaction processes during vacuum-ultraviolet irradiation of water ice. *Journal of Photochemistry and Photobiology C: Photochemistry Reviews*, *16*, 46-61.

Yokochi, R., & Marty, B. (2006). Fast chemical and isotopic exchange of nitrogen during reaction with hot molybdenum. *Geochemistry, Geophysics, Geosystems*, *7*(7).

Yokochi, R., Marboeuf, U., Quirico, E., & Schmitt, B. (2012). Pressure dependent trace gas trapping in amorphous water ice at 77 K: Implications for determining conditions of comet formation. *Icarus*, *218*(2), 760-770.

Young, E. D., Galy, A., & Nagahara, H. (2002). Kinetic and equilibrium mass-dependent isotope fractionation laws in nature and their geochemical and cosmochemical significance. *Geochimica et Cosmochimica Acta*, *66*(6), 1095-1104.

Z

Zahnle, K. J., Gacesa, M., & Catling, D. C. (2019). Strange messenger: A new history of hydrogen on Earth, as told by Xenon. *Geochimica et Cosmochimica Acta*, *244*, 56-85.

Zimmermann, L., Füri, E., & Burnard, P. (2015). Purification des gaz rares sous ultravide-Méthodes de purification. *Techniques de l’ingénieur, (J6635)*, 1-23.

Zimmermann, L., & Bekaert, D. (2020). Analyse des gaz rares par spectrométrie de masse statique-Théorie et Instrumentation. *Techniques de l’ingénieur*.

Appendix

Appendix A

Appendix Table A1: Source settings for the GV Helix MC

Appendix Table A2: Source settings for the Helix MC$^+$

Appendix Table A3: Xenon isotope ratios in ices formed at 28K, 50K and 70K.

Appendix Table A4: Argon and nitrogen isotope ratios in ices formed at 28K and 50K.

Appendix Figure A1: Signals conversion and theoretical precision on mass spectrometers.

Appendix Figure A2: Evolution of Xe release from an ice irradiated for 5 minutes at 120K

Appendix Figure A3: Xenon isotope composition of ices formed at 28K, 50K and 70K.

Appendix Table A1: Source settings for Ar and Xe on the GV Helix MC.

Parameter	Argon	Xenon
Acceleration Reference	4 500 V	4 500 V
Trap Current	**250 µA**	**280 µA**
Trap Voltage	15 V	15 V
Electron Energy	-74.9 V	-79 V
Ion repeller	-5.5 V	-4.6 V
Filament voltage	2.37 V	2.5 V
Y Focus	76 %	76.8 %
Y Bias	11 V	13.6 V
Z Focus	4 %	4 %
Z bias	68.3 V	60.4 V

Appendix Table A2: Source settings for nitrogen and argon measurements on the Helix MC$^+$ mass spectrometer.

Parameter	Settings
Acceleration Reference	9 900 V
Trap Current	**50 µA**
Trap Voltage	40 V
Electron Energy	70 eV
Ion Repeller	-6.18 V
Extraction Lens	81%
Extraction Focus	28.53 %
Extraction Symmetry	1.59 %
Horizontal Symmetry	-3.39 %
Field	3.16 V
Flatapole	-0.5 V
Rotation Quad	4 %
Vertical Deflection	80 V
Horizontal Deflection	60 V

		^{40}Ar (V)	±	$^{40}Ar/^{36}Ar$	±	$^{38}Ar/^{36}Ar$	±
Standards reproducibility					0.75%		0.37%
Starting composition		0.1803	0.0038	293.3	1.7	0.1995	0.0029
		0.1512	0.0032	287.9	1.7	0.1895	0.0030
		0.2068	0.0044	291.7	1.6	0.1862	0.0026
		0.0446	0.0009	279.9	2.8	0.1963	0.0075
		0.3267	0.0069	293.5	1.6	0.1910	0.0023
28K	Trapped	0.3756	0.0000	289.8	1.6	0.1890	0.0022
50K	Trapped	0.1342	0.0000	313.0	1.9	0.1870	0.0035
		0.2169	0.0000	312.5	1.8	0.1974	0.0027
		0.5304	0.0001	317.2	1.7	0.1927	0.0022

		^{28}N (fA)	±	$\delta^{15}N$ (‰)	±
Standards reproducibility					1 ‰
Starting composition		10906	5	-6.1	1.3
		11137	4	-6.1	1.3
		12550	2	-5.8	1.1
		4539	4	-11.0	2.7
		8337	3	-5.2	1.2
		7233	5	-4.9	1.5
50K	Trapped	1281	1	2.4	2.6
		1551	2	16.2	2.5
		9514	4	23.9	1.3
		2623	3	12.9	2.0
		2030	2	10.5	1.7
		10764	4	27.4	1.2
		6390	1	27.4	1.3
		14686	7	27.4	1.3

Appendix Table A4: Argon isotope ratios of the starting gas and the trapped phase of ices formed at 28K and 50K. The nitrogen isotope composition is given in permil deviation relative to air ($^{15}N/^{14}N_{atm}$ = 0.003676, Nier, 1950 and $\delta^{15}N_{atm}$ = 0 ‰ by definition). In the case of nitrogen, the isotope composition is dependent on the signal size (non-linearity effect, Chapter 2).

			^{132}Xe (V)	±	^{128}Xe/^{132}Xe	±	^{129}Xe/^{132}Xe	±	^{130}Xe/^{132}Xe	±	^{131}Xe/^{132}Xe	±	^{134}Xe/^{132}Xe	±	^{136}Xe/^{132}Xe	±
Standards reproducibility					0.26%		0.04%		0.16%		0.05%		0.06%		0.17%	
Starting composition (bottle)			0.05 to 0.30		0.0720	0.0001	0.9902	0.0005	0.1525	0.0001	0.7908	0.0002	0.3867	0.0001	0.3281	0.0002
28K	Frozen	1	0.0154	0.0004	0.0722	0.0014	0.9961	0.0023	0.1502	0.0013	0.7962	0.0020	0.3877	0.0018	0.3277	0.0016
		2	0.0559	0.0014	0.0721	0.0004	0.9936	0.0007	0.1525	0.0003	0.7922	0.0006	0.3865	0.0005	0.3269	0.0005
	Trapped	1	0.0868	0.0022	0.0728	0.0002	0.9940	0.0010	0.1532	0.0003	0.7933	0.0008	0.3868	0.0004	0.3280	0.0004
		2	0.0836	0.0021	0.0723	0.0002	0.9923	0.0010	0.1533	0.0003	0.7915	0.0008	0.3870	0.0005	0.3284	0.0004
		3	0.2432	0.0062	0.0720	0.0001	0.9923	0.0004	0.1526	0.0001	0.7910	0.0003	0.3864	0.0002	0.3283	0.0002
50K	Frozen	1	0.0644	0.0016	0.0728	0.0003	0.9918	0.0007	0.1542	0.0003	0.7904	0.0006	0.3870	0.0005	0.3272	0.0004
	Trapped	1	0.1146	0.0029	0.0727	0.0002	0.9918	0.0006	0.1532	0.0002	0.7920	0.0005	0.3862	0.0003	0.3276	0.0003
		2	0.1263	0.0032	0.0723	0.0002	0.9924	0.0006	0.1529	0.0002	0.7915	0.0004	0.3868	0.0003	0.3275	0.0003
		3	0.2196	0.0056	0.0719	0.0001	0.9921	0.0004	0.1527	0.0001	0.7919	0.0003	0.3858	0.0002	0.3273	0.0002
		4	0.1961	0.0050	0.0719	0.0001	0.9919	0.0003	0.1524	0.0001	0.7914	0.0002	0.3858	0.0002	0.3272	0.0002
70K	Frozen	1	0.1755	0.0044	0.0719	0.0001	0.9899	0.0007	0.1526	0.0002	0.7901	0.0006	0.3877	0.0003	0.3283	0.0003
	Trapped	1	0.0929	0.0024	0.0728	0.0002	0.9921	0.0010	0.1535	0.0003	0.7904	0.0008	0.3881	0.0005	0.3291	0.0004
		2	0.2121	0.0054	0.0720	0.0001	0.9914	0.0004	0.1525	0.0001	0.7916	0.0003	0.3869	0.0002	0.3283	0.0002
		3	0.0851	0.0022	0.0728	0.0003	0.9933	0.0013	0.1544	0.0003	0.7913	0.0010	0.3877	0.0006	0.3294	0.0005
		4	0.1956	0.0049	0.0720	0.0001	0.9902	0.0004	0.1525	0.0001	0.7904	0.0003	0.3863	0.0002	0.3281	0.0002
		5	0.2150	0.0054	0.0717	0.0001	0.9905	0.0003	0.1523	0.0001	0.7908	0.0002	0.3868	0.0002	0.3279	0.0002
		6	0.1792	0.0045	0.0724	0.0001	0.9907	0.0007	0.1532	0.0001	0.7910	0.0006	0.3871	0.0003	0.3286	0.0002
		7	0.2578	0.0065	0.0720	0.0001	0.9906	0.0005	0.1526	0.0001	0.7917	0.0004	0.3870	0.0002	0.3280	0.0002
		8	0.2281	0.0058	0.0719	0.0001	0.9899	0.0003	0.1521	0.0001	0.7908	0.0003	0.3863	0.0001	0.3276	0.0001
		9	0.3448	0.0087	0.0721	0.0001	0.9919	0.0004	0.1526	0.0001	0.7916	0.0003	0.3869	0.0002	0.3278	0.0002
		10	0.1563	0.0040	0.0723	0.0001	0.9920	0.0006	0.1528	0.0002	0.7909	0.0005	0.3867	0.0003	0.3283	0.0003
		11	0.2369	0.0060	0.0717	0.0001	0.9907	0.0004	0.1525	0.0001	0.7912	0.0003	0.3857	0.0002	0.3281	0.0002

Table continued

			^{132}Xe (V)	±	^{128}Xe/^{132}Xe	±	^{129}Xe/^{132}Xe	±	^{130}Xe/^{132}Xe	±	^{131}Xe/^{132}Xe	±	^{134}Xe/^{132}Xe	±	^{136}Xe/^{132}Xe	±
50K Irradiated	Frozen	1	0.1122	0.0028	0.0724	0.0002	0.9911	0.0007	0.1532	0.0002	0.7915	0.0006	0.3860	0.0004	0.3282	0.0003
		2	0.0784	0.0020	0.0725	0.0003	0.9908	0.0010	0.1530	0.0003	0.7917	0.0008	0.3857	0.0005	0.3269	0.0004
		3	0.1906	0.0048	0.0723	0.0001	0.9923	0.0005	0.1526	0.0001	0.7907	0.0004	0.3860	0.0003	0.3271	0.0002
		4	0.2405	0.0061	0.0721	0.0001	0.9934	0.0004	0.1530	0.0001	0.7919	0.0003	0.3860	0.0002	0.3270	0.0002
	Trapped	1	0.0731	0.0018	0.0731	0.0003	0.9918	0.0011	0.1539	0.0003	0.7918	0.0008	0.3870	0.0005	0.3276	0.0005
		2	0.3126	0.0079	0.0718	0.0001	0.9918	0.0002	0.1525	0.0001	0.7914	0.0002	0.3856	0.0001	0.3269	0.0001
	Late trapped	1	0.0294	0.0007	0.0744	0.0007	0.9997	0.0016	0.1544	0.0007	0.7937	0.0013	0.3882	0.0010	0.3271	0.0010
		2	0.1131	0.0029	0.0718	0.0002	0.9933	0.0006	0.1525	0.0002	0.7921	0.0004	0.3851	0.0003	0.3259	0.0003
		3	0.0869	0.0022	0.0723	0.0002	0.9924	0.0009	0.1532	0.0003	0.7923	0.0007	0.3858	0.0004	0.3262	0.0004
		4	0.2064	0.0052	0.0722	0.0001	0.9946	0.0004	0.1527	0.0001	0.7925	0.0003	0.3851	0.0002	0.3261	0.0002

Appendix Table A3: Xenon isotope ratios (uncorrected) measured in the frozen and trapped phases of ices formed at 28K, 50K and 70K. the standard reproducibility of a given ratio is the standard deviation of the standards (n = 23). The starting composition is the isotope composition of the gas contained in the bottle and the given uncertainty is the standard error (n = 13), and the contribution from the reproducibility. Uncertainties of the ratios measured in the ice are the sum of the internal error of the measurement and the reproducibility (see Chapter 2). All uncertainties at 1σ.

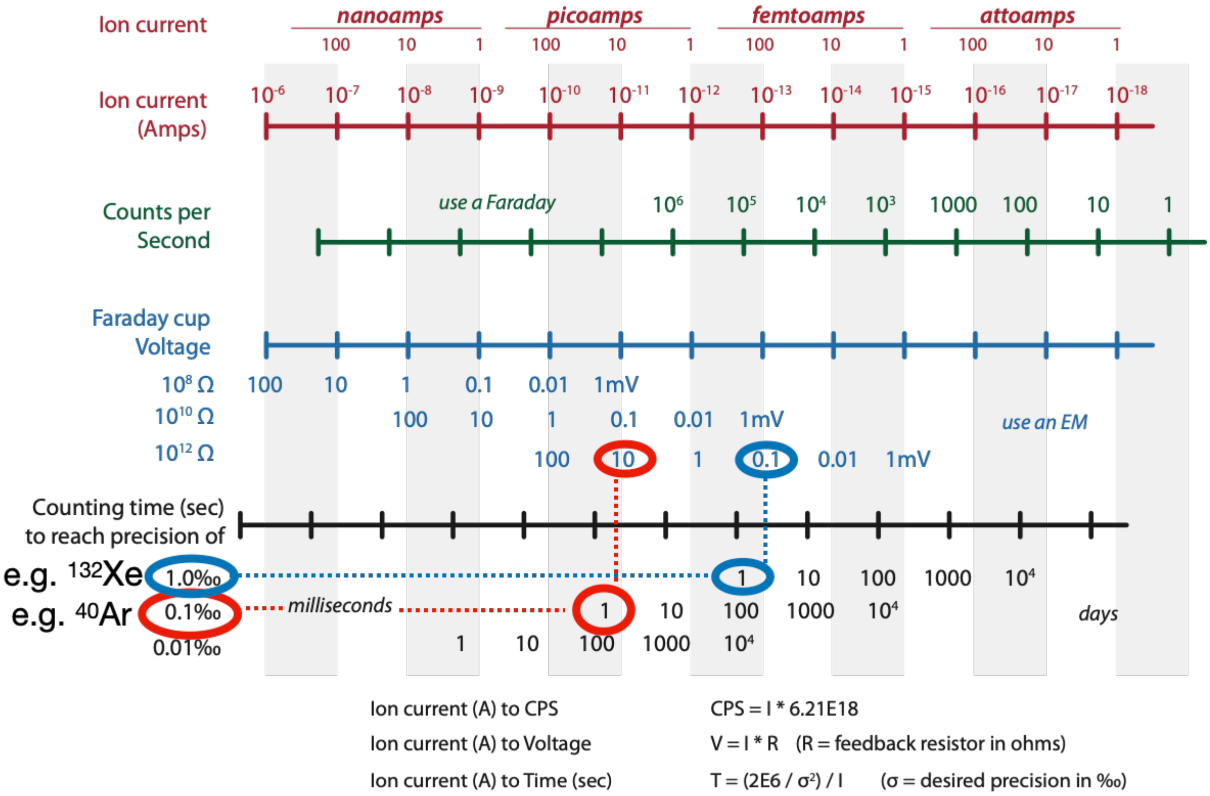

Appendix Figure A1: Conversions between signal measured in ampers and volts, and the precision that can be reached for a given signal and counting time (taken in Caltech courses on IRSM). For example, ^{40}Ar from standards is measured at ~1 V using a 10^{11} Ω Faraday cup on the GV Helix MC. This is equivalent to 10 V on a 10^{12} Ω Faraday cup (red circle). With a counting time of 1 second, the precision on the measurement can theoretically reach 0.1‰. This is what we observe for the internal error on the ^{40}Ar signal measurement (Figures 2.10 and 2.12). Isotope ^{132}Xe is measured at a lower signal (~0.1 V) also for 1 second, leading to a precision of ~1‰ (Figures 2.11 and 2.14).

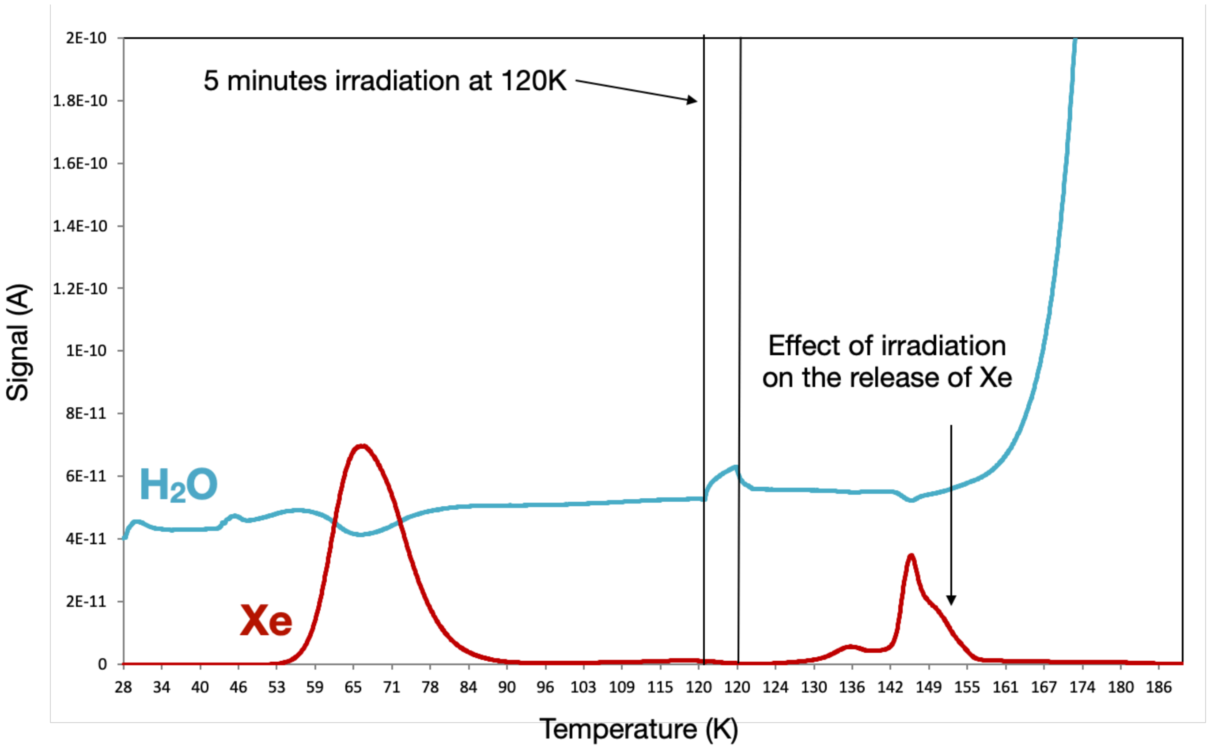

Appendix Figure A2: Evolution of Xe and water signals measured by the QMS released from the ice heated at 1K/min between 28K (deposition temperature) and 190K. The temperature was maintained for 5 minutes at 120K, while irradiating the surface of the ice using the photon lamp. The release of Xe at ~145K is not spread over several peaks as observed after 35 minutes of irradiation (Figure 3.11) but still differs from the pattern of a non-irradiated ice (Figure 3.4).

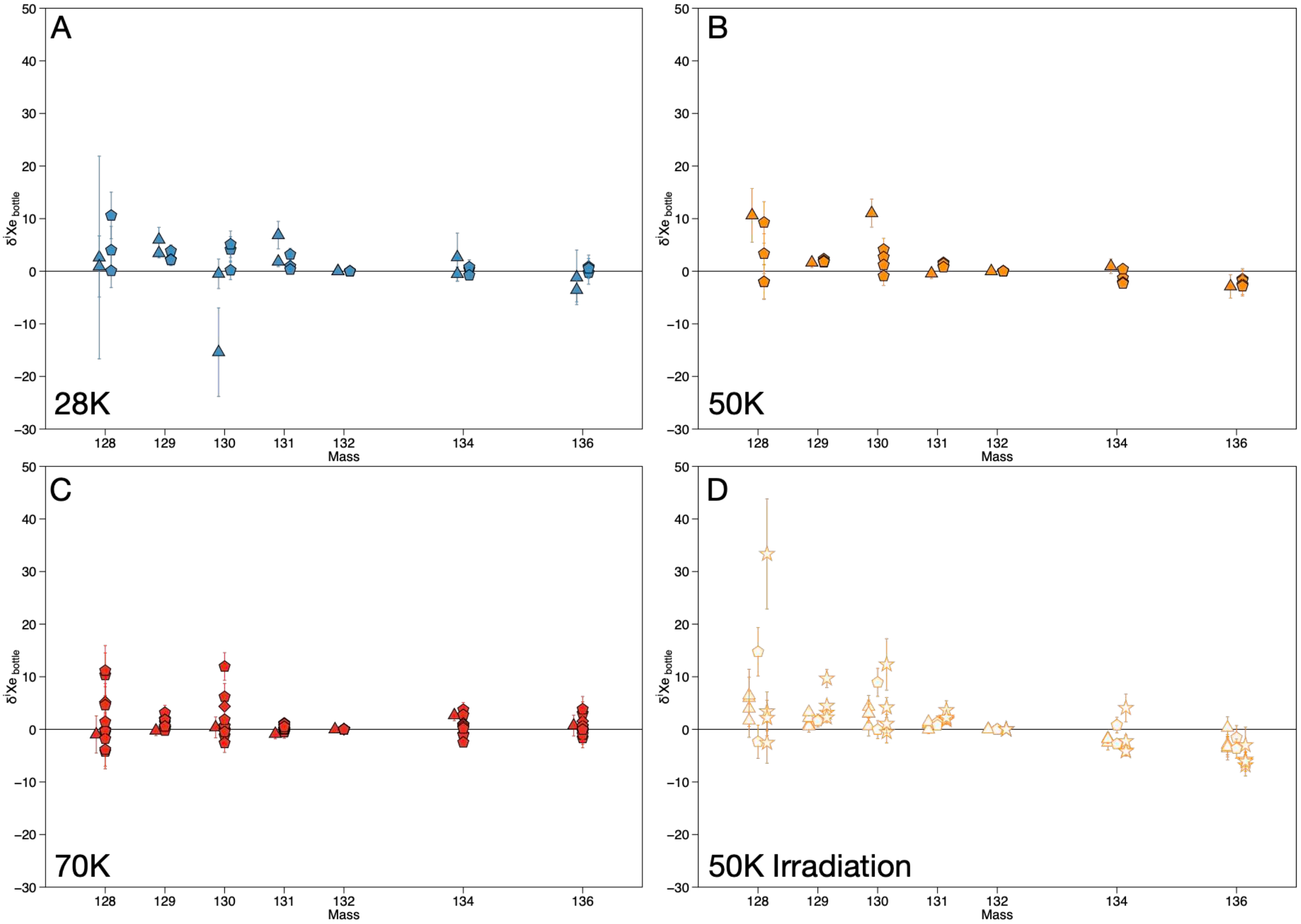

Appendix Figure A3: Xenon isotope composition of the frozen phase (diamonds) and the trapped phase (pentagons) for ices formed at 28K (**A**), 50K (**B**) and 70K (**C**) without irradiation. Experiments with irradiation during deposition were performed at 50K (D), with star symbols showing the composition of the "late trapped phase", as described in the main text Chapter 4. Experiments were reproduced several times, and gas was analysed multiple times when in sufficient amounts.

Supplementary Material for Chapter 4

Mass-dependent isotope fractionation laws

Considering three isotopes 1, 2 and 3, with masses m1, m2 and m3, and two isotope ratios 1/2 and 3/1, the mass-dependent relation between the fractionation factor α of each ratio can be written as (Young et al. 2002; Dauphas & Schauble 2016):

$$\alpha_{1/2} = {\alpha_{3/1}}^{\beta}$$

With the exponential factor β depending on the type of fractionation:

Equilibrium fractionation:

$$\left.\frac{1}{m1} - \frac{1}{m2}\middle/\frac{1}{m1} - \frac{1}{m3}\right.$$

Kinetic fractionation:

$$\left.ln\left(\frac{m1}{m2}\right)\middle/ln\left(\frac{m1}{m3}\right)\right.$$

Gravity/centrifugal fractionation:

$$\left.(m1 - m2)\middle/(m1 - m3)\right.$$

Appendix B

“Possible Discontinuous Evolution of Atmospheric Xenon Suggested by Archean Barites“, article published in Chemical Geology in 2021

Chemical Geology 581 (2021) 120405

Contents lists available at ScienceDirect

Chemical Geology

journal homepage: www.elsevier.com/locate/chemgeo

Invited research article

Possible discontinuous evolution of atmospheric xenon suggested by Archean barites

Matthieu G. Almayrac[a,*], Michael W. Broadley[a], David V. Bekaert[a,b], Axel Hofmann[c], Bernard Marty[a]

[a] Université de Lorraine, CNRS, CRPG, F-54000 Nancy, France
[b] Marine Chemistry and Geochemistry Department, Woods Hole Oceanographic Institution, Woods Hole, MA 02543, USA
[c] Department of Geology, University of Johannesburg, Johannesburg, South Africa

ARTICLE INFO

Editor: Don Porcelli

Keywords:
Archean barite
Noble gases
Xenon anomalies
Archean atmosphere

ABSTRACT

The Earth's atmosphere has continually evolved since its formation through interactions with the mantle as well as through loss of volatile species to space. Atmospheric xenon isotopes show a unique and progressive evolution during the Archean that stopped around the Archean-Proterozoic transition. The Xe isotope composition of the early atmosphere has been previously documented through the analysis of fluid inclusions trapped within quartz and barite. Whether this evolution was continuous or not is unclear, requiring additional analyses of ancient samples, which may potentially retain remnants of the ancient atmosphere. Here we present new argon, krypton and xenon isotopic data from a suite of Archean and Proterozoic barites ranging in age from 3.5 to 1.8 Ga, with the goal of providing further insights in to the evolution of atmospheric Xe, whilst also outlining the potential complications that can arise when using barites as a record of past atmospheres. Xenon released by low temperature pyrolysis and crushing of two samples which presumably formed around 2.8 and 2.6 Ga show Xe isotope mass dependent fractionation (MDF) of 11‰.u^{-1} and 3.4‰.u^{-1}, respectively, relative to modern atmosphere. If trapped Xe is contemporaneous with the respective formation age, the significant difference in the degree of fractionation between the two samples provides supporting evidence for a plateau in the MDF-Xe evolution between 3.3 Ga and 2.8 Ga, followed by a rapid evolution at 2.8–2.6 Ga. This sharp decrease in MDF-Xe degree suggests the potential for a discontinuous temporal evolution of atmospheric Xe isotopes, which could have far reaching implications regarding current physical models of the early evolution of the Earth's atmosphere.

1. Introduction

The evolutionary history of the Earth's atmosphere can be elucidated through the analysis of atmospheric remnants residing within the geological record. Due to their chemical inertness, noble gases constitute powerful tracers of the physical processes that have occurred in the atmosphere since its formation. Previous analyses of Archean, Proterozoic and Phanerozoic rocks have shown that some specific samples have kept a record of the ancient atmosphere at different stages of its evolution (Cadogan, 1977; Pujol et al., 2011; Pujol et al., 2013; Stuart et al., 2016; Avice et al., 2017; Avice et al., 2018; Bekaert et al., 2018). Among the noble gases, xenon is the most promising to decipher the early evolution of the atmosphere. Xenon isotopes trapped in fluid inclusions and organic matter residing in Archean-aged rocks have been shown to have isotopic compositions intermediate between the modern atmospheric value and planetary precursors, indicating the atmosphere progressively evolved through time via mass dependent fractionation (MDF; Pujol et al., 2011; Avice et al., 2017). Specifically, Xe isotopic signatures measured in Archean-aged samples show that the ancient atmosphere was enriched in light isotopes relative to its present-day composition, and that the degree of mass fractionation relative to its modern composition decreased with time, finally reaching its current composition at around ~2 Ga (Avice et al., 2018).

Modern atmospheric Xe is fractionated by ~30–40‰ per atomic mass unit (u) relative to its presumed initial composition (U—Xe, Pepin, 1991; Marty et al., 2017). Because isotope fractionation appears to be limited to Xe (Pujol et al., 2011; Avice et al., 2018), a thermal (mass-dependent) process is unlikely to be responsible for Xe escape to space. Xenon does however have a lower first ionization potential than other noble gases (Hébrard and Marty, 2014; Zahnle et al., 2019). Notably

---

* Corresponding author.
E-mail address: matthieu.almayrac@univ-lorraine.fr (M.G. Almayrac).

https://doi.org/10.1016/j.chemgeo.2021.120405
Received 8 January 2021; Received in revised form 7 May 2021; Accepted 22 June 2021

solar UV photons with wavelengths below 100 nm that are able to ionize Xe were potentially more abundant during the Archean and the Hadean eons than today (Ribas et al., 2005). Hébrard and Marty (2014) proposed that the formation of organic haze in the high atmosphere could preferentially trap heavy Xe^+ isotopes, thus preferentially retaining atmospheric Xe heavy isotopes relative to the escaping, lighter ones. However, this model did not detail the mechanism by which Xe^+ escaped to space. A more recent model proposed that escaping hydrogen ions formed by the photo-dissociation of water vapour were able to drag Xe^+ up, with the lighter isotopes escaping to space more easily than the heavier ones (Zahnle et al., 2019). In this model, Xe escaped as an ion lifted up by H^+ along polar magnetic field lines, hence requiring both high-energy EUV (extreme ultra-violet) irradiation from the young Sun and a H-rich atmosphere during the Archean eon relative to modern composition, until the Great Oxidation Event. This Xe-escape mechanism could potentially solve both features of the "xenon paradox" (Ozima and Podosek, 2002): (i) Xe elemental depletion by a factor of ~10 compared to the expected noble gas elemental pattern defined by chondrites (Ozima and Podosek, 2002; Bekaert et al., 2020a), and (ii) isotopic fractionation favouring the heavy Xe isotopes relative to potential cosmochemical precursors.

Determining whether the progressive isotopic evolution of atmospheric Xe was continuous, or not, could provide unique constraints on the evolution of solar activity and Sun-Earth interactions (Ribas et al., 2005; Claire et al., 2012; Zahnle et al., 2019), episodes of extreme mantle degassing (Abbott and Isley, 2002; Marty et al., 2019), and the relationship between atmospheric escape processes and the Great Oxidation Event (Gumsley et al., 2017). To document further the evolution of atmospheric Xe isotopic composition, additional analyses of xenon isotopes trapped in ancient rocks are needed. Barites are promising candidates because of their pervasiveness during the Archean eon and high preservation potential thanks to their low reactivity (Huston and Logan, 2004). Previous works have shown that xenon in barites is in isotopic equilibrium with the atmosphere at the moment of their formation, potentially providing a compositional record of the ancient atmosphere (Meshik et al., 2001; Pujol et al., 2009). This approach requires the samples, in particular the host phases of trapped noble gases, to be accurately dated, which can be challenging as barites are often secondary with respect to the main rock formation (e.g., hydrothermal veins or secondary replacement; Heinrichs and Reimer, 1977).

One promising avenue for providing accurate ages for Archean barites is to use the radioactive decay of ^{130}Ba (~0.1% isotopic abundance) to ^{130}Xe (Meshik et al., 2001; Pujol et al., 2009). Two main decay chains through which ^{130}Xe is produced from Ba are the double β^+ decay ($2\beta^+$) and the double electron capture (2EC) on ^{130}Ba. The primary decay is 2EC with a half-life historically estimated from proton-neutron quasi-particle random phase approximations (*pn*-QRPAs) to be 4.2×10^{21} yr (Hirsch et al., 1994). From the analysis of 200 Ma barites, Meshik et al. (2001) estimated the half-life to be $2.2 \pm 0.5 \times 10^{21}$ yr, consistent with the model-derived value. Subsequently, Pujol et al. (2009) obtained a value of $6.0 \pm 1.1 \times 10^{20}$ yr, one order of magnitude lower than what had been previously proposed, from the analysis of Archean (3.5 Ga) barite from the North Pole formation (Australia). Meshik and Pravdivtseva (2017) questioned this determination by arguing that ^{130}Xe could have been contributed by Xe isotopes produced by cosmic rays at the surface of the Earth. Using the same data set, Meshik and Pravdivtseva (2017) hence estimated the low limit for this half-life to be $>2.4 \times 10^{21}$ yr after correction for cosmogenic effects, more in line with previous estimates (Meshik et al., 2001). These discrepancies highlight the inherent uncertainty associated with the ^{130}Ba—^{130}Xe dating method, and underscore the need for all the potential secondary Xe productions in barites to be thoroughly described and quantified.

Given that barites can be affected by secondary productions of Xe, using barites as an archive of ancient atmospheric Xe requires the careful deconvolution of different potential Xe components. The main production pathways for Xe within barites are from (i) spontaneous fissions of ^{238}U ($T_{1/2} = 4.47$ Gyr) which produces ^{131,132,134,136}Xe, (ii) interactions between galactic cosmic rays (GCR) and heavy elements such as Ba at the surface of the Earth that significantly produce ^{124,126,128,129,130}Xe through spallation reactions, (iii) neutron activation (with neutrons being thermalized from GCR or nuclear reactions within the crust), and finally (iv) other radioactivity reactions such as the decay of ^{130}Ba (Meshik et al., 2001). Using barites as an atmospheric archive therefore requires the successful deconvolution of the five potential Xe components: fractionated Xe from the ancient atmosphere (hereafter Xe_{AA}), fissiogenic Xe (hereafter Xe_f), cosmogenic Xe (hereafter Xe_c), $^{130}Xe^*$ from the radioactive decay of ^{130}Ba, and modern atmospheric Xe (hereafter Xe_{MA}) adsorbed onto grain surfaces or trapped in alteration phases from more recent fluids. In this work, we have undertaken high precision measurements of Ar, Kr and Xe elemental and isotopic compositions in a suite of barites with purported ages ranging from 1.8 to 3.4 Ga, in order to re-evaluate the usefulness of barites as archive for Archean atmospheric Xe.

2. Samples

A series of five barite samples were selected for this study. All samples originate from the Kalahari Craton in South Africa and Zimbabwe. Samples BAVE1 and BAFT11 are from the Barberton greenstone belt (South Africa), sample LPB4 is from the Limpopo Belt (South Africa), and samples Z10/6 and DM4 are from Zimbabwean deposits mined for barites in the past. The samples range in age from ~1.8 Ga (LPB4) to 3.5 Ga (BAVE1). As described below, these ages originate from the surrounding rock units and constitute either maximum or formation ages for the barites and trapped Xe.

Barite samples from the Barberton greenstone belt have a sedimentary-exhalative origin (Reimer, 1980). Sample BAVE1 is from the Theespruit Formation and is associated with felsic volcaniclastic rocks that have been dated by U—Pb on zircon and bulk Sm—Nd methods at 3.53 Ga (Van Kranendonk et al., 2009). The sample consists of an intergrowth of barite and quartz crystals and has a granoblastic texture, which is related to amphibolite-grade metamorphism the rocks experienced at 3.23 Ga. BAFT11 barite sample is derived from the Mapepe Formation of the Fig Tree Group date at ~3.26 Ga (Heinrichs and Reimer, 1977; Drabon et al., 2019). It consists of partially recrystallized barite crystals (mm-cm size) in a sandy matrix of reworked barite crystals.

Z10/6 and DM4 represent coarsely crystalline barite sampled from veins at Argosy and Dodge mines, Zimbabwe, respectively. Barite crystals show some growth banding defined by fluid inclusions, although secondary inclusions trails are also present. The veins are associated with Archean lithologies and have been subjected to deformation and regional metamorphism (Reimer, 1990), regarded to have taken place at ~2.6 Ga (Jelsma and Dirks, 2002). The barite sample Z10/6 was collected from veins that are associated with <2.90 Ga Belingwean to Bulawayan Group greenstone successions (Wilson et al., 1995) and undated, but likely Neoarchaean granitoids, therefore constraining the age of Z10/6 to between 2.60 and 2.90 Ga. In the following we use an approximate age of 2.8 Ga for this sample.

At Dodge mine, sample DM4 barite was taken from a stratiform horizon within Bulawayan greenstones as described by Reimer (1990). The absolute age of the barite is unknown, but on the basis of field relationships it likely formed between 2.60 and ~ 2.70 Ga, the maximum age of the greenstones around the mine (Jelsma and Dirks, 2002). In the following we use an approximate age of 2.6 Ga for this sample.

LPB4 barite, from the Paleoproterozoic red bed succession of the Soutpansberg Group (Reimer, 1995), has a maximum age of 1.85 Ga, as suggested by U—Pb dating of zircons (Geng et al., 2014). Samples contain both detrital barite and *syn*-sedimentary to early diagenetic barite crystals (mm-size) with well developed growth zoning defined by variations in fluid inclusion abundance.

3. Methods

3.1. Bulk chemistry analysis

Aliquots of each sample were analysed for bulk chemistry at the S.A.R.M (Service d'Analyse de Roche et Minéraux), at CRPG, Nancy (France). Abundances of major, minor and trace elements were determined using ICP-OES and ICP-MS (see Carignan et al., 2001 for preparation and analytical methods). Since samples were crushed and dissolved, these results describe only the composition of mineral matrix and not the composition of fluid inclusions. Results are presented in Table S1, Supplementary Material. Among the 55 elements analysed, Ba, K, U, and Th are of particular interest for this study because they can affect noble gas isotope compositions through secondary processes.

3.2. Sample preparation for noble gas mass spectrometry

Barite samples were prepared for noble gas analysis by firstly gently crushing aliquots of the samples into 1–5 mm sized chips. Grains smaller than 1 mm were removed to limit contamination of atmospheric Xe adsorbed onto the grains (high surface/volume ratios). The remaining grains were then examined and handpicked under a binocular microscope to remove samples exhibiting surficial impurities. Before and after picking, the samples were cleaned with acetone in an ultrasonic bath to remove any dust or organic matter from the surface, and dried in an oven at 90 °C for 30 min. Several aliquots weighing 1 to 2 g were prepared for each barite sample (Table 1).

Ancient atmospheric Xe is expected to be found in both the mineral and fluid phases of the barites. Cosmogenic productions of Xe isotopes (from spallation reaction on Ba isotopes), which can over-print the tenuous Archean atmospheric signature, principally occur, and should remain within the crystalline matrix (see Section 5.1.1). To distinguish between the different Xe components, we utilised both crushing and stepwise heating in an attempt to separate noble gases hosted in fluid inclusions and trapped in mineral lattices. Samples were first loaded in stainless steel crushers (see Avice et al., 2017 for more details), before being baked overnight under high vacuum at 200 °C in order to remove any adsorbed atmospheric noble gases. The samples were then crushed to release the noble gases held within fluid inclusions. Extracted noble gases were circulated through an in-line getter filled with Ti-sponge and silver wool at 600 °C to remove reactive components and sulfur compounds such as SO_2, respectively. Pujol et al. (2009) demonstrated the efficiency of silver wool to purify the enormous amount of SO_2 and O liberated during pyrolysis of barites ($BaSO_4$). The in-line getter was reactivated every few extractions and between each new sample. The silver wool was changed once after half the barites were analysed. For each analysis, the purification of the gas lasted 30 min. Krypton and xenon were then separated from argon using a quartz cold finger held at liquid N_2 temperature for 20 min. Typically, 5% of the Kr and < 1% of the Xe was not trapped in the quartz cold finger and therefore was lost in the Ar fraction, this loss does not produce any significant isotopic fractionation (this was verified by analysing air standards following the same protocol as the sample purification). The remaining Ar was sequentially purified with two series of additional Ti-sponge getters (two at 550 °C and the other two at 60 °C), for 10 min each, before being expanded to the Thermo Fisher Helix MC PLUS mass spectrometer for analysis. Argon was analysed using peak jumping mode, with ^{40}Ar measured on the axial faraday collector and ^{36,38}Ar measured on the axial compact dynode electron multiplier. Krypton and xenon were then subsequently released from the quartz finger at room temperature and purified the same way as Ar prior to analysis. Krypton and xenon were admitted to the mass spectrometer simultaneously, although only Xe isotopes were measured during crushing extractions. Xenon isotopes were analysed using peak jumping mode over 20 repeat analytical cycles on the axial compact dynode electron multiplier.

Crushing residues typically weighing ~500 mg (diameter > 750 μm) were recovered, wrapped in tin (Sn) foil and loaded in a stainless steel induction furnace (Zimmermann et al., 2018), which was then baked at 160 °C for 24 h. For this extraction, we used stepwise heating at three different temperature steps of 15 min each: ~800 °C, ~1300 °C and ~1800 °C (Table 2). The released gas was purified and analysed following the same procedure as outlined for crushing, although this time Kr was also analysed just after Xe following the same procedure.

Over the sequence of analyses, the mass spectrometer sensitivity and instrumental mass discrimination were controlled by measuring known standards of gas with known abundances and atmospheric isotopic compositions. Blanks were all essentially atmospheric and were subtracted from the sample analysis. Average blank values, reproducibility and mass discrimination of the mass spectrometer are presented Table S2, Supplementary Material. Typical blanks contributions during crushing extraction for Ar and Xe were < 5% and < 20%, respectively. For step-heating blanks, an empty tin foil was dropped in the furnace crucible and a full 800 °C–1300 °C-1800 °C run was performed. At the 1800 °C temperature step the blank contribution for Kr and Xe was ~50% for both. Due to the high Ar blanks at 1300 °C and 1800 °C steps (higher than the Ar signal of the sample), we do not report the Ar data for the samples at these temperatures. This high blank contribution results from the crucible degassing excessive amount of Ar at high temperature because it was manufactured under an Ar atmosphere (Zimmermann et al., 2018). Ar diffusion from the crucible at 800 °C is small, but becomes more important at >1300 °C steps, hence why we do not report Ar data for the 1300 °C and 1800 °C temperature steps.

Following the approach of Avice et al. (2017), the results for a given sample correspond to the average of all the corresponding aliquots (same experimental and analytical procedure for each aliquots). Errors are calculated using standard error (standard deviation divided by $\sqrt{n-1}$ where n = number of aliquots analysed for a given sample, 1σ; the error propagation method is detailed in Supplementary Material).

4. Results

The abundances and isotopic compositions of noble gases released by crushing and step heating are given in Tables 1,2 and in supplementary tables.

4.1. Crushing results

Argon extracted by crushing of the five barite samples present abundances ranging from 2.84 × 10^{-12} mol.g^{-1} to 7.00 × 10^{-9} mol.g^{-1}. Samples DM4 and Z10/6 have maximum ^{40}Ar/^{36}Ar ratios up to 1795 ± 8 and 7349 ± 126, respectively, an order of magnitude higher than the modern atmospheric value of 298.6 ± 0.3 (Lee et al., 2006). Samples BAVE1, BAFT11 and LPB4 have ^{40}Ar/^{36}Ar ratios of 299.2 ± 0.4, 315.3 ± 0.5 and 345.9 ± 0.5 respectively, closer to the modern atmospheric value (see Ar results Table S3, Supplementary Material).

The abundances of ^{132}Xe extracted by crushing range from 2.04 × 10^{-17} to 4.04 × 10^{-14} mol.g^{-1} (Table 1 and Table S4, Supplementary Material), comparable to abundances previously measured in Archean barites (Pujol et al., 2009). Sample LPB4 shows the highest Xe content of 4.04 × 10^{-14} mol.g^{-1}, which may be the result of higher levels of air contamination considering that the ^{40}Ar/^{36}Ar ratio (346) is close to air. Only Z10/6 and DM4 samples have Xe isotopic compositions significantly different from the present atmospheric composition (Fig. 1 and Fig. 2a). DM4-crushing displays excesses for the light isotopes ^{124,126,128,129}Xe up to 30‰ (using delta notation, $\delta^{i}Xe = [(^{i}Xe/^{130}Xe)_{sample}/(^{i}Xe/^{130}Xe)_{air} - 1] * 1000$, where *air* refers to the modern atmospheric composition, Basford et al., 1973), and an atmospheric composition for heavy isotopes (Fig. 1). In contrast, Z10/6-crushing shows excesses for the heavy isotopes ^{131,132,134,136}Xe ranging from 10‰ to 100‰, suggesting addition of fissiogenic Xe (Porcelli and Ballentine, 2002, Fig. 2a). It also displays possible excesses in the light

Table 1

Xenon abundances and corrected isotopic ratios obtained in the five barites by crushing. Several aliquots were made for sample Z10/6, DM4. All aliquots were crushed several times to ensure all gas was released. If not specified, the second crush did not release gas above blank. Isotopic ratios are normalised to isotope ^{130}Xe, see Table S4 for normalization to ^{132}Xe.

Sample	#	Mass (g)	^{132}Xe (10^{-17} mol.g^{-1})	±	^{124}Xe/^{130}Xe	±	^{126}Xe/^{130}Xe	±	^{128}Xe/^{130}Xe	±	^{129}Xe/^{130}Xe	±	^{131}Xe/^{130}Xe	±	^{132}Xe/^{130}Xe	±	^{134}Xe/^{130}Xe	±	^{136}Xe/^{130}Xe	±
Z10/6	1	1.919	75.68	1.32	0.02400	0.00095	0.02079	0.00096	0.47424	0.01267	6.51423	0.15779	5.24632	0.12730	6.75400	0.16339	2.74699	0.06731	2.40574	0.05936
	2 first crush	1.639	194.50	4.02	0.02345	0.00088	0.02267	0.00083	0.47092	0.01397	6.48535	0.18296	5.24695	0.15013	6.73519	0.19122	2.76423	0.07999	2.42147	0.07053
	2 s crush	–	339.00	5.27	0.02404	0.00068	0.02205	0.00077	0.47249	0.01044	6.50102	0.13738	5.28248	0.11014	6.73179	0.14148	2.71788	0.05696	2.38690	0.05173
			533.50	6.62																
DM4	1	0.966	166.75	3.20	0.02432	0.00105	0.02214	0.00117	0.46505	0.01264	6.51344	0.16783	5.20964	0.13446	6.57442	0.16934	2.55486	0.06784	2.17353	0.05829
	2	1.985	30.70	0.17	0.02381	0.00031	0.02217	0.00028	0.47445	0.00397	6.52545	0.05163	5.22933	0.04110	6.62750	0.05193	2.55546	0.02047	2.16490	0.01711
	3 first crush	1.527	101.05	2.22	0.02364	0.00124	0.02247	0.00122	0.47359	0.01596	6.52230	0.19496	5.24709	0.15552	6.63126	0.19667	2.57255	0.07618	2.19631	0.06849
	3 s crush	–	153.21	2.90	0.02388	0.00074	0.02160	0.00099	0.47773	0.01291	6.51065	0.16421	5.21807	0.13174	6.62121	0.16824	2.55637	0.06594	2.17427	0.05559
			254.26	3.65																
LPB4	1 first crush	1.076	3980.41	134.90	0.02289	0.00122	0.02250	0.00131	0.45989	0.02240	6.47736	0.30797	5.20978	0.24862	6.61769	0.31398	2.54873	0.12167	2.14794	0.10258
	1 s crush	–	61.24	1.58	0.02113	0.00125	0.02112	0.00116	0.45337	0.01812	6.51887	0.22978	5.23848	0.18646	6.62825	0.23264	2.53771	0.09180	2.17931	0.08157
			4041.65	134.91																
BAFT11	1	2.011	128.72	1.90	0.02142	0.00082	0.02122	0.00068	0.45434	0.01071	6.41350	0.13006	5.17858	0.10563	6.49371	0.12981	2.51127	0.05274	2.13681	0.04409
BAVE1	1	1.396	2.04	0.06	0.02253	0.00109	0.02440	0.00111	0.47135	0.01827	6.47435	0.23869	5.23958	0.19434	6.59297	0.24601	2.53556	0.09447	2.14732	0.08016
Atmosphere		Basford et al. (1973)			0.02337	0.00008	0.02180	0.00011	0.47150	0.00070	6.49600	0.00900	5.21300	0.00800	6.60700	0.00500	2.56300	0.00400	2.17600	0.00300

Table 2

Xenon abundances and corrected isotopic ratios obtained in the five barites by heating at 800 °C, 1300 °C and 1800 °C. Isotopic ratios are normalised to ^{132}Xe, see Table S7 for normalization to ^{130}Xe. Sample DM4 aliquot 3 at 1800 °C is lower than blank. The 1300 °C and 1800 °C steps of aliquot one for sample BAFT11 was omitted from the average since it is different from the two other aliquots at 3σ.

Sample	#	Mass (g)	Heating step (°C)	^{132}Xe (10^{-17} mol. g-1)	±	^{124}Xe/^{132}Xe	±	^{126}Xe/^{132}Xe	±	^{128}Xe/^{132}Xe	±	^{129}Xe/^{132}Xe	±	^{130}Xe/^{132}Xe	±	^{131}Xe/^{132}Xe	±	^{134}Xe/^{132}Xe	±	^{136}Xe/^{132}Xe	±
Z10/6	1	0.425	800 °C	5.33	0.05	0.00367	0.00085	0.00342	0.00072	0.07444	0.00524	0.98358	0.03081	0.15023	0.00901	0.79774	0.02361	0.40659	0.01656	0.35194	0.01219
			1300 °C	2.02	0.04	0.00524	0.00060	0.00775	0.00106	0.07979	0.00389	0.98012	0.01902	0.15756	0.00693	0.94041	0.01950	0.38134	0.00986	0.32795	0.00716
			1800 °C	4.21	0.03	0.00454	0.00065	0.00663	0.00099	0.07757	0.00348	0.97386	0.01903	0.16309	0.00521	0.89135	0.01873	0.37847	0.01102	0.33631	0.00876
	2	0.603	800 °C	10.04	0.08	0.00364	0.00045	0.00349	0.00049	0.07069	0.00326	0.97131	0.01954	0.14923	0.00602	0.77978	0.01900	0.41081	0.00889	0.36178	0.00930
			1300 °C	13.52	0.11	0.00584	0.00055	0.00762	0.00071	0.07953	0.00269	0.97862	0.01655	0.15873	0.00514	0.94975	0.02162	0.39829	0.01025	0.34270	0.00905
			1800 °C	10.20	0.08	0.00451	0.00067	0.00431	0.00061	0.07227	0.00299	0.98690	0.01914	0.15272	0.00433	0.83078	0.01646	0.38362	0.00906	0.33338	0.00741
	3	0.281	800 °C	10.71	0.10	0.00385	0.00067	0.00336	0.00061	0.07354	0.00442	0.98341	0.03340	0.14972	0.00870	0.79360	0.01913	0.40476	0.01197	0.34454	0.01148
			1300 °C	10.92	0.12	0.00610	0.00077	0.00874	0.00153	0.08249	0.00532	0.99671	0.01873	0.16098	0.00616	0.98924	0.03855	0.39304	0.01156	0.34174	0.00849
			1800 °C	9.64	0.09	0.00426	0.00050	0.00383	0.00064	0.07522	0.00344	0.98806	0.02345	0.15655	0.00435	0.79366	0.02033	0.38769	0.01303	0.33325	0.01094
	4	0.382	800 °C	5.66	0.08	0.00354	0.00102	0.00353	0.00061	0.07425	0.00456	0.98588	0.03629	0.15426	0.00747	0.79588	0.02857	0.39849	0.01441	0.34582	0.01617
			1300 °C	12.74	0.11	0.00636	0.00072	0.00783	0.00110	0.07808	0.00402	0.99728	0.02384	0.15983	0.00487	0.98472	0.02649	0.39186	0.00794	0.32911	0.01114
			1800 °C	5.69	0.06	0.00451	0.00061	0.00438	0.00048	0.09280	0.00434	0.98390	0.02246	0.15638	0.00629	0.81548	0.01960	0.38466	0.00967	0.32774	0.00895
DM4	1	0.336	800 °C	4.91	0.09	0.00377	0.00068	0.00320	0.00046	0.09052	0.00622	0.97674	0.02901	0.15311	0.00861	0.78622	0.02882	0.38125	0.01799	0.33325	0.01392
			1300 °C	3.67	0.06	0.00461	0.00115	0.00420	0.00076	0.07187	0.00755	0.96813	0.04729	0.15285	0.01252	0.81724	0.03360	0.38638	0.01632	0.32237	0.01444
			1800 °C	4.48	0.06	0.00357	0.00065	0.00311	0.00052	0.07651	0.00424	0.99950	0.02988	0.15970	0.00718	0.79852	0.02700	0.39059	0.01368	0.34371	0.01262
	2	0.809	800 °C	13.50	0.08	0.00362	0.00025	0.00323	0.00044	0.07121	0.00263	0.98756	0.01227	0.15215	0.00326	0.78740	0.01388	0.38786	0.00789	0.32760	0.00708
			1300 °C	32.34	0.19	0.00369	0.00024	0.00348	0.00031	0.07179	0.00276	0.98765	0.01426	0.15276	0.00286	0.78986	0.01072	0.38424	0.00500	0.32433	0.00475
			1800 °C	9.06	0.06	0.00379	0.00048	0.00370	0.00045	0.07202	0.00302	0.99022	0.01461	0.15166	0.00448	0.79508	0.01276	0.38636	0.00635	0.32538	0.00631
	3	0.505	800 °C	6.69	0.07	0.00358	0.00066	0.00319	0.00080	0.07552	0.00528	0.98876	0.02999	0.15368	0.00957	0.78709	0.02437	0.38749	0.01438	0.32708	0.01390
			1300 °C	3.05	0.04	0.00387	0.00092	0.00451	0.00061	0.07174	0.00562	1.00024	0.03629	0.15870	0.00951	0.81083	0.02198	0.38046	0.02018	0.32508	0.01559
			1800 °C	–	–	–	–	–	–	–	–	–	–	–	–	–	–	–	–	–	–
LPB4	1	0.506	800 °C	4.56	0.07	0.00331	0.00064	0.00316	0.00045	0.07264	0.00663	0.98997	0.03700	0.15023	0.00903	0.78663	0.02620	0.38773	0.01990	0.32883	0.01517
			1300 °C	3.65	0.05	0.00473	0.00121	0.00546	0.00090	0.07188	0.00558	0.96692	0.03789	0.15148	0.00813	1.35557	0.08185	0.39954	0.01645	0.34666	0.01359
			1800 °C	2.28	0.03	0.00510	0.00090	0.00633	0.00122	0.07776	0.00435	0.97821	0.02810	0.15560	0.00652	1.56903	0.06570	0.39274	0.01262	0.35202	0.01193
BAFT11	1	0.389	800 °C	5.52	0.07	0.00373	0.00081	0.00357	0.00096	0.06986	0.00613	1.00067	0.03702	0.15249	0.00649	0.80393	0.02639	0.38912	0.01507	0.33241	0.01537
			1300 °C	4.31	0.08	0.00411	0.00078	0.00603	0.00127	0.06507	0.00445	0.82818	0.04012	0.13349	0.01075	2.26399	0.30480	0.54647	0.03904	0.53212	0.04323
			1800 °C	4.51	0.07	0.00594	0.00090	0.01078	0.00134	0.07403	0.00445	0.86501	0.02728	0.14639	0.00806	5.04380	0.66279	0.51198	0.02113	0.51034	0.02348
	2	1.039	800 °C	3.94	0.04	0.00349	0.00053	0.00308	0.00044	0.06802	0.00368	0.96813	0.02386	0.14681	0.00568	0.79098	0.02324	0.40813	0.01310	0.35585	0.00956
			1300 °C	7.43	0.06	0.00399	0.00059	0.00604	0.00075	0.04574	0.00411	0.54251	0.05848	0.09062	0.00765	2.71467	0.29101	0.84726	0.07323	0.94723	0.09289
			1800 °C	2.10	0.02	0.00736	0.00111	0.01218	0.00150	0.05828	0.00324	0.55996	0.02958	0.10508	0.00641	6.17832	0.68199	0.80802	0.04000	0.89996	0.06586
	3	0.510	800 °C	4.77	0.09	0.00392	0.00065	0.00345	0.00080	0.07065	0.00534	0.97637	0.03263	0.15092	0.00623	0.79542	0.02739	0.39458	0.01440	0.33880	0.02045
			1300 °C	4.51	0.05	0.00490	0.00089	0.00693	0.00112	0.05702	0.00474	0.66684	0.05260	0.10952	0.00778	2.99626	0.43321	0.72579	0.06335	0.78025	0.08838
			1800 °C	2.19	0.02	0.00725	0.00110	0.01022	0.00137	0.06854	0.00444	0.68524	0.03282	0.11993	0.00616	5.34693	0.65702	0.69441	0.03317	0.74902	0.04253
BAVE1	1	0.420	800 °C	6.65	0.08	0.00351	0.00105	0.00325	0.00087	0.07327	0.00282	0.99106	0.03198	0.14925	0.00736	0.78644	0.03258	0.37720	0.01840	0.33013	0.01673
			1300 °C	3.59	0.03	0.00439	0.00097	0.00548	0.00131	0.07458	0.00442	0.97116	0.02038	0.15216	0.00752	0.88660	0.02658	0.40739	0.01380	0.35320	0.01046
			1800 °C	10.01	0.07	0.00417	0.00062	0.00449	0.00055	0.07145	0.00278	0.97417	0.01514	0.14754	0.00391	0.85140	0.01559	0.40074	0.01404	0.35285	0.00834
	2	0.446	800 °C	4.62	0.07	0.00332	0.00092	0.00323	0.00102	0.07022	0.00454	0.98222	0.03868	0.15294	0.00860	0.77736	0.03108	0.38488	0.01600	0.32147	0.01564
			1300 °C	4.04	0.06	0.00509	0.00101	0.00605	0.00114	0.07494	0.00570	0.96844	0.03679	0.14811	0.00822	0.93505	0.03099	0.40071	0.01618	0.34881	0.01725
			1800 °C	10.99	0.10	0.00402	0.00048	0.00354	0.00043	0.07276	0.00325	0.98075	0.02008	0.14929	0.00396	0.79157	0.01898	0.39581	0.01047	0.34005	0.00766
			Atmosphere	Basford et al. (1973)		0.00353	0.00001	0.0033	0.00002	0.07136	0.0009	0.98320	0.00120	0.15136	0.00012	0.78900	0.00110	0.38790	0.00060	0.32940	0.00040

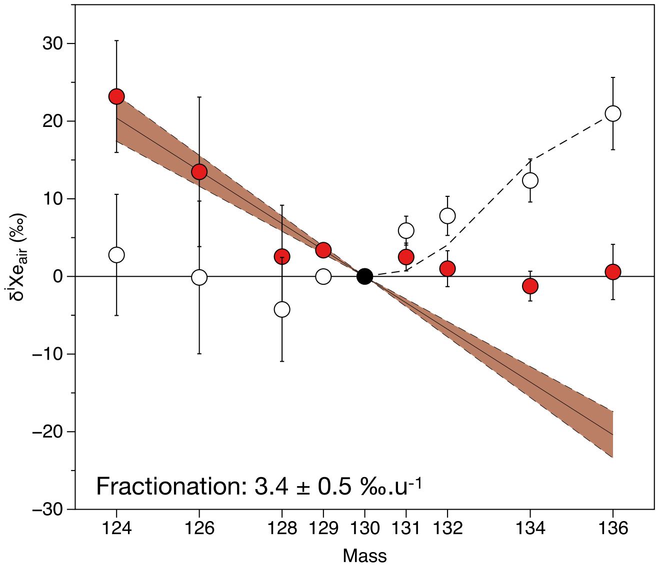

Fig. 1. Xe isotopic composition of the DM4 crushing step (full circles; error bars are 1σ, standard error) in δ^iXe values (defined as $\delta^i\mathrm{Xe} = ((^i\mathrm{Xe}/^{130}\mathrm{Xe})_{\mathrm{sample}}/(^i\mathrm{Xe}/^{130}\mathrm{Xe})_{\mathrm{air}}$ - 1)*1000, *air* subscript referring to the modern atmospheric composition, Basford et al., 1973). The error bar on isotope ^{129}Xe is smaller than the symbol size. Excesses of ^{124,126,128,129}Xe isotopes are consistent with a mass dependent fractionation (MDF) of 3.4 ± 0.5‰.u^{-1} (red shaded area represents 1σ standard error). When corrected for MDF (open symbols), the heavy isotopes spectrum is consistent with contribution of fissiogenic Xe from U (dashed line). (For interpretation of the references to colour in this figure legend, the reader is referred to the web version of this article.)

isotopes, but associated uncertainties are too large, especially for ^{126}Xe, to reach a firm conclusion. Crushing of LPB4, BAFT11 and BAVE1 samples released xenon with isotopic compositions similar to that of the modern atmosphere (Table 1 and Fig. S5,S6,S7, Supplementary Material).

4.2. *Step heating results*

Argon released at 800 °C (the only step giving Ar signals above blank level) shows ^{40}Ar abundances ranging from 0.65 to 4.42 × 10^{-10} mol.g^{-1}, and ^{40}Ar/^{36}Ar up to 13,200 ± 1700 for BAFT11 barite (Table S5, Supplementary Material). Total abundances of ^{84}Kr released during step heating (800 °C, 1300 °C and 1800 °C) range from 1.42 mol.g^{-1} to 7.77 × 10^{-16} mol.g^{-1}. Krypton isotopic ratios measured in the first 6 samples by step heating were similar (within 1σ) to the modern atmospheric composition (Basford et al., 1973), regardless of the temperature step (Table S6, Supplementary Material). Therefore, for the remaining 7 samples, krypton was not analysed.

At the 800 °C extraction step, ^{132}Xe concentrations range from 0.39 mol.g^{-1} to 1.35 × 10^{-16} mol.g^{-1} (Table 2 and Table S7, Supplementary Material). At this step, sample Z10/6 is the only one to exhibit an isotopic signature distinct from that of the atmosphere, with $^{124\text{-}128}$Xe/^{130}Xe and ^{134,136}Xe/^{130}Xe both in excess of atmospheric values (Fig. 2b). Sample DM4, contrary to the crushing extraction, does not show any significant isotopic deviation from the modern atmospheric composition (Fig. S4, Supplementary Material).

At higher temperature, typical ^{132}Xe abundances range from 2.05 mol.g^{-1} to 4.14 × 10^{-16} mol.g^{-1} (total abundance released from the two high temperature steps, Table 2). Xenon fractions released at 1300 °C and 1800 °C are isotopically similar for all samples. To aid simplicity we will therefore use the 1300 °C step in the following section, when discussing the high temperature release. All five samples (Fig. 3, using ^{132}Xe for isotope normalization at high temperature steps) show significant excesses in ^{124,126,128}Xe/^{132}Xe, with the ^{124,126,128}Xe/^{132}Xe ratios being comparable to those expected for cosmogenic production. The samples also exhibit strong monoisotopic excesses of ^{131}Xe, with δ^{131}Xe values ranging from 20‰ to ~2800‰, for DM4 and BAFT11, respectively. In addition, LPB4, BAFT11 and BAVE1 show excesses in $^{134\text{-}136}$Xe that are in agreement with the ^{238}U fissiogenic pattern (Fig. 3).

5. Discussion

Crushing and step-heating of the barites revealed a wide spread of xenon isotopic anomalies that result from the simultaneous release of various components. Isotopic spectra are required to be thoroughly deconvoluted and interpreted in order to isolate possible primary signatures inherited from the Archean atmosphere.

5.1. *Archean atmosphere trapped in barite fluid inclusions*

5.1.1. *Decoupling of the fluid inclusions and matrix composition: Components, host phases and diffusion of Xe*

Archean barites are expected to possess a variety of noble gas components. This can include components of primary origin, such as the Archean atmosphere or secondary components, resulting from nuclear reactions (U fission, spallation on Ba, ^{130}Ba neutron activation and radioactivity). These components can be hosted in either the fluid inclusions, the matrix, or both. In order to separate the different components held within the fluid inclusions and the matrix, different extraction methods can be employed, with crushing preferentially releasing gas from the fluid inclusions whilst step-heating will release all the remaining gas held within the matrix and un-cracked fluid inclusions. However, it should be noted that the possibility for Xe, and other noble gases to diffuse from one phase to the other could complicate the identification of components, especially the primary ancient atmosphere which is likely to be the most tenuous (~10‰ variations) and subject to overprinting by secondary component (~100–1000‰ variations).

Crushing of Z10/6 barite revealed an unambiguous secondary fissiogenic component Xe$_{\mathrm{f}}$ for isotopes $^{131\text{–}132\text{-}124\text{-}136}$Xe (Fig. 2a), resulting from the spontaneous fission of ^{238}U. However, bulk chemistry analysis of the matrix revealed that Z10/6 did not contain detectable amount of uranium (Table S1, <0.07 ppm). This is in agreement with the observation that no Xe$_{\mathrm{f}}$ was found from high temperature (1300 °C an 1800 °C) pyrolysis extraction on this barite (Fig. 2c,d). The detection of Xe$_{\mathrm{f}}$ within the fluid inclusion and not the matrix of Z10/6 indicates that either (i) the fluid component already contained excess Xe$_{\mathrm{f}}$, as it has been shown to be the case for ^{40}Ar (Avice et al., 2017), a likely possibility due to interaction between the fluids and the crust, or (ii) the fluids carried a source of U that was not incorporated into the barite matrix. The absence of Xe$_{\mathrm{f}}$ in the matrix furthermore suggest that Xe from the fluid inclusions has remained isolated since their formation, with limited diffusion of noble gases either in or out.

Conversely, samples BAVE1, LPB4 and BAFT11 have detectable amount of U (0.11 ppm, 0.12 ppm and 1.27 ppm, respectively, Table S1) yet do not present Xe$_{\mathrm{f}}$ during crushing or heating at low temperature (800 °C, Fig. S5–6-7). They do however show large Xe$_{\mathrm{f}}$ excess when heated to higher temperature (1300 °C, Figs. 3 and 1800 °C, Fig. S5–6-7). This indicates that these barites only have U in their matrix, and that the Xe$_{\mathrm{f}}$ component remained in the matrix and did not diffuse in the fluid inclusions.

Taken together, these observations are consistent with little or no diffusion of Xe between fluid inclusions and matrix. Additionally, this confirms that extraction by crushing only liberates gas from fluid inclusions, as does pyrolysis at 800 °C, and that high temperature extraction (1300 °C and 1800 °C) releases gas from the matrix (and any remaining fluid inclusions by extension).

5.1.2. *DM4 barite: Ancient atmosphere revealed by crushing*

Xenon released during crushing of sample DM4 shows excesses in the

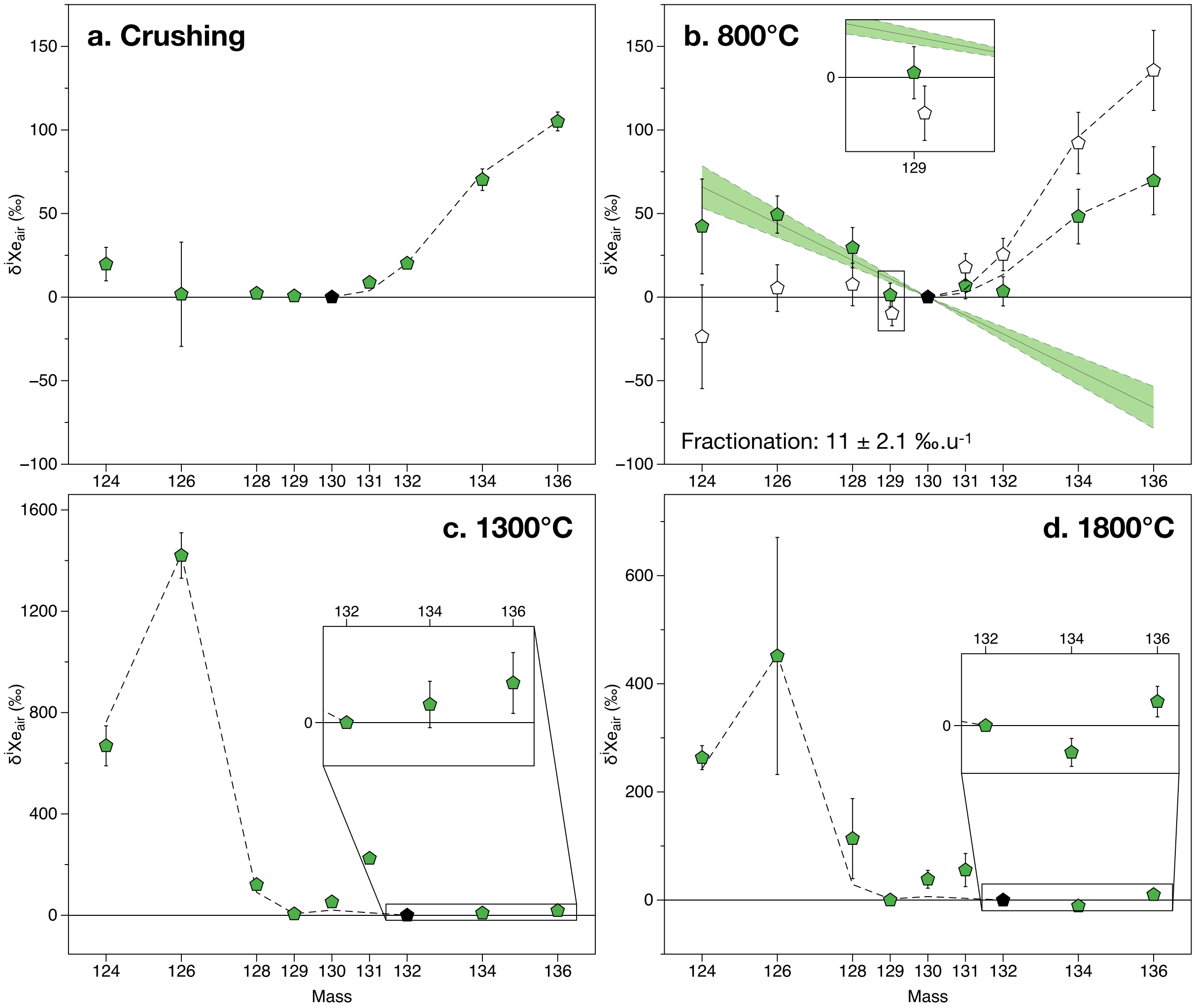

Fig. 2. Isotopic spectra of Xe released by crushing and step-heating of Z10/6 barite. a. Crushing. Excesses of $^{131-136}$Xe are compared with the expected fission spectra of ^{238}U anchored on ^{136}Xe (dashed line). b. 800 °C. Full symbols represent the measured composition. Green shaded area is the MDF fit of 11 ± 2.1‰.u^{-1} (1σ) using light isotopes $^{124\text{-}130}$Xe. Open symbols are the measured data corrected for MDF. After correction, the ^{238}U fission spectrum fits the $^{131-136}$Xe excesses (dashed line) as in Fig. 1. Note a depletion of ^{129}Xe relative to the MDF line, as expected for Archean atmospheric Xe (Avice et al., 2017; Marty et al., 2019). c. 1300 °C. Strong evidence for cosmogenic contribution for light isotopes by spallation reaction, monoisotopic excess of ^{131}Xe and negligible excess in δ^{136}Xe = 18 ± 14‰. The dashed line is the fit of the expected production pattern of Xe isotopes from interaction between high-energy particles (300 MeV protons, Kaiser, 1977) and Ba isotopes, anchored on ^{126}Xe. d. 1800 °C. Similar pattern as 1300 °C release, with smaller excesses due do higher atmospheric contamination. Note the difference in normalizing isotopes, ^{130}Xe for crushing and 800 °C steps, and ^{132}Xe for 1300 °C and 1800 °C steps. (For interpretation of the references to colour in this figure legend, the reader is referred to the web version of this article.)

light Xe isotopes ^{124,126,128,129}Xe relative to the modern atmospheric composition (Fig. 1). These excesses decrease systematically from ^{124}Xe to ^{129}Xe, which is consistent with a mass-dependent fractionation (MDF) of 3.4 ± 0.5‰.u^{-1} (1σ, error-weighted linear regression using ^{124,126,128,129,130}Xe with IsoplotR© software, Vermeesch, 2018). Assuming that the noble gases within the fluid inclusions were in isotopic equilibrium with the atmosphere during rock formation, then this MDF signature should be representative of the atmosphere at the time of Xe trapping (Pujol et al., 2011; Pujol et al., 2013; Avice et al., 2017; Avice et al., 2018). When corrected for MDF, the heavy Xe isotopes ($^{131-136}$Xe) are consistent with secondary contribution of fissiogenic $^{131-136}$Xe from ^{238}U (Fig. 1). We therefore suggest that DM4 fluid inclusions possess both a MDF signature and fissiogenic Xe excesses. Although the possibility for the light isotope excesses to results from cosmogenic reactions with Ba cannot be entirely excluded, we consider it unlikely because (i) crushing is unlikely to liberate Xe isotopes produced in the crystal matrix (although in some cases release of cosmogenic He by crushing has been observed, Yokochi et al., 2005; Broadley et al., 2016) and most importantly (ii) the measured isotopic ratios ^{124}Xe/^{130}Xe and ^{126}Xe/^{130}Xe do not fit the expected cosmogenic production ratios (Fig. S1; Kaiser, 1977).

5.1.3. Z10/6 Barite: 800 °C

Barites heated at 800 °C present a Xe isotopic composition indistinguishable (within 1σ uncertainty) from the modern atmospheric composition with the exception of sample Z10/6 (Fig. 2b). This is in contrast with extractions at higher temperature where all five barites present anomalies up to 100–1000‰ in the light isotopes, fissiogenic isotopes or both, relative to the modern Xe atmospheric composition (Fig. 2c,d and Fig. 3). This strongly suggests that (i) the 800 °C extraction step does not significantly release Xe held in the crystal matrix (which would diffuse out at higher temperature), and (ii) the gas released from Z10/6 at 800 °C was extracted from fluid inclusions that were not released during crushing. Heating at 800 °C thus may have permitted the release of Xe trapped in fluid inclusions by thermal cracking (or decrepitation, Ulrich and Bodnar, 1988). This is supported

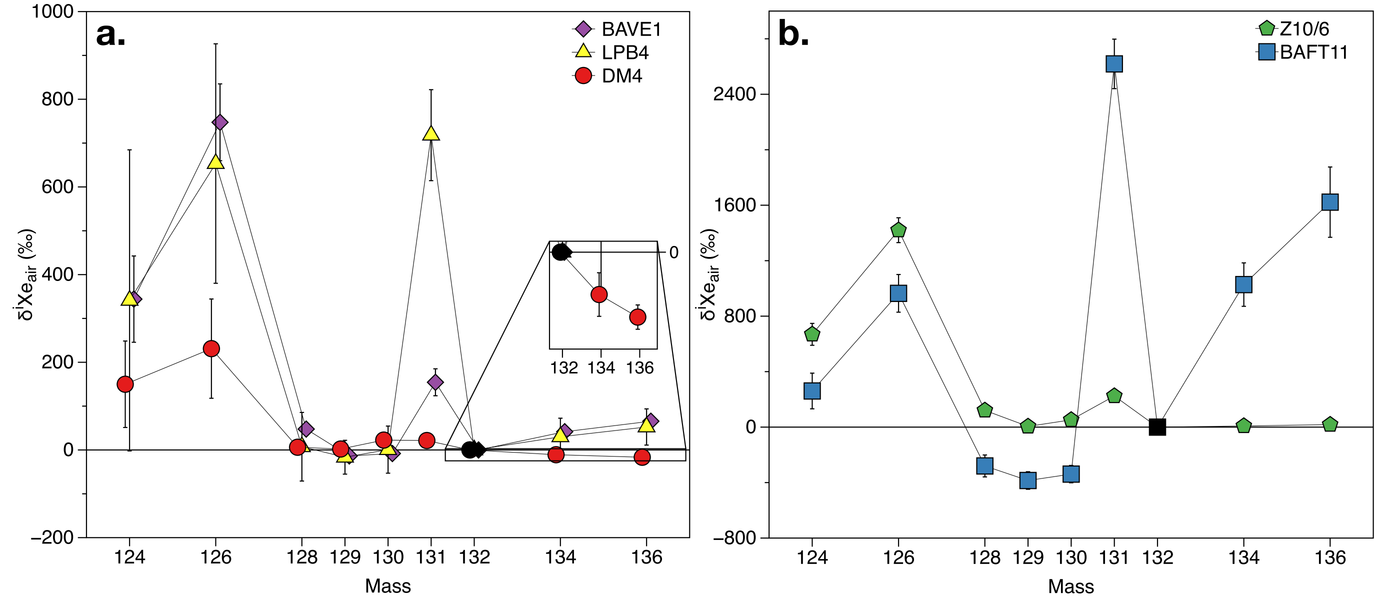

Fig. 3. Isotopic spectrum of Xe released at 1300 °C temperature step of the five sample. a. DM4 in red circles, LPB4 in yellow triangles, BAVE1 in purple diamonds. b. BAFT11 in blue squares, Z10/6 in green pentagrams. Isotopic composition is given using the δ^{i}Xe normalised to ^{132}Xe and the composition of modern atmosphere. Note the change in scale in several hundreds of ‰ compared to extraction 800 °C and crushing (Figs. 1 and 2). Three main signatures are identified here (i) ^{124,126,128}Xe excess coming from spallation production (ii) ^{131}Xe mono-isotopic excess from neutron capture on ^{130}Ba (iii) ^{134,136}Xe from the fission of ^{238}U; ^{132}Xe being also produced by this fission and used for normalization, BAFT11 sample displays virtual depletions of ^{128,129,130}Xe relative to air. The lines joining the symbols are for visual aid. (For interpretation of the references to colour in this figure legend, the reader is referred to the web version of this article.)

by the similarity of the light isotope excesses between crushing and 800 °C extraction step of Z10/6. Although the uncertainties of the crushing extraction are large, such that it is difficult to draw broad conclusions, the agreement between the crushing and 800 °C extractions suggests that both released an ancient atmospheric component. Furthermore, both the crushing and the 800 °C temperature step release a significant amount of fissiogenic Xe, which is not seen in the higher temperature steps. This further confirms the genetic link between the crushing and 800 °C step in the case of Z10/6.

The $^{124\text{-}130}$Xe isotopes gives the degree of MDF for sample Z10/6 to be 11 ± 2.1‰.u^{-1} (1σ, Fig. 2b). Enrichments in the light isotopes of xenon could represent MDF but are also subject to contribution by cosmogenic isotopes. However, in this case we consider the addition of cosmogenic Xe from the matrix to be unlikely for the following reasons. Firstly, as is it the case for sample DM4 (crushing results), the relative ratios of light isotopes do not fit the expected ratios of cosmogenic reactions (Fig. S2), and isotopes produced in the barite matrix are usually released at temperatures higher than 800 °C (Meshik et al., 2001). Secondly, $^{131\text{–}136}$Xe (Xe$_f$) produced by spontaneous ^{238}U fission are released during crushing and 800 °C heating, but not during higher temperature steps. The extremely low U content of the Z10/6 matrix (below detection <0.07 ppm, Table S1) is consistent with the lack of Xe$_f$ at high temperature. The release of Xe$_f$ at 800 °C however suggests a contribution from the fluid inclusions. Thirdly, if the excesses of light isotopes resulted from a matrix contribution by diffusion, then one should also expect a mono-isotopic excess of ^{131}Xe, as observed at the 1300 °C and 1800 °C extraction steps (Fig. 2c,d), which is not the case at 800 °C or by crushing (Fig. 2a,b). Finally, we observe a similarity in the ^{136}Xe excess of the Xe$_f$ component between crushing ($\delta^{136}Xe = 105 \pm 6$‰, Fig. 2a) and 800 °C extraction after considering mass dependent fractionation of 11‰.u^{-1} on the Xe spectrum ($\delta^{136}Xe_{corrected} = 136 \pm 24$‰, Fig. 2b). We therefore consider the addition of cosmogenic Xe from the matrix for sample Z10/6 to be unlikely, whilst acknowledging that it cannot categorically be ruled out.

In sample Z10/6 a depletion of ^{129}Xe relative to the MDF trend (δ^{129}Xe a few ‰ below the MDF regression) is observed in the 800 °C extraction step (Fig. 2b). Such ^{129}Xe depletion relative to the MDF trend has been previously observed in Archean quartz (Avice et al., 2017) and Archean organic matter (Bekaert et al., 2018), but not in Proterozoic and Phanerozoic samples (Avice et al., 2017). This ^{129}Xe deficit is regarded as a potential signature of the Archean atmosphere, which contained less mantle-derived ^{129}Xe than recent atmospheric gases (Avice et al., 2017; Marty et al., 2019). The isotopic spectrum of Xe released from Z10/6 at 800 °C shows a depletion in ^{129}Xe after correction for the isotopic mass dependent fractionation with $\Delta^{129}Xe = -9.8 \pm 7.4$‰ ($\Delta^{129}$Xe is defined as the distance between the observed value and that expected for isotope fractionation of modern air, 1σ, Fig. 2b). This observation supports the proposition of a non-linear degassing rate of the mantle through time, with a burst of mantle activity at the end of the Archean around 2.5 Ga, required to explain modern atmospheric ^{129}Xe concentration (Marty et al., 2019).

Samples BAFT11 and BAVE1, although older (3.3 and 3.5 Ga, respectively), do not present any mass-fractionated Xe extracted by crushing or pyrolysis at 800 °C. This infers that (i) the fluid inclusion content in these barites was too low to provide enough Xe concentration for proper analysis and/or (ii) air contamination was too important resulting in the barites to have a modern atmospheric Xe composition, overprinting the Archean component. Future studies utilising barites as a record of the ancient atmosphere should therefore concentrate on obtaining samples with large number of fluid inclusions, where secondary cosmogenic production should be minimal.

5.2. *Secondary contributions from fissiogenic, cosmogenic and radiogenic reactions*

5.2.1. *Identifying the ^{130}Xe excesses*

In order to investigate the radioactive decay of ^{130}Ba to ^{130}Xe, barite samples were heated at sufficient temperature (1300 °C and 1800 °C) to release Xe trapped in the matrix. The half-life of ^{130}Ba has been estimated to be between $6.0 \pm 1.1 \times 10^{20}$ yr (Pujol et al., 2009) and $2.2 \pm 0.5 \times 10^{-21}$ yr (Meshik et al., 2001), depending on interpretation of cosmogenic contamination on ^{130}Xe (Meshik and Pravdivtseva, 2017). The current recommended value for this half-life is 2.1 (+3.0/−0.8) x 10^{21} yr (Barabash, 2020).

At 1300 °C extraction, cosmogenic (spallation reaction from neutrons on Ba producing $^{124\text{-}131}$Xe, Xe$_c$) and fissiogenic (spontaneous fission of ^{238}U producing $^{131–136}$Xe, Xe$_f$) reactions contribute to the ^{130}Xe/^{132}Xe ratio, in addition to radiogenic ^{130}Xe* from ^{130}Ba decay (see 1300 °C release pattern Fig. 3). Therefore, to identify and quantify ^{130}Xe* we need to first correct our spectra from Xe$_f$ and Xe$_c$ production (Fig. S3). The procedure for correcting the Xe isotopic spectra for Xe$_f$ and Xe$_c$ contributions is described in Supplementary Material. After both Xe$_f$ and Xe$_c$ corrections, Z10/6, DM4, LPB4 and BAFT11 barites show small excesses in ^{130}Xe, which likely originates from the decay of ^{130}Ba (see Fig. S3 for BAFT11), and various excesses in ^{131}Xe, up to 3000‰ for barite BAFT11 (see section 5.2.2 ^{131}Xe anomaly).

Sample Z10/6 presents the highest ^{130}Xe* of $1.1 \pm 0.2 \times 10^{-18}$ mol. g^{-1} (where ^{130}Xe* is the difference between ^{130}Xe measured, corrected for Xe$_f$ and Xe$_c$, and atmospheric ^{130}Xe). Using Meshik et al. (2001)'s or Pujol et al. (2009)'s half-life constants for the radioactive decay of ^{130}Ba gives ages for Z10/6 barite of ~1.5 Ga or 0.4 Ga, respectively. The other barites DM4, LPB4 and BAFT11 show even lower ^{130}Xe* abundances with higher relative uncertainties. Age computation for these barites leads to less that 1 Ga, regardless of the half-life chosen. Given the expected Archean age of these four barites (except for LPB4 dated around 1.8 Ga) and the low ^{130}Xe* (compared to what was obtained for Archean barite by Pujol et al. (2009)), we conclude that these calculated ages do not represent the ages of the barites. This could be the result of the resetting of the ^{130}Ba—^{130}Xe chronometer by some secondary metamorphic process, or as we speculate, it is likely due to the low precision on the ^{130}Xe* calculation presented here. A major source of uncertainty on calculating ^{130}Xe* is the important secondary production of cosmogenic $^{124\text{-}131}$Xe (up to several hundreds for δ^{126}Xe) and the difficulty in precisely quantifying and correcting for it (Meshik and Pravdivtseva, 2017). ^{130}Ba—^{130}Xe dating cannot therefore be readily applied to ancient barites such as those studied here, despite the fact that samples were specifically chosen because of their presumed low exposure to cosmic rays (DM4 and Z10/6 were sampled from within a mine). In fact all samples were exposed to cosmic rays for between 17 Kyr (DM4) and 208 Kyr (Z10/6), which is similar to, but lower, than that previously found in Archean barite (270 Kyr; Srinivasan, 1976). However, the possibility still remains that younger or better shielded samples, with less secondary cosmogenic production, could be used in the future to date barites using the decay of ^{130}Ba, as was previously done in Meshik et al. (2001).

5.2.2. *^{131}Xe anomaly*

After correction for Xe$_f$ and Xe$_c$ productions, the high temperature releases present excesses of ^{131}Xe for the five samples (up to 3000‰ for barite BAFT11 from Barberton, South Africa, Fig. S3). Monoisotopic ^{131}Xe production is likely the result of neutron capture reactions on ^{130}Ba (Srinivasan, 1976), with neutrons being mainly produced from uranium and thorium within the barites. ^{238}U produces neutrons directly by spontaneous fission of U and indirectly through α,n reactions on ^{18}O, with the α particles being produced by the radioactive decay of ^{238}U and ^{232}Th. The barite samples include in this study indeed present a correlation ($R^2 = 0.97$) between their U content and their ^{131}Xe/^{132}Xe ratio (Fig. 4). Interestingly, sample Z10/6 has a relatively high δ^{131}Xe of up to 230‰ despite its low U and Th contents (<0.01 ppm). Similar ^{131}Xe excesses have been found in U-free samples by Li et al. (1994) who proposed that they originated from activation by epithermal neutrons from U—Th decay in the surrounding rocks. Epithermal neutrons produced in the surrounding rock units could then interact with nearby barites given that the mean free path is on the order of 1 m in igneous rocks (Li et al., 1994). Z10/6 barite formed as a vein in granitoids, therefore making it more prone to this type of ^{131}Xe production. Our results therefore support the previous observations by Li et al. (1994) that ^{131}Xe excess is essentially a consequence of the presence of U—Th in barites, or, in rare cases, of U—Th within surrounding units.

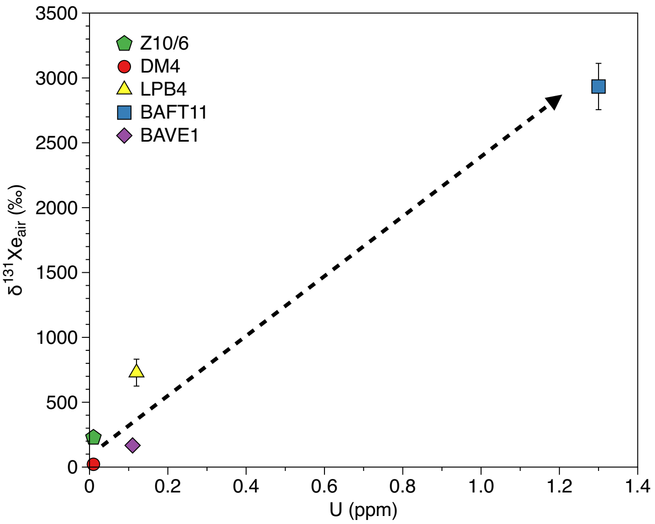

Fig. 4. Correlation between measured δ^{131}Xe versus the U content (ppm) of the five barites analysed for this study. DM4 in red circle, LPB4 in yellow triangle, BAVE1 in purple diamond, BAFT11 in blue square, Z10/6 in green pentagram. Arrow represents the correlation between the U content and the resulting excess of ^{131}Xe from successive nuclear reactions (Section 5.2.2). Arrow fit the data with $R^2 = 0.97$. (For interpretation of the references to colour in this figure legend, the reader is referred to the web version of this article.)

5.3. *Evidence for a step evolution of atmospheric Xe isotopes*

5.3.1. *Observations*

The degree of mass dependent Xe fractionation found in Archean-aged samples appears to be correlated with age, with older samples being more fractionated relative to the modern atmospheric composition than younger samples (Pujol et al., 2011; Avice et al., 2018). In the case of a continuous evolution, the degree of MDF of trapped Xe can in principle be used to estimate an approximate MDF Xe age of the barites using the relation between age and MDF (Holland et al., 2013; Bekaert et al., 2018). Bekaert et al. (2018) proposed a power law fit to the evolution of atmospheric MDF-Xe with time, with MDF$_{Xe}$ (‰.u^{-1}) = 0.238*t(Ga)$^{3.41}$.

The degrees of MDF-Xe of Z10/6 and DM4 as a function of their estimated ages are shown Fig. 5. The MDF-Xe of Z10/6 does not fit the expected power law when using the proposed barite age of 2.8 Ga (Reimer, 1980). According to the Xe evolution model given above, Z10/6 barite would be 3.1 ± 0.2 Ga (1σ). This hypothesis is improbable because the age of the greenstone formations are unlikely older than 2.9 Ga (Wilson et al., 1995). A similar mismatch between the modelled (by MDF$_{Xe}$ dating) and measured ages has already been identified by Avice et al. (2018) in a 2.74 Ga quartz from Fortescue Group, having a MDF-Xe of 13 ± 1.2‰ u^{-1} (1σ). These two samples (Z10/6 and Fortescue) have MDF-Xe comparable to those of older samples such as Barberton quartz (12.9 ± 1.2‰ u^{-1} at 3.3 ± 0.05 Ga, Avice et al., 2017) or North Pole quartz (15 ± 5‰ u^{-1} at 3.1 ± 0.4 Ga, Pujol et al., 2013). Therefore our data taken together with those from Avice et al. (2018) suggest that the evolution of MDF-Xe was potentially not as regular as previously suggested. These samples instead provide supporting evidence for a plateau in the isotopic evolution of atmospheric Xe between 3.3 Ga and 2.7 Ga, as suggested Fig. 5.

Interestingly, DM4 barite appears to present an unexpectedly low MDF-Xe degree of 3.4 ± 0.5‰.u^{-1}. Using the power law from Bekaert et al. (2018), DM4 barite would have a MDF-Xe age of 2.2 ± 0.1 Gyr which is significantly younger than the Neoarchaean age of the surrounding rocks (Wilson et al., 1995). It is possible that DM4 barite (or its trapped fluid inclusions) could be younger that the host rock formation. However, we also note the striking similarity of DM4 MDF-Xe with that

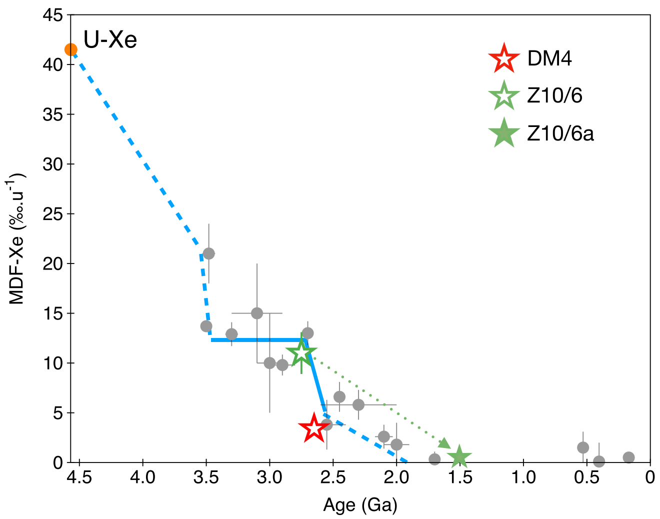

Fig. 5. Evolution of the mass dependent fractionation in ‰.u^{-1} of xenon trapped in samples with variable ages (grey circles, Avice et al. (2018) and ref. therein). U—Xe stands for the initial Xe isotopic composition of the atmosphere (Pepin, 1991). New data from DM4 and Z10/6 samples (from crushing and heating at 800 °C, respectively) are reported as red and green open stars, respectively. Error bars on the age are smaller than symbol size. The green full star represent the potential position of Z10/6a sample if the light isotope excesses are considered spallogenic and not mass-fractionated, and considering the age computed by the ^{130}Ba—^{130}Xe dating system. (For interpretation of the references to colour in this figure legend, the reader is referred to the web version of this article.)

of a 2.55 Ga quartz from Quetico Belt (3.8 ± 2.5‰.u^{-1}, Avice et al., 2018). Taken together, Z10/6 and DM4 MDF support the scenario of a rapid decrease in the atmospheric MDF around 2.5–2.6 Ga (Fig. 5), hence suggesting a disrupted, rather than a regular, evolution of the atmospheric Xe isotopic fractionation over geological periods of time.

Finally, we do not exclude the possibility for the mass fractionation in barite Z10/6 to be the result of secondary cosmogenic production of light Xe isotopes by spallation reaction. If this were the case, sample Z10/6 would not contain any signature of mass fractionated Archean atmosphere. Consequently, to explain why no fractionated ancient atmosphere were found in this fluid inclusion-rich sample, we could consider that the age of the barite was over-estimated. Fig. 5 shows the position Z10/6 would have if it is considered to not contain ancient atmospheric Xe in its fluid inclusion, and assuming that the formation age computed by the ^{130}Ba—^{130}Xe dating system of ~1.5 Ga were accurate.

5.3.2. Potential implications

5.3.2.1. Origin of the mass dependent fractionation of atmospheric Xe. The currently favoured explanation to account for both the depletion of atmospheric Xe relative to other noble gases and the evolution of its isotopic composition through time (i.e., the “xenon paradox”, Ozima and Podosek (2002)) is the progressive escape to space of Xe^{+} ions, dragged away from the Earth by escaping H^{+} during the Archean and Hadean eons (Avice et al., 2018; Zahnle et al., 2019).

The evolution of atmospheric Xe isotopes through time therefore relates to how much hydrogen escaped from the Earth, and hence the evolution of Earth’s oxidation state over time. However, to account for both Xe’s fractionation and depletion, Zahnle et al. (2019)‘s hydrodynamic escape model predicts that Xe escape must have been limited to small apertures or short episodes. It suggests that Xe escape was restricted to polar windows by a geomagnetic field, or dominated by outburst of high solar activity, or limited to transient episodes of abundant hydrogen, or a combination of these. These outcomes in Zahnle et al. (2019)‘s model appear in very good agreement with our suggestion of a discontinuous (rather than a regular and protracted) evolution of atmospheric Xe’s isotope fractionation and escape to space. Better constraining the duration and extent of these bursts of atmospheric Xe escape will be critical to determine the exact amount of H that has been lost to space over geological times, and hence constrain both the evolution of the mass of the ocean and the oxidation of the Earth’s surface through time. Given that changes in the atmospheric Xe isotopes through the Archean stop after the Great Oxidation Event (analogous to the disappearance of sulfur mass independent fractionation signatures in sedimentary rocks, S-MIFs, between 2.5 and 2.4 Ga; Warke et al., 2020), Xe systematics potentially also tell us about O_2 and CH_4 levels in the Hadean and Archean atmosphere (Catling and Zahnle, 2020). S-MIFs are indeed considered to result from the UV photolysis of SO_2 in the oxygen poor Archean atmosphere (Farquhar and Wing, 2003), implying that Xe and S isotopic evolution may be conjointly linked to the evolution of the solar UV flux in the Archean.

Whether the atmospheric Xe isotopic composition evolved continuously or discontinuously would have far reaching implications regarding its potential use as a dating tool, for instance concerning the dating of Archean organic matter (Bekaert et al., 2018; Bekaert et al., 2020b) or regarding the determining of the residence time of groundwaters based on their Xe isotopic composition (Holland et al., 2013). Crucially, a discontinuous evolution of atmospheric Xe isotopes would also potentially impact models simulating the onset age of effective volatile recycling by subduction from Xe isotope systematics (Péron and Moreira, 2018; Parai and Mukhopadhyay, 2018). For instance, a step in Xe isotopic evolution at 2.7 Ga potentially indicates that the atmosphere reached a Xe isotopic composition close to modern composition earlier than previously considered. Although it is at present not possible to predict how much a discontinuous evolution of atmospheric Xe through time would impact the times of subduction onset proposed by Péron and Moreira (2018) and Parai and Mukhopadhyay (2018) (roughly 2.8 Ga and 2.5 Ga, respectively), we speculate that the potential for the atmosphere to have reached a modern-like Xe isotopic composition earlier than previously considered may ultimately lead to a revision of the onset of subduction toward older values.

5.3.2.2. An increase in the atmospheric Xe MDF at the end of the Archean?. The MDF-Xe relative to present-day atmosphere decreased over time, progressively making the overall atmospheric Xe budget isotopically heavier with time. However, published data suggest a potential increase of MDF-Xe around 2.5 Ga from 4‰.u^{-1} at 2.6 Ga to 6.6‰.u^{-1} at 2.45 Ga (Venetry belt quartz, Avice et al., 2018). Such an increase could have resulted from the contribution of mantle Xe having a chondritic composition to the already fractionated atmospheric Xe. This would require intense mantle degassing occurring at that time, independently proposed to account for the change of the ^{129}Xe deficit in the Archean atmosphere (Marty et al., 2019). However, mass balance predicts that intense mantle degassing at that time would be insufficient by one order of magnitude to supply enough mantle-derive chondritic Xe to change the MDF-Xe degree of the Archean atmosphere (Supplementary Materials). Therefore we suspect that the apparent MDF-Xe inversion around 2.5 Ga is an artefact on the real evolution of atmospheric Xe due to the lack of precision on both MDF-Xe calculation and sample ages. Improving the precision of atmospheric Xe’s isotopic evolution through time will help better understand the process(es) and conditions under which it was mass fractionated. Specifically, more constraints on Xe atmospheric fractionation around 2.7–2.4 Ga appear to be critical to better understand the atmospheric hydrodynamic processes that led to the Great Oxidation Event between 2.50 Ga and 2.43 Ga (Sessions et al., 2009; Warke et al., 2020).

6. Conclusion

We analysed the Xe isotopic composition of five barites dated from

3.5 Ga to 1.8 Ga through crushing and step-heating. Extractions at high temperature (1300 °C and 1800 °C) revealed variable excesses in ^{131}Xe isotope for the five barites, up to 3000% for barite BAFT11, resulting from neutron capture on ^{130}Ba. ^{130}Xe excesses were also identified, but too low to compute ages using the ^{130}Ba—^{130}Xe radioactive decay because of important contributions from the secondary production of cosmogenic xenon isotopes ^{124,126,128,129,130}Xe. Crushing and heating at 800 °C revealed for two barites, DM4 and Z10/6 which contained sufficient fluid inclusions, the isotopic composition of Xe in the atmosphere when they formed. DM4 (~2.6 Ga) and Z10/6 (~2.8 Ga) barites present a Xe isotopic signature mass dependently fractionated by 3.4 ± 0.5‰.u^{-1} and 11 ± 2.1‰.u^{-1}, respectively, relative to the modern atmosphere. Along with previous analyses of Xe in Archean rocks, these results potentially show a step at 2.7 Ga in the evolution of the atmospheric MDF-Xe degree. This suggests that the process fractionating xenon isotopes was discontinuous in time, rather than a regular evolution as previously thought. The main consequence of this observation is the reconsideration of the use of the MDF-Xe degree as a dating tool for Archean aged samples or models of volatile recycling initiation.

The following are the supplementary data related to this article.

Data availability

All data produced and used in this study are given in the excel files in the Supplementary Material.

Declaration of Competing Interest

The authors declare that they have no known competing financial interests or personal relationships that could have appeared to influence the work reported in this paper.

Acknowledgments

This work was funded by the ERC grant No. 695618 to B.M. We thank the S.A.R.M for providing elemental bulk analyses of the barites. We thank Laurent Zimmerman for technical mentorship and assistance. We thank David Byrne for fruitful discussions. We thank the three anonymous reviewers for their comments and suggestions, which significantly improved the paper. This is CRPG contribution 2786.

Appendix A. Supplementary data

Supplementary data to this article can be found online at https://doi.org/10.1016/j.chemgeo.2021.120405.

References

Abbott, D.H., Isley, A.E., 2002. The instensity, occurrence, and duration of superplume events and eras over geological time. J. Geodyn. 34, 265–307. https://doi.org/10.1016/S0264-3707(02)00024-8.

Avice, G., Marty, B., Burgess, R., 2017. The origin and degassing history of the Earth's atmosphere revealed by Archean xenon. Nat. Commun. 8, 1–9. https://doi.org/10.1038/ncomms15455.

Avice, G., Marty, B., Burgess, R., Hofmann, A., Philippot, P., Zahnle, K., Zakharov, D., 2018. Evolution of atmospheric xenon and other noble gases inferred from Archean to Paleoproterozoic rocks. Geochim. Cosmochim. Acta 232, 82–100. https://doi.org/10.1016/j.gca.2018.04.018.

Barabash, A., 2020. Precise Half-Life Values for Two-Neutrino Double-β Decay: 2020 Review. Universe 6 (10), 159.

Basford, J.R., Dragon, J.C., Pepin, R.O., Coscio Jr., M.R., Murthy, V.R., 1973. Krypton and xenon in lunar fines. In: Proceedings of the 4th Lunar Science Conference, pp. 1915–1955.

Bekaert, D.V., Broadley, M.W., Delarue, F., Avice, G., Robert, F., Marty, B., 2018. Archean kerogen as a new tracer of atmospheric evolution: Implications for dating the widespread nature of early life. Sci. Adv. 4, 1–23. https://doi.org/10.1126/sciadv.aar2091s.

Bekaert, D.V., Broadley, M.W., Marty, B., 2020a. The origin and fate of volatile elements on Earth revisited in light of noble gas data obtained from comet 67P/Churyumov-Gerasimenko. Sci. Rep. 10, 1–18. https://doi.org/10.1038/s41598-020-62650-3.

Bekaert, D.V., Broadley, M.W., Delarue, F., Druzhinina, Z., Paris, G., Robert, F., Sugitani, K., Marty, B., 2020b. Xenon isotopes in Archean and Proterozoic insoluble organic matter: a robust indicator of syngenecity? Precambrian Res. 336, 105505. https://doi.org/10.1016/j.precamres.2019.105505.

Broadley, M.W., Ballentine, C.J., Chavrit, D., Dallai, L., Burgess, R., 2016. Sedimentary halogens and noble gases within Western Antarctic xenoliths: Implications of extensive volatile recycling to the sub continental lithospheric mantle. Geochim. Cosmochim. Acta 176, 139–156. https://doi.org/10.1016/j.gca.2015.12.013.

Cadogan, P.H., 1977. Palaeoatmospheric argon in Rhynie chert. Nature 268, 38–41. https://doi.org/10.1038/268038a0.

Carignan, J., Hild, P., Mevelle, G., Morel, J., Yeghicheyan, D., 2001. Routine analyses of trace elements in geological samples using flow injection and low pressure on-line liquid chromatography coupled to ICP-MS: a study of geochemical reference materials BR, DR-N, UB-N, AN-G and GH. Geostand. Newslett. 25, 187–198. https://doi.org/10.1111/j.1751-908x.2001.tb00595.x.

Catling, D.C., Zahnle, K.J., 2020. The Archean atmosphere. Sci. Adv. 6, eaax1420.

Claire, M.W., Sheets, J., Cohen, M., Ribas, I., Meadows, V.S., Catling, D.C., 2012. The evolution of solar flux from 0.1 nm to 160 μm: Quantitative estimates for planetary studies. Astrophys. J. 757 https://doi.org/10.1088/0004-637X/757/1/95.

Drabon, N., Galić, A., Mason, P.R., Lowe, D.R., 2019. Provenance and tectonic implications of the 3.28–3.23 Ga Fig tree Group, Central Barberton greenstone belt, South Africa. Precambrian Res. 325, 1–19.

Farquhar, J., Wing, B.A., 2003. Multiple sulfur isotopes and the evolution of the atmosphere. Earth Planet. Sci. Lett. 213, 1–13. https://doi.org/10.1016/S0012-821X(03)00296-6.

Geng, H., Brandl, G., Sun, M., Wong, J., Kröner, A., 2014. Zircon ages defining deposition of the palaeoproterozoic soutpansberg group and further evidence for eoarchaean crust in South Africa. Precambrian Res. 249, 247–262. https://doi.org/10.1016/j.precamres.2014.05.020.

Gumsley, A.P., Chamberlain, K.R., Bleeker, W., Söderlund, U., De Kock, M.O., Larsson, E.R., Bekker, A., 2017. Timing and tempo of the great oxidation event. Proc. Natl. Acad. Sci. U. S. A. 114, 1811–1816. https://doi.org/10.1073/pnas.1608824114.

Hébrard, E., Marty, B., 2014. Coupled noble gas-hydrocarbon evolution of the early Earth atmosphere upon solar UV irradiation. Earth Planet. Sci. Lett. 385, 40–48. https://doi.org/10.1016/j.epsl.2013.10.022.

Heinrichs, T.K., Reimer, T.O., 1977. A sedimentary barite deposit from the Archean Fig tree Group of the Barberton Mountain Land (South Africa). Econ. Geol. 72, 1426–1441. https://doi.org/10.2113/gsecongeo.72.8.1426.

Hirsch, M., Muto, K., Oda, T., Klapdor-Kleingrothaus, H.V., 1994. Nuclear structure calculation of β+β+, β+/EC and EC/EC decay matrix elements. Zeitschrift für Phys. A Hadron. Nucl. 347, 151–160. https://doi.org/10.1007/BF01292371.

Holland, G., Lollar, B.S., Li, L., Lacrampe-Couloume, G., Slater, G.F., Ballentine, C.J., 2013. Deep fracture fluids isolated in the crust since the Precambrian era. Nature 497, 357–360.

Huston, D.L., Logan, G.A., 2004. Barite, BIFs and bugs: Evidence for the evolution of the Earth's early hydrosphere. Earth Planet. Sci. Lett. 220, 41–55. https://doi.org/10.1016/S0012-821X(04)00034-2.

Jelsma, H.A., Dirks, P.H., 2002. Neoarchaean tectonic evolution of the Zimbabwe Craton. Geol. Soc. Spec. Publ. 199 (1), 183–211.

Kaiser, W.A., 1977. The excitation functions of Ba (p, X) ^{M} Xe (M — 124-136) in the energy range 38-600 MeV; the use of 'cosmogenic' xenon for estimating 'burial' depths and 'real' exposure ages. Philos. Trans. R. Soc. London. Ser. A Math. Phys. Sci. 285, 337–362. https://doi.org/10.1098/rsta.1977.0074.

Lee, J.Y., Marti, K., Severinghaus, J.P., Kawamura, K., Yoo, H.S., Lee, J.B., Kim, J.S., 2006. A redetermination of the isotopic abundances of atmospheric Ar. Geochim. Cosmochim. Acta 70, 4507–4512. https://doi.org/10.1016/j.gca.2006.06.1563.

Li, B., Lee, J.T., Manuel, O.K., 1994. Anomalous 131Xe in barites. Earth Planet. Sci. Lett. 123, 71–79. https://doi.org/10.1016/0012-821X(94)90258-5.

Marty, B., Altwegg, K., Balsiger, H., Bar-Nun, A., Bekaert, D.V., Berthelier, J.J., Bieler, A., Briois, C., Calmonte, U., Combi, M., De Keyser, J., Fiethe, B., Fuselier, S.A., Gasc, S., Gombosi, T.I., Hansen, K.C., Hässig, M., Jäckel, A., Kopp, E., Korth, A., Le Roy, L., Mall, U., Mousis, O., Rème, H., Owen, T., Rubin, M., Sémon, T., Tzou, C.Y., Waite, J.H., Wurz, P., 2017. Xenon isotopes in 67P/Churyumov-Gerasimenko show that comets contributed to Earth's atmosphere. Science (80-.) 356, 1069–1072. https://doi.org/10.1126/science.aal3496.

Marty, B., Bekaert, D.V., Broadley, M.W., Jaupart, C., 2019. Geochemical evidence for high volatile fluxes from the mantle at the end of the Archaean. Nature 575, 485–488. https://doi.org/10.1038/s41586-019-1745-7.

Meshik, A., Pravdivtseva, O., 2017. Weak Decay of Tellurium and Barium Isotopes in Geological Samples: Current Status, 020702, pp. 2016–2018. https://doi.org/10.7566/jpscp.14.020702.

Meshik, A.P., Hohenberg, C.M., Pravdivtseva, O.V., Kapusta, Ya.S., 2001. Weak decay of 130Ba and 132Ba: geochemical measurements. Phys. Rev. C 64, 352051–352056. https://doi.org/10.1103/PhysRevC.64.035205.

Ozima, M., Podosek, F.A., 2002. Noble gas Geochemistry, second ed. Cambridge University Press, Cambridge.

Parai, R., Mukhopadhyay, S., 2018. Xenon isotopic constraints on the history of volatile recycling into the mantle. Nature 560, 223–227.

Pepin, R.O., 1991. On the origin and early evolution of terrestrial planet atmospheres and meteoritic volatiles. Icarus 92, 2–79. https://doi.org/10.1016/0019-1035(91)90036-S.

Péron, S., Moreira, M., 2018. Onset of volatile recycling into the mantle determined by xenon anomalies. Geochemical Perspect. Lett. 9, 21–25. https://doi.org/10.7185/geochemlet.1833.

Porcelli, D., Ballentine, C.J., 2002. Models for distribution of terrestrial noble gases and evolution of the atmosphere. Rev. Mineral. Geochem. 47, 411–480.

Pujol, M., Marty, B., Burnard, P., Philippot, P., 2009. Xenon in Archean barite: Weak decay of 130Ba, mass-dependent isotopic fractionation and implication for barite formation. Geochim. Cosmochim. Acta 73, 6834–6846. https://doi.org/10.1016/j.gca.2009.08.002.

Pujol, M., Marty, B., Burgess, R., 2011. Chondritic-like xenon trapped in Archean rocks: a possible signature of the ancient atmosphere. Earth Planet. Sci. Lett. 308, 298–306. https://doi.org/10.1016/j.epsl.2011.05.053.

Pujol, M., Marty, B., Burgess, R., Turner, G., Philippot, P., 2013. Argon isotopic composition of Archaean atmosphere probes early Earth geodynamics. Nature 498, 87–90. https://doi.org/10.1038/nature12152.

Reimer, T.O., 1980. Archean sedimentary baryte deposits of the Swaziland Supergroup (Barberton Mountain Land, South Africa). Precambrian Res. 12, 393–410. https://doi.org/10.1016/0301-9268(80)90037-6.

Reimer, T.O., 1990. Archaean barite deposits of Southern Africa. J. Geol. Soc. India 35, 131–150.

Reimer, T.O., 1995. The Proterozoic baryte deposits of southern Africa. In: Barton, J.M., Copperthwaite, Y.E. (Eds.), Extended Abstracts, Centennial Geocongress. Rand Afrikaans University, Johannesburg, pp. 99–102.

Ribas, I., Guinan, E.F., Gudel, M., Audard, M., 2005. Evolution of the Solar activity over Time and Effects on Planetary Atmospheres. I. High-Energy Irradiances (1–1700 a). Astrophys. J. 622, 680–694. https://doi.org/10.1086/427977.

Sessions, A.L., Doughty, D.M., Welander, P.V., Summons, R.E., Newman, D.K., 2009. The continuing puzzle of the great oxidation event. Curr. Biol. 19, R567–R574.

Srinivasan, B., 1976. Barites: anomalous xenon from spallation and neutron-induced reactions. Earth Planet. Sci. Lett. 31, 129–141. https://doi.org/10.1016/0012-821X(76)90104-7.

Stuart, F.M., Mark, D.F., Gandanger, P., McConville, P., 2016. Earth-atmosphere evolution based on new determination of Devonian atmosphere Ar isotopic composition. Earth Planet. Sci. Lett. 446, 21–26. https://doi.org/10.1016/j.epsl.2016.04.012.

Ulrich, M.R., Bodnar, R.J., 1988. Systematics of stretching of fluid inclusions; II, Barite at 1 atm confining pressure. Econ. Geol. 83, 1037–1046.

Van Kranendonk, M.J., Kröner, A., Hegner, E., Connelly, J., 2009. Age, lithology and structural evolution of the c. 3.53 Ga Theespruit Formation in the Tjakastad area, southwestern Barberton Greenstone Belt, South Africa, with implications for Archaean tectonics. Chem. Geol. 261, 115–139. https://doi.org/10.1016/j.chemgeo.2008.11.006.

Vermeesch, P., 2018. IsoplotR: a free and open toolbox for geochronology. Geosci. Front. 9, 1479–1493. https://doi.org/10.1016/j.gsf.2018.04.001.

Warke, M.R., Di Rocco, T., Zerkle, A.L., Lepland, A., Prave, A.R., Martin, A.P., Ueno, Y., Condon, D.J., Claire, M.W., 2020. The great oxidation event preceded a paleoproterozoic “snowball earth”. Proc. Natl. Acad. Sci. U. S. A. 117, 13314–13320. https://doi.org/10.1073/pnas.2003090117.

Wilson, J.F., Nesbitt, R.W., Fanning, C.M., 1995. Zircon geochronology of Archaean felsic sequences in the Zimbabwe craton: a revision of greenstone stratigraphy and a model for crustal growth. Geol. Soc. Spec. Publ. 95, 109–126. https://doi.org/10.1144/GSL.SP.1995.095.01.07.

Yokochi, R., Marty, B., Pik, R., Burnard, P., 2005. High ^{3}He/^{4}He ratios in peridotite xenoliths from SW Japan revisited: Evidence for cosmogenic ^{3}He released by vacuum crushing. Geochem. Geophys. Geosyst. 6, n/a. https://doi.org/10.1029/2004GC000836.

Zahnle, K.J., Gacesa, M., Catling, D.C., 2019. Strange messenger: a new history of hydrogen on Earth, as told by Xenon. Geochim. Cosmochim. Acta 244, 56–85. https://doi.org/10.1016/j.gca.2018.09.017.

Zimmermann, L., Avice, G., Blard, P.H., Marty, B., Füri, E., Burnard, P.G., 2018. A new all-metal induction furnace for noble gas extraction. Chem. Geol. 480, 86–92. https://doi.org/10.1016/j.chemgeo.2017.09.018.

Appendix C

“The end of the isotopic evolution of atmospheric xenon“, article published in Geochemical Perspectives Letters in 2022

Geochemical Perspectives Letters

The end of the isotopic evolution of atmospheric xenon

L. Ardoin[1,2]*, M.W. Broadley[1], M. Almayrac[1], G. Avice[3], D.J. Byrne[1], A. Tarantola[4], A. Lepland[5], T. Saito[6], T. Komiya[7], T. Shibuya[6], B. Marty[1]

Abstract

https://doi.org/10.7185/geochemlet.2207

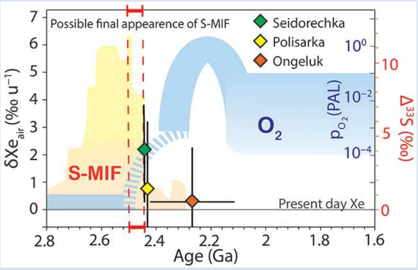

Noble gases are chemically inert and, as such, act as unique tracers of physical processes over geological timescales. The isotopic composition of atmospheric xenon, the heaviest stable noble gas, evolved following mass-dependent fractionation throughout the Hadean and Archaean aeons. This evolution appears to have ceased between 2.5 and 2.1 Ga, around the time of the Great Oxidation Event (GOE). The coincidental halting of atmospheric Xe evolution may provide further insights into the mechanisms affecting the atmosphere at the Archaean-Proterozoic transition. Here, we investigate the isotopic composition of Xe trapped in hydrothermal quartz from three formations around the GOE time period: Seidorechka and Polisarka (Imandra-Varzuga Greenstone Belt, Kola Craton, Russia) with ages of 2441 ± 1.6 Ma and 2434 ± 6.6 Ma, respectively, and Ongeluk (Kaapvaal Craton, South Africa) dated at 2114 ± 312 Ma (Ar-Ar age) with a host formation age of 2425.6 ± 2.6 Ma (upper bound). From these analyses we show that Xe isotope fractionation appears to have ceased during the time window delimited by the ages of the Seidorechka and Polisarka Formations, which is concomitant with the disappearance of mass-independent fractionation of sulfur isotopes (MIF-S) in the Kola Craton. The disappearance of Xe isotope fractionation in the geological record may be related to the rise in atmospheric oxygen and, thus, can provide new insights into the triggering mechanisms and timing of the GOE.

Received 29 October 2021 | Accepted 1 February 2022 | Published 10 March 2022

Introduction

Due to their chemical inertness, noble gases (He, Ne, Ar, Kr, Xe) constitute powerful geochemical tracers for constraining physical processes occurring in the Earth's atmosphere. Atmospheric xenon is of particular interest because its isotopic composition is highly mass-dependently fractionated (MDF) by 41.5 ‰ u^{-1} when compared to its presumed primitive ancestor U-Xe (Pepin, 1991). Studies of palaeo-atmospheric Xe trapped in Archaean rocks (mainly as fluid inclusions in hydrothermal quartz) have shown that the evolution of isotopic fractionation of Xe was a long-term process that took place during the Hadean and the Archaean aeons. This protracted MDF appears to be unique to Xe, with no evidence that the other noble gases underwent progressive fractionation (Pujol *et al.*, 2011; Avice *et al.*, 2018; Almayrac *et al.*, 2021). Such Xe specific evolution has been attributed to preferential, non-thermal escape of xenon from the Earth's atmosphere to space upon ionisation by solar UV photons (Pujol *et al.*, 2011; Hébrard and Marty, 2014; Avice *et al.*, 2018) and subsequent entrainment by escaping hydrogen ions (Zahnle *et al.*, 2019). Available data indicate that the evolution of the isotopic composition of atmospheric xenon ceased at some point between 2.6 and 1.8 Ga (Avice *et al.*, 2018).

Xenon is the second atmospheric element for which a stable isotope fractionation during the Archaean aeon has been observed, with the mass-independent fractionation of sulfur isotopes (MIF-S) being characteristic for Archaean age samples (Farquhar and Wing, 2003; Philippot *et al.*, 2018). The MIF-S signature was likely produced by interactions between volcanic sulfur species and ultraviolet radiation, and shows a sharp transition and collapse during the Great Oxidation Event (GOE) (Farquhar and Wing, 2003). Conversely, the Xe isotope evolution was a gradual and cumulative process, causing atmospheric Xe to become increasingly fractionated with time. Furthermore, the GOE is understood to have stopped the generation of MIF-S, as ozone from free oxygen in the atmosphere shielded solar UV photons. For Xe, it is not clear if the GOE was also responsible for stopping Xe^+ escape, and which environmental parameters (*e.g.*, atmospheric composition, hydrogen escape, solar activity) may have changed to prevent Xe from escaping the Earth's atmosphere.

---

1. Université de Lorraine, CNRS, CRPG, F-54000 Nancy, France
2. Now at: Université Libre de Bruxelles CP160/03 Av. F.D. Roosevelt 50, 1050 Brussels, Belgium
3. Université de Paris, Institut de physique du globe de Paris, CNRS, F-75005 Paris, France
4. Université de Lorraine, CNRS, GeoRessources laboratory, BP 70239, F-54506, Vandœuvre-lès-Nancy, France
5. Geological Survey of Norway, 7491 Trondheim, Norway
6. Institute for Extra-cutting-edge Science and Technology Avant-garde Research (X-star), Japan Agency for Marine-Earth Science and Technology (JAMSTEC), 2-15, Natsushima-cho, Yokosuka 237-0061, Japan
7. Department of Earth Science and Astronomy, University of Tokyo, Tokyo, Meguro, 153-8902, Japan
* Corresponding author (email: lisa.ardoin@ulb.be)

In order to investigate the end of atmospheric MDF-Xe and to assess if it was coincidental with the GOE, we have analysed noble gases extracted from fluid inclusions from well-characterised hydrothermal quartz with ages encompassing that of the GOE. Using a new cumulative crushing technique, adapted from the procedure first used by Péron and Moreira (2018), allows the extraction of gas from much larger sample quantities, resulting in smaller analytical uncertainties (Supplementary Information). This is required to detect the low levels of Xe fractionation relative to the modern atmosphere that are observed close to the GOE. The samples measured in this study are, from oldest to youngest, Seidorechka (FD1A) and Polisarka (FD3A) Sedimentary Formations (Imandra-Varzuga Greenstone Belt, Kola Craton, Russia), and from the Ongeluk Formation (Kaapvaal Craton, South Africa). Depositional ages of FD1A and FD3A have been constrained between 2501.5 ± 1.7 Ma and 2441 ± 1.6 Ma (Amelin *et al.*, 1995), and 2441 ± 1.6 Ma and 2434 ± 6.6 Ma (Brasier *et al.*, 2013), respectively. The lower bounds of these time intervals are defined by the ages of overlying volcanic formations that are considered contemporaneous with quartz veining in underlying sediments. The Ongeluk Formation has been dated at 2114 ± 312 Ma (Ar-Ar age; Saito *et al.*, 2018) with an upper bound defined by the host formation age of 2425.6 ± 2.6 Ma (Gumsley *et al.*, 2017).

Preservation of Ancient Atmospheric Xe

Fluid inclusions can potentially preserve the noble gas signature of the ancient atmosphere (Pujol *et al.*, 2011). The petrographical study of the inclusions of the Ongeluk Formation performed by Saito *et al.* (2018) and our study of samples from the Kola Craton (FD1A and FD3A) indicate that a majority of the fluid inclusions have been trapped during quartz growth (Supplementary Information). The Ar and Xe content of the quartz fluid inclusions were measured using a Thermofisher Helix MC Plus© mass spectrometer at CRPG. The new extraction method was performed on FD1A and FD3A and consists of accumulating the extracted gases after crushing steps in an empty and previously evacuated steel bottle (Péron and Moreira, 2018; Péron *et al.*, 2021).

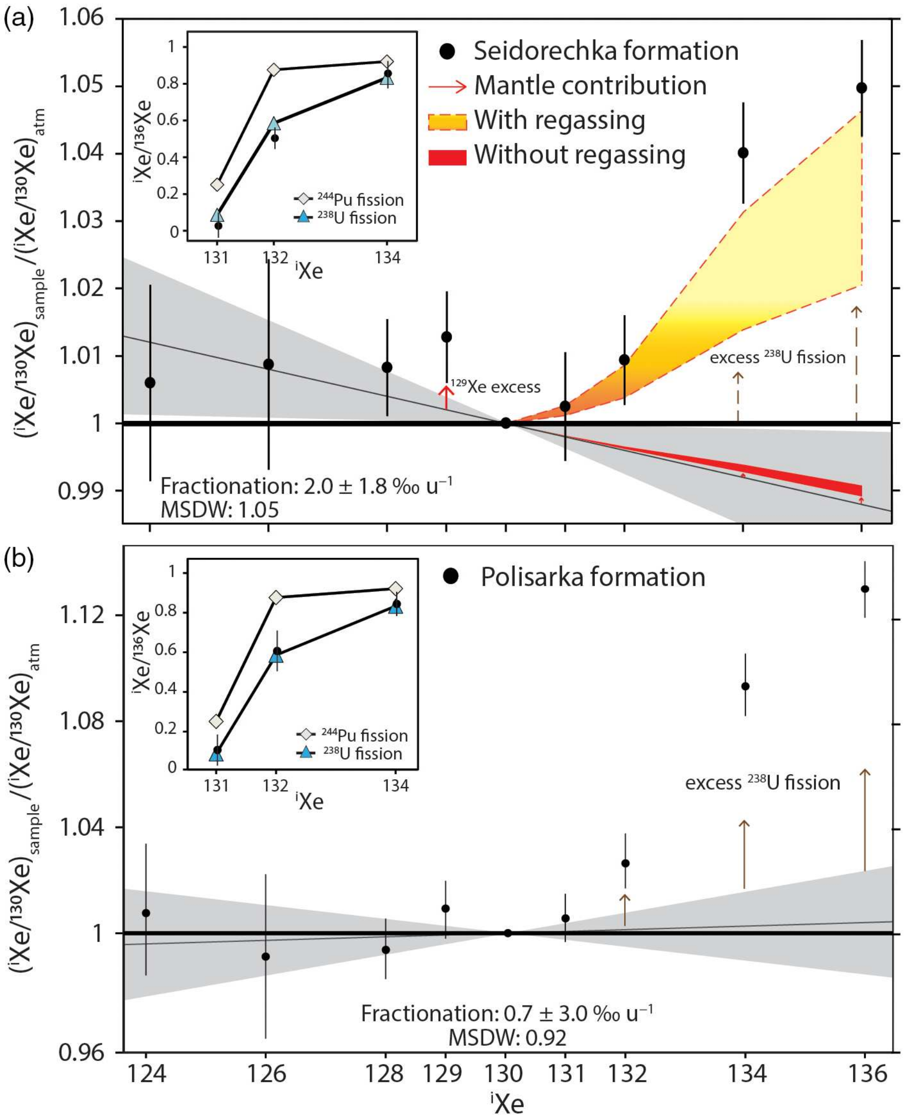

Figure 1 Isotopic spectrum of Xe released from fluid inclusions in **(a)** sample FD1A and **(b)** sample FD3A. The grey line and its associated envelope (2σ) correspond to the isotopic trend of the ^{124,126,128,130}Xe. **(a)** Mantle excesses of ^{131,132,134,136}Xe are estimated using the ^{129}Xe excess (Supplementary Information). Individual error bars are at 2σ.

Table 1 Isotopic ratio of the noble gases released by crushing and Xe fractionation. The fractionation was calculated from the ^{124,126,128}Xe/^{130}Xe ratios. The ratios are the weighted average of several replicates (Table S-3).

Samples	^{124}Xe	^{126}Xe	^{128}Xe	^{129}Xe	^{131}Xe	^{132}Xe	^{134}Xe	^{136}Xe	^{40}Ar/^{36}Ar	Xe Fractionation (‰ u^{-1})
	^{130}Xe = 1									
Air Ozima and Podosek (2002)	0.0234	0.0218	0.4715	6.496	5.213	6.607	2.563	2.176	298	
Ongeluk fm	0.0233	0.0220	0.4707	6.540	5.188	6.632	2.603	2.229	4570	**−0.3**
errors (2σ)	±0.0005	±0.0004	±0.0040	±0.066	±0.050	±0.640	±0.220	±0.020	±1488	±2.4
FD1A	0.0235	0.0220	0.4745	6.578	5.235	6.669	2.666	2.284	3010	**−2.0**
errors (2σ)	±0.0004	±0.0004	±0.0034	±0.026	±0.068	±0.044	±0.0192	±0.016	±504	±1.8
FD3A	0.0235	0.0216	0.4684	6.554	5.243	6.778	2.801	2.458	3639	**0.7**
errors (2σ)	±0.0006	±0.0006	±0.0054	±0.056	±0.044	±0.056	±0.028	±0.024	±610	±3.0

All our analyses present an excess of ^{40}Ar relative to modern atmospheric Ar with a minimum ^{40}Ar/^{36}Ar ratio of 1760 ± 18, from one crush of the Ongeluk Formation (Table S-4), attesting to limited exchange, if any, with modern atmospheric Ar. The ^{131,132,134,136}Xe excesses detected for all our samples correspond to a contribution from the spontaneous fission of ^{238}U (Fig. 1). We computed linear regressions on ^{124,126,128}Xe/^{130}Xe isotope ratios using the IsoplotR software (Vermeesch, 2018). The oldest sample, FD1A, presents a fractionation of 2.0 ± 1.8 ‰ u^{-1} (2σ; Fig. 1a) compared to the present day atmosphere. The FD3A (0.7 ± 3.3 ‰ u^{-1}, Fig. 1b) and Ongeluk quartz (–0.3 ± 2.4 ‰ u^{-1}, Fig. S-2), the youngest samples, do not display a resolvable MDF-Xe signature beyond uncertainty at 2σ (Table 1). Compared to modern atmospheric Xe (^{129}Xe/^{130}Xe = 6.50; Ozima and Podosek, 2002), the samples preserve small excesses of radiogenic ^{129}Xe (^{129}Xe/^{130}Xe of 6.58 ± 0.04, 6.55 ± 0.06 and 6.54 ± 0.07 for FD1A, FD3A and Ongeluk Formation samples, respectively). It is the opposite of what is usually observed in samples from the Archaean aeon (Avice *et al.*, 2017; Bekaert *et al.*, 2018). The monoisotopic depletion in ^{129}Xe within the Archaean atmosphere is thought to have been compensated by the progressive release of ^{129}Xe from the mantle throughout the Archaean aeon (Marty *et al.*, 2019). The ^{129}Xe excess in the oldest sample, FD1A, is therefore likely to be due to a local input of mantle-derived Xe in the hydrothermal fluids from which the quartz precipitated. A mantle Xe input could potentially account for the light Xe isotope excesses measured in the samples, especially when considering Xe in the Archaean mantle was likely primordial (chondritic; Broadley *et al.*, 2020). We ruled out this possibility because the ^{128}Xe/^{130}Xe of FD1A is inconsistent with mixing between the primordial mantle and modern atmosphere (Fig. S-4), and atmospheric regassing of the mantle was likely to be inefficient during the Archaean aeon (Péron and Moreira, 2018). Mantle contributions are then negligible (Table S-1; Supplementary Information) and excesses of ^{124,126,128}Xe in FD1A are considered to reflect the ancient atmospheric composition.

Link between Xe Fractionation and MIF-S

From our analyses we have shown, for the first time, that MDF-Xe signals disappear between two well-characterised Kola Craton sedimentary formations, implying that the fractionation process stopped between 2441 ± 1.6 Ma and 2434 ± 6.6 Ma (Fig. 2). Previous data from Avice *et al.* (2018) indicated that MDF-Xe was observable throughout the Archaean and into the Palaeoproterozoic era until 2 Ga. The difference between these previous data and our new results can be explained by (i) the age of the fluid inclusions containing the atmospheric Xe, and (ii) the precision required to distinguish between the present day atmosphere and the small extent of isotope fractionation of Xe present in fluid inclusion formed close to the cessation of Xe evolution. The fluid inclusion inventory reflects the atmospheric composition at the last equilibration with the atmosphere, which may be different from the age of quartz precipitation. Thus, the 6.5 ± 1.5 ‰ u^{-1} recorded in the 3.7 Ga Isua rocks that was attributed to a resetting metamorphic event at 2.3 Ga (Avice *et al.*, 2018) may, in fact, reflect an older atmospheric composition. Because the gas accumulation method is more precise than those used previously (Avice *et al.*, 2018), we could identify a slight MDF-Xe for sample FD1A at the 2σ precision level. Considering the 2σ error range for the fractionation of Xe in previously studied 2.1 ± 0.1 Ga Gaoua (Burkina Faso) and the 2.0 ± 0.1 Ga Carnaiba (Brazil) samples gives values of 2.6 ± 4.2 and 1.8 ± 4.4 ‰ u^{-1} for the fractionation of atmospheric Xe (Avice *et al.*, 2018). These values are both within uncertainty of modern atmosphere, and therefore it is not clear whether they, in fact, contained a fractionated atmospheric Xe signature.

The MDF-Xe evolution results from a poorly understood cumulative process, which took place during the Hadean and Archaean periods. Storage of Xe^{+} into an organic haze and the contemporary loss of the residual Xe from space could explain the observed fractionation (Hébrard and Marty, 2014). This process would stop in an O_2-rich atmosphere that would halt the production of the haze. However, this possibility would still necessitate the escape of non-trapped Xe and therefore an additional, not yet identified, process is required. The escape of hydrogen ions to space entraining Xe^{+} has been also previously suggested to account for both the oxidation of the atmosphere and the unique fractionation of Xe isotopes (Zahnle *et al.*, 2019). Consequently, this model leads to the oxidation of the surface reservoirs, including the crust, to the point where O_2 became stable enough to compete with atmospheric reduced gases, such as H_2 and CH_4 (Zahnle *et al.*, 2019). According to our data, the MDF-Xe signal disappears and the present day composition is reached between ~2441 and ~2434 Ma (Fig. 2). Sustaining a continuous escape of ionised hydrogen from the Earth formation until the GOE depends on many parameters including the strength of the Earth's magnetic field, the level of solar extreme ultraviolet (EUV) irradiation and the amount of hydrogen present in the atmosphere (Zahnle *et al.*, 2019). In the case of discrete escape episodes rather than a constant rate of atmospheric Xe-loss, our results imply a final burst occurring simultaneously with the initiation of the GOE.

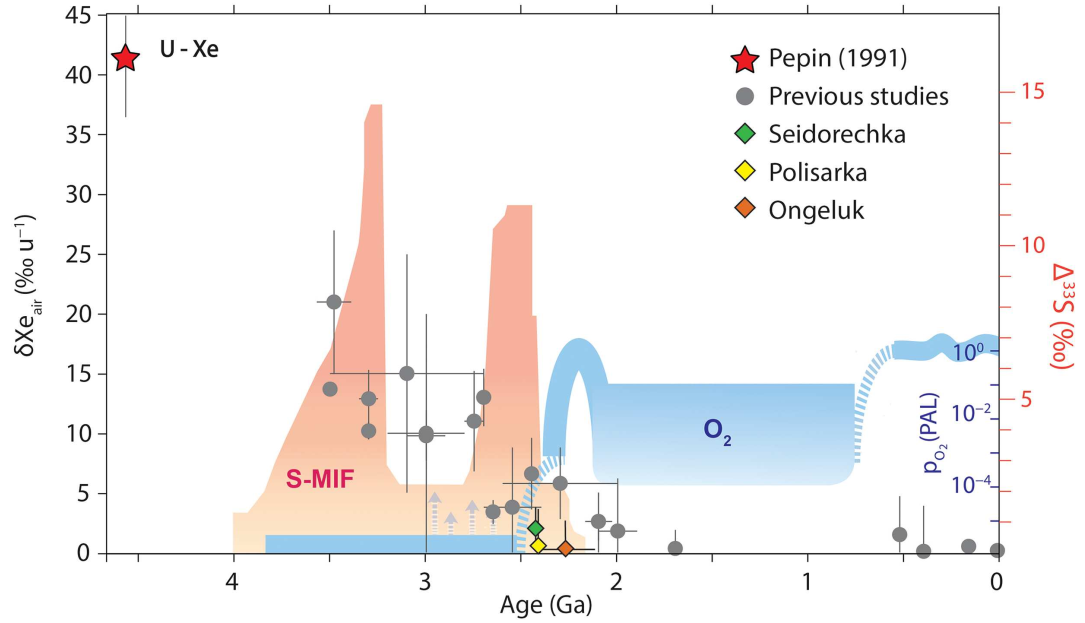

Figure 2 Records of atmospheric oxygen (O_2, blue; Lyons *et al.*, 2014), mass-independent fractionation of sulfur isotopes (MIF-S, orange; data from Killingsworth *et al.*, 2019) and mass dependent fractionation of xenon isotopes throughout Earth's history (Pepin, 1991; Avice *et al.*, 2018; Almayrac *et al.*, 2021), uncertainties are at 2σ.

The end of MDF-Xe between FD1A and FD3A is coincident with the disappearance of MIF-S as recorded in the sedimentary rocks hosting the quartz veins (Warke *et al.*, 2020). Sulfur isotopes represent an instantaneous record of the oxidation states of the atmosphere, at a local scale. MDF-Xe is the result of a cumulative process at global scale so it is likely that these geochemical markers would not be exactly simultaneous in their cessation. In light of the S-Xe relationship, it appears that the atmospheric process traced by Xe isotopes is linked with the oxidation state of the terrestrial atmosphere (Avice *et al.*, 2018).

The formation of the ozone layer as a consequence of O_2 rise in the atmosphere accounts for the end of the MIF-S signature (Farquhar and Wing, 2003; Lyons *et al.*, 2014). However, MIF-S signals could be preserved under oxidative weathering and then obscure the MIF/MDF transition due to a memory effect (Philippot *et al.*, 2018). This leads to a delay between the rise of oxygen and the disappearance of MIF-S signals of about 2.32 Ga (Gumsley *et al.*, 2017; Poulton *et al.*, 2021). Moreover, some environments may require more time to adapt and become permanently oxygenated after the end of hydrogen escape (Lyons *et al.*, 2014). Contrary to the MIF-S, hydrodynamic escape is not affected by the ozone formation (Zahnle *et al.*, 2019), and may be more sensitive to O_2 availability. Thus, the end of MDF-Xe fractionation could mark the time when atmospheric escape of hydrogen ceased, and ceased to contribute to the change of the redox ratio of Earth's surface reservoirs. It is important to underline the fact that Xe fractionation is a cumulative process: local variation of the signal cannot occur, unlike sulfur (Philippot *et al.*, 2018). In light of this, Xe is a reliable tracer and may better constrain the rise of oxygen levels within the atmosphere.

Conclusion

We have measured an isotopically fractionated Xe composition of 2.0 ± 1.8 ‰ u^{-1} relative to modern atmosphere at 2441 ± 1.6 Ma. A slightly younger sample of 2434 ± 6.6 Ma does not record any such fractionation, and is indistinguishable from the modern atmospheric composition. The disappearance of isotopically fractionated Xe signals could be a consequence of O_2 accumulation in the atmosphere. A temporal link between the disappearance of the Xe isotopes fractionation and the MIF-S signature at the Archaean-Proterozoic transition is clearly established for the Kola Craton. The mass-dependent evolution of Xe isotopes is the indication of a cumulative atmospheric process that may have played an important role in the oxidation of the Earth's surface (Zahnle *et al.*, 2019), independently of biogenic O_2 production that started long before the permanent rise of O_2 in the atmosphere (Lyons *et al.*, 2014).

Acknowledgements

This study was supported by the European Research Council (ERC) under the European Union's Horizon 2020 research and innovation programme (PHOTONIS Advanced Grant # 695618). We thank the Super-Cutting-Edge Grand and Advanced Research (SUGAR) Program, Institute for Extra-Cutting-Edge Science and Technology Avant-Garde Research (X-star). We thank Laurent Zimmerman for technical mentorship and assistance. Christophe Thomazo is thanked for the sampling opportunity. The anonymous reviewers are thanked for their constructive suggestions.

Editor: Maud Boyet

Additional Information

Supplementary Information accompanies this letter at https://www.geochemicalperspectivesletters.org/article2207.

Cite this letter as: Ardoin, L., Broadley, M.W., Almayrac, M., Avice, G., Byrne, D.J., Tarantola, A., Lepland, A., Saito, T., Komiya, T., Shibuya, T., Marty, B. (2022) The end of the isotopic evolution of atmospheric xenon. *Geochem. Persp. Let.* 20, 43–47. https://doi.org/10.7185/geochemlet.2207

References

Almayrac, M.G., Broadley, M.W., Bekaert, D.V., Hofmann, A., Marty, B. (2021) Possible discontinuous evolution of atmospheric xenon suggested by Archean barites. *Chemical Geology* 581, 120405. https://doi.org/10.1016/j.chemgeo.2021.120405

Amelin, Yu. V., Heaman, L.M., Semenov, V.S. (1995) U-Pb geochronology of layered mafic intrusions in the eastern Baltic Shield: Implications for the timing and duration of Paleoproterozoic continental rifting. *Precambrian Research* 75, 31–46. https://doi.org/10.1016/0301-9268(95)00015-W

Avice, G., Marty, B., Burgess, R. (2017) The origin and degassing history of the Earth's atmosphere revealed by Archean xenon. *Nature Communications* 8, 15455. https://doi.org/10.1038/ncomms15455

Avice, G., Marty, B., Burgess, R., Hofmann, A., Philippot, P., Zahnle, K., Zakharov, D. (2018) Evolution of atmospheric xenon and other noble gases inferred from Archean to Paleoproterozoic rocks. *Geochimica et Cosmochimica Acta* 232, 82–100. https://doi.org/10.1016/j.gca.2018.04.018

Bekaert, D.V., Broadley, M.W., Delarue, F., Avice, G., Robert, F., Marty, B. (2018) Archean kerogen as a new tracer of atmospheric evolution: Implications for dating the widespread nature of early life. *Science Advances* 4, eaar2091. https://doi.org/10.1126/sciadv.aar2091

Brasier, A.T., Martin, A.P., Melezhik, V.A., Prave, A.R., Condon, D.J., Fallick, A.E. (2013) Earth's earliest global glaciation? Carbonate geochemistry and geochronology of the Polisarka Sedimentary Formation, Kola Peninsula, Russia. *Precambrian Research* 235, 278–294. https://doi.org/10.1016/j.precamres.2013.06.007

Broadley, M.W., Barry, P.H., Bekaert, D.V., Byrne, D.J., Caracausi, A., Ballentine, C.J., Marty, B. (2020) Identification of chondritic krypton and xenon in Yellowstone gases and the timing of terrestrial volatile accretion. *Proceedings of the National Academy of Sciences* 117, 13997–14004. https://doi.org/10.1073/pnas.2003907117

Farquhar, J., Wing, B.A. (2003) Multiple sulfur isotopes and the evolution of the atmosphere. *Earth and Planetary Science Letters* 213, 1–13. https://doi.org/10.1016/S0012-821X(03)00296-6

Gumsley, A.P., Chamberlain, K.R., Bleeker, W., Söderlund, U., De Kock, M.O., Larsson, E.R., Bekker, A. (2017) Timing and tempo of the Great Oxidation Event. *Proceedings of the National Academy of Sciences* 114, 1811–1816. https://doi.org/10.1073/pnas.1608824114

Hébrard, E., Marty, B. (2014) Coupled noble gas–hydrocarbon evolution of the early Earth atmosphere upon solar UV irradiation. *Earth and Planetary Science Letters* 385, 40–48. https://doi.org/10.1016/j.epsl.2013.10.022

Killingsworth, B.A., Sansjofre, P., Philippot, P., Cartigny, P., Thomazo, C., Lalonde, S.V. (2019) Constraining the rise of oxygen with oxygen isotopes. *Nature Communications* 10, 4924. https://doi.org/10.1038/s41467-019-12883-2

Lyons, T.W., Reinhard, C.T., Planavsky, N.J. (2014) The rise of oxygen in Earth's early ocean and atmosphere. *Nature* 506, 307–315. https://doi.org/10.1038/nature13068

Marty, B., Bekaert, D.V., Broadley, M.W., Jaupart, C. (2019) Geochemical evidence for high volatile fluxes from the mantle at the end of the Archaean. *Nature* 575, 485–488. https://doi.org/10.1038/s41586-019-1745-7

Ozima, M., Podosek, F.A. (2002) *Noble Gas Geochemistry*. Second Edition, Cambridge University Press, Cambridge. https://doi.org/10.1017/CBO9780511545986

Pepin, R.O. (1991) On the origin and early evolution of terrestrial planet atmospheres and meteoritic volatiles. *Icarus* 92, 2–79. https://doi.org/10.1016/0019-1035(91)90036-S

Péron, S., Moreira, M. (2018) Onset of volatile recycling into the mantle determined by xenon anomalies. *Geochemical Perspectives Letters* 9, 21–25. https://doi.org/10.7185/geochemlet.1833

Péron, S., Mukhopadhyay, S., Kurz, M.D., Graham, D.W. (2021) Deep-mantle krypton reveals Earth's early accretion of carbonaceous matter. *Nature* 600, 462–467. https://doi.org/10.1038/s41586-021-04092-z

Philippot, P., Ávila, J.N., Killingsworth, B.A., Tessalina, S., Baton, F., Caquineau, T., Muller, E., Pecoits, E., Cartigny, P., Lalonde, S.V., Ireland, T.R., Thomazo, C., van Kranendonk, M.J., Busigny, V. (2018) Globally asynchronous sulphur isotope signals require re-definition of the Great Oxidation Event. *Nature Communications* 9, 2245. https://doi.org/10.1038/s41467-018-04621-x

Poulton, S.W., Bekker, A., Cumming, V.M., Zerkle, A.L., Canfield, D.E., Johnston, D.T. (2021) A 200-million-year delay in permanent atmospheric oxygenation. *Nature* 592, 232–236. https://doi.org/10.1038/s41586-021-03393-7

Pujol, M., Marty, B., Burgess, R. (2011) Chondritic-like xenon trapped in Archean rocks: A possible signature of the ancient atmosphere. *Earth and Planetary Science Letters* 308, 298–306. https://doi.org/10.1016/j.epsl.2011.05.053

Saito, T., Qiu, H.N., Shibuya, T., Li, Y.B., Kitajima, K., Yamamoto, S., Ueda, H., Komiya, T., Maruyama, S. (2018) Ar–Ar dating for hydrothermal quartz from the 2.4 Ga Ongeluk Formation, South Africa: Implications for seafloor hydrothermal circulation. *Royal Society Open Science* 5, 180260. https://doi.org/10.1098/rsos.180260

Vermeesch, P. (2018) IsoplotR: A free and open toolbox for geochronology. *Geoscience Frontiers* 9, 1479–1493. https://doi.org/10.1016/j.gsf.2018.04.001

Warke, M.R., Di Rocco, T., Zerkle, A.L., Lepland, A., Prave, A.R., Martin, A.P., Ueno, Y., Condon, D.J., Claire, M.W. (2020) The Great Oxidation Event preceded a Paleoproterozoic "snowball Earth". *Proceedings of the National Academy of Sciences* 117, 13314–13320. https://doi.org/10.1073/pnas.2003090117

Zahnle, K.J., Gacesa, M., Catling, D.C. (2019) Strange messenger: A new history of hydrogen on Earth, as told by Xenon. *Geochimica et Cosmochimica Acta* 244, 56–85. https://doi.org/10.1016/j.gca.2018.09.017

Résumé de la thèse en français

Ce travail de thèse questionne l'origine des comètes et leur évolution au sein du système solaire depuis les dernières 4,56 milliards d'années. Les comètes, étant principalement composées de silicates, de matière organique et de glace, font partie des corps les plus riches en éléments volatils du système solaire. Ces éléments volatils, tel que l'hydrogène (H), l'azote (N) et le carbone (C) jouent un rôle majeur dans les processus physiques et chimiques de formation planétaire, et font parti des éléments indispensables au développement de la vie telle qu'on la connaît sur Terre. A ce jour, la mission Rosetta par l'Agence Spatiale Européenne (ESA) en 2014 sur la comète 67P/Churyumov-Gerasimenko (67P/C-G) est la seule mission à avoir étudié avec précision la composition (élémentaire et isotopique) des éléments volatils présent dans la queue d'une comète. Ces données précieuses ont apporté des arguments importants en faveur de l'apport d'éléments cométaires sur Terre, mais dont la nature et l'origine demeurent pour la plupart encore incomprises.

L'objectif de cette thèse était de créer en laboratoire des glaces dites « cométaires », c'est-à-dire formée à très basse températures (entre ~25K et 80K) et pressions (~10^{-5} à 10^{-8} mbar), et d'étudier le comportement des éléments volatils contenu dans ces glaces. En comparant ces mesures aux mesures effectuées sur la comète 67P/C-G, l'idée est d'apporter des contraintes (température, composition initiale) sur l'environnement de formation des comètes. Pour cela, l'étude se focalise sur les gaz rares lourds, argon, krypton et xénon (qui ont été mesurée sur 67P/C-G) et l'azote (sous forme de diazote N_2), qui sont des éléments volatils inertes chimiquement, et dont les comportements élémentaires et isotopiques dépendent uniquement des processus physiques qui peuvent avoir lieu dans les glaces cométaires.

I. Développements expérimentaux au « Laboratoire Gaz Rares »

La majeure partie de cette thèse a été consacrée au développement du dispositif expérimentale EXCITING (Exporing Xenon in Cometary Ices by Trapping and Irradiating Noble Gases) permettant la formation de glace cométaire, présenté **Figure A**. EXCITING est composé de tubes en acier dans lesquels la pression est maintenu autour de 10^{-8} mbar par une pompe turbo-moléculaire, et à travers lesquels des gaz peuvent circuler d'un volume à un autre. Ce dispositif permet de condenser des mélanges (initialement sous forme gazeuse) de N_2, de gaz rares et d’eau (l’espèce majoritaire dans les glaces cométaires) sur une plaque refroidie jusqu’à 28K, la température présumée de formation des glaces cométaires (Rubin et al. 2015).

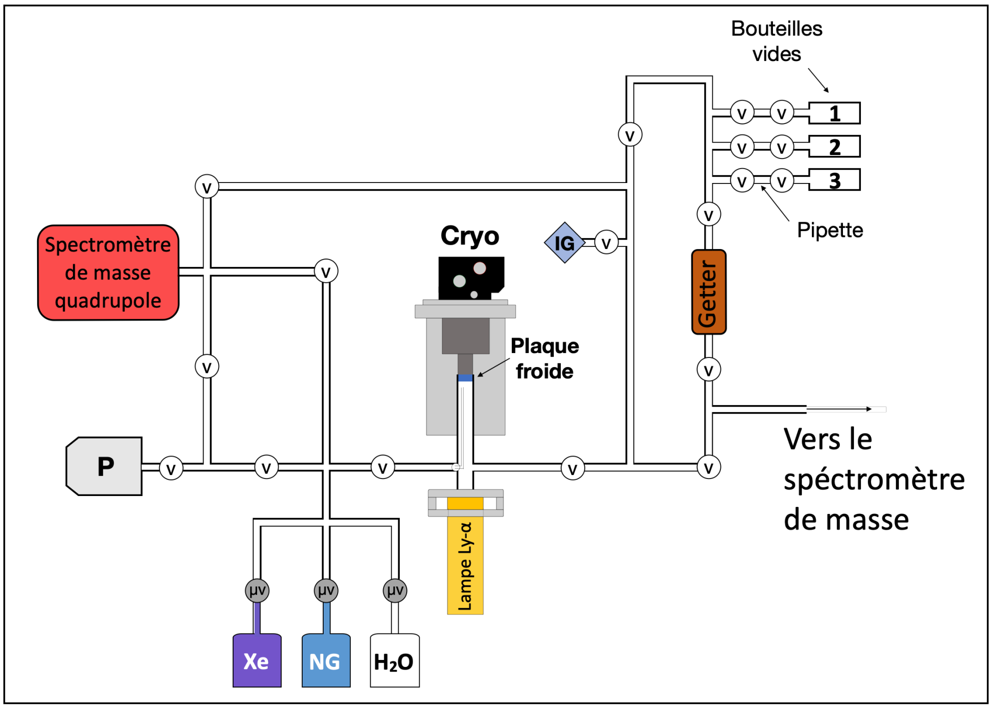

Figure A : Schéma du dispositif expérimental EXCITING. v : vanne ultra-vide. µv : vanne micrométrique à contrôle de flux. Cryo : système cryogénique (ou piège cryogénique). IG : gauge ionique. P : pompe turbo-moléculaire. La bouteille « NG » contient un mélange de gaz rares (Ne, Ar, Kr et Xe) et de diazote (N_2).

Lors de la phase de chauffage de la glace, qui simulerait l’évolution thermique d’une comète qui entrerait dans le système solaire interne, les gaz libérés par la glace peuvent être analysés par un spectromètre de masse quadrupole (QMS) pour leur abondance, ou par spectrométrie de masse statique gaz rare pour leurs isotopes. Une autre part importante de la thèse a été le développement de l’analyse de l’argon et du xénon sur un spectromètre GV Instrument Helix MC, et de l’azote sur un Thermo Fisher Helix MC$^+$.

II. Comportement élémentaire des gaz rares et de l’azote dans les glaces cométaires

Toute la thèse repose sur l’observation suivante : lors de la formation d’une glace cométaire à basse pression et température à partir de la condensation d’eau (principalement) et d’autres éléments traces (comme les gaz rares), cette glace a une structure amorphe (et non pas cristalline comme sur Terre par exemple) et est capable de piéger une grande quantité d’éléments volatils dans sa structure (Ghormley 1967). Lors du réchauffement d’une telle glace, les éléments volatils non-piégés sublime à leur température respective (entre 40K et 80K pour les gaz rares par exemple), puis les phases piégées sont libérées plus tardivement, vers 145K, lorsque la glace amorphe se transforme en glace cristalline (Bar-Nun et al. 1985), avant la sublimation de l'eau vers 160K (**Figure B**). La composition de cette phase piégée (qui est celle que l'on retrouve dans la queue des comètes, comme mesurée sur 67P/C-G) dépend des conditions initiales en température et en composition (Notesco et al. 2003), et peut donc apporter des contraintes sur l'environnement de formation des glaces cométaires.

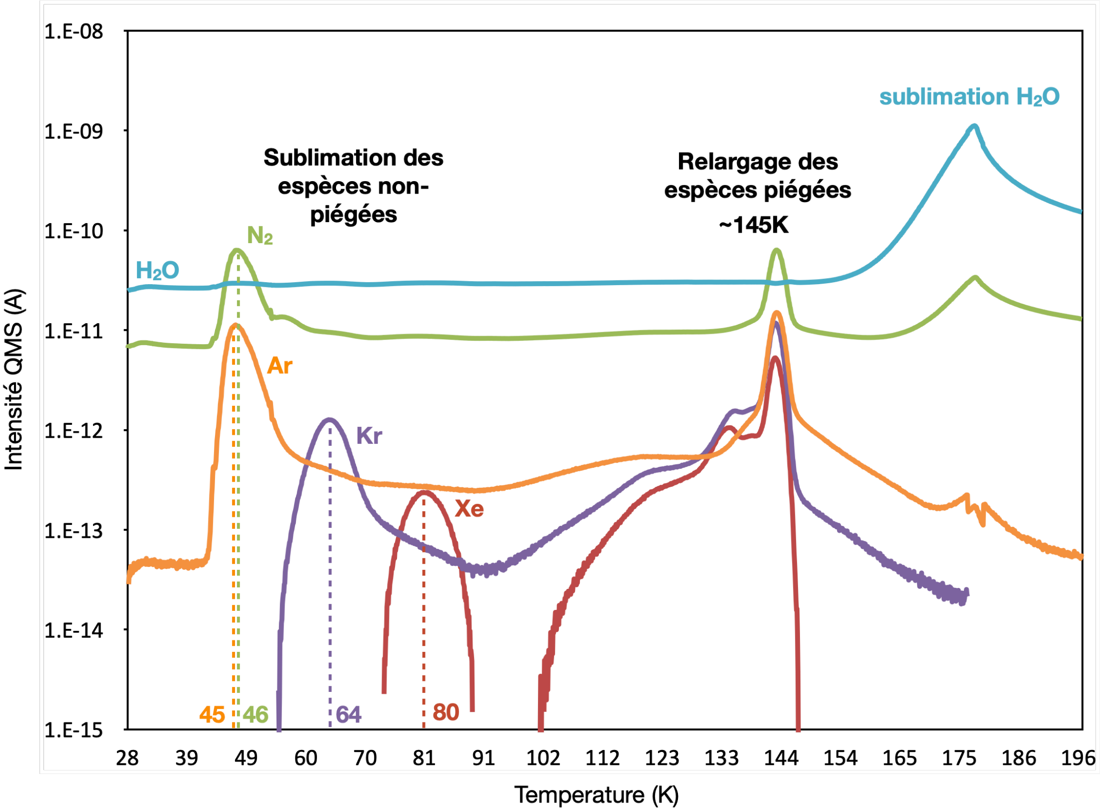

Figure B : Libération de N_2, Ar, Kr, Xe et H_2O pendant le chauffage de 28 à 200 K à une vitesse de 1 K/min d'une expérience commençant par un mélange H_2O:N2:Ar:Kr:Xe. Une fraction de chaque espèce est condensée sur, ou sous, la glace d'eau et se sublime une fois la température de sublimation atteinte. Les fractions piégées dans la glace sont libérées simultanément à environ 145 K, avant que l'eau ne commence à se sublimer à 160 K. Notez l'échelle logarithmique pour l'intensité du signal.

J'ai réalisé des séries d'expériences avec des glaces formées à différentes températures (28K, 40K, 50K, 60K, 70K et 80K) et rapport H_2O:gaz rares, pour comparer avec les expériences passées de Bar-Nun & Owen (1998) et Notesco et al. (2003) ainsi que la composition en Ar, Kr et Xe de la comète 67P/C-G (Rubin et al. 2018). Ces données sont reportées **Figure C**. Nous obtenons que ce sont des températures de formation autour de 70K qui permettent au mieux de reproduire les rapports élémentaires ^{132}Xe/^{36}Ar et ^{84}Kr/^{36}Ar de la comète 67P/C-G. Le rapport $^{28}N_2/^{36}Ar$ de la comète, plus élevé que la composition solaire (Lodders 2003) est aussi reproduit par EXCITING. Cette température de formation conteste le milieu interstellaire, ou les nuages moléculaire, où la température avoisine les 10-30K (Le Petit et al. 2004), comme environnement de formation des glaces cométaires, et favorise par conséquent une formation plus tardive dans la nébuleuse proto-solaire.

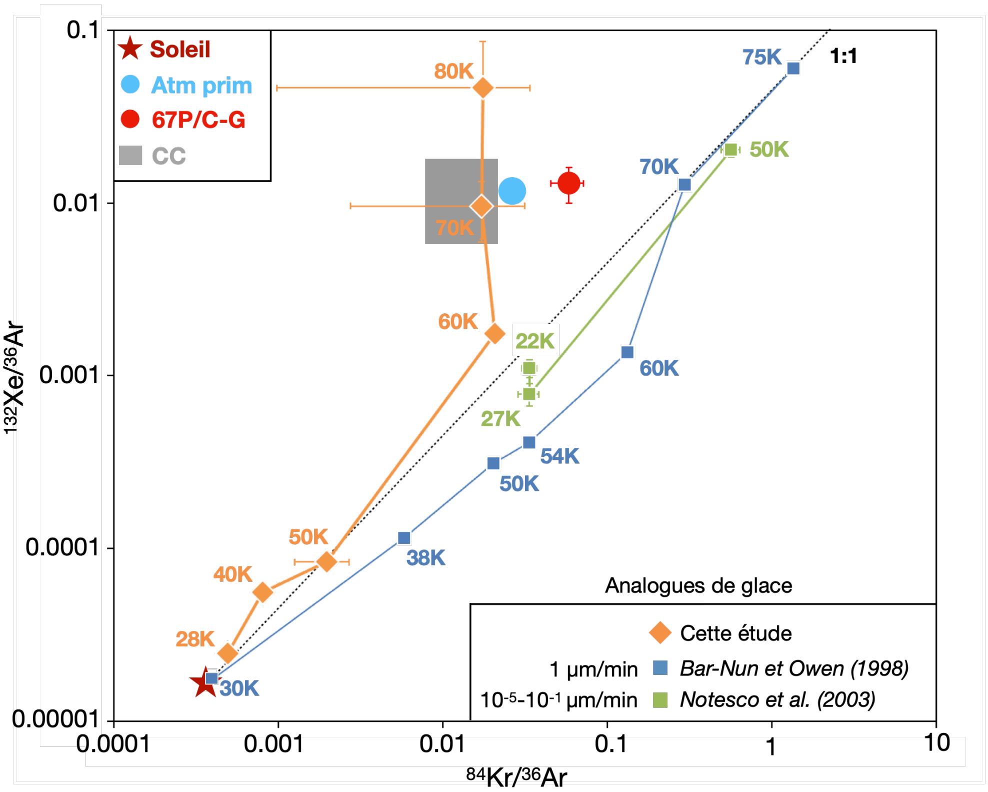

Figure C : $^{84}Kr/^{36}Ar$ vs $^{132}Xe/^{36}Ar$ avec différent pôles cosmochimique notable : Soleil (Lodders 2003 ; Meshik et al. 2014), CC (gamme de composition des chondrites carbonées, compilation de Bekaert et al. 2020), 67P/C-G (comète 67P/Churyumov-Gerasimenko, Rubin et al. 2018) et Atm prim (composition initiale de l'atmosphère avant l'échappement atmosphérique du xénon, Zahnle et al. 2018). Les carrés (bleu et vert, de Bar-Nun & Owen (1998) et de Notesco et al. (2003), respectivement) et losanges orange (cette étude) montrent la composition des glaces cométaires expérimentales en considérant une composition initiale de type solaire, selon différentes températures de formation. Les barres d'incertitudes sont l'écart type d'expériences répétées à 1 σ. Notre étude et celle de Bar-Nun & Owen montrent une augmentation en $^{132}Xe/^{36}Ar$ lorsque les glaces sont formées au-delà de 60K. Bien que cette déviation de la droite 1:1 soit nécessaire pour reproduire la composition de 67P/C-G, aucune de ces expériences n'y parvient.

III. Comportement isotopique des gaz rares et de l'azote dans les glaces cométaires

En plus de la composition « élémentaire » en azote et gaz rares des glaces formées par EXCITING, j'ai réalisé des analyses isotopiques ultra-précises (de l'ordre du ‰) du N_2, Ar et Xe en utilisant la spectrométrie de masse statique gaz rares. Ces analyses isotopiques avaient pour objectif de tester si les signatures isotopiques exotiques présentes dans les comètes (très différentes de la signature solaire ou celles des météorites pour l'azote et le xénon) pouvaient être produite par le piégeage de ces éléments dans la glace amorphe des comètes. Les analyses des 3 isotopes de l'argon (^{36,38,40}Ar) et 7 du xénon (^{128,129,130,131,132,134,136}Xe) ont été réalisées pour les phases non-piégées et piégées dans les glaces d'EXCITING, pour des températures de formation entre 28K et 80K. Après de nombreux paramètres expérimentaux testé pour s'assurer des résultats, il se trouve que le piégeage de ces gaz rares dans la glace amorphe et leur relargage ne modifie pas leur signature isotopique de façon significative. Notamment, les variations en xénon de la comète 67P/C-G (Marty et al. 2017) par rapport à la composition solaire, qui a apporté la première preuve directe de l'apport d'élément cométaire sur Terre, n'ont pas pu être reproduites. Concernant la composition isotopique en azote des comètes, avec des rapports ^{15}N/^{14}N (δ^{15}N = +900 ‰, Bockelée-Morvan et al. 2015) largement supérieur à la composition atmosphérique (δ^{15}N = 0 ‰, Nier 1950) ou solaire (δ^{15}N = -400 ‰, Marty et al. 2011), celle-ci a été étudiée grâce au développement des mesures isotopique d'azote par spectrométrie gaz rare au cours de la thèse. L'azote piégé dans une glace formée à 50K sur EXCITING est bien enrichie en isotope lourd, mais seulement d'une dizaine de ‰ (Figure D), négligeable par rapports aux larges excès en ^{15}N des comètes. Cela semble indiqué que les fractionnements isotopiques (de l'azote mais aussi du xénon) mesurés dans les comètes sont des signatures héritées de leur environnement de formation, et non pas obtenu par fractionnement isotopique de gaz de composition de type solaire/nébuleuse proto-solaire lors du piégeage dans la glace amorphe.

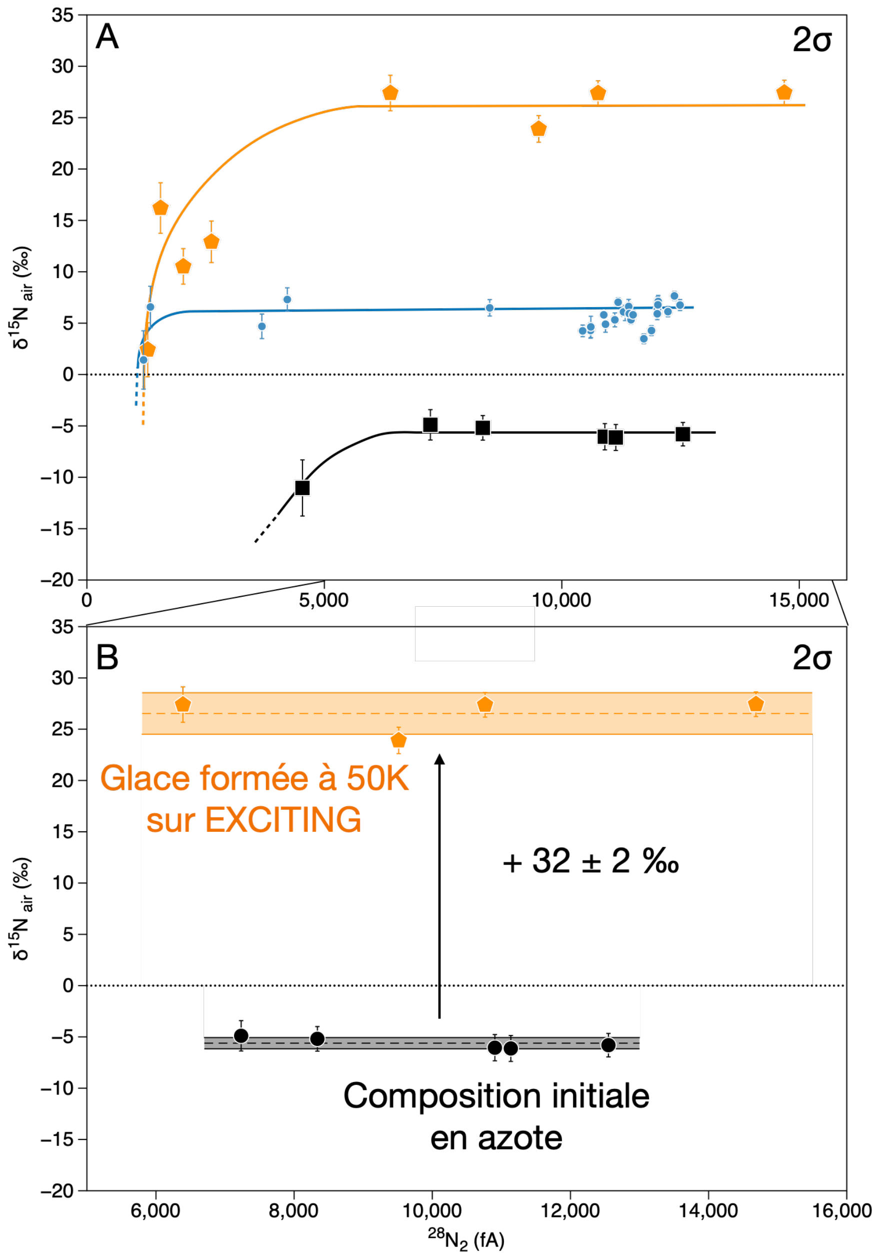

Figure D : **a.** Composition isotopique de l'azote, en déviation en ‰ par rapport à la composition atmosphérique (Nier, 1950), du gaz initial utilisé sur EXCITING (carrés noirs), des gaz étalons (cercles bleus) et des glaces formées à 50K (pentagones orange), en fonction de l'abondance de $^{28}N_2$ mesurée. Les lignes montrent qu'en dessous d'une certaine abondance de N_2, la composition isotopique n'est plus linéaire avec la taille du signal. **b.** Même graphique centré là où la composition en azote du gaz initial est linéaire. Les enveloppes représentent l'erreur standard des analyses multiples. La glace formée à 50K est enrichie en isotope lourd ^{15}N de ~32‰ par rapport à la composition de départ. Toutes les incertitudes sont à 2σ.